Spray Evaporative Cooling of Vibrating Surfaces with Application to Automotive Combustion Engines

Jisjoe Thalackottore Jose

A Thesis Submitted Towards the Requirement for the Degree of

Doctor of Philosophy

University of Sussex

September 2019

ABSTRACT

This thesis examines spray evaporative cooling of vibrating surfaces with application to automotive engines. Two-phase evaporative cooling is advantageous because it uses the latent heat of vaporisation which has a much higher transfer rate than single-phase forced convection as employed in conventional engine cooling systems. There is no existing literature on the effect of boundary motion in spray boiling heat transfer. A theoretical and experimental study of spray boiling heat transfer conducted for engine vibration conditions are presented. Numerical simulations using Volume of Fluid method are presented to investigate droplet impingent and onset of evaporation on vibrating surfaces. Experimental investigation of spray boiling heat transfer on vibrating surfaces is presented. Control of engine evaporative cooling using a transient 1D conduction model that represent the engine cylinder head wall is investigated using a spray boiling heat transfer correlation. A Proportional Integral (PI) control model for evaporative cooling, created using Matlab Simulink, that solves 1D transient conduction through a cylinder head, is presented. Simulations were undertaken for control of the gas-side metal temperature of the cylinder head for step-by-step change in engine load from full-load to half-load. Results showed that control is achieved under one second during the engine load changes with total gas-side metal temperature fluctuations being less than 5 ^{O}C.

Numerical simulations were undertaken for a droplet with a diameter of 49 micrometer impinging on a vibrating surface for a range of vibration amplitudes and frequencies of 0.02 mm to 10 mm, and 1000 Hz to 10 Hz, respectively. An enhancement of heat transfer is seen at high frequencies, whereas heat transfer deteriorated at high amplitudes. To verify theoretical findings three experimental rigs have been designed and built as part of a research team effort. Experiments of spray boiling heat transfer at two different sub-cooling levels (5 ^{o}C and 15^{o}C) are presented for wall vibration amplitudes and frequencies of 0.02 mm to 7 mm, and 400 Hz to 10 Hz, respectively. An enhancement of heat transfer was seen at high frequencies for 15 ^{o}C sub-cooling, whereas heat transfer deteriorated at high amplitudes for both degrees of sub-cooling. Numerical simulation results are qualitatively compared to experimental results, to check whether any correlation in heat transfer exists between a spray and a droplet. The heat transfer from droplet evaporation was found to be only half that of the spray evaporation experiments and it was concluded that, no obvious correlation exists. Experimental results are analysed against vibrational Reynolds number and it was found that heat transfer starts to deteriorate after a vibrational Reynolds number of 1000. A dynamic correlation was created by adding a term containing vibrational Reynolds number to an existing correlation. This was to calculate critical heat flux for vibrating surfaces.

ACKNOWLEDGEMENTS

I would like to express my sincere gratitude to my supervisor Professor Julian Dunne who supported me throughout the four years of my studies by offering invaluable guidance and suggestions about not only studies but also life as a research student.

I would like to thank my second supervisor Dr Luise Ponce Cuspinera, who provided me with invaluable suggestions about research throughout the progression of my studies.

My special thanks to Dr Chris Long for helping me with test rig experiments, and also for guidance on heat transfer problems as well as experimental research.

I would like to thank Senior Technician Mr Ian Wallis at the University of Sussex workshop for all his help with manufacturing the required parts for the test rigs, who also provided great ideas regarding the design of components.

My special thanks to Fellow research student Mr Alireza Sarmadian, who spent countless number of hours in helping me with conducting experiments.

I would like to sincerely thank all the project members of the ESPSRC Evaporative Cooling Systems project.

I would like to thank Jean-Pierre and Joan for all the love and support they showed me throughout my life here as a student.

Last but not least, I would like to thank my parents and sister, for their never-ending love and support that helped me get here.

Table of Contents

List of Figures

List of Tables

Chapter 1. INTRODUCTION

Executive Summary

Current highly downsized engines make use of almost all the potential of conventional cooling systems. Conventional cooling systems use single phase convection. But a cooling system with higher heat removal capabilities is required for higher power, more compact downsized engines, particularly for hybrid electric vehicles. Boiling utilises latent heat of vaporisation which provides a much higher heat flux with less liquid (compared to forced convection), and spray boiling has the highest heat removal capability among all types of boiling, which could be used to cool engines. It is also very efficient owing to the use of latent heat. First, a review of engine evaporative cooling systems is conducted. The review shows that evaporatively cooled engines have not entered series production even though all the published work states the many advantages exist. These advantages include: higher efficiency owing to reduced parasitic losses, more even temperatures across the cooled surfaces, and better knock control. The reasons however that these systems have not reached series production (and any associated disadvantages) remain unknown as the published literature lacks this information. A review of different types of boiling is given which includes pool boiling, flow boiling, and spray boiling. It was found that the effect of surface vibration has hardly been studied. This is one major area where evaporatively cooled engines could have a problem because engines vibrate significantly during its operation. It was also found that control of engine evaporative cooling was only marginally mentioned in the literature.

Based on these findings, the objectives of the study were set to gain a better understanding of the control of evaporative cooling as well as the effect of surface vibration on spray evaporative heat transfer. As spray evaporative cooling heat transfer has very high heat removal capabilities, this was the mode of heat transfer chosen in the study.

First, to examine control of spray evaporative cooling of an engine, a one-dimensional, transient conduction, control model was created. This was designed to control the gas-side metal temperature of an engine cylinder-head. Cooling of the coolant-side metal was exploited by a nucleate boiling heat flux correlation model for spray evaporation. Simulations were undertaken for step-by-step load changes of the engine load from full-load to half-load. A Proportional Integral (PI) controller was employed to control the nozzle flow rate and the results showed that sufficient control could be achieved within one second under engine load changes.

To establish the effect of vibration on full spray evaporative heat transfer, it is unfortunately computationally extremely expensive to simulate full spray evaporation. Simulating droplet

impingement and evaporation is however much more practical, owing to its reduced complexity. In fact single droplet simulation results can be compared with measured spray evaporative heat transfer, to establish whether there is any correlation between the two. Droplet impingement dynamics and onset of evaporation simulations were therefore conducted for the range of amplitudes and frequencies of 0.02 mm to 10 mm, and 1000 Hz to 10 Hz, respectively. These amplitudes and frequencies cover the range of vibration produced by modern downsized engines. Results showed that at higher frequencies, there is an enhancement in heat transfer, whereas for high amplitudes, heat transfer deteriorates.

In order to understand the effect of vibrating surfaces on spray evaporative heat transfer, an experimental dynamic test rig was designed, manufactured, and commissioned at the University of Sussex for the testing of spray evaporation on flat vibrating surfaces. The research was undertaken alongside an EPSRC-funded Evaporative Cooling Systems project in the Dynamics, Control, and Vehicle Research Group. The project also involved design and build of a static pool boiling rig and a static spray boiling rig. The dynamic rig, with a test piece representing an engine cylinder-head geometry was also created. The author was involved in the design of three rigs, which paved the way for the flat surface test piece for the dynamic rig. The objective of the static pool boiling rig, and the static spray boiling rig, were to gain experience in taking temperature measurements for pool boiling as well as spray boiling. The engine cylinder-head geometry test piece on the dynamic rig was to undertake experiments to check the effect of vibrating surfaces on overall cooling of a test piece that approximated a real engine. Temperature at only one point was measured to indicate cooling. The flat surface test piece was designed to restrict heat transfer in one dimension, and was fitted with thermocouples at multiple locations to measure heat flow.

Experiments were conducted using the dynamic rig with a flat test piece for the range of amplitudes and frequencies of 0.02 mm to 7 mm, and 400 Hz to 10 Hz, respectively. Two sub-cooling levels were used and the results showed that, for stationary conditions, the critical heat flux for the 5 ^{o}C sub-cooling was higher than the 15 ^{o}C sub cooling. Comparing the stationary results with vibrating cases, for the sub-cooling of 5 ^{o}C, showed an enhancement in the critical heat flux at high frequencies. For both the sub-cooling levels, critical heat flux had deteriorated at high amplitudes. The lowest critical heat fluxes for both the sub-cooling levels were measured at an amplitude of 7 mm, where the reduction in critical heat fluxes were ~60.5 % and ~55.5 % respectively.

These experimental results were compared qualitatively with single droplet simulations, where only the onset of evaporation was simulated. The heat flux values from the simulations turned out to be only half that of the measured critical heat fluxes from the experiments. Even though, for both the

experiments and simulations, heat flux values were high at high frequencies and lower at high amplitudes. The magnitude of the differences in the heat flux between simulation and measurement, for similar vibration conditions, was very high. This indicates that simulation of droplet impingement and onset of evaporation results cannot be used to correlate full spray evaporative heat transfer.

A dimensionless number was employed for further analysis of experimental results with respect to vibration. The Vibrational Reynolds Number (Re_v) was used to do this. Analysis of the critical heat flux with respect to Re_v showed that at low Re_v (i.e below 1000), the critical heat flux was close to the stationary condition. Critical heat flux started to deteriorate with increase in Re_v above 1000. With increasing Re_v (i.e. above 1000), the critical heat flux continues to decrease. A correlation, including an additional term of Re_v, was created by modifying the Mudawar and Estes [1] correlation for critical heat flux. This correlation is for calculating the spray evaporative critical heat flux with respect to boundary motion, and can be used for control simulation and design.

Background

A conventional automotive *internal combustion engine* (ICE) is generally cooled by single-phase liquid convection but a considerable amount of fuel energy is lost to the coolant owing to the large amount of liquid flowing to the areas of the engine that can operate at higher temperatures. High coolant velocities are required to cool the areas of engine with high heat flux but this overcool other parts of the engine. Even though precision cooling of engines addresses this challenge by having different cross sectional areas to achieve different flow rates, for the areas of the engine with different heat fluxes, a uniform temperature throughout the cylinder-head is still not achieved [2]. The coolant mass could be reduced by adopting more compact coolant jackets but this would impose unacceptable flow, pressure and pumping losses. Moreover, to increase fuel efficiency and to reduce emissions, engines are being increasingly downsized. This reduces the area available for heat transfer, resulting in an increase of heat rejection per unit area. The available thermal data for highly downsized engines shows that conventional cooling systems are almost running at their limit with cooling heat fluxes of up to 1.2 MW/m^2. And the large temperature difference in very high temperature areas causes localized nucleate boiling. Therefore boiling is one form of heat transfer that is already being used to cool engines [2]. But it is also very important for future engines to be as compact and light as possible for use in hybrid electric vehicles as range extender generators. It is therefore very likely that such aggressively downsized engines, with very compact cooling jackets, will need to exploit more areas of localised cooling using nucleate boiling. This trend towards more localised boiling justifies the switch to total evaporative cooling.

Evaporative cooling systems (ECS) have the potential to only need very small amounts of coolant to cool high heat flux areas because the enthalpy of vaporisation is being utilised. Therefore, a smaller coolant pump can be used, which results in a significant reduction in parasitic losses. Two-phase spray evaporative cooling also offers very specific advantages such as a more uniform temperature distribution across cooled surfaces which gives better control over knock and noxious emissions. ECS are already used in air coolers, power plant, and electronics [3]. Heat flux in boiling is many times higher than single-phase convection, which makes it suitable for cooling high heat fluxes. Boiling can generally be classified into three types: pool boiling, flow boiling, and spray boiling. Of these three, spray boiling offers the highest rate of heat transfer with the minimum coolant flow rates. Pais et al [4], in their experiments, measured heat fluxes of up to 12MW/m^2 under laboratory conditions, which is approximately ten times higher than the maximum heat flux (critical heat flux) in pool boiling. This makes spray evaporative boiling the most promising candidate for cooling automotive ICEs but there are several unexplored challenges that needs to be examined.

For example, the physics involved in spray impingement, the formation of liquid film, and its subsequent boiling, is not yet fully understood. The heat transfer, which is of most interest from a cooling perspective, can be calculated by different empirical correlations developed by various researchers based on their experimental results. However, these experiments were undertaken on static heating surfaces. But the hot cooling surfaces on an automotive engine are always 'moving' while the engine is running [3]. There has hardly been any previous experimental work performed on spray boiling with vibrating boundaries. Although some numerical simulations have been published, none of these are experimentally verified. It is therefore imperative to look into the effect of boundary motion, both theoretically and experimentally, on spray impingement dynamics, and the heat transfer associated with it. It will help to create predictive models and correlations for spray evaporative heat transfer under boundary motion. Developed models and correlations could be used to design and control of evaporative cooling systems. The study of impingement dynamics of a spray is at present not practical numerically. But studies involving a single droplet are potentially possible. It is hypothesised that data generated for a single droplet could be used to predict the heat transfer associated with a cloud of droplets, essentially a spray, by adding new parameters (arising from a comparative study of spray and droplet boiling). This approach can then be verified using the experiments. Focusing on a fundamental study of a single droplet and what can be learned from it in relation to a full evaporative spray is the main activity of this thesis. As the literature shows, an approach involving moving boundaries, is wholly appropriate.

1.1. Literature Review

The literature review starts by reviewing previous engine evaporative cooling systems. It provides the history of the development of engine ECS, starting with the earliest and the most basic form, going through various types of ECS that have been developed over the past 100 years. Many of the advantages of ECS claimed by different authors are presented here. It also gives an insight into the lack of its exploitation in series production vehicles by addressing issues that are not clearly mentioned in the literature. It then talks about different types of boiling process, and the heat transfer involved. Namely, pool boiling, flow boiling and spray boiling. A review of previous works on heating surface orientation and surface characteristics is provided. The previous experimental and numerical work on the effect of mechanical vibration on boiling heat transfer in the three types of boiling are then described. Droplet impingement dynamics and dynamic contact angle models are then reviewed. A review of the boiling heat transfer correlations is provided in Chapter-2.

1.1.1. IC Engine Evaporative Cooling Systems

Research on evaporative cooling systems for automotive engines dates back a century [5] [6]. There have been numerous inventions and patents on several types of ECS. Some had been tested in vehicle prototypes but none made it to series production [6] [7] [8]. The reasons for this are not clear. An automotive ECS could be described as a closed-loop system in which the coolant boils off from the coolant jackets when the coolant side wall temperature is higher than the saturation temperature. The vapour produced is then condensed and put back into the coolant jacket. The earliest designs used 'hopper cooling', the most elementary form of evaporative cooling, in which the engine was surrounded by a bath of water, which as it boils off, more water is poured into the hopper as necessary. Figure 1.1 shows the diagram of an engine with '*hopper cooling*' [5].

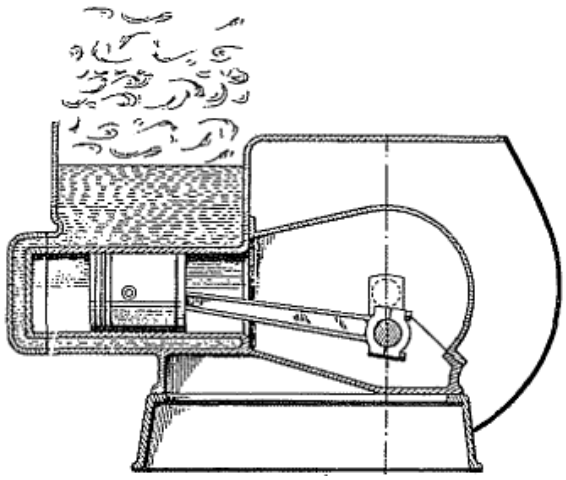

Figure 1.1: An internal combustion engine with hopper cooling [5]**.**

It was inconvenient to keep filling with water to keep it at the required level. This design was later modified with a condenser to condense the steam and recirculate the condensate. A closed loop design of engine ECS is given in figure 1.2. It shows an internal combustion engine (ICE) evaporative cooling system in which the saturated liquid from a separator tank enters the engine coolant jacket, which gets vaporised by the excess temperature of coolant jacket walls. The vapour is then transferred into the separator tank where the liquid and vapour are separated. The separated liquid is then fed into the engine whereas the vapour is transferred to the condenser. The vapour is condensed into saturated liquid, and pumped into the separator tank where it is mixed with the separated liquid. The latent heat during vaporisation and condensation is used here to achieve cooling where there is only a very low temperature differential, which allows the engine to run at uniform temperatures [5].

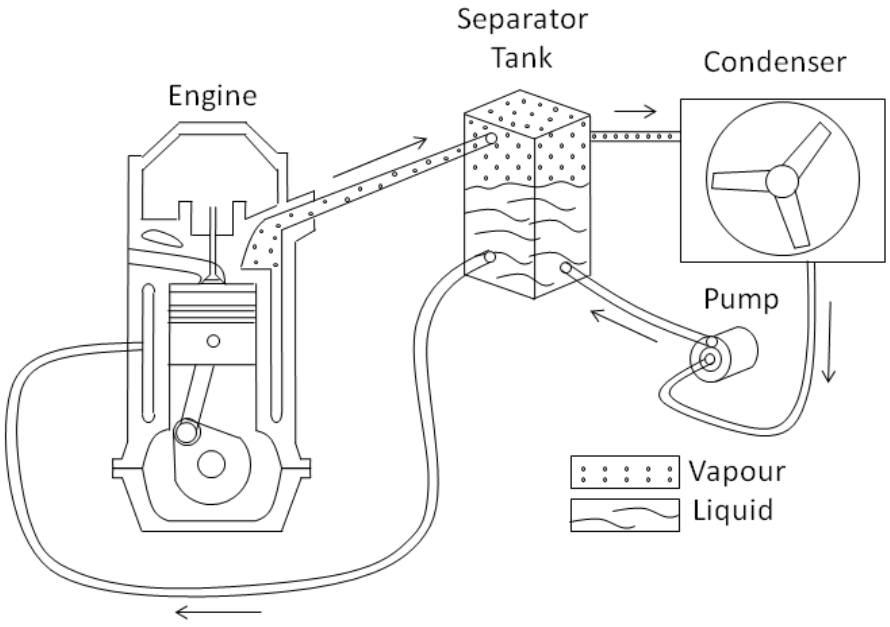

Figure 1.2: Schematic diagram of an internal combustion engine evaporative cooling system [5]**.**

The 1920s saw a lot research in automotive evaporative cooling systems. One of the biggest contributions was made by the Harrison Radiator Corp. Harrison (1926) [6], the President of Harrison Radiator Corp. describes 7 years of experimentation in evaporative cooling systems. Harrison obtained the idea of using evaporative cooling from Wellington W. Muir in 1918, who already had patents on cooling-systems. Harrison mentions the use of two different pumps for circulating of boiling water and condensate. The general idea was not totally new but received some opposition from the industry. The main pump circulates hot water, whereas the secondary pump returns the condensate to the cylinder-block under all conditions to maintain the required level. In February 1919, a car fitted with the system was driven more than 2000 miles through ice and snow,

they claim satisfactorily. The main challenge was found to be keeping the centrifugal pump feeding the condensate to the engine without becoming air locked, as air-locking resulted in intermittent flow. Over the following 7 years they tested several hundred cars fitted with different types of arrangements clocking-up more than 500,000 miles of operation.

Kubozuka et al (1987) [7] of Nissan Motor Co., Ltd described an evaporative cooling system for IC engines. They performed two experiments, one using a boiler (pool boiling) as a substitute for the cylinder head, and the other a real engine experiment. Figure 1.3 and 1.4 respectively show the boiler test apparatus, and the evaporative cooling system with the engine. The results showed that a more uniform temperature distribution among the engine structure is possible owing to the boiling characteristics (in which more heat is removed from the hotter surfaces than colder ones). This makes knock control much easier owing to the reduction of local hot spots allowing more power from the same engine to be achieved. A higher heat transfer coefficient is achieved using a condenser or a condensing radiator compared to that of a conventional convection-based radiator. One of their important findings was that the wall temperature could be controlled accurately by varying the system pressure. At higher engine loads, reduced pressure would increase boiling, whereas at low loads, a higher pressure could suppress the boiling. Evaporative cooling was found to be highly responsive in controlling the coolant and wall temperatures. In their boiling test apparatus, the distance between the heating surface and the adjacent wall/roof, ΔR, were varied to see if its effect on the maximum heat flux were achievable. It was found that when the clearance ΔR~=10.5 mm, its effect on heat flux is negligible and the heat flux hardly varies with anymore increase in the clearance.

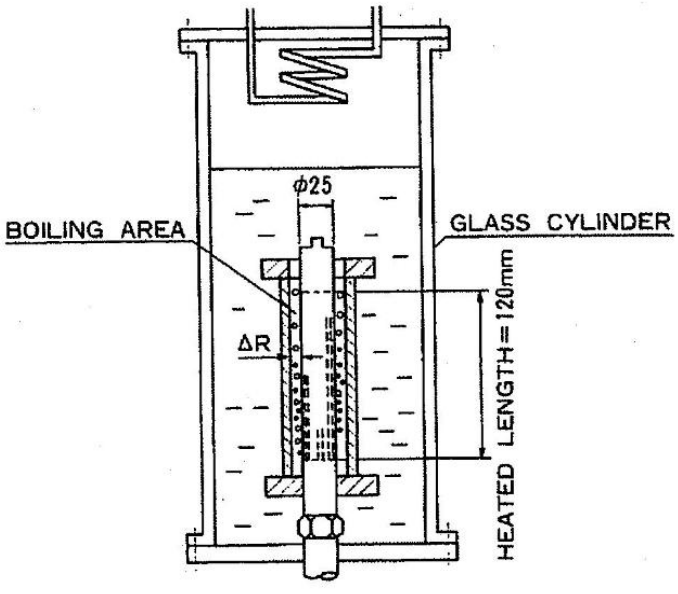

Figure 1.3: Nissan boiling test apparatus [7]**.**

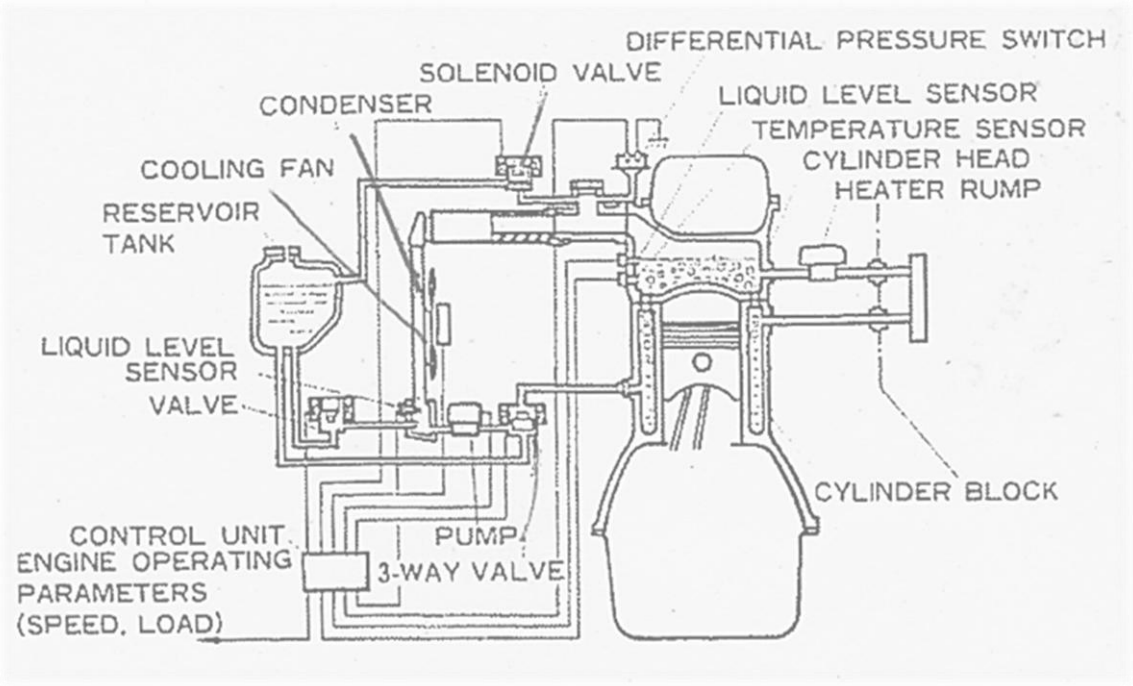

Figure 1.4: Nissan evaporative cooling system [7]**.**

Kim et al (1990) [8] developed a new evaporative cooling system for small four-stroke engines. Figure 1.5 shows their evaporative cooling system. It is a basic system consisting of an ICE, a condenser, a circulating pump, a thermostatic air vent, and an air reservoir. Unlike the previous systems, this system has a special feature: a thermostatic air vent. While the engine is running, the temperature controlled air vent helps the system to operate at, or slightly above, atmospheric pressure by letting air escape into the atmosphere (but not the coolant). The air vent closes when hot coolant touches the air vent capsule. When the engine is not in operation, air is let into to the system through the air vent to maintain atmospheric pressure in the coolant circuit. An engine with this system was tested and the results were reported as being satisfactory. The air removal system performed well during normal engine operation with improved fuel consumption and power. The other important finding was that there was reduced heat release to the coolant. They concluded that with this cooling system the engine would benefit from better fuel economy and durability.

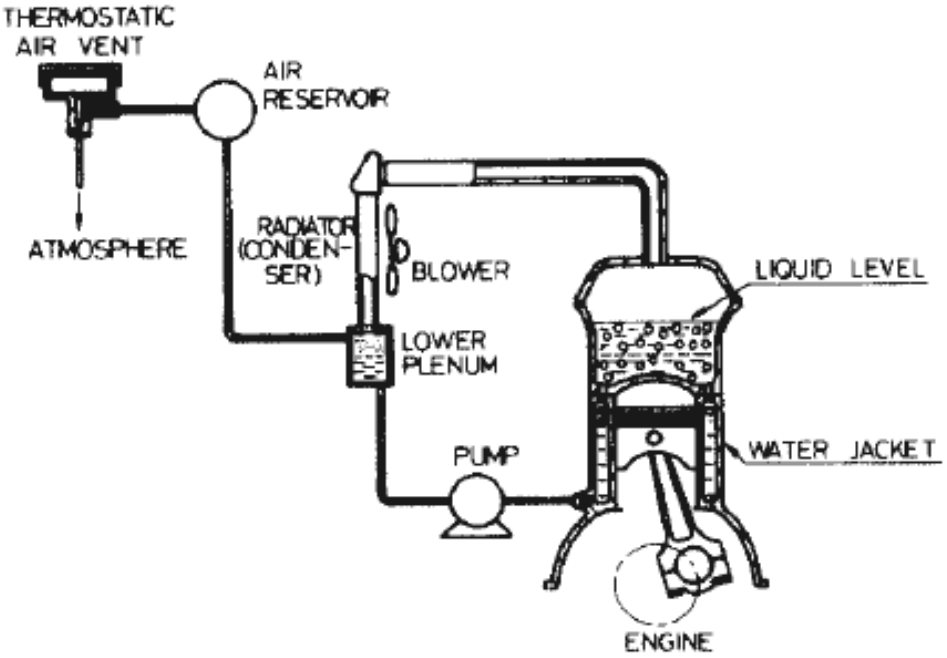

Figure 1.5: Evaporative cooling system developed by Kim et al [8]**.**

Pretscher and Ap (1993) [9] of Valeo Engine Cooling Systems have tested an evaporative cooling system called 'Nucleate Boiling Engine Cooling System', in a climate controlled wind-tunnel. The system consists of an ICE, condenser, water pump, liquid/vapour-separator, expansion tank and a fan control unit. Based on their knowledge on the above mentioned components, they tested two different types of cooling-circuits in a car. Both cooling systems are based on nucleate boiling, one is completely filled, the other is partially filled. It is found that the completely filled system has more advantages compared to a conventional cooling system even though both systems are capable of providing sufficient cooling of the engine. Their findings show some major advantages: the cylinder head has a more even temperature distribution, the system is less expensive owing to fewer components, it has a smaller expansion tank (2 litres compared to 5 litres), and there is less corrosion.

Calculations based on the published empirical spray evaporative cooling data show that the coolant flow rates would reduce from 1.25 L/min/kW (of engine brake power) for conventional cooling to less than 0.05 L/min/kW for evaporative spray cooling. This is expected to reduce the pumping power requirements by 95% [10] [11].

Most of the developers of engine evaporative cooling systems have claimed that it provides better results than conventional cooling systems. Almost all the authors have mentioned the more even temperature distribution obtained across the cooled surface, which results in reduced knocking.

Some have claimed reduced part-load fuel consumption and improved specific power. But none of these systems have been put into production vehicles, and the associated literature lacks an explanation for this. This raises a concern about evaporatively cooling automotive internal combustion engines. But it should be noted that none of these developers have addressed the effect of engine vibration on boiling heat transfer, and its impact on the cooling system. Control of boiling at the critical heat flux region could also be an issue as the boiling process can be very unstable and could lead to transition boiling [10]. Before discussing relevant literature on boiling studies, it is appropriate to restate the basic physical principle involved.

1.1.2. Principles of Boiling Processes and Boiling Heat Transfer

Boiling is a physical phenomenon that results in a phase change of a liquid to vapour when its vapour pressure is equal to, or above, the pressure exerted on the liquid by its surroundings. The minimum temperature required for a liquid to have its vapour pressure equal to the pressure exerted on it by its surroundings is called its boiling point. A fluid at a temperature equal to its boiling point is called saturated fluid. It could either be a saturated liquid which is about to vaporise, or a saturated liquid-vapour combination, or even a saturated vapour which is about to condense. The enthalpy of vaporisation determines the energy required for the phase change of a liquid to vapour without any increase in temperature. The boiling point of water at atmospheric pressure by definition is ~100^{o}C. Boiling could be classified as pool boiling, flow boiling and spray boiling. Boiling is a process which occurs at the solid-liquid interface when the surface temperature is higher than the saturation temperature of the liquid; evaporation is the process where vapour escapes the liquid at the liquid-vapour interface.

1.1.2.1. Pool Boiling

Pool boiling is the boiling of a liquid without any externally imposed flow or agitation. A pool boiling curve for water at atmospheric pressure is shown in figure 1.6 which gives the heat flux (q) and associated boiling process as a function of the wall excess temperature: $\Delta T_{ex} = T_w - T_{sat}$, where T_w is the wall temperature and T_{sat} is the saturation temperature. The wall 'excess' temperature is the temperature of the hot surface above the saturation temperature of the liquid. The pool boiling curve shows four major boiling regimes: i) Natural convection boiling, ii) Nucleate boiling, iii) Transition boiling, and iv) Film boiling

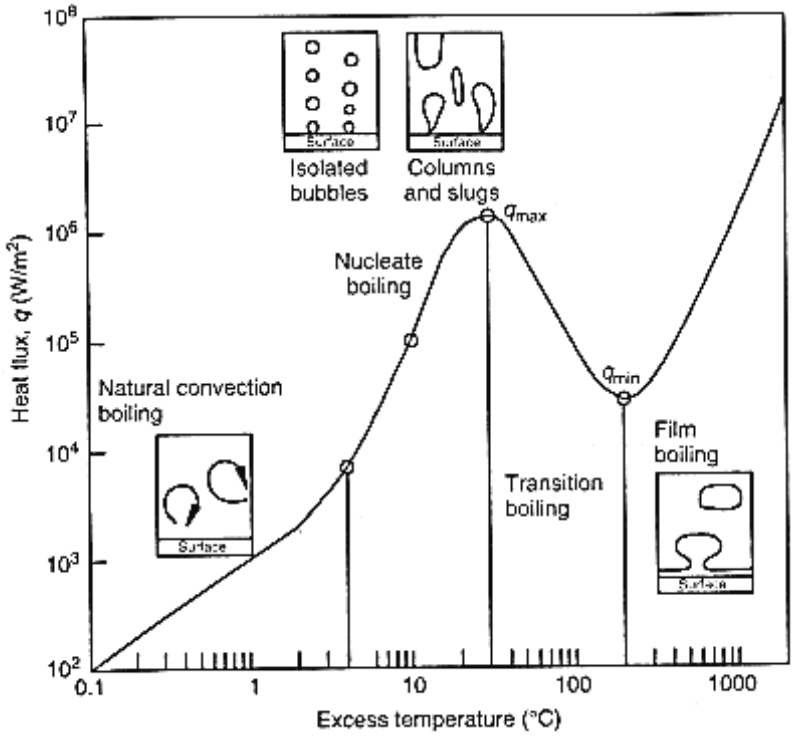

Figure 1.6: Pool boiling curve [12]**.**

Boiling starts with natural convection boiling where the excess temperature is below 4 °C, in which the liquid in the vicinity of the heated surface becomes superheated and rises. Free convection causes sustained fluid motion owing to buoyancy effects. Some bubbles may be formed but these are mostly air.

When ΔT_{ex} is increased, separate vapour bubbles form at *nucleation sites* and rise. Nucleation sites can be imperfections on a surface, such as cracks, where the fluid could be heated by a larger surface area. If the bulk liquid temperature is below saturation temperature, the rising vapour bubbles condense in it, which is called *sub-cooled boiling*. The rising vapour bubbles break free from the surface if the bulk liquid temperature is above the saturation temperature and this is called *saturated nucleate boiling*. Further increase in ΔT_{ex} results in higher production rate of vapour bubbles which then combine to form larger slugs and columns of vapour. Liquid is agitated owing to the motion of these bubbles. When ΔT_{ex} is above ~10 °C, the rate of increase in heat transfer coefficient decreases with increase in ΔT_{ex}. This inflection point, i.e. when ΔT_{ex}=~10 °C, is considered to be caused by the formation of 'slugs' and 'columns' of vapour from the bubbles that is being produced at a high rate. At atmospheric pressure, the *maximum heat flux* (q_{max}) or *critical heat flux* (CHF) occurs at ΔT_{ex}=~30 °C.

Further increase in ΔT_{ex} reduces the q until it reaches the *minimum heat flux* (q_{min}), which occurs at a temperature called *Leidenfrost* temperature. The boiling regime between the q_{max} and q_{min} is

called the *transition boiling* regime in which larger areas of heater surface are covered with an unstable vapour film. The heater surface is occasionally dry or in macroscopic contact with liquid. Boiling varies between vapour film and the slugs and columns of nucleate boiling.

Further increase in ΔT_{ex} leads the boiling to the regime called *Film Boiling,* in which a stable film of vapour covers the heater surface. In this regime, there is hardly any direct contact between the heater surface and the liquid. Heat flux again increase with ΔT_{ex} and radiation contributes to a significant amount of total heat transfer. If the melting point of the heating surface is high enough, q will then exceed the q_{max} at a very high ΔT_{ex} [12].

1.1.2.1.1. Surface Characteristics and Bubble Formation

In nucleate boiling, surface defects play a major role in bubble nucleation under low heat flux conditions. Surfaces with microscopic cavities and crevices usually have air trapped, when submerged in a liquid. This combination of gas and liquid can act as a nucleus for bubble growth. Homogeneous bubble formation requires a very high excess temperature whereas nucleation from wall crevices only requires relatively small excess temperatures which could be only several degrees Celsius. Evaporation causes the microbubble in the crevice to grow. Kang (2000) [13] has studied the effect of surface roughness on pool boiling. It was found that increased surface roughness results in better heat transfer. Again, the cause of increased heat transfer is due to the higher density of cavities present in the rough surface compared to a smooth surface. From the above, it is understood that nucleate boiling largely depends on the cavities and crevices present on the surface. So that the material, surface finishing, oxidation and contamination, all play an important role in nucleate boiling [14].

1.1.2.1.2. Surface Orientation and Pool Boiling

For pool boiling, the book by Ghiaasiaan [14] states that surface orientation with respect to gravity has very little effect on fully developed boiling and has a strong effect on partial boiling and film boiling. The fully developed nucleate boiling regime is where the slugs and jets form. Experiments by Yang et al (1997) [15] studied the pool-boiling critical heat flux with respect to the heater surface orientation and size. For downward facing plates, the critical heat flux has reduced with increasing heater size owing to the difficulty of bubble escape for the wider section. When the surface orientation changes from vertical to horizontal downward facing orientation, the CHF decreases and it reaches a transition angle, where there is a drastic reduction of the CHF. The transition angle was found to be -80^{o}. The surface angle and size do not largely affect pool-boiling for upward facing plates compared to downward facing plates. Another important finding from the experiments is that the CHF occurs first at the lower position of the heater surface with increase in the inclination angle.

Rainey and You (2001) [16] have tested two heater surfaces: plain and microporous coated, to understand the effect of heater orientation and size on pool boiling. For the plain surface, boiling increased slightly from 0^o to 45^o and highly decreased from 90^o to 180^0. The reason for the decrease in boiling, when the heater surface starts to face downwards, is found to be same as before, namely that the vapour bubbles have difficulty departing.

1.1.2.2. Flow Boiling

Forced *convection boiling*, or *'flow' boiling*, is the boiling of a liquid under externally imposed flow. It is similar to pool boiling but more complex. Two types of flow are considered, one is for upward flow and the other is horizontal flow. Fluid flowing upwards through a vertical channel has heat being added to it by the heating surface around it whereas for flow in horizontal channels, the effect of gravity and buoyancy play an important role. For automotive engine cooling applications, both vertical and horizontal flows are of interest as the geometries in the cylinder-head require the coolant to flow through passages that can have a multiple variety of cross-sections and orientations. In any type of boiling, the initial condition with respect to the saturated condition of the fluid being heated, is very important as it basically determines whether initially any single-phase convection will happen and the contribution of it in the associated heat transfer involved. A much lower temperature below saturation generally means a higher rate of single-phase convection initially leading in to two-phase boiling when the temperature is above saturation temperature.

1.1.2.2.1. Boiling of Vertical Flow

Figure 1.7 shows the heat transfer coefficient and flow boiling regimes in a heated vertical pipe as a function of the distance from the inlet. The flow enters the tube as pure saturated liquid and the first regime is the forced convection regime where it could be predicted using conventional single-phase pipe flow correlations. As the flow moves upwards, generation of bubbles happen, similar to bubble formation in pool boiling. The heat transfer coefficient increases due to bubble formation and its motion. More heat being added to it, results in the increase in the rate of bubble formation where slugs form due to the bubbles being combined. The quality of vapour in this regime is very low at approximately 1%. The heat transfer coefficient keeps increasing and reaches its peak when the flow becomes almost fully annular. The next flow boiling regime occurs further away from the inlet. In annular flow, a vapour core forms in the centre and liquid covers the surface where the heat transfer is through liquid convection and then evaporation happens at the liquid-vapour interface. When more heat is added to the flow, it finally ends ups in the regime where the walls are dry and the flow is just a mist of vapour at a quality of 25% or more. The heat transfer coefficient starts decreasing until 'mist' flow i.e. after the flow has become fully annular. Finally, when there is pure

vapour flow, single-phase forced convection correlations can be used to predict the heat transfer using the appropriate vapour properties [12].

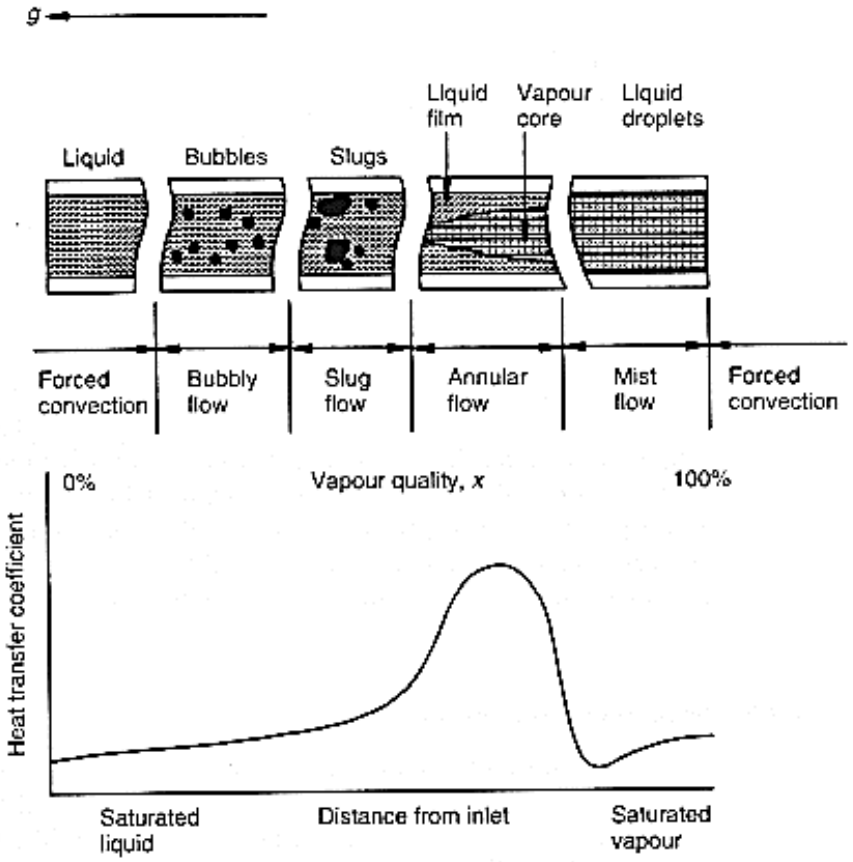

Figure 1.7: Flow boiling curve for a vertical tube [12]**.**

1.1.2.2.2. Boiling of Horizontal Flow

Horizontal flow boiling is very similar to vertical flow boiling as far as the boiling regimes are concerned. The differences largely occur from the annular flow regime and afterwards owing to the effect of gravity and buoyancy. Figure 1.8 shows the flow boiling regimes and associated heat transfer of fluid flow through a uniformly heated horizontal tube under moderate heat flux. The flow enters the tube as a single-phase liquid and depending on how close it is to saturation, a certain amount of forced convection occurs. At a small distance from the inlet, bubbles start to form and the heat transfer coefficient starts to increase with the distance from inlet. Further away from the inlet, higher rate of bubble formation results in it being combined to form plugs, which is associated with a higher rate of increase of heat transfer coefficient. The next boiling regime is the annular flow regime in which partial dryout occurs when the liquid film thickness reduces at the top surface inside the tube. In the dryout zone, when the annular flow starts transforming into mist flow, the liquid film on the top surface dries out first. The heat transfer coefficient reaches its peak at this point and after that it keeps reducing with increase in distance from the inlet. Full surface dryout occurs and

the mist flow gradually transforms in to single-phase vapour flow, where the heat transfer is minimum and single-phase forced convection correlations can again be used to predict the heat transfer with appropriate fluid properties [14].

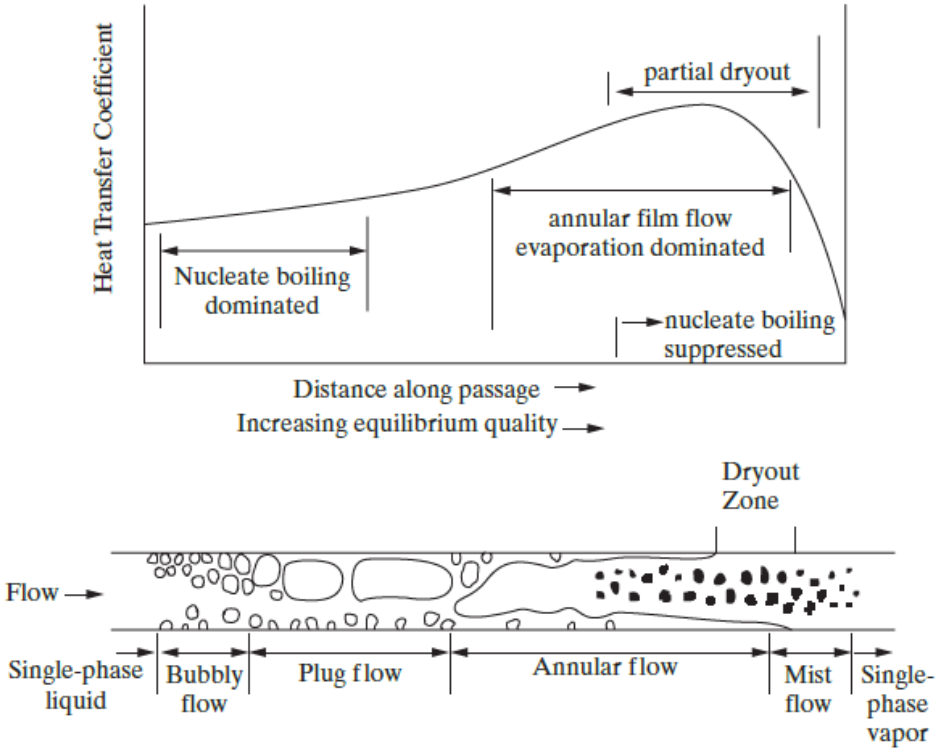

Figure 1.8: Flow and heat transfer regimes in a uniformly heated horizontal tube with moderate heat flux [14]**.**

1.1.2.2.3. Surface Characteristics and Flow Boiling

Cheng and Chen (2001) [17] studied the effect of upward flow boiling heat transfer in a tube with axial micro grooves. The grooves were rectangular in shape with a depth of 0.5 mm and a width of 0.3 mm. Experiments were conducted for three different mass fluxes of 410, 610, and 810 kg/m^2 s for a heat flux range of 0 to 550 kW/m^2. Results have shown that there is 1.6 to 2.7-fold increase in the heat transfer coefficient. The comparisons were made with experimental results of flow boiling through a smooth tube. Compared to the smooth tube, the micro grooves increased the pressure drop slightly. The wall superheat in the tube with grooves was found to be lower than in the smooth tube. Experiments were conducted by M. Piasecka (2014) [18] on the use of enhanced surface in flow boiling heat transfer in a rectangular mini-channel. A vertical mini-channel of 1 mm in depth was used with a one-sided heating surface having various depressions. It was found that compared to a plain heating surface, the enhanced surface causes the boiling to occur at a lower heat flux. The reason, as described earlier is, for the case of pool boiling, the higher density of nucleation sites.

1.1.2.3. Spray Boiling

The boiling process involving spray boiling is similar to pool and flow boiling but the major difference being the complex dynamic process of spray impingement onto the heater surface. The heat fluxes associated with spray boiling are many times higher than in pool boiling or flow boiling. The volumetric flux (flow rate divided by the area covered by the spray) and the diameter of the liquid drops play an important role in heat transfer in spray boiling. Surface tension and viscosity also play an important role as it highly influences the spray characteristics. Variations in other fluid properties do not largely affect the heat transfer. Depending on the application, different types of spray nozzles are used to create a spray with the required spray characteristics. Spray cooling mainly seeks application in high power density electronics, steel quenching, and also in low pressure environments especially for cooling purposes in space as it is capable of high heat dissipation and meets the desired thermal control requirements [19]. Another popular application of spray cooling is cryogen spray cooling for laser dermatologic surgeries with R-134 being the most common cryogen [20]–[24].

1.1.2.3.1. Heat Transfer in Spray Boiling

Like pool boiling, spray boiling also follows similar boiling regimes. It starts from single-phase convection, then, if the surface temperature is sufficiently higher than the saturation temperature, nucleate boiling occurs. After reaching critical heat flux, the heat flux reduces and reaches a minimum when the surface temperature is equal to *Liedenfrost* temperature. If the surface temperature exceeds the *Leidenfrost* temperature, film boiling occurs, where the vapour film doesn't allow continuous liquid-surface contact [25].

Single-phase convection can be split into two stages: One stage is during the droplet impingement, and the other stage is film convection [19]. Depending on the velocity of the droplet, a certain amount of forced-convection occurs. The single-phase forced-convection heat transfer coefficient associated with droplet impingement is high owing to high liquid momentum. When the liquid momentum is high, nucleation does not occur, as the wall superheat cannot become large enough for boiling. The evaporation efficiency is therefore much higher for light sprays as it can produce a more static liquid film over the surface than heavy sprays, as these cause more liquid movement. Therefore, volumetric flux is one of the most important factors determining the heat transfer in spray cooling. After the droplets have settled down to a liquid film, some single phase convection occurs and then the wall superheat is high enough for nucleate boiling [26].

The two-phase regime starts when the liquid film becomes superheated and bubbles start to form. The bubbles get larger, absorbing heat, and rise due to buoyancy, causing liquid movement which

then leaves the liquid film at the liquid-vapour interface. When the superheat is high enough, numerous bubbles go through this process, causing nucleate boiling. The nucleate boiling regime is the major constituent of the heat transfer in evaporative spray cooling. The bubbles can be separated into two classes based on the location of their nucleation centres. One class is *surface nucleation* bubbles; the other class is the *secondary nucleation* bubbles. Bubbles with nucleation centres occurring on the heating surface are referred to as surface nucleation bubbles whereas the nucleation centres occurring on the droplet surface are referred to as secondary nucleation bubbles. As in the case of pool boiling, surface nucleation bubbles are also generally formed in nucleation sites such as cavities or crevices where there is generally trapped air. The secondary nucleation bubbles are formed by vapour carried by droplets. Vapour transforms into bubbles when the droplets impinge on the liquid film surface, and these bubbles get released when a droplet impinges on the heating surface. These bubbles then grow in volume as in surface nucleation, absorbing heat, and then escaping from the liquid film as vapour. The spray cooling review paper by Cheng et al. (2016) [19] mentions that the bubble heat transfer model for pool boiling could be applied for bubble heat transfer in spray cooling. They also mention that the bubble nucleation density in spray cooling is higher than in pool boiling and the life cycle is an order of magnitude lower than in pool boiling. This generally confirms why the heat transfer in spray cooling is much higher than in pool boiling. The other heat transfer phenomenon occurring in the two-phase regime is liquid film evaporation. There is a temperature gradient across the liquid film as the film inner temperature and the heating surface temperature are higher than the liquid-vapour/liquid-gas interface. The liquid film cools the surface by conduction and the evaporation occurs at the liquid-vapour/liquid-gas interface [25]. Increase in the superheat leads to the critical heat flux (CHF), which is the peak heat flux in spray boiling. It is not yet fully understood what causes the boiling to reach the CHF and there are many different theories to predict the trigger mechanism of CHF. Whilst using air-water atomizing nozzle and an ultra-smooth surface, under laboratory conditions the maximum measured CHF in spray boiling is 12MW/m^2 [19].

1.1.2.3.2. Spray Characteristics and Spray Boiling

The process of two-phase spray cooling involves high pressure liquid pushed through a nozzle, which breaks down into droplets. The size of the droplets depends on the size of the orifice, the pressure droplet, and the amount of turbulence generated. Turbulence increases with pressure drop where the spray gets finer. These droplets impinge on the hot surface to form a thin liquid film which is very good for heat transfer as it helps faster evaporation. There are different types of spray nozzle available on the market. Some of these are full cone sprays, flat fan sprays, and hollow cone sprays. Solid cone sprays are of interest as it spreads the spray over a surface without leaving any dry

patches although the spray distribution is not the same everywhere on the surface.

Some of the most important spray characteristics are: the flow rate, the spray angle, the spray height, the volumetric flux, and the mean droplet diameter for the entire spray. The flow rate (which is basically dependent on the pressure drop) increases with pressure drop. Bernoulli's principle can be used to predict the flow rate through a nozzle if the inlet and exit pressures, and the orifice diameters are known. The spray angle is important because the cooling area (covered by a spray) could change with the pressure drop owing to the change in the spray angle with respect to pressure differential. As a cooling system design parameter, the distance between the nozzle and the heating surface is also important. If the spray height is too high, there is a chance that droplets combine to form larger droplets which can decrease evaporation efficiency. The *Sauter Mean Diameter* (SMD) is a widely used measure to specify the average droplet diameter for a spray [19] [26] [27]. Consider an object which has a certain surface area to volume ratio, the SMD is the diameter of a sphere which has the surface area to volume ratio equal to that of the object [19]. Even though the volumetric flux is more influential in heat transfer, droplet velocity which depends on the size of the droplet, determines the droplet impingent dynamics and the formation of liquid film. But the droplet velocity and volumetric flux are interdependent. A higher volumetric flux generally means a higher droplet velocity. The higher the velocity, the flatter the liquid droplet will be, which helps form a thinner liquid film initially. On impact, If there are imbalances between inertia and surface tension forces, then bouncing, splashing and breakup phenomena can occur [25, pp. 154–155]. Having reviewed the spray parameters that affect spray boiling heat transfer, the volumetric flux was found to have a major effect on heat transfer. The variation in parameters such as droplet size and velocity (which determines the momentum of droplets) ultimately lead to the variation in volumetric flux as it determines the amount of liquid being sprayed on the surface.

1.1.2.3.3. Spray Orientation and Spray Boiling

A study by Rybicki and Mudawar (2006) [28] concluded that orientation virtually has no influence on spray boiling heat transfer as long as there is no liquid build-up on the heating surface. They have experimented with both upward and downward sprays. Silk et al (2006) [29] examined the effect of enhanced surfaces and spray axis inclination for spray boiling heat transfer. Experiments were undertaken for a spray with an inclination of up to 45^{o}. Spray inclination was found to increase the heat flux compared to the no-inclination case. The results showed an increase in heat flux by 23% for a flat surface.

1.1.2.3.4. Surface Characteristics and Spray Boiling

There have been many studies to establish the effect of surface characteristics in two-phase spray

cooling. Researchers have used different types of micro structured surface, coated surfaces, fins, pyramids, and porous tunnels to study its effect on heat transfer. Hsieh and Yao (2006) [30] studied the effect of square silicon micro-studs in evaporative spray cooling using water. The results show that there is an increase in cooling performance mainly due to the micro-structure being able to retain more water on the heater surface owing to capillary forces replenishing the surface with water. Experiments by Kim et al (2004) [31] looked into the effect of evaporative spray cooling in plain and microporous coated surfaces. The studies were performed on flat and cylindrical heaters, and micron size aluminium particles were used to create the surface. Again the capillary pumping phenomenon in the microporous cavities connecting each other, played an important role in increased heat transfer. Sodtke and Stephan (2007) [32] examined two-phase spray cooling on micro pyramids of different height to understand the effect on heat transfer compared to a smooth surface. Experiments were initially conducted using a full cone spray on a smooth heater surface. They found that the length of the three-phase contact line (water, vapour, copper) increased with heat flux. A study on micro structured surfaces was performed, where results showed that there is a significant heat transfer enhancement by using the micro structured surface. In this case also, the effect of capillary forces is believed to be the cause for increase in heat transfer. Silk et al (2006) [29] conducted research on evaporative spray cooling of surface enhancements such as cubic pin-fins, pyramids, and straight fins. Heat flux enhancement was evident, and straight fins were found to be most effective, followed by cubic fins and pyramids. The results from these different experiments showed that the effect of capillary forces plays an important role in heat transfer enhancement. Surface enhancement is therefore a possible option for improving evaporative cooling efficiency. The key factor in choosing a surface is how much increase in surface area (available for heat transfer) it can bring compared to that of a flat surface as increase in surface area increases the heat added to the liquid.

1.1.2.3.5. Cryogen Spray Cooling

Aguilar et al [21] measured heat flux and heat transfer coefficients of cryogen spray cooling using R134a as the cryogen. The R134a has a boiling temperature of -26 ^{O}C at atmospheric pressure. For the experiments, the cryogen is kept in a container at a pressure of 6.6 bar at a temperature of 25 ^{O}C for it to be at saturation before it is being delivered through a nozzle. A heat flux as high as 1.3 MW/m^2 was measured at a test surface temperature of -7 ^{O}C with a heat transfer coefficient of 40000 W/m^{2}K. Pikkula et al [20] studied the effect of droplet size as well as spray density on heat transfer using R-134a as the Cryogen. Their results showed that there is a maximum of 14% difference in heat removal for a mass output difference by a factor of 6 (i.e. the coolant mass on the surface between 70 mg – 519.6 mg) with a droplet size difference by a factor of 2 (16.2 µm – 34 µm).

Chen et al [24] conducted a theoretical study of cryogen spray cooling using various cryogens. The cryogens used were R134a, R404A and R1234yf, and for each cryogen the maximum heat flux was determined to be 262.1 KW/m^2, 407.5 KW/m^2 and 225.8 KW/m^2 respectively. Cryogen spray cooling was not chosen for the research presented in this thesis owing to its much lower operating temperatures as well as the lower heat flux removal capabilities for it to be used in engine cooling.

1.1.3. The Effect of Vibration on Boiling Heat Transfer

Boiling heat transfer alone is very complex. Adding boundary motion to the heating surface makes the physics even more difficult to understand. Even though there are not many publications available, several experimental studies have been reported by researchers to understand the effect of vibration on the boiling process and the heat transfer associated with it. A study of boundary motion in boiling heat transfer is very important if it needs to be applied to cool internal combustion engines, as engines vibrate at different amplitudes and frequencies while running. Understanding the vibration amplitudes and frequencies in engines is crucial in determining the vibration characteristics for experiments that need to be undertaken in addition to studying previous experimental results. There are some exciting numerical simulation publications on spray boiling heat transfer with moving boundaries but no publications have been found on experimental work.

Sathyabhama and Prashanth (2015) [33] have studied the enhancement of boiling heat transfer in pool boiling with surface vibration. They used a circular copper plate as the heating surface, with vertical vibration induced on it. The studies were performed with water as the coolant at atmospheric pressure. At low frequency and amplitudes, the heat transfer coefficient was found to increase to a maximum of 26% with vibration intensity. Vibration intensity is represented by vibrational Reynolds number. At high frequency and amplitudes, vibration has a negative effect on heat transfer. For a fixed amplitude of 2 mm, the heat transfer coefficient increases up to a frequency of 10 Hz. For a fixed frequency of 5 Hz, heat transfer increases up to an amplitude of 2.5 mm. They assume many reasons for the enhanced heat transfer with vibration: e.g. to quote: "*An increase in flow turbulence caused due to the surface vibration, thinning of the boundary layer, increase in the bubble growth rate, and change in the wetting angle are assumed to be the reasons for the heat transfer improvement*"

Atashi et al (2014) [34] conducted experiments to study the effect of vibrations in pool boiling heat transfer. They used a vertical cylindrical heater at different heat fluxes. The frequencies used were 10, 15, 20 and 25 Hz and the maximum heat transfer enhancement was found to be at the frequency of 25 Hz. Their conclusion was that low frequency vibrations can improve heat transfer because a vibrating surface creates more nucleation sites and turbulence which results in higher heat transfer

due to generation of smaller bubbles.

Kim et al (2002) [31] have studied the effect of mechanical vibration, for flow boiling, focusing on the critical heat flux in a heated vertical annulus under atmospheric conditions. Their experiments were performed for a mass flux of 115 kg/m^2/s and 215 kg/m^2/s with and without vibration. A maximum CHF increase of 16.4% was seen at the mass flux of 215 kg/m^2/s and 13.4% increase at a mass flux of 115 kg/m^2/s. The maximum CHF enhancement was seen at frequency of 30 Hz and a vibration amplitude of 0.5 mm. This was found to be due to the externally imposed vibration matching the natural frequency of the heater section. Another set of experiments, for a mass flux of 50 kg/m^2/s and 400 kg/m^2/s, were undertaken without externally imposed vibration. At the onset of nucleate boiling, vibration amplitude was increased because of the flow change from subcooled to nucleate boiling.

Wang et al (2016) [35] numerically simulated droplets impinging onto a liquid film on a moving boundary with two-phase heat transfer. A 2-D Volume of Fluid method was used for the simulations. Their study involved single or multiple droplets impacting onto a liquid film where a vapour bubble is growing. Two different spray conditions were simulated: Light and dense sprays. The light sprays were simulated by a droplet impacting onto the liquid film, whereas the dense sprays were simulated by four droplets impacting onto the liquid film one after another. The frequencies used for boundary vibration were: 200 Hz, 400 Hz and 800 Hz. And the amplitudes used were: 0.025 mm, 0.05 mm, 0.1 mm, 0.5 mm, 0.75 mm and 1 mm. Under the light spray conditions, compared to the static condition, heat flux improved by 3.1 to 8.1% for all amplitudes at a frequency of 200 Hz. It was identified that the improvement in heat transfer was because of improved liquid spreading which enhances convection. At the frequency of 800 Hz, heat transfer was reduced by 58.2%, compared to the static condition. It was observed that the reduction in heat transfer was due to the lack of cold liquid coming into contact with the vibrating surface. Higher amplitudes also tend to reduce heat flux owing to earlier film breakage. The simulations for dense sprays showed that the maximum heat flux was higher than light sprays for static conditions. Compared to the static case, dense sprays also showed improvements in average heat flux for most of the frequencies and amplitudes. It was because of better contact between the cold liquid and the vibrating surface. An improvement of 0.2% to 21.6% in time averaged heat flux was observed for the frequencies of 200 Hz and 400 Hz across the range of amplitudes. At the frequency of 800 Hz, the time averaged heat flux reduced by 3.2% and 11.2% for the amplitudes of 0.75 mm and 1 mm respectively.

1.1.4. Dynamic Contact Angle Models for the Prediction of Droplet Impingement Dynamics

When a droplet impinges on a hot surface with sufficient super heat (excess temperature), the initial mode of heat transfer is single-phase convection, before it starts to evaporate. A droplet after impact oscillates for a while before it starts to settle down by losing its momentum due to viscous forces. A droplet only starts to evaporate after most of its momentum is lost and has come to an almost static state. There can be scenarios where a droplet with a very high momentum can overcome the surface tension force and shatter into multiple pieces after impact. This part of the literature review concentrates only on the droplets that stay as a single body of fluid after impact during an oscillation process.

To calculate the droplet impingement dynamics, until it settles down to a static state, a 'contact angle' needs to be specified. The contact angle is the angle that the outer surface of a liquid, in contact with a solid, makes with the solid, in the presence of another fluid (i.e. a gas (air or water vapour) in this case). The meeting point of these three phases is called the 'three-phase contact line'. A volume of liquid sitting statically on a surface has a static contact angle. But this is not the case when the liquid is moving. Young's equation [36]:

$$\sigma \cos(\theta^0) = \sigma_{sv} - \sigma_{sl} \tag{1.1}$$

Equates the static/equilibrium contact angle to the solid/vapour surface tension and the solid/liquid surface tension. For better accuracy of the calculations, a dynamic contact angle needs to be specified. Several researchers have conducted simulations on droplet impingement dynamics with various contact angle models. Sikalo et al (2005) [37] undertook experiments as well as numerical simulations on dynamic contact angle of spreading droplet on impact. Their simulations used several empirical correlations for the prediction of the contact angle. The comparison of their numerical simulations results with experiments showed that the empirical models did not predict the changes in contact angle very well. Another study that showed the importance of using a good contact angle model was by Roisman et al (2008) [38]. A recent paper by Hu et al (2015) [39] also studied the contact angle effects stating its importance in modelling droplet impingement problems.

Looking back into the contact angle problem, a 'no slip' condition is generally assumed where the liquid meets the solid surface. This creates a stress singularity at the interface due to the moving contact line while spreading. Cox (1985) [40] developed a slip-condition between the liquid and the surface to remove the stress singularity at the contact line. Sikalo et al (2005) [37], in their paper on

dynamic contact angle of spreading droplets, reviewed several contact angle models. The Cox [40] model is given as:

$$Ca = \left(ln(\varepsilon^{-1}) - \frac{Q_1}{f(\theta_D)} + \frac{Q_2}{f(\theta_w)}\right)^{-1} [g(\theta_D) - g(\theta_w)] + O\left(\frac{1}{\ln(\varepsilon^{-1})}\right)^3 \quad (1.2)$$

The dynamic contact angle is equated to capillary number with a dimensionless parameter ε associated with the micro-region of the contact line. The constants Q_1 and Q_2 are associated with outer flow and wall slip. The functions f and g relate to the dynamic and microscopic static wall contact angle. The capillary number is given as $Ca = v\mu/\sigma$.

Another model mentioned in the Sikalo paper [37] is the empirical correlation by Kistler. This uses an inverse Hoffman function for the calculation of the dynamic contact angle. The correlation by Kistler is based again on the capillary number. The Kistler dynamic contact correlation is:

$$\theta_D = f_{Hoff}\left[Ca + f_{Hoff}^{-1}(\theta_e)\right] \quad (1.3)$$

where θ_D is the dynamic contact angle, θ_D is the equilibrium contact angle, and the Hoffman function is given as:

$$f_{Hoff}(x) = arccos\left\{1 - 2\,tanh\left[5.16\left(\frac{x}{1 + 1.31x^{0.99}}\right)^{0.706}\right]\right\} \quad (1.4)$$

Blake and Coninck (2002) [41] developed a simpler model using a new theory based on a combination of multiple theories, i.e. the molecular kinetic theory of wetting, the out of balance surface tension force, and the Frenkel-Eyring activated-rate theory of transport in liquids [42]. The viscous effects are modelled using the activation free energy of wetting and also included the effect of solid-liquid interactions. The dynamic contact angle model by Blake and Coninck (without the solid-liquid interactions effects) is given by equation (1.5).

$$v_{cl} = \frac{2k_s h\lambda}{\mu_l v_l} sinh\left[\frac{\sigma_l}{2nk_b T}\left(cos\theta^0 - cos\theta^d\right)\right] \quad (1.5)$$

where v_{cl} is the contact line velocity, k_s is the frequency of the molecular displacements, h is Plank's constant, λ is the length of each molecular displacements μ_l is the dynamic viscosity of the liquid, v_l is the molecular volume, n is the number of absorption sites per unit length, k_b is the

Boltzmann's constant, T is the temperature of the liquid, θ^0 is the static contact angle, and θ^d is the dynamic contact angle.

Equation (1.5) sets limits on the maximum speed of wetting and dewetting, which can be calculated using equations (1.6) and (1.7) respectively.

$$v_{cl180} = \frac{2k_s h\lambda}{\mu_l v_l} sinh\left[\frac{\sigma_{lv}}{2nk_b T}(cos\theta^0 + 1)\right] \quad (1.6)$$

$$-v_{cl0} = \frac{2k_s h\lambda}{\mu_l v_l} sinh\left[\frac{\sigma_{lv}}{2nk_b T}(1 - cos\theta^0)\right] \quad (1.7)$$

The maximum wetting velocity is achieved when the dynamic contact angle is 180^o, and the maximum dewetting velocity is reached when the dynamic contact angle is 0^0. Trying to wet a surface with a velocity higher than the maximum wetting velocity will cause entrapment of the fluid being displaced, and trying to dewet a surface with a velocity higher than the maximum dewetting velocity will also fail.

1.1.5. Numerical Simulations of Droplet Impingement Dynamics and Evaporation

Chen et al (2016) [43] numerically simulated droplet impingement dynamics and evaporation. The contact angle model used was Blake and Coninck theory [41] but omitting the effect of solid-liquid interactions. Their results were validated against dynamic droplet impingement experimental data by Dong et al (2006) [44]. The results validated were for a water droplet with a diameter of 49 µm impinging on a surface with a velocity of 4m/s. The temporal evolution of the droplet shape and the dimensionless wetting diameter were compared between the numerical simulation and experimental data. The numerical simulation results were in good agreement with the experimental data.

The work by Chen et al (2016) [43], was to identify spray cooling mechanisms including two-phase cooling of impinging droplets. A 'Volume of Fluid' method was used for the numerical simulations. After the model is validated against experimental data, for droplet impingement dynamics, using the Blake and Coninck dynamic contact angle model [41], they performed several sets of numerical simulations for several different cases. Some of those sets include droplet velocity effect, droplet size effect, and surface wettability effect. All of the cases mentioned, used a droplet diameter of 60 µm except for the study on the effect of droplet diameter on droplet impingement and evaporation. The droplet diameter effect simulations were for droplet diameters ranging from 30 µm to 100 µm. They found that, by assessing the volume of the droplet, there is hardly any evaporation during the

highly dynamic phase after droplet impact. It has been identified from the droplet velocity simulations that velocity has little effect on droplet evaporation. Droplet velocity influences the dynamic phase and higher velocities result in increased critical heat flux. As noted by many authors, who have conducted experiments in spray cooling, Chen et al (2016) [43] also found that droplet size affects the cooling efficiency. It was identified that heat transfer per unit mass for smaller droplets, is higher due to the shorter dynamic phase and faster evaporation. The surface wettability analysis showed that heat transfer improves for better wettability.

Briones and Ervin (2010) [45] conducted numerical simulations as well as experiments for droplet impingement dynamics and evaporation on an unheated surface. The simulations were for micrometer sized droplets. The numerical simulations were conducted using the VOF method. They used different contact angle models and Blake's [41] contact angle model was found to give better results.

Several studies looked into the effect of dynamic contact angle on simulating droplet impingement dynamics without heat transfer. These studies also give valuable information about different methods of numerically simulating droplet impingement dynamics and implementing contact angle models.

Sikalo et al (2005) [37] undertaken experiments as well as numerical simulations of droplet impingement dynamics. A VOF, two-phase model was used for the simulations. Navier-Stokes equations were solved using a code named 'COMET'. Similar to other VOF methods, 'volume concentration' was assigned with a value of 1 for the fully liquid phase and 0 for the fully gaseous phase. A 2-D axisymmetric model was used to simulate normal droplet impact but some 3-D simulations were used to check its accuracy. The 2-D axisymmetric model results were in very good agreement with the 3-D model results. It was found that accurate capture of contact line movement required cell sizes equivalent to intermolecular distances (But it would however be impractical to numerically simulate it owing to massive computational power requirements). They replaced the singularity at the moving contact line with a local force with some degree of dependence to contact line velocity. The contact line velocity was calculated by numerically differentiating contact line radius with respect to time. The model by Kistler was used to calculate the dynamic contact angle. The contact angle used was an apparent contact angle, which was applied far away from the microscopic region. The experiments undertaken were for a droplet diameter of 2.45 mm with a velocity ranging from 1.04 m/s to 4.1 m/s. Two liquids were used: glycerin and water. Wall surfaces used for the experiments were made of glass and wax. The numerical simulations were in good agreement with the experimental data. Temporal evolution of the droplet shape and the spread

diameter, and the dynamic contact angle during the impact process were compared between the experiments and numerical simulations.

Hu et al (2015) [39] numerically simulated a water droplet impinging onto a wax substrate using COSMOL. A 2-D axisymmetric model was used for the simulations. The correlation by Kistler was again used to model the dynamic contact angle. They also ran simulations using a static contact angle and also an advancing-receding contact angle. Similar to the findings by Sikalo et al [37], Hu et al [39] also mentioned the need of very fine grids near the contact line, to accurately capture it. An apparent contact angle far from the contact line was used to avoid the use of very fine grids. This reduced computational requirements, which otherwise would be impractical. The advancing-receding contact angles were based on the contact line velocity. When the contact line velocity was equal to, or above 0, the advancing contact angle was used, and when the contact line velocity was below 0, the receding contact angle was used. Numerical simulations were performed for a droplet diameter of 2.7 mm with an impact velocity of 1.17 m/s. Whilst using the static and advancing-receding contact angle models, droplet rebound and two secondary droplet break-ups were observed. The simulations which used the dynamic contact angle were in better agreement with the existing experimental data. The dimensionless spreading diameter and the droplet height were used to compare the numerical simulations with the experimental results. It was noted that the contact angle models did not affect the initial spreading phase but the receding and recoiling phases were affected by the contact angle setup.

Having reviewed the literature a position has been reached where there are clearly gaps in knowledge. The thesis objectives are now stated.

1.2. The Objectives of the Study

The literature shows that many researchers have identified the very high potential of heat transfer in boiling and many other advantages that evaporative cooling offers, which led them to develop various evaporative cooling systems for automotive internal combustion engines. But none of these systems went into series production, and the reasons for this are not stated in the associated literature. The challenges involved could therefore only be speculated at because it is unlikely that vehicle manufacturers would disclose this information. The challenges involved could only be speculated by a study of the boiling process involved because it is unlikely to find the disadvantages of these systems as it is potentially confidential and very valuable information that engine manufacturer do not want to disclose. A deep examination of the boiling heat transfer shows that some aspects of boiling may have not been addressed. It is hypothesised that difficulty in controlling evaporative cooling and the effect of vibration in boiling heat transfer may have played a big role. It

is evident that state-of-the-art highly downsized engines are making use of almost the full potential of conventional single-phase liquid convection systems. But a cooling system with higher heat transfer rates is required to cope with further downsizing. The review of pool, flow, and spray boiling showed that spray boiling has the highest rate of heat transfer. As spray boiling is identified to be the most efficient form of heat transfer which could be used for engine cooling, unexplored areas such as the control of spray evaporative cooling of engines, and the effect of vibration in spray boiling need to be examined. To establish whether the plant is controllable, we need to use a dynamic evaporative cooling heat transfer model (such as a dynamic correlation or a CFD simulation). In the absence of a dynamic correlation, the first thing to check is whether the process is controllable under static conditions. If it is shown to be so, then this will justify the generation of dynamic heat transfer model justifying detailed experimental verification. There are existing correlations for calculating heat transfer in spray boiling, which could initially be used to check whether sufficient control of spray evaporative cooling could be achieved under transient engine load changes. One approach to predict the effect of boundary motion in spray cooling is identified to be the use of numerical simulations. But simulating the evaporation of a full spray may be computationally impractical, as the level of detail that needs to be captured is very high along with very fast transient nature of spray impingement as well as evaporation. Single droplet simulation seems much more practical and the literature shows examples of droplet impingement dynamics and evaporation simulations which were validated against experimental data. Also, two-phase spray evaporation is still not a well-established area of research which requires experimental results to validate the simulation results. It is therefore more practical at this stage to conduct experiments to understand full spray evaporative heat transfer on vibrating boundaries. The measured full spray data can then be used to advance dynamic correlation models (which could be used for control system design). But equally important would be to establish whether single droplet simulation can give any insight into full spray heat transfer in the presence of boundary motion. Based on these requirements, the objectives of the thesis are stated as follows.

- To create a one-dimensional control model representing an engine cylinder head wall, based on a validated static spray evaporative correlation model, and to check whether spray evaporative cooling can be controlled on engines running with transient loads.
- To perform numerical simulations of droplet impingement dynamics and evaporation using appropriate models to examine the effect of moving boundaries on droplet evaporative heat transfer and to establish whether there is any correlation between single-droplet evaporative cooling and spray evaporative cooling.
- To design an experimental test-rig to examine spray boiling with moving boundaries for a

flat heating surface.

- To perform spray boiling experiments on a vibrating flat surface with vibration amplitudes and frequencies in the range of 0.1 mm to 10 mm, and 1000 Hz to 10 Hz, respectively, (corresponding to typical engine-in-vehicle conditions) to identify only the effect of vibration with all other parameters that affect spray boiling heat transfer kept constant (such as flow rate, velocity, droplet size etc.).
- To examine the possibility of creating a dynamic correlation to predict spray evaporative heat transfer on moving boundaries.

The experimental research work was actually carried out as part of an EPSRC Evaporative Cooling Systems project (EP/M005755/1) in the Dynamics, Control, and Vehicle Research group at the University of Sussex. The project had three industrial partners, Ricardo, Denso, and Ford. The doctoral research work undertaken by the author is clearly identified throughout the thesis.

1.3. Outline of the thesis

Chapter 2 provides a review of existing correlations for calculating heat flux and temperatures at different regimes of pool, flow and spray boiling. It also looks into correlations for calculating spray parameters such as the Sauter Mean Diameter. Chapter 3 goes through the design and modelling of a transient 1-D control model developed to simulate heat transfer through the cylinder head wall of a spray evaporatively cooled engine. The results for simulations representing heat flow rates and load changes of a highly downsized engine producing 100 KW/L are then discussed. In chapter 4, numerical simulations of droplet impingement dynamics and two-phase heat transfer with, and without, moving boundaries are presented. The design, manufacture and commissioning of the experimental test-rigs are discussed in Chapter 5. Three different test-rigs mentioned are: I) A static pool boiling rig II) A static spray boiling rig, and III) A dynamic spray boiling rig with a flat test piece as well as a test piece representing engine cylinder-head geometry. The results from the experiments undertaken on all the test-rigs are described in Chapter 6 where a comparison is made between the full spray heat transfer measurements under dynamic conditions, and single droplet simulations. A dynamic correlation model for heat transfer with moving boundaries is also discussed. Chapter 7 concludes the work described in this thesis and makes suggestions for future wok on the subject.

Chapter 2. BOILING CORRELATIONS

Calculating boiling heat transfer is very difficult owing to the complex nature of the physical process involved. Generally, the boiling process starts with the formation of bubbles and then the vapour bubbles gets bigger and detaches from the solid-liquid interface owing to buoyancy. When the temperature is sufficiently high, this process becomes more violent with the formation of slugs and columns, before reaching the maximum heat transfer point. Further increase in temperature causes unstable boiling which leads to a point where vapour blanketing occurs, at which the heat transfer is very low [12, Ch. 7]. In order to analytically calculate heat transfer, all these processes need to be fully understood. The physics of boiling processes are not yet fully understood owing to its complexity.

Full analytical models for a liquid spray that undergoes a phase change are not yet available to calculate spray boiling heat transfer. One way to tackle this issue is by numerically solving this problem. This provides more information on the physical process itself along with heat transfer. But numerical simulations of spray impingent and evaporation are computationally extremely expensive and not practical. Droplet impingement and evaporation simulations are much more feasible owing to the much lesser complex process as well as the much smaller scale at which the details needs to be captured.

For numerical simulations, there are other difficulties such as predicting the surface characteristics, the bubble formation, and the bubble growth. It is especially difficult to predict the number of crevices and its density, and its distribution over an entire surface. It becomes even more complex if the heat transfer needs to be calculated for a heating surface with a complex geometry [25, Ch. 6]. Therefore, empirical correlations are generally used to calculate boiling heat transfer.

Researchers create empirical correlations that fit their experimental results. Empirical correlations are generally used to calculate boiling heat transfer owing to their ease of use. There are many empirical correlations available, because many researchers have fitted their data to a correlation for the range of experiments that they have undertaken. It is therefore important that in order to calculate heat transfer in boiling, a correlation that suits the boiling regime as well as other parameters (temperature, pressure, flow rate etc.) must be selected.

In this chapter, the most common correlations used for the calculation of pool boiling and flow boiling heat transfer up to the peak heat flux are first briefly explained. A review of the existing spray boiling correlations, focusing on various spray parameters, is then conducted.

2.1. Pool Boiling Correlations

2.1.1. Nucleate Boiling Correlation

The correlation developed by Rohsenow (1951) [46] is one of the oldest nucleate boiling correlations, which can be used to calculate the heat flux q, with respect to excess temperature. Rohsenow created the correlation from his experimental results. It uses a 'surface characteristics and wettability' parameter, C_{sf}, which is different for different solid-fluid combinations. Some of the solid-liquid combinations for which the correlation can be used are: water with platinum and brass, benzene with chromium, and ethyl alcohol with chromium. The typical error in Rohsenow's correlation [46] in calculating q for a known wall temperature is 100%, and 25% in calculating the excess temperature for a known q. The Rohsenow's nucleate boiling correlation [12, p. 219] is:

$$q = \mu_l h_{fg} \left(\frac{g(\rho_l - \rho_v)}{\sigma} \right)^{1/2} \left(\frac{C_{Pl}(T_w - T_{sat})}{C_{sf} h_{fg} P_{r_l}^n} \right)^3 \tag{2.1}$$

where μ_l is the dynamic viscosity, h_{fg} is the latent heat of vaporistaion, g is the acceleration due to gravity, ρ is the density, σ is the surface tension, C_P is the specific heat capacity, T_w is the wall temperature, T_{sat} is the saturation temperature, and $P_{r_l}^n$ is the Prandtl number. The subscripts l and v stand for liquid, and vapour phases respectively. A Prandtl number of 1 must be used for water, and for other liquids it takes a value of 1.7. This correlation can be used for different combinations of liquid and heating surface materials and a table of C_{sf} values is given in [12, p. 220].

2.1.2. Critical Heat Flux Correlation

Lienhard and Dhir (1973) [47] developed a correlation to calculate the critical heat flux q_{max}, in pool boiling. Lienhard and Dhir's correlation [12, p. 220] is given as:

$$q_{max} = C_o h_{fg} \rho_v \left(\frac{\sigma g(\rho_l - \rho_v)}{\rho_v^2} \right)^{1/4} \tag{2.2}$$

where C_o is a coefficient dependent on the shape and orientation of the surface, h_{fg} is the latent heat of vaporisation, g is the acceleration due to gravity, ρ is the density, and σ is the surface tension. The subscripts l and v stand for liquid, and vapour phases respectively.

Lienhard and Dhir (1973) [47] conducted experiments for peak heat flux data for many different liquids (including distilled water, Methanol, Acetone etc) on flat and cylindrical heater surfaces. They

created the correlation from the peak heat fluxes determined from the experiments. The shape and orientation coefficient, C_o, has a value of 0.149 and 0.116, for a horizontal plate and a cylindrical surface respectively. The maximum error in their calculations of critical heat flux from their experiments for the horizontal plate was 7.7 %.

2.2. Flow Boiling Correlation

The heat transfer due to flow of a viscous fluid over a surface is determined by the boundary layers it form near the surface. The boundary layers determine the velocity and temperature profiles near the surface. The velocity of a viscous fluid flow on a surface is zero. The distance at which the velocity transitions from zero to 99% of the free stream velocity defines the thickness of the velocity boundary layer. Similarly, the distance at which the liquid temperature at the wall transitions to 99% of the free stream value defines the thermal boundary layer thickness. Figure 2.1 shows the profiles of the thermal and velocity boundary layers.

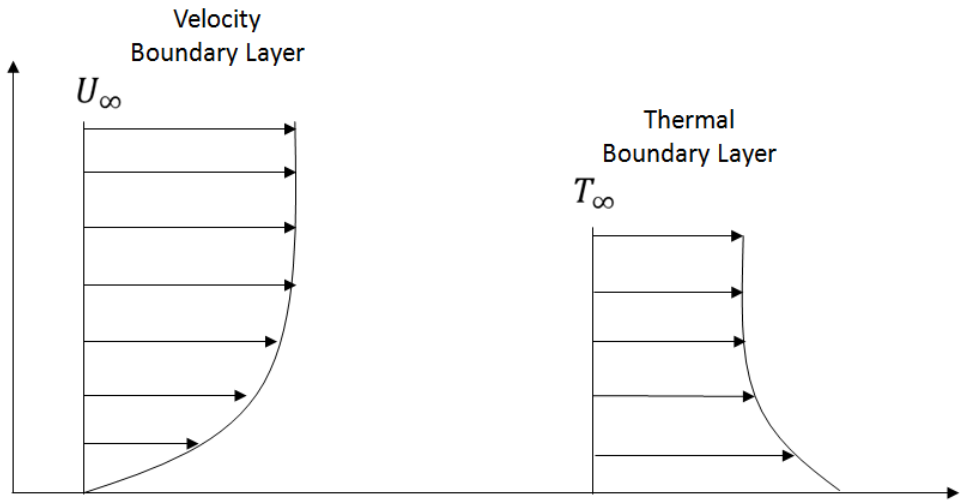

Figure 2.1: Velocity and thermal boundary layers.

There are three dimensionless numbers which are used to determine heat transfer through forced convection. These are the Nusselt number, the Reynolds number, and the Prandtl number. The Nusselt number is a ratio of convective to conductive heat transfer, the Reynolds number is a ratio of inertial forces to viscous forces, and the Prandtl number is a ratio of momentum diffusivity to thermal diffusivity. The equations of the Nusselt number, Reynolds number and Prandtl number are given below.

$$Nusselt\ number, Nu = \frac{hL}{K} \tag{2.3}$$

where h is the heat transfer coefficient, L is the characteristic length and K is the thermal conductivity.

$$Reynolds\ number, Re = \frac{\rho u L}{\mu} \tag{2.4}$$

where ρ is the density, u is the velocity, L is the characteristic length and μ is the dynamic viscosity.

$$Prandtl\ number, Pr = \frac{C_p \mu}{K} \tag{2.5}$$

where C_p is the specific heat, μ is the dynamic viscosity and K is the thermal conductivity.

In order to calculate the heat transfer in forced convection, the Nusselt number is generally equated to the Reynolds number and the Prandtl number with some constant and powers attached to it. It has the general form

$$Nu = a\ Re^b Pr^c \tag{2.6}$$

where a, b and c are the constant and powers of the equation. These values are generally determined by experiments for different flow scenarios. It can be seen from equation (2.6) that increasing the Reynolds number and Prandtl number should increase the heat transfer. Reynolds number determines the turbulence in a flow. Increase in velocity results in the increase of turbulence. With increasing turbulence, both the velocity and the thermal boundary layer thicknesses reduce which results in a larger temperature gradient. Hence the increase in heat transfer with respect to increase in turbulence.

The correlation of Chen (1966) [48] is one of the most successful and widely used correlation for predicting saturated flow boiling heat transfer. For predicting flow boiling in engines, researchers have used either the correlation in its original form or a modified version of it. The experiments undertaken by Finlay et al. [49] and Campbell et al. [2], on flow boiling in engines, have used the Chen's correlation as the base for predicting their experimental results. Chen's correlation uses two terms to calculate the total heat transfer, assumed to comprise of macro-convective and micro-convective heat transfer. The macro-convective heat transfer component is derived from single-phase forced convection, whereas the micro-convective term is for the heat transfer from nucleate boiling. Two dimensionless functions, *Chen's suppression factor* or Bubble-growth suppression factor S, and Reynolds number function F, are used to consider the interaction of two mechanisms. S is the ratio of the effective superheat to the total superheat of the wall, and F is the ratio of the two–phase

Reynolds number to the liquid Reynolds number. Predictions using Chen's correlation was found to have an average deviation of ±12% compared to experimental data. The correlation was tested for water within a pressure and velocity range of 8 to 505 PSIA, and 0.2 to 14.7 ft/s respectively. The macro-convective heat transfer coefficient is given as:

$$h_{mac} = 0.023(Re_l)^{0.8}(Pr_l)^{0.4}\left({}^{K_l}/_{D}\right)F \tag{2.7}$$

where Re is the Reynolds number, Pr is the Prandtl number, K is the thermal conductivity, D is the characteristic length, and F is the Reynolds number factor. The micro-convective heat transfer coefficient is given in equation (2.8).

$$h_{mic} = 0.00122\left(\frac{{K_l}^{0.79}{C_{Pl}}^{0.45}{\rho_l}^{0.49}{g_c}^{0.25}}{\sigma^{0.5}{\mu_l}^{0.29}\lambda^{0.24}{\rho_v}^{0.24}}\right)(\Delta T)^{0.24}(\Delta P)^{0.75}S \tag{2.8}$$

where ρ is the density, g_c is the gravitational constant, σ is the surface tension, μ is the dynamic viscosity, λ is the latent heat of vaporisation, ΔT is the excess temperature, ΔP is the difference in vapour pressure and S is the boiling suppression factor. The subscripts l and v in equations (2.7) and (2.7) stand for liquid and vapour phases respectively.

2.3. Spray Boiling Correlations

Similar to other types of boiling, spray boiling correlations are also mostly empirical. The most widely used correlations for calculating the spray characteristics with single-phase and two-phase heat transfer for spray cooling are given shortly. In order to calculate the heat transfer in spray boiling, most correlations use an average droplet diameter representing the entire spray. Sauter mean diameter is one of the most popular measures used to specify the mean spray droplet diameter as now explained. Sauter mean diameter is the diameter of a sphere having the same surface area to volume ratio of an object which could have any shape.

2.3.1. Sauter Mean Diameter (SMD) Correlation

Mudawar and Estes (1995) [26] developed a correlation for Sauter Mean Diameter (SMD) based on their experimental results for fluids with different values of surface tension. Sprays were tested using a Phase Doppler Particle Analyser (PDPA), which is a non-intrusive technique for determining the spray hydrodynamic parameters. The correlation is based on both the Reynolds number and the Weber number at the nozzle exit. Mudawar and Estes [26] claim that, even though there are many correlations available for predicting SMD for various sprays, there is none available for full cone sprays. The mean absolute error in predicting the SMD for coolants FC-72 and water was found to be

12.4%. The SMD correlation for full cone nozzles is given as:

$$\frac{d_{32}}{d_o} = 3.67\left[We_{d_o}{}^{1}/_{2} Re_{d_o}\right]^{-0.259} \tag{2.9}$$

where d_{32} is the SMD, d_0 is the characteristic length selected for the correlation (which is the orifice diameter) We_{d_o} is the orifice Weber number, and Re_{d_o} is the orifice Reynolds number. The orifice flow Weber number, and Reynolds number, are given in equations (2.10) and (2.11) respectively.

$$We_{d_o} = \frac{\rho_g \left(\frac{2\Delta P}{\rho_l}\right) d_o}{\sigma} \tag{2.10}$$

$$Re_{d_o} = \frac{\rho_l \left(\frac{2\Delta P}{\rho_l}\right)^{1/2} d_o}{\mu_l} \tag{2.11}$$

where ΔP stands for the pressure difference across the nozzle, ρ is the density, σ is the surface tension, and μ is the dynamic viscosity. The subscripts g and l stand for gas and liquid respectively. The velocity calculation for both the Weber number and the Jacob number assumes the liquid to be inviscid.

2.3.2. Single-Phase Correlation

There are several correlations based on experimental results for single-phase heat transfer with water as the coolant. Some of these correlations are developed by Mudawar and Valentine (1989) [27], Mudawar and Rybicki (2006) [28], Karwa et al (2007) [50], and Cheng et al (2011) [51]. The correlations by Mudawar and Valentine (1989) [27], and Cheng et al (2011) [51] are described below.

Mudawar and Valentine (1989) created a single-phase heat transfer correlation from their experimental results for water sprays having a volumetric flux of 0.6 $m^3/s/m^2$ to 10 $m^3/s/m^2$. These experiments used water at a temperature range of 22.5 ^oC to 60.5 ^oC. The correlation by Mudawar and Valentine(1989) [27] is given below:

$$Nu = 2.512 Re_s^{0.76} Pr_f^{0.56} \tag{2.12}$$

Where Nu is the Nusselt number, Re_s is the spray Reynolds number, and Pr_f is the fluid Prandtl number.

Cheng et al (2011) correlated single-phase heat transfer from their experimental results for spray flow rates of 3.6 L/h, 4.2 L/h, and 5.2 L/h respectively. The Cheng et al correlation is as follows:

$$Nu = 0.036Re^{1.04}We^{0.28}Pr^{0.51}(3.02 + \varepsilon^{1.53}) \quad (2.13)$$

which is a correlation between Nusselt number Nu, and Reynolds number Re, Weber number We, Prandtl number Pr and a dimensionless temperature ε i.e. the ratio of the temperature difference between the surface and the fluid to the saturation temperature of the fluid.

2.3.3. Two-Phase Heat Flux Correlation

Mudawar and Valentine (1989) [27] conducted various experiments for water spray boiling, and they created a nucleate boiling correlation based on their experimental results. Their experiments were for water at a temperature of 22.5 °C to 23.5 °C. The Mudawar and Valentine spray nucleate boiling correlation is given below.

$$q^{"} = 1.87 \times 10^{-5}\left(T_{surf} - T_f\right)^{5.55} \quad (2.14)$$

where $q^{"}$ is the nucleate boiling heat flux, T_{surf} is the surface temperature, and T_f is the fluid temperature.

Hsieh et al (2004) [52] developed a nucleate boiling heat flux correlation based on their experimental study on spray cooling using water and the refrigerant R-134a as coolants. Experiments were for a range of Weber numbers of 50 to 152, and 80 to 231, for R-134a and water respectively. The spray boiling heat flux is correlated using the modified boiling number Bo_m:

$$Bo_m = C(We)^m(Ja)^n \quad (2.15)$$

where C, m and n are coefficients dependent on the liquid and for water, the values of C, m, and n are 15.6, 0.59, and 1.68 respectively. The spray Weber number and Jacob number are given as:

$$We = \frac{\rho_l {u_0}^2 d_{32}}{\sigma_l} \quad (2.16)$$

$$Ja = \frac{C_l \Delta T}{h_{fg}} \quad (2.17)$$

where u_0 is the mean spray impingement velocity and C_l is the specific heat capacity of the liquid. The spray Weber number is a dimensionless number representing the ratio of spray inertia forces to the surface tension forces whereas the Jacob number is a dimensionless number representing the ratio of spray sensible heat to latent heat.

Mudawar and Estes (1995) [26] developed a correlation for calculating critical heat flux in spray boiling, in which spray sub-cooling is taken into consideration. The correlation was developed using data from spray boiling experiments for FC-72 and water as coolants. For water as the coolant, the Mudawar and Valentine (1989) [27] experimental results were used. These experiments were for droplet sauter mean diameters in the range of 0.546 mm to 1.351 mm. The corresponding range of volumetric fluxes were 0.0006 $m^3/s/m^2$ to 0.00996 $m^3/s/m^2$ respectively. The water spray boiling experiments had a sub-cooling of 76.5 ^oC to 77.5 ^oC. In this correlation, the local volumetric flux has a very high influence in the calculation of critical heat flux. The critical heat flux correlation by Mudawar and Estes [26] is given as:

$$\frac{q_{max}}{\rho_g h_{fg} Q^{"}} = 2.3\left(\frac{\rho_l}{\rho_g}\right)^{0.3}\left(\frac{\rho_l Q^{"} d_{32}}{\sigma}\right)^{-0.35} \times \left(1 + 0.0019\frac{\rho_l C_{Pl}\Delta T_{sub}}{\rho_g h_{fg}}\right) \qquad (2.18)$$

where q_{max} is the critical heat flux, $Q^{"}$ is the local volumetric flux, and ΔT_{sub} is the spray sub-cooling.

Liang and Mudawar (2017) [53], provides a comprehensive review of spray cooling, including numerous correlations for single phase heat transfer, nucleate boiling heat transfer, and critical heat flux.

All these boiling correlations are useful in calculating heat transfer in different boiling regimes, but a lot of it involves fitting the experimental data. It is imperative to use a correlation at the desired range of parameters for which it was created for. It is likely that large errors could occur if out of range conditions are used. The calculated values must be checked against any experimental data for validation. These correlations are also very useful for creating evaporative cooling models. A single regime correlation could be used if the model only deals with one boiling regime. If multiple boiling regimes are simulated, it is critical that a combination of different correlations must be employed.

Chapter 3. TRANSIENT ONE-DIMENSIONAL EVAPORATIVE COOLING CONTROL MODEL

The review of the literature of IC engine evaporative cooling as well as different types of boiling processes lead to the question of whether it is possible to satisfactorily control evaporative cooling of an engine. To examine this issue, a model to simulate the evaporative cooling of a engine cylinder-head wall has been created. To simplify the problem, and for easier analysis of heat flow, a one-dimensional transient conduction model was employed. The heat transfer on the gas-side (namely the combustion chamber side) of the cylinder-head wall was modelled using an instantaneous in-cylinder gas temperature and heat transfer coefficient over a full four stroke cycle. Similarly, on the coolant-side, a model calculating the evaporative heat flux was employed using a boiling correlation. Two types of evaporative cooling were employed: pool boiling and spray boiling. Even though flow boiling was initially considered, and was to be employed as the second type of evaporative cooling, it was later dropped because much higher heat transfer rates are available from spray boiling. A control model was created using Matlab Simulink, and was used to simulate pool boiling and spray boiling as the mode of cooling.

3.1. Modelling of Engine Cylinder-Head Wall Heat Transfer

3.1.1. In-Cylinder Heat Transfer Model

In order to calculate the heat transfer into the cylinder-head wall, two parameters are required: the in-cylinder gas temperature and the heat transfer coefficient. The instantaneous gas temperature and the heat transfer coefficient, along with the instantaneous gas side metal temperature provide the heat flow. It was identified that the most recent highly downsized engines produce a peak power output of ~100 KW/L whilst generating a maximum heat flux of 1.2 MW/m^2 at the hottest areas of the cylinder-head. A 1 litre gasoline engine producing a power output of 100 KW/L was simulated using the commercial engine simulation code AVL Boost, to obtain instantaneous in-cylinder gas temperatures and heat transfer coefficients. Simulations were undertaken for a 4-stroke engine running on full load at a speed of 5000 rpm. The model was only intended to get engine in-cylinder conditions that qualitatively represent four stroke engine behaviour loaded to produce 100 KW/L. A four stroke gasoline model from an AVL Boost example was modified by increasing the intake pressure until the engine produced a power output of 100 KW/L. A Woschni heat transfer model, along with a Vibe heat release model, were used to model the heat transfer. The data generated was not verified against measured in-cylinder gas temperatures and heat transfer coefficients as these were not available, neither was the model updated to represent geometries of a 100 KW/L engine. Given that the model was intended purely for qualitative

purposes, no model verification was attempted. The cycle averaged heat transfer coefficient and gas temperature were calculated to be 510.5 W/m^{2}K and 1060 K respectively. Data in the simulation was effectively sampled at a rate of one sample per degree crank angle. Figures 3.1 and 3.2 show the corresponding heat transfer coefficients and gas temperatures.

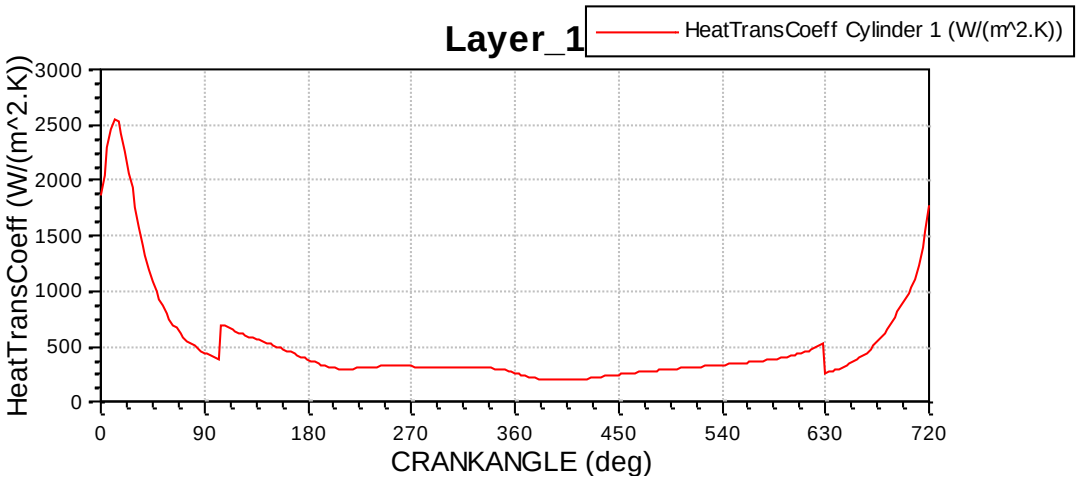

Figure 3.1: Simulated in-cylinder heat transfer coefficient against crank angle.

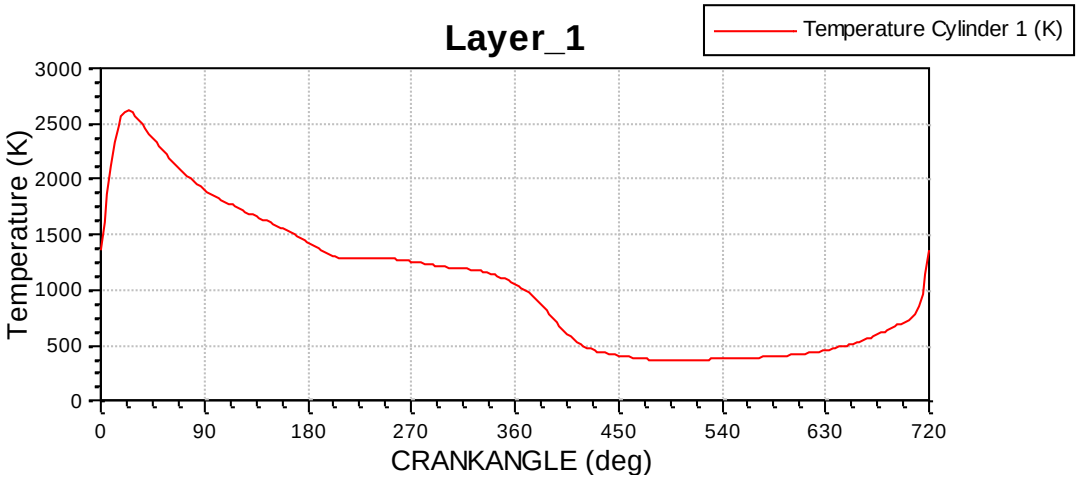

Figure 3.2: Simulated in-cylinder gas temperature against crank angle.

3.1.2. Wall Conduction Model

To solve the heat conduction problem, a finite difference method [54] was used to model the transient heat transfer through the cylinder-head wall. This method provides an explicit solution for transient conduction. A 1-D model (rather than a 3-D model) was used to simplify the problem, and also to save computation time. It is actually to interpret the results from 1-D analysis. This is because the heat transfer is only in one direction, which helps to better understand the effect of thermal diffusivity over the thickness of the material and to easily determine the time it takes for the change

of temperature to occur at any point of the model with respect to the change in heat flow at the boundaries.

To employ the 1-D finite difference method, a grid system needs to be created across the thickness of the material. The cylinder-wall had to be split into several grid points for the calculation of temperature at each point. The cylinder-head wall was represented by a 7 mm thick metal slab in the model. It was spatially discretised into five grid points as shown in figure 3.3

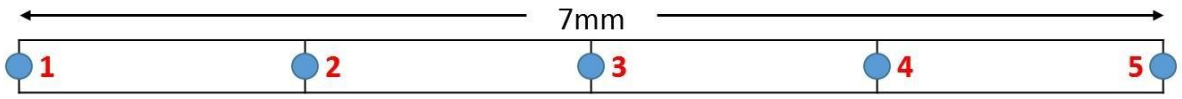

Figure 3.3: Cylinder-head wall spatially discretised by five grid points.

where the grid point 1 is the gas side boundary and grid point 5 is the coolant side boundary. Aluminium was chosen as the material for the cylinder-head and its properties are given in Table 3.1.

Table 3.1: Properties of the material used in the model.

Material property	Value
Thermal Conductivity, *K*	150 W/m K
Density, ρ	2700 kg/m^3
Specific Heat Capacity, C_P	910 J/kg K
Thermal diffusivity, α	6.105 x 10^{-5} m^2/s

The transient conduction model is based on a Taylor series approximation of the one-dimensional Fourier equation as described in the numerical method explained in the book by Long [54, pp. 80–81]. The 1-D Fourier Diffusion equation assumes heat conduction is only in one direction [54] which is given as:

$$\frac{\partial^2 T}{\partial x^2} = \frac{1}{\alpha}\frac{\partial T}{\partial t} \tag{3.1}$$

where T is the temperature, x is the position, α is the thermal diffusivity, and t is the time. The spatial derivative on the left hand side can be approximated as

$$\frac{\partial^2 T}{\partial x^2} \approx \frac{T_{(i+1)} - 2T_i + T_{(i-1)}}{\delta x^2} \tag{3.2}$$

and the temporal derivative on the right hand side can be approximated as

$$\frac{1}{\alpha}\frac{\partial T}{\partial t} \approx \frac{T_i^{(n+1)} - T_i^{(n)}}{\alpha \delta T} \tag{3.3}$$

The subscript '*I*' stands for the grid point of interest, and '*i-1*' and '*i+1*' are the grid points on the left and right of the grid point *i* respectively. The superscript '*n*' stands for the current time step, and '*n+1*' stands for the next time step. Substituting equations (3.2) and (3.3) into (3.1), produces the following equation:

$$\frac{T_{(i+1)}^{(n)} - 2T_{(i)}^{(n)} + T_{(i-1)}^{(n)}}{\delta x^2} = \frac{T_{(i)}^{(n+1)} - T_{(i)}^{(n)}}{\alpha \delta T} \tag{3.4}$$

To calculate the temperature at a grid point, for the next time step, equation (3.4) can be re-arranged into the form:

$$T_{(i)}^{(n+1)} = \delta Fo.T_{(i+1)}^{(n)} + (1 - 2\delta Fo)T_{(i)}^{(n)} + \delta Fo.T_{(i-1)}^{(n)} \tag{3.5}$$

where $\delta Fo = {}^{\alpha \delta t}/_{\delta x^2}$ is the Fourier number, where δt is the time step size, and δx is the distance between the grid points. For grid points on the boundary, where there is no grid point on one side, an imaginary grid point can be used. The temperature of the imaginary grid point can be calculated by

$$T_{imag} = T_{adj} + \frac{2\delta x q}{k} \tag{3.6}$$

where q is the heat flux that needs need to be applied at both boundaries of the conduction model (i.e. the heat flux into the metal from the in-cylinder conditions, and the heat flux taken away from the metal through evaporative cooling), and subscripts '*imag*' and '*adj*' represent the imaginary grid point outside of the grid, and the grid point adjacent to the boundary grid point inside the grid respectively. The imaginary point is assumed to be an imaginary extension of the material with the same thermal conductivity as well as experiencing the same heat flux as the material so that a numerical solution could be obtained.

The equations derived for the temperatures at grid points 1 to 5 in figure 3.3 are given below.

$$T_1^{n+1} = \delta Fo T_{(2)}^{(n)} + (1 - 2\delta Fo)T_1^n + \delta Fo\left(\frac{2\delta x h_{gas}\left(T_{gas} - T_2^n\right)}{k}\right) \quad (3.7)$$

$$T_2^{n+1} = \delta Fo T_{(3)}^{(n)} + (1 - 2\delta Fo)T_2^n + \delta Fo T_1^n \quad (3.8)$$

$$T_3^{n+1} = \delta Fo T_{(4)}^{(n)} + (1 - 2\delta Fo)T_3^n + \delta Fo T_2^n \quad (3.9)$$

$$T_4^{n+1} = \delta Fo T_{(5)}^{(n)} + (1 - 2\delta Fo)T_4^n + \delta Fo T_3^n \quad (3.10)$$

$$T_5^{n+1} = \delta Fo\left(T_{(3)}^{(n)} + \frac{2\delta x q}{k}\right) + (1 - 2\delta Fo)T_5^n + \delta Fo T_4^n \quad (3.11)$$

The stable solution of equations (3.7) to (3.11) requires the time step size to meet the stability criteria defined as:

$$\delta Fo(1 + \delta Bi) < 0.5 \quad (3.12)$$

where $\delta Bi = {\delta x h}/{k}$ is the Biot number. Numerical stability of equation (3.7) requires

$$\delta t < \frac{0.5\ \delta x^2}{\alpha\left(1 + {\delta x h}/{k}\right)} \sim = 0.025s \quad (3.13)$$

But to fully capture the highly transient nature of heat transfer through the engine cylinder-head wall, a time step was chosen equal to the duration it takes for the crank angle to rotate one degree. For an engine speed of 5000rpm, the time step size was therefore calculated to be 1/30000 s which was numerically very stable

3.1.3. Implementation of the Cooling Models

Equation (3.11) requires an instantaneous heat flux value to model the heat transfer associated with the cooling method used. Either boiling correlations or experimental data could be used to calculate the heat flux on the coolant side. It can be seen from the literature that experimental data for heat flux are generally plotted against excess temperature or temperature difference between the heating surface and the coolant. Similarly, for the calculation of heat flux, most correlations depend on the excess temperature.

To develop a control model, the variables that can be used for control of heat transfer need to be identified. Even though there are many variables that affect boiling heat transfer, most of these are constant for a given set of hardware. Table 3.2 provides a list of some of these variables which are fixed by the hardware.

Table 3.2: List of variables that affect boiling heat transfer which are generally fixed by the hardware.

Parameter	Relevant To	Note
Surface area available for heat transfer	Pool, flow and spray boiling	The surface area available for heat transfer is generally fixed by the hardware but in the case of spray boiling, it can sometimes vary depending on the specific hardware used. The cone angle of the spray can vary depending on the pressure difference across the nozzle.
Coolant passage diameter/cross section	Flow boiling	It determines the distribution of the coolant flow velocity and are not usually variable.
Spray height and droplet diameter	Spray boiling	The spray height is fixed by the system and the droplet diameter can vary depending on the pressure drop across the nozzle. But the droplet diameter cannot be controlled.

Table 3.3 provides the list of variables, relevant to each type of boiling, that highly affects boiling heat transfer, which are not fixed by the hardware. These can be used as control variables.

Table 3.3: List of variables that affect each type of boiling heat transfer which can be used as control variables.

Parameter	Relevant To	Note
Coolant chamber pressure	Pool, flow and spray boiling	The chamber pressure determines the saturation temperature of the liquid. Higher pressures suppress boiling whereas lower pressures promote boiling.
Flow rate/Volumetric flux	Flow and spray boiling	Determines the heat flux for a given excess temperature or temperature difference between the coolant and the heating surface
Coolant sub-cooling	Pool, flow and spray boiling	Determines the level of initial stage of boiling heat transfer: single phase convection (forced or free). Higher sub-cooling leads to more single-phase convection.

Figure 3.4 shows the spray evaporative cooling model developed. It uses a PI controller to control the gas-side metal temperature at a constant value (for varying engine load) by varying the nozzle flow rate. The gas-side heat transfer is modelled by the gas temperature and the wall heat transfer coefficient generated by the Boost simulation. The wall conduction is modelled by the numerical solution of the Fourier's transient 1D equation. The coolant-side heat transfer is modelled by a spray evaporative correlation. The details of the simulation and results are discussed later in section 3.3.

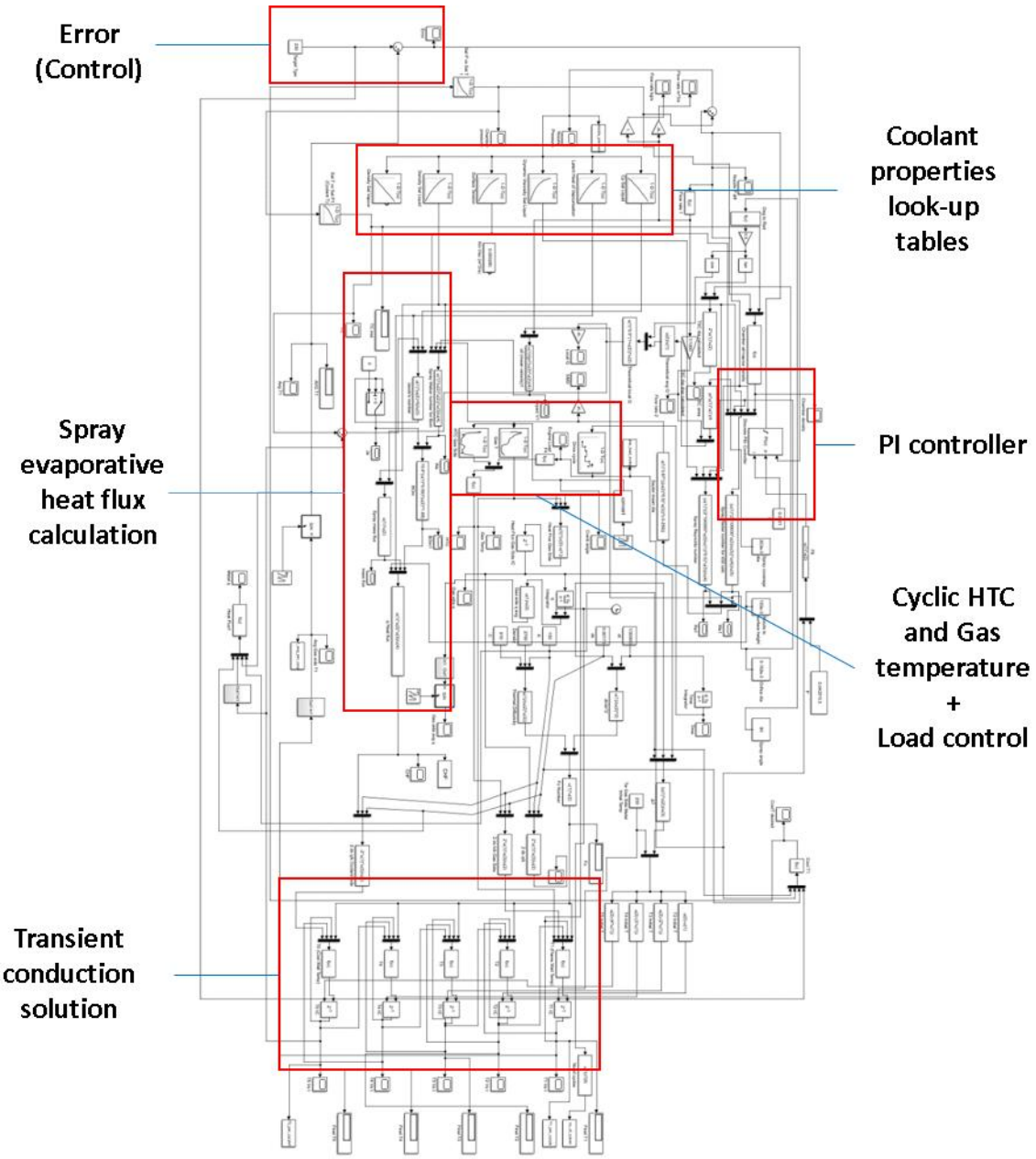

Figure 3.4: Simulink model of the spray evaporative cooling control model.

3.2. Pool Boiling Cooling Model Simulations without Control to Examine 1-D Thermal Diffusivity

Before explaining the control model, pool-boiling model with extremely high metal temperatures was simulated to study the effect of thermal diffusivity across the thickness of the cylinder-head wall. The extreme temperature scenario simulated a condition corresponding to the gas-side metal temperature equal to the transient in-cylinder gas temperature, in which the cylinder-head wall is cooled by pool boiling. This didn't actually involve any control, and the coolant chamber pressure was fixed at 1 atm. The objective was to find the spatial distribution of metal temperature from the gas-side to the coolant-side, and to see the effect of highly fluctuating gas-side metal temperature

on the coolant-side metal temperature. The pool boiling heat transfer model was based on an experimental heat flux [54, p. 217], for a coolant saturation pressure of 1 atm for water as the coolant.

The gas-side metal temperature T1 was set equal to the transient gas temperature obtained from AVL Boost for an engine producing 100 KW/L. Grid point 5 simulated the metal surface temperature subjected to a heat flux provided by the pool boiling relationship [54, p. 217]. A look-up table was used to input the pool boiling heat flux based on the excess temperature. The constant inputs used in the model are shown in Table 3.4. Table 3.5 shows the grid point temperatures per engine cycle.

Table 3.4: Constant inputs for both the control model and the extreme case scenario.

Input Name	Value
Time Step, dt	1/30000 s
Grid Size, dx	1.75mm
Metal Thermal Conductivity	150 W/m K
Metal Density	2700 kg/m^3
Metal Specific Heat Capacity C_P	910 J/kg K

3.2.1. Results and Discussion

Form the simulation, the mean temperature during the 4-stroke cycle and their deviations were calculated for each grid point. Table 3.5 shows the mean grid point temperatures per engine cycle and its deviation.

Table 3.5: Transient spatial temperature distribution in extreme case scenario.

Grid Point Number	Distance From Gas Side Metal Surface (mm)	Mean Temperature (^{O}C)	Deviation (^{O}C)
1	0	783.35	±635.57
2	1.75	778.07	±41.54
3	3.5	773.72	±3.05
4	5.25	769.40	±0.23
5	7	765.08	±0.03

From the results, a deviation of ~636 ^{o}C per cycle was observed on the gas-side metal temperature whereas on the coolant-side, this has reduced to almost zero. Results show that there is very small (or negligible) fluctuation of the coolant-side metal temperature owing to the highly fluctuating gas-

side metal temperature. Figure 3.5 shows the spatial distribution of mean temperature and its deviation over the thickness of the metal.

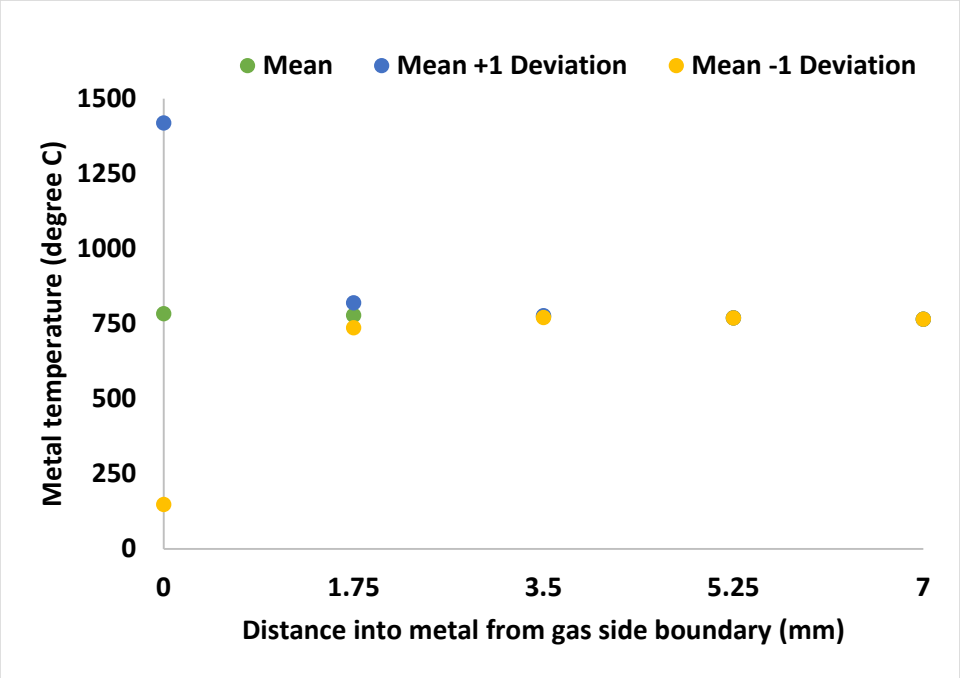

Figure 3.5: Spatial distribution of temperature over metal thickness.

The pool boiling cooling model results showed that the fluctuating gas-side metal temperature hardly has any effect on the coolant-side metal temperature. This indicates that the transient in-cylinder conditions per cycle should not pose a difficulty for control of cooling as the temperature fluctuations diffused over the thickness of the metal.

3.3. Spray Boiling Control Model Simulations

The correlation by Hsieh et al (2004) [52], mentioned in the spray boiling correlations in Chapter 2, was chosen to model the spray boiling heat transfer. This correlation is based on a modified boiling number which was developed using their experimental results on spray boiling using water and refrigerant R-134a. They have undertaken experiments using sprays with spray Weber numbers ranging from 50 to 231. This correlation was chosen, as the range of Weber numbers in their experiments are similar to the range of Weber numbers for the spray nozzle chosen for the spray boiling control model. The correlation by Hsieh et al [52] is given as:

$$Bo_m = C(We)^m(Ja)^n \tag{2.15}$$

where C, m and n are coefficients dependent on the liquid, and for water, the values of C, m, and n are 15.6, 0.59, and 1.68 respectively. The spray Weber number and Jacob number are given in equations (2.16) and (2.17):

$$We = \frac{\rho_l {u_0}^2 d_{32}}{\sigma_l} \tag{2.16}$$

and

$$Ja = \frac{C_l \Delta T}{h_{fg}} \tag{2.17}$$

The Sauter mean diameter d_{32} was calculated using the correlation by Mudawar and Estes (1995) [1], given by:

$$\frac{d_{32}}{d_o} = 3.67 \left[{We_{d_o}}^{1/2} Re_{d_o} \right]^{-0.259} \tag{2.9}$$

The orifice flow Weber and Reynolds number are given as:

$$We_{d_o} = \frac{\rho_g \left(\frac{2\Delta P}{\rho_l}\right) d_o}{\sigma} \tag{2.10}$$

and

$$Re_{d_o} = \frac{\rho_l \left(\frac{2\Delta P}{\rho_l}\right) d_o}{\mu_l} \tag{2.11}$$

A spray cooling control model using the above correlations was created in Matlab Simulink using the finite difference equation (3.11) derived for node 5. A PI controller with gain scheduling with respect to engine load changes was employed to control the nozzle flow rate. The control target was to maintain a constant gas-side metal temperature (T1) at different engine loads by controlling the coolant-side metal temperature (T5). The nozzle flow rate was controlled by the PI controller to provide the required heat flux, which is equal to the heat flux going into the cylinder-head wall from the gas-side. Based on the engine load, the cycle averaged heat flux through the cylinder-head wall was calculated. The coolant-side metal temperature, to give the desired gas-side metal temperature, was then calculated using the heat flux, the temperature gradient, and the metal thermal conductivity. A coolant temperature with 5 ^{o}C sub-cooling to the calculated coolant-side metal

temperature, and a chamber pressure for the coolant without sub-cooling to be at saturation were then set. Look up tables were employed to specify the coolant temperature and chamber pressure. All the liquid properties were set appropriately, using look-up tables, to account for their variations with respect to temperature. The diagram of the Matlab Simulink control model created is give in Appendix A.

Simulations were performed to control the gas-side metal temperature at a constant 230 ^{O}C during the transient operation of the engine. A load change from full-load to half-load was simulated to check the effectiveness of the controller. At full load, the maximum heat flowing through the cylinder-head wall was 1.6 MW/m^2. The heat transfer coefficients and gas temperatures, as shown in figures 3.1 and 3.2, were scaled to achieve the maximum heat flux of 1.6 MW/m^2. The total simulation time was an engine running time of 60 s. The engine load input was used to schedule the gains linearly. The gains were multiplied by 1 for full-load and was reduced linearly with respect to the load. Table 3.6 shows the spray and control parameters [4] used for the simulations.

Table 3.6: Spray and simulation parameters [55]**.**

Nozzle orifice diameter (mm)	0.152
Spray height (mm)	103
Spray coverage diameter (mm)	203
Solid cone angle (^{O})	90
Proportional gain	0.02125
Integral gain	0.0001
Control criteria	Ziegler-Nichols method for proportional control with arbitrarily-chosen integral gain but small enough to achieve optimum control without large fluctuations
Time step size (s)	1/30000

3.3.1. Results and Discussion

Figure 3.6 shows the cycle averaged gas-side metal temperature, the instantaneous coolant-side metal temperature, and the coolant temperature from the simulations. It can be seen from figure 3.6 that good control of the gas-side metal temperature was achieved. The gas-side metal temperature fluctuates within a range of 5 ^{o}C between load changes and settles down within 0.7 s. The coolant-side metal temperature fluctuated initially during the load change and it was because of the sudden drop in load. The effect of thermal diffusivity can be clearly observed, as a fluctuation of

the coolant-side metal temperature by around 30 ^{O}C only results in the fluctuation of the gas-side metal temperature by 5 ^{O}C.

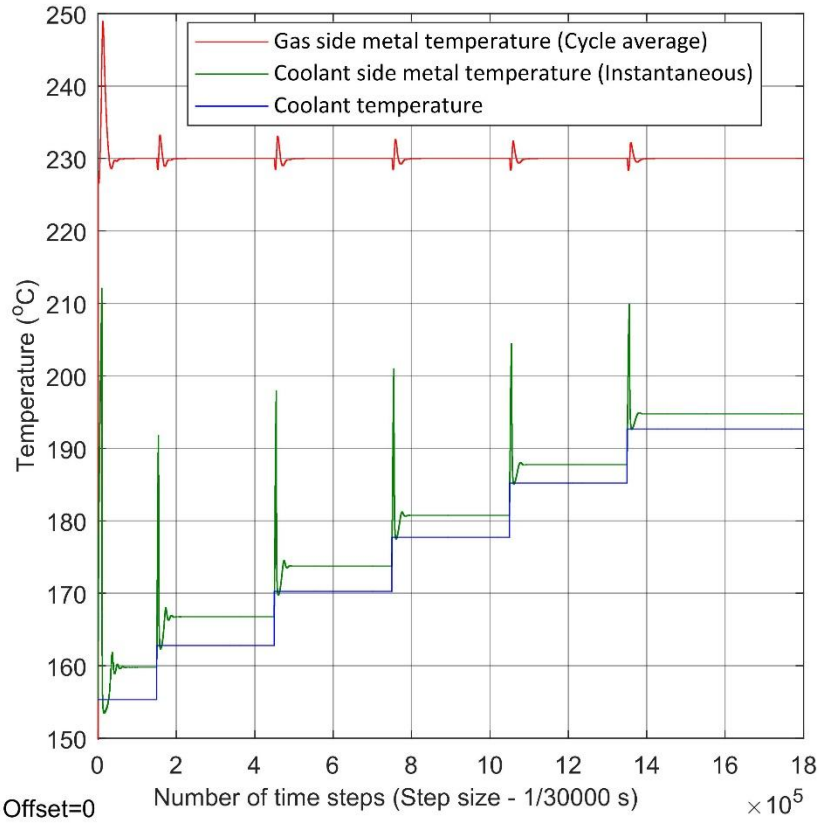

Figure 3.6: Gas side metal temperature (cycle averaged), coolant side metal temperature and the coolant temperature over the duration of the simulation.

Figure 3.7 shows the chamber pressure over the duration of the simulation, set by the coolant temperature (for it to be at saturation). The chamber pressure at full-load was low to allow for easier boiling at a lower coolant-side metal temperature. Coolant-side metal temperature increases with decreasing load, to maintain a constant gas-side metal temperature, as the heat flow through the cylinder-head wall lowers with the reducing load.

Figure 3.8 shows the coolant side heat flux and figure 3.9 shows the spray mass flux, over the duration of the simulations. During load changes, the nozzle flow rate fluctuated, causing the mass flux to fluctuate, which resulted in the overshoot of heat fluxes. These heat flux values were many times higher than what is going into the wall. This can be seen as a drawback of the model as the heat flux was calculated using a correlation and did not fully account for the physics of the cooling process. In the real-world conditions, these heat flux overshoots would not happen.

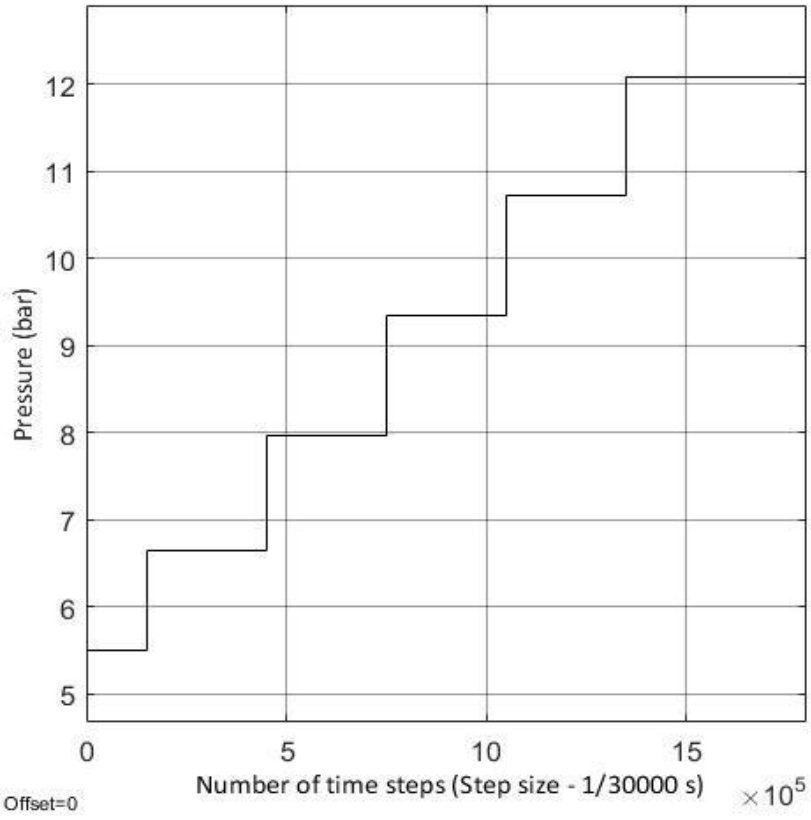

Figure 3.7: Chamber pressure over the duration of the simulation.

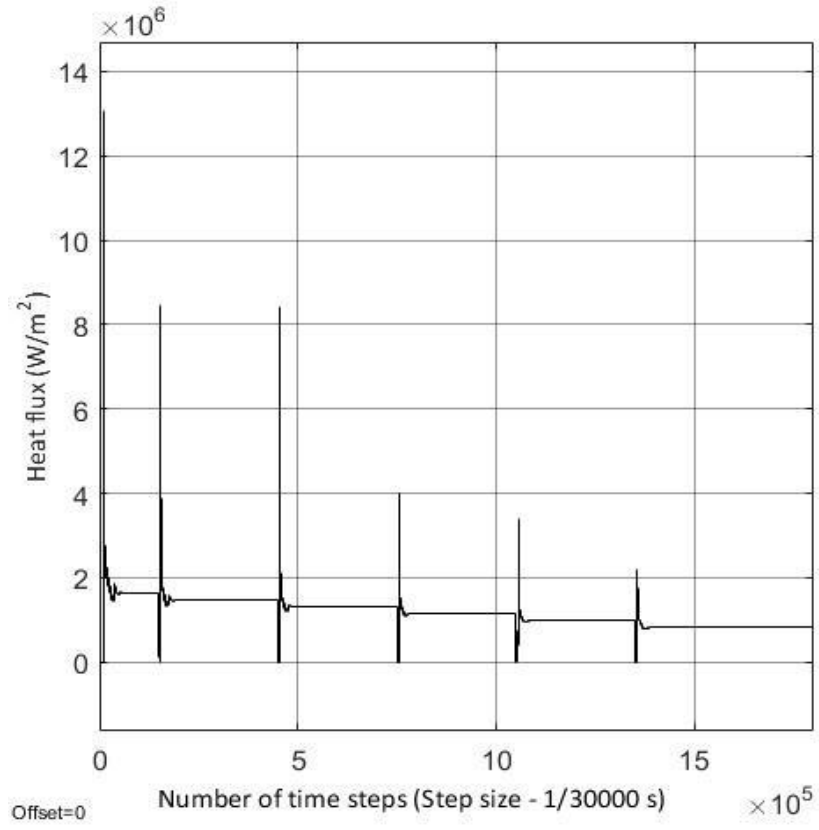

Figure 3.8. Spray evaporative heat flux over the duration of the simulation

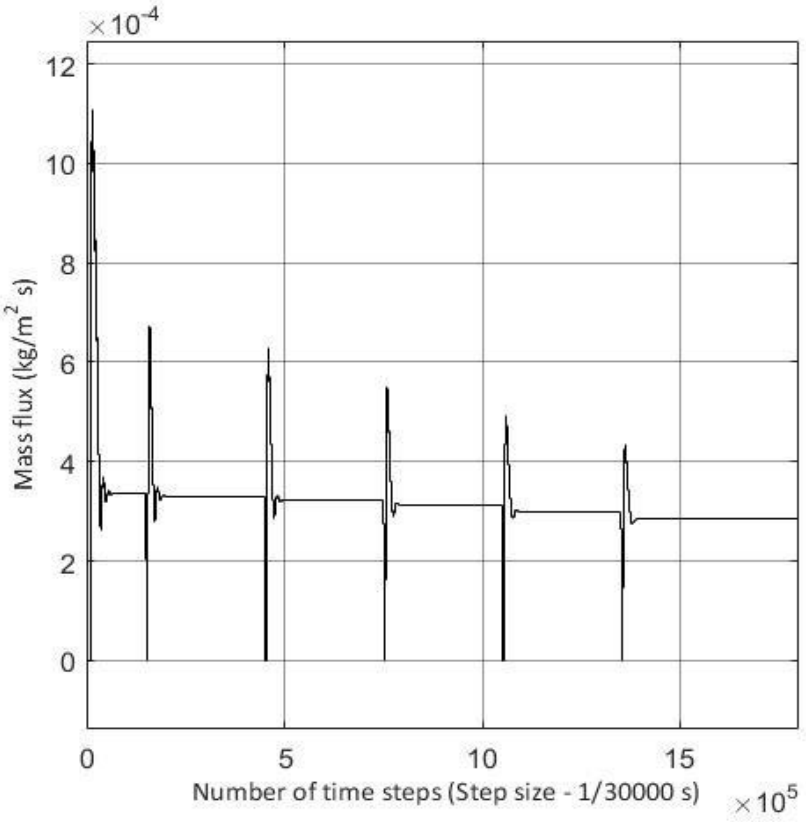

Figure 3.9: Spray mass flux over the duration of the simulation.

3.3.2. Estimation of Error in the Control Model

In order to estimate the error in the control model, an error analysis of the complete model needs to be performed. A complete error analysis requires the error in each parameter used, but the error in many of the parameters used in modelling the spray cooling heat transfer is unknown. The known error in some of the important parameters are: 1.) Heat transfer correlation - ±1.05% 2.) Sauter Mean Diameter Correlation - ±25% and 3.) Liquid properties - ±1.76%. The error in other important parameters such as the nozzle flow rate and spray cone angle are not available. The nozzle flow rate is calculated using an equation provided by the supplier and it doesn't specify an error value. Both the nozzle flow rate and cone angle are used to calculate the mass flux of the spray. Mass flux is one of the major parameters that determine the spray cooling heat flux and its error could not be calculated.

As the error in spray cooling heat transfer couldn't be calculated owing to the lack of information on error values of each individual parameters, it was decided to conduct an error analysis of the transient conduction model which incorporates the gas-side heating, the transient conduction through the wall and the spray cooling. Transient, cycle (4 stroke) averaged values of the heat flux representative of the engine was applied at gas-side. On the coolant-side, a transient heat transfer coefficient and a coolant temperature which would produce a heat flux equivalent to the gas-side

heat flux was applied. The coolant temperature, deduced using conduction equation, was set at a value that would give a gas side metal temperature of 230 ^{O}C. The engine heat flux was changed step by step from 1.6 MW/m^2 to 1.2 MW/m^2. Similarly, the heat transfer coefficient and the coolant temperature were also changed step by step on the coolant side according to the heat flux applied at the gas-side. A duration of 10 s was applied between each step change to allow for heat transfer to reach a steady state (same as in the spray cooling control model simulation). The gas-side and coolant-side metal temperatures were then measured from the simulation. Using the plane wall conduction method [54, pp. 22–25], the steady state temperatures for the gas-side and the coolant-side were calculated. These calculated values were then compared with the simulated values. The errors are deduced as the difference of the simulated values from the calculated values. Figure 3.10 shows the simplified Simulink model whereas Table 3.7 provides the values of calculated coolant-side metal temperature, coolant-side heat transfer coefficient, and coolant temperature applied for each step.

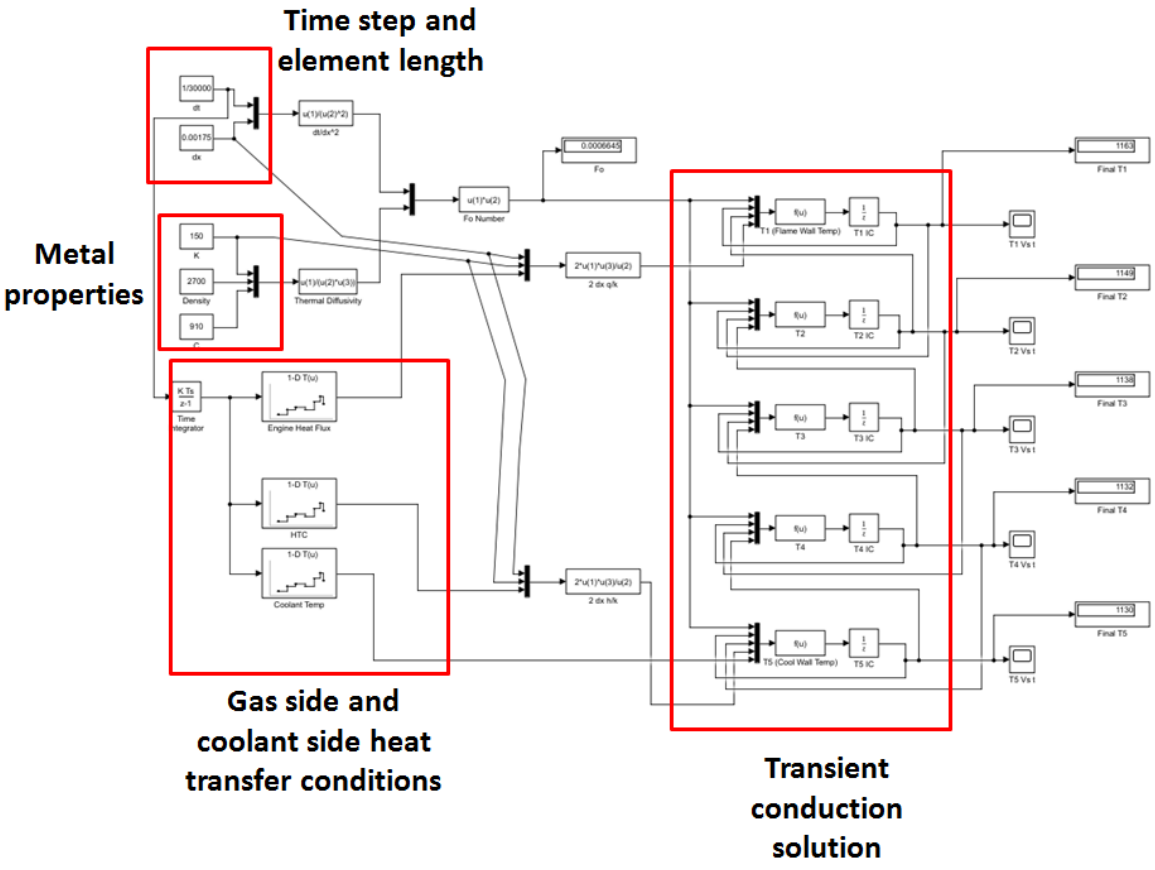

Figure 3.10: Simplified Simulink model created for error analysis.

Table 3.7: Calculated coolant side metal temperature, coolant side heat transfer coefficient and coolant temperature.

Heat flux (MW/m^2)	Coolant side metal temperature (^oC)	Coolant side heat transfer coefficient (W/m^2K)	Coolant temperature (^oC)
1.6	155.33	53333.33	125.33
1.2	164.67	46666.66	134.67
1.4	174.00	40000.00	144.00

The results show that, between step changes, the simulated temperatures vary with respect to the gas-side heat flux and then reaches a steady state. Figure 3.11 shows the simulated gas-side and the coolant-side metal temperatures over the duration of the simulation. At steady state, the simulated temperatures were same as the temperatures calculated using the plane wall equation. This shows that the conduction model incorporating the gas-side and the coolant-side through transient conduction are free from modelling errors as well numerical errors. Even though the conduction model was found to be free from modelling and numerical errors, the spray cooling heat transfer calculation in the main model is expected to have errors from the combination of errors from the correlations used as well as the individual parameter errors.

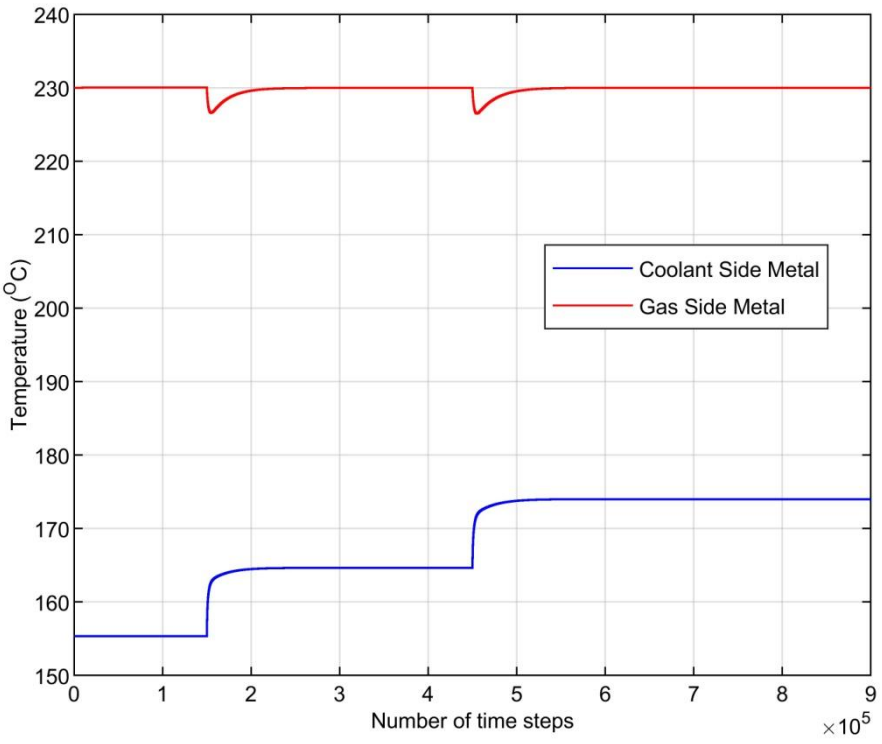

Figure 3.11: Simulated gas side and coolant side metal temperatures.

3.4. Conclusion of Chapter 3

Simulations were performed to identify two aspects of control of evaporative cooling. One with respect to transient in-cylinder condition and the other was spray evaporative cooling under engine load changes. The first simulation was for pool boiling cooling without an active control, which checked the effect of fluctuating gas-side metal temperatures equal to the in-cylinder gas temperature on the coolant-side metal temperature. Results showed that the fluctuations of gas side metal temperature only causes a fluctuation of the coolant-side metal temperature by ± 0.03% around its mean value and this would not pose a difficulty for the control of evaporative cooling.

The next simulation was for engine load changes from full-load to half-load. A PI algorithm with gain scheduling linear to engine load was employed to maintain the gas-side metal temperature at 230 ^{o}C by controlling the coolant flow rate. A spray nucleate boiling heat flux correlation was used to calculate the cooling heat flux. Results showed that sufficient control could be achieved within 0.7s during load changes, without large fluctuations in the gas side metal temperature.

Because it has been demonstrated under static conditions that the process is controllable, this provides us with motivation to undertake experimental verifications under dynamic conditions as addressed in Chapter 5 and Chapter 6. Before then ,as an interim step towards a CFD model, Chapter 4 studies a fundamental impingement dynamic simulation of a droplet with boiling.

Chapter 4. NUMERICAL SIMULATION OF DROPLET IMPINGEMENT DYNAMICS AND ONSET OF EVAPORATIVE HEAT TRANSFER

To address the second objective of the thesis, namely to establish whether single droplet prediction can tell us anything about evaporative spray heat transfer, a numerical study is needed. Numerical simulations of single droplet impingement dynamics and onset of evaporation on stationary and moving boundaries are needed to understand the effect of boundary motion on spray evaporative heat transfer for water. ANSYS Fluent, Volume of Fluid (VOF) method has been used to model the multiphase problem. A dynamic contact angle model was implemented to improve the accuracy of the simulations. The droplet impingement model was validated against experimental data available from literature [44]. Droplet full evaporation simulations were not performed owing to very long running times (of the order of weeks per single simulation) required using the computational resources available.

Four sets of droplet impingement simulations were performed: i) Isothermal stationary boundary ii) Stationary boundary with onset of evaporative heat transfer iii) Isothermal moving boundary, and iv) Moving boundary with onset of evaporative heat transfer. Simulations were performed for droplet diameters of 30 µm, 49 µm, 75 µm, and 100 µm, of which droplet diameters of 30 µm, 75 µm, and 100 µm were used only for the isothermal case to first establish a droplet rebound criterion. These droplet diameters were selected to cover the range of micrometre sized droplets produced by fine misting nozzles which have the lowest flow rates of any full cone nozzles [56]. The range of droplet velocities used for the simulations were 1 to 7.5 m/s of which the thermal simulations were for a droplet velocity of 1m/s. The moving boundary simulations were performed for amplitudes and frequencies ranging from 0.02 mm to 10 mm, and 10 Hz to 1000 Hz respectively. This covers the range of frequencies and amplitudes generated by a downsized 3 cylinder gasoline engine producing 100 KW/L. The engine vibration frequencies and amplitudes were deduced from engine mount acceleration data supplied by Ford Motor Company Dunton Technical Centre.

The isothermal simulation results were analysed for droplet rebound and a criterion for droplet rebound was formulated. In chapter 6, the evaporative heat transfer simulation results are compared against experimental data to check whether single droplet simulation could be utilised to predict evaporative heat transfer on stationary and moving boundaries for a cloud of droplets, essentially a spray. An attempt has been made to modify an existing spray evaporative heat transfer correlation to account for the effect of vibration.

The running time for simulations, on a workstation with two 3.5 GHz processors having 8 physical cores and 16 threads, were between several hours for the shorter duration isothermal simulations, but up to four days for the evaporation simulations with boundary motion. The single droplet simulation running times show that it would be computationally prohibitively expensive to simulate evaporation of a spray impinging on a vibrating surface, as a spray (i.e. a cloud of droplets) makes the problem much more complex.

4.1. Numerical Model

A 2D axisymmetric two-phase numerical model was created using the VOF method. The VOF method was chosen as it is one of the most popular and widely used methods to simulate droplet impingement owing to its efficiency and accuracy. A 2D axisymmetric model was created as it is computationally less expensive and sufficiently accurate for a single droplet impingement problem. Researchers have successfully simulated droplet impingement dynamics with dynamic contact angle models applied to it. Their results agreed well with experimental data [33][38][40][52][53]. Blake and Coninck's [41] dynamic contact angle model based on contact line velocity was employed to solve the contact angle problem owing to its accuracy, and simplicity to implement [43], [45]. Researchers have also incorporated different evaporation models to their VOF numerical models for droplet impingement and produced results that agree well with experimental data [38][40]. The Lee Evaporation-Condensation model was employed to calculate the phase change due to evaporation owing to its simplicity for implementation [59].

4.1.1. ANSYS Fluent VOF Model

The ANSYS FLUENT VOF method allows the modelling of two or more fluids which are immiscible (i.e liquids that do not mix together). It is a tracking technique used to track the interface between the fluids by assigning a volume fraction for each fluid in a computational cell. Adding the volume fractions of all phases in a control volume gives unity. Volume averaged values are used to represent all the variables and properties which are shared by the phases [60].

A two phase (liquid and gas) transient model was created in ANSYS FLUENT using the VOF method. The gas phase was assigned as the primary phase and the liquid phase as the secondary phase. The VOF method solves a continuity equation for the volume fraction to track the interface between the phases which is given by the following equation.

$$\frac{1}{\rho_q}\left[\frac{\partial}{\partial t}\left(\alpha_q \rho_q\right) + \nabla \cdot \left(\alpha_q \rho_q \overrightarrow{v_q}\right) = S_{\alpha_q} + \sum_{p=1}^{n}\left(\dot{m_{pq}} - \dot{m_{qp}}\right)\right] \tag{4.1}$$

where q is the identifier for the fluid, ρ is the density, α is the volume fraction, $\vec{v}$ is the velocity vector, $\dot{m_{pq}}$ is the mass transfer from phase p to q, $\dot{m_{qp}}$ is the mass transfer from phase q to p, and S_{α_q} is a source term for mass, which in this case is from evaporation. The evaporation model used in the model is discussed later in this chapter.

Depending on the volume fraction of the q^{th} fluid, three conditions are possible in a cell. If $\alpha_q = 0$: the cell is empty with the q^{th} fluid; if $\alpha_q = 1$: the cell is full with the q^{th} fluid; and if $0 < \alpha_q < 1$: the cell contains an interface between the two fluids.

The volume fraction of the primary phase is not solved but calculated from the volume fraction solved for the secondary phase using the constraint given below.

$$\sum_{q=1}^{n} \alpha_q = 1 \tag{4.2}$$

i.e. the sum of the volume fractions of all the phases is equal to unity.

An explicit time formulation was used for solving the volume fraction owing to its better numerical accuracy compared to the implicit formulation and it has the following form.

$$\frac{\alpha_q^{n+1}\rho_q^{n+1} - \alpha_q^n \rho_q^n}{\Delta t} V + \sum_f \left(\rho_q U_f^n \alpha_{q,f}^n\right) = \left[\sum_{p=1}^{n} \left(\dot{m_{pq}} - \dot{m_{qp}}\right) + S_{\alpha_q}\right] V \tag{4.3}$$

in which n+1 is the index for the current time step, n is the index for previous time step, $\alpha_{q,f}$ is the face value of the q^{th} volume fraction, V is the volume of cell and U_f is the volume flux through the face based on normal velocity. In order to calculate a material property in a cell, the volume fraction of the phases is used. For a system with several phases, all the material properties are calculated by volume fraction averaging [60].

The ANSYS Fluent VOF method solves only one momentum equation throughout the domain and the velocity field from the solution is shared between all the phases. Through density and dynamic viscosity properties, the momentum equation is dependent on the volume fractions of all the phases. The momentum equation is as follows.

$$\frac{\partial}{\partial t}(\rho\, \vec{v}) + \nabla \cdot (\rho \vec{v}\vec{v}) = -\nabla P + \nabla \cdot [\mu(\nabla \vec{v} + \nabla \vec{v}^T)] + \rho \vec{g} + \vec{F} \tag{4.4}$$

where P is the pressure, μ is the dynamic viscosity and $\vec{F}$ is the body force.

To calculate droplet impingement dynamics and evaporation, surface tension at the interface need to be considered. The addition of surface tension to the model was achieved using the Continuum Surface Force (CSF) model available in ANSYS FLUENT. The ANSYS FLUENT CSF model is based on a model proposed by Brackbill et al [61]. Considering a case where the surface tension is constant along the surface/interface, the pressure difference across the surface can be shown dependent on the surface tension as well as the curvature of the interface:

$$p_2 - p_1 = \sigma\left(\frac{1}{R_1} + \frac{1}{R_2}\right) \tag{4.5}$$

in which p_1 and p_2 are the pressures on either side of the surface, σ is the surface tension, and R_1 and R_2 are two radii perpendicular to each other which are used to measure the curvature of the surface. The CSF model computes the surface curvature (k) in terms of the divergence of the unit normal ($\hat{n}$) at the interface as follows.

$$k = \nabla \cdot \hat{n} \tag{4.6}$$

The unit normal is calculated as

$$\hat{n} = \frac{n}{|n|} \tag{4.7}$$

where n is the surface normal calculated as the gradient of the liquid-phase volume fraction (α_l).

$$n = \nabla \cdot \alpha_l \tag{4.8}$$

Turning to the CSF model, a source term is added to the momentum equation, which has the following form for a two-phase problem.:

$$F_\sigma = \sigma_{lg}\frac{\rho k_l \nabla \alpha_l}{\frac{1}{2}(\rho_l + \rho_g)} \tag{4.9}$$

where the subscripts l and g stand for liquid and gas phases respectively, and ρ is the volume-averaged density.

Another important requirement for modelling droplet impingement is the ability to specify a time dependent contact angle at the three-phase contact line. In ANSYS Fluent VOF, along with the surface tension model, there is an option to specify the contact angle or the wall adhesion angle. Again, this model is based on the work by Brackbill et al [61]. Specifying the contact angle modifies the surface normal in cells adjacent to the wall which results in a curvature of the interface at the

contact line. The equation, based on the contact angle, for the surface normal at the cell adjacent to the wall is given below.

$$\hat{n} = \hat{n}_w cos\theta_w + \hat{t}_w sin\theta_w \tag{4.10}$$

where θ_w is the contact angle, and $\hat{n}_w$ and $\hat{t}_w$ are the unit vectors normal and tangential to the wall [60]. A time dependent dynamic contact angle model was implemented using user defined functions which is discussed later in this chapter.

The ANSYS Fluent VOF energy equation has the following form.

$$\frac{\partial}{\partial t}(\rho E) + \nabla \cdot \left(\vec{v}(\rho E + p)\right) = \nabla \cdot (k \nabla T) + S \tag{4.11}$$

in which E is the energy, T is the temperature, k is the thermal conductivity, S is the source term for contributions from phase change at the interface [43]. Energy, E and temperature, T are used as mass averaged variables. The mass averaged energy,E, is defined as

$$E = \frac{\sum_{q=1}^{n} \alpha_q \rho_q E_q}{\sum_{q=1}^{n} \alpha_q \rho_q} \tag{4.12}$$

where density, ρ and thermal conductivity, k are volumetrically averaged properties.

The ANSYS Fluent default phase change model, Lee Model for Evaporation-Condensation [59], was employed to include mass transfer caused by phase change. The following vapour transport equation governs the liquid to vapour mass transfer.

$$\frac{\partial}{\partial t}(\alpha_v \rho_v) + \nabla \cdot \left(\alpha_v \rho_v \overrightarrow{V_v}\right) = \dot{m}_{lv} - \dot{m}_{vl} \tag{4.13}$$

in which α_v is the vapour volume fraction, ρ_v is the vapour density, $\overrightarrow{V_v}$ is the vapour phase velocity, $\dot{m}_{lv}$ is the rate of mass transfer from liquid to vapour due to evaporation, and $\dot{m}_{vl}$ is the rate of mass transfer from vapour to liquid due to condensation. The equations for the rates of mass transfer due to evaporation and condensation are given below

$$\dot{m}_{lv} = C_e \alpha_l \rho_l \frac{T_l - T_{sat}}{T_{sat}} \tag{4.14}$$

$$\dot{m}_{vl} = C_c \alpha_v \rho_v \frac{T_{sat} - T_v}{T_{sat}} \tag{4.15}$$

where C_e and C_c are coefficients for evaporation and condensation respectively, and the default value of 0.1 was used for both. The subscripts l, v, and sat stand for liquid, volume, and saturation respectively.

4.1.2. Temporal and Spatial Discretisation, and Solver Setup

As described in the previous section, an explicit volume fraction formulation was chosen for the simulations. The explicit volume fraction formulation uses a different time step from the rest of the transport equations. The volume fraction time step is called the sub-time step. In order to calculate the sub-time step a separate Courant number is required. Based on the Courant number specified, a criterion formed of velocity or flux, or the combination of both, determines the sub-time step size. There are several criteria available in ANSYS FLUENT VOF to calculate the sub-time step size. The Hybrid method, which uses a combination of velocity and flux average was chosen [62]. The Hybrid method was chosen because the sub-time step needs to be small enough to capture both velocity and flux (especially near the wall on which droplet impacts) as well as for better convergence.

The control volumes in ANSYS Fluent require the computation and balancing (with source terms) of convection and diffusion fluxes at the control volume faces. Upwind schemes are used for the interpolation of face values from the discrete values of a scalar quantity stored in the cell centres. The Second Order Upwind scheme was used for the spatial discretisation owing to its higher accuracy. [63].The Geometric Reconstruction Scheme (Geo-Reconstruct) was used to interpolate the face fluxes when a cell is near the interface between two faces. Geo-Reconstruct was chosen for the droplet impingement and evaporation problem as it is the most accurate interpolation method available in ANSYS Fluent. It uses a piecewise-linear method which assumes a linear interface slope within a cell [60].

The ANSYS FLUENT pressure-based solver was employed to solve the governing equations. For pressure-velocity coupling, the SIMPLEC algorithm was used. The Least Squares Cell-Based method was chosen for gradient calculations as it is the least computationally expensive method whilst providing sufficient accuracy compared to more superior computationally expensive methods [63]. The Body Force Weighted scheme was employed to interpolate the pressure values at the control volume faces owing to its better performance for VOF simulations where two fluids with large density differences are present [43]. For temporal discretisation, the First Order Implicit transient formulation was enabled for the discretisation of the governing equations [63].

4.1.3. Numerical Domain and Boundary Conditions

An axisymmetric model was created using a 2-D square geometry meshed with quadrilateral elements of the same size. The 2-D numerical domain represents a cylindrical container when

revolved around its axis. The three sides of the domain had a 'wall' boundary condition applied to it and one side was assigned with the 'axis' boundary condition. In ANSYS Fluent, the X-axis acts as the axis of symmetry for the axisymmetric model so the axis of the domain had to be aligned with the X-axis. One of the sides assigned as a wall was the impact surface which was aligned to the Y-axis. The two other sides represent the top and side walls of the cylinder. For validation of the numerical model, which is discussed in the next section, two different meshes were used, one with an element size of 1 μm and the other with an element size of 0.5 μm. Both were meshed using quadrilateral elements of the same size.

Four different domain sizes were used for the four different droplet sizes. The domain was just large enough to contain the spreading of the droplet after impact. The dimensions of the domain were kept to a minimum to keep the simulation time to a minimum. For the droplet diameters of 30 μm, 49 μm, 75 μm and 100 μm, the square domain had a side length equal to 60 μm, 100 μm, 150 μm, and 200 μm respectively.

The material properties for water with respect to temperature were loaded to the numerical model by employing the piecewise-linear fit method that required a table of data for each material property with respect to temperature.

After initialisation of the flow field in the entire numerical domain, where initial values of pressure, temperature, velocities and the volume fraction are provided, the droplet velocity and its volume fraction were patched-on to a circular cell region marked for the size of droplet required. For all the simulations, droplets were initially patched 2 μm above the impact surface. This provides the opportunity for the fluid around to move and have some velocity due to a droplet travelling at a certain speed before droplet impact occurs. Figure 4.1 shows a schematic of the numerical domain having an element size of 0.5 μm with boundary conditions applied to it.

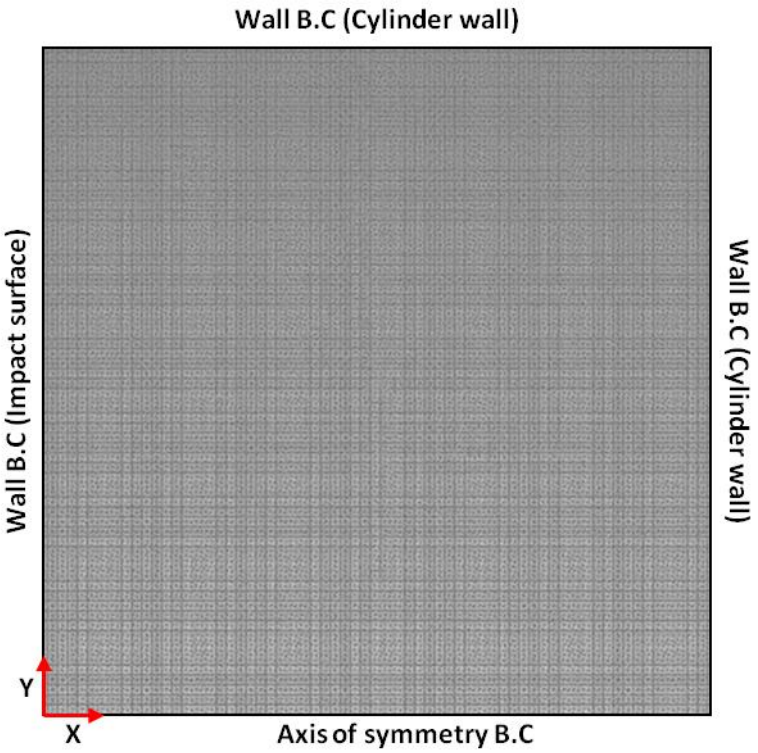

Figure 4.1: Numerical domain of the axisymmetric model meshed with an element size of 0.5 µm.

4.1.4. Implementation of Dynamic Contact Angle Model, Wall Vibration Model and Data Saving

The dynamic contact angle model by Blake and Coninck's [41] was implemented at the wall boundary condition for the impact surface using ANSYS Fluent user defined functions (UDF). The Blake and Coninck's model requires one variable from the domain, which is the spreading velocity of the contact line to calculate the instantaneous/dynamic contact angle using the following equation.

$$v_{cl} = \frac{2k_s h\lambda}{\mu_l v_l} sinh\left[\frac{\sigma_l}{2nk_b T}\left(cos\theta^0 - cos\theta^d\right)\right] \tag{4.16}$$

where v_{cl} is the contact line velocity, k_s is the frequency of the molecular displacements, h is the Plank's constant, λ is the length of each molecular displacements μ_l is the dynamic viscosity of the liquid, v_l is the molecular volume, n is the number of absorption sites per unit length, k_b is the Boltzmann's constant, T is the temperature of the liquid, θ^0 is the static contact angle, and θ^d is the dynamic contact angle. Values of the properties used in equation (4.16), as given in Chen et al (2016) [43], for water as the wetting liquid are given in table 4.1.

Table 4.1: Values of the properties required for the dynamic contact angle equation for water as the wetting liquid.

Property	Value
Frequency of molecular displacements, k_s	4.5276 X 10^{10} Hz
Plank's constant, h	6.62607004 X 10^{-34} kg/s
Length of each molecular displacement, λ	0.5 X 10^{-9} m
Molecular volume, v_l	3 X 10^{-29} m^3
Number of absorption sites per unit length, n	4 X 10^{18} m^{-1}
Boltzmann's constant, k_b	1.38064852 X 10^{-23} $J.K^{-1}$

Equation (4.16) sets limits to the maximum wetting velocity as well as the minimum dewetting velocity. When the spreading velocity is above the maximum wetting velocity, a contact angle of 180^o is applied whereas when the de-spreading velocity is below the minimum dewetting velocity, a contact angle of 0^o is applied. The maximum wetting velocity and the minimum dewetting velocity are calculated by solving the equation (4.16) for the maximum wetting dynamic contact angle and the minimum dewetting dynamic contact angle as given in equations (4.17) and (4.18) respectively.

$$v_{cl180} = \frac{2k_s h\lambda}{\mu_l v_l} sinh\left[\frac{\sigma_{lv}}{2nk_b T}(cos\theta^0 + 1)\right] \tag{4.17}$$

and

$$-v_{cl0} = \frac{2k_s h\lambda}{\mu_l v_l} sinh\left[\frac{\sigma_{lv}}{2nk_b T}(1 - cos\theta^0)\right] \tag{4.18}$$

To implement the model using equations (4.17) and (4.18), two different UDF codes were written in C (programming code) by making use of predefined macros supplied by ANSYS called the DEFINE macros. The DEFINE macros are required to access simulation domain properties from the program and to input values back in to the program, after the required calculations have been performed using the written code. To write the contact angle model UDF codes, two different DEFINE macros were used, DEFINE_ADJUST and DEFINE_PROFILE. DEFINE_ADJUST macros are used to modify any ANSYS Fluent variables that are not directly passed as arguments, which means the variable and the domain from which it needs access needs to be specified using identifiers called 'Threads'.

DEFINE_PROFILE macros are used to implement custom boundary profiles that vary with time and space [64].

A code using the DEFINE_ADJUST macro was written to calculate the velocity of the contact line. In ANSYS fluent, a 'No Slip' condition was applied with the Wall Adhesion Model which means the velocity components of the fluid in contact with the wall is zero. But the three-phase contact line moves during the spreading and de-spreading of the droplet. To solve this problem, the droplet interface surface was assumed to be like a sheet that unrolls and rolls over a surface. The part of the sheet in contact with the wall has a velocity of zero but when the sheet unrolls or rolls over the surface, the boundary line (contact line) of the area in contact with surface moves. Based on this idea, a cell zone was created in the domain for the row of cells adjacent to the cells attached to the wall. The velocity component in the Y-direction in the cell zone created was accessed for the cells with density higher than 500 Kg/m^3 to make sure only the velocity of the liquid movement was accessed. Two different data access macros were used for this, i.e. C_V(c,t) and C_R(c,t) for accessing the Y-velocity and the density in the cells respectively [64]. After the velocities were accessed, the velocity with the highest magnitude was chosen as the contact line velocity. Another code using the DEFINE_PROFILE macro calculates the dynamic contact angle based on the contact line velocity using equation (4.13) and applying it at the wall as a boundary condition at the beginning of each time step. The code also sets the maximum and minimum contact angle based on the maximum wetting velocity and the minimum dewetting velocity respectively. The vibration model was also applied to the wall using a UDF. A code was written using the DEFINE_PROFILE macro to apply a velocity to the wall with respect to the simulation physical time using a sinusoidal wave based on the amplitude and frequency specified.

The three codes mentioned above write the instantaneous contact line velocity and dynamic contact angle, and wall velocity respectively in separate files for analysis. One more code was written to save the instantaneous droplet spreading diameter using the DEFINE_ADJUST macro. Using the data access macro, C_R(c,t), the code counts the number of cells attached to the wall having a density of more than 500 kg/m^3. For simulations consisting of heat transfer, maximum and average instantaneous wall surface heat fluxes were saved using report files under ‘Solution Monitors’.

4.1.5. Solution Control and Validation of Model

All the simulations were performed for a global Courant number of 0.5 with variable time stepping. The variable time stepping was employed in order to reduce the simulation time compared to a fixed time step where a very small time step would be needed to satisfy the Courant number criteria for the whole range of the simulation. Applying variable time stepping adjusts the size of the time step

according to the movement of the fluid through the domain. It uses the largest time step possible throughout the simulation for the Courant number specified. An initial time step size of 10 ns was specified with a minimum and maximum time step size of 1 ns and 1 μs respectively. These very small time step sizes were chosen to capture the highly transient nature of droplet impingement dynamics. For each time step, the maximum number of iterations per time step was set to 20. For solving the volume fraction equation, a Courant number of 0.25 was set for calculating the sub-time step.

The model was validated against experimental data by Dong et al [44]. Their experiments were for the visualisation of inkjet drop formation and deposition which was recorded using a slow speed camera making use of a pulsed laser and signal generators. The data used for comparison was for a water droplet with a diameter of 49 μm and a velocity of 4 m/s impacting on gold coated silicon wafers which had a static contact angle of 110^{O}.

A water droplet with a diameter of 49 μm at a velocity of 4 m/s impacting on the surface was simulated with the dynamic contact angle model applied to the wall. The dynamic contact angle was being calculated using the static contact angle of 110^{O} to imitate the wetting parameters of the gold silicon wafers as used in the Dong et al experiments [44]. The energy equation was switched off for this problem as no heating was applied to the wall similar to Dong et al's experiments. It is not known what the ambient temperature was at which Dong eta al experiments were undertaken. An ambient temperature of 20 ^{O}C was used to set the material properties for the simulations. Two meshes were used, one with an element size of 1 μm, and the other with an element size of 0.5 μm. Both were meshed with quadrilateral elements of the same size. The numerical simulation results from both the meshes are compared against the experimental data for the dimensionless spreading diameter, D, as well as for the droplet shape. Figure 4.2 shows the plot of temporal evolution of D from the numerical simulations as well as the Dong et al [44] experiments for a duration of 500 μs.

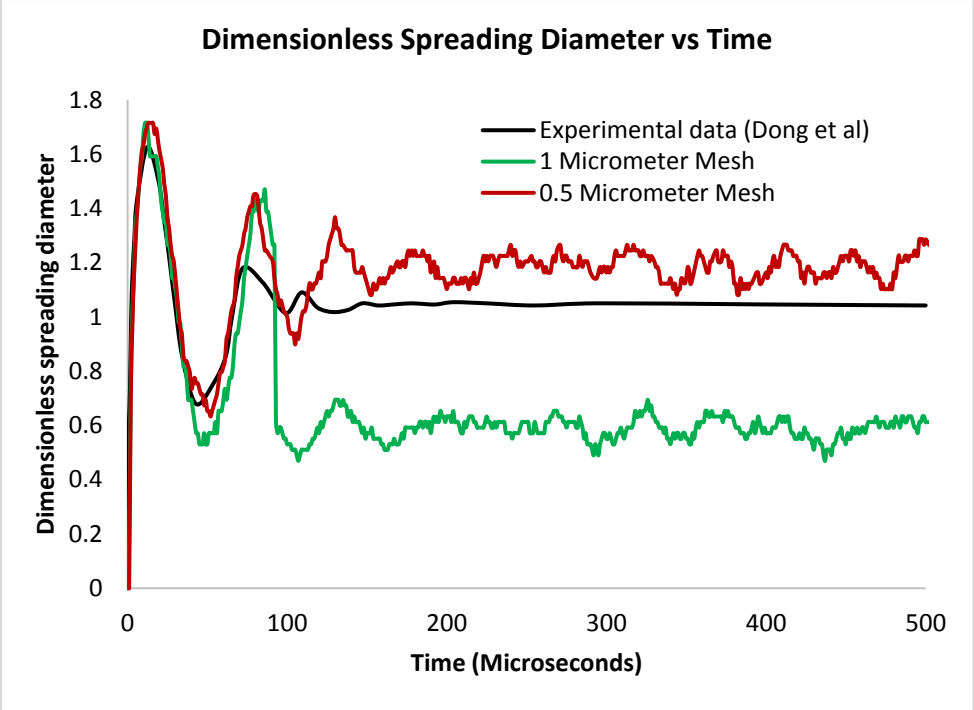

Figure 4.2: Comparison of numerical and experimental dimensionless spreading diameter.

Comparison of the dimensionless spreading diameter shows that 0.5 µm element size mesh produced the best results and is in good agreement with the experimental data. For the first droplet oscillation after impact, the numerical D from both the meshes closely follows the experimental D. After the first oscillation, D for the 0.5 µm element size mesh stays close to the experimental D but unlike the experimental D which settled down after the first three oscillations, D for the 0.5 µm element size mesh continues to oscillate with an amplitude of ~0.1. If a linear curve fit is applied to the oscillating part of D for the 0.5 µm element size mesh, it has an error of approximately +0.1 compared to the experimental D. The small amplitude oscillating part of D for the 1 µm element size mesh has an error of approximately -0.5 compared to the experimental D. Figure 4.3 shows the comparison of temporal evolution of the numerical droplet shape for the 0.5 µm element size mesh and the experiment for a duration of 295 µs.

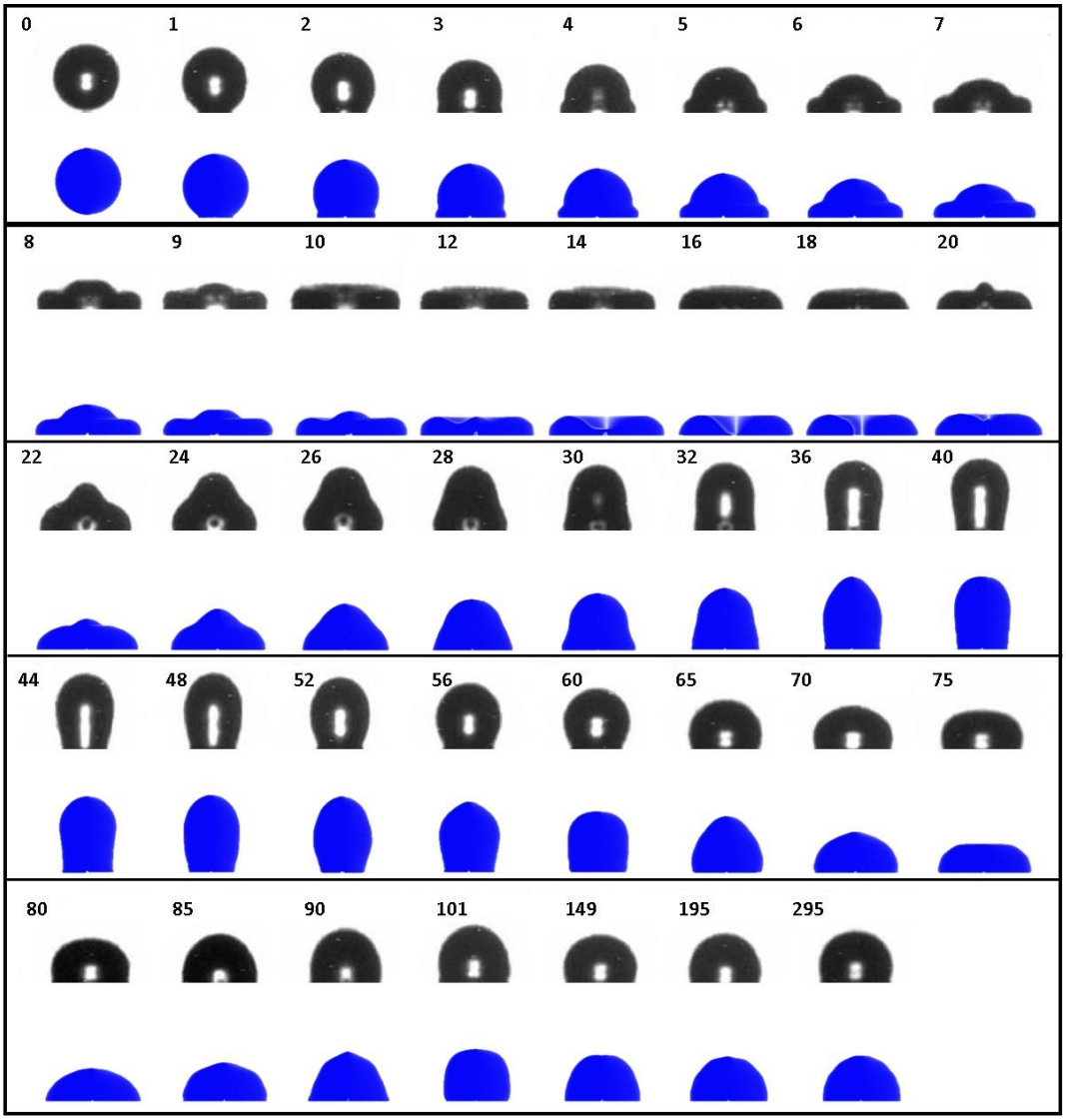

Figure 4.3: Temporal evolution of experimental (black) and numerical (blue) droplet shape during droplet impingement. The time for each droplet shape is given above in microseconds.

The numerical temporal evolution of the droplet shape after impact is very similar to that of the experiment. At the time of 10 µs, there is a small difference in the droplet shape between the experiment and numerical simulation. The droplet had almost flattened into a disc shape in the experiment whereas in the simulation, it still had a 'bump' in the centre. But after one microsecond, the droplet in the simulation has flattened into a disc shape. Similarly, at the time of 20 µs, the droplet in the experiment was first to oscillate back, as can be seen by the 'bump' in the centre, whereas in the simulation, the droplet has not produced the 'bump' yet which it did after one microsecond. It can be said that, during the first oscillation, the droplet impingement dynamics in the numerical simulation is one microsecond behind the experiment. For the rest of the time, the droplet impingement dynamics in the simulation is close to that of experiment with minor differences in droplet dome shape.

The numerical simulation using the 0.5 µm element size mesh took approximately 18 hours to simulate 500 µs of physical time. The element and the time step size could be further reduced to increase accuracy but it would considerably increase the simulation time. Hence, the 0.5 µm element size mesh was chosen to run the simulations. It was not attempted to validate droplet evaporation, also owing to time constraints as it can be seen from the literature that the time it takes for full evaporation of a droplet is of the order of tens of milliseconds [43]. The simulations involving evaporation were ran for approximately 1000 µs of physical time in which the droplets starts to evaporate. Each simulation took between two and four days depending on the droplet velocities as well as the amplitudes and frequencies of wall vibration. Figure 4.4 shows the plot from 500 µs to 1000 µs of a simulation where a 49 µm droplet with an impact velocity of 1 m/s impinged on the surface and has started to evaporate. The droplet has an initial temperature of 100 ^{O}C and the wall stays at a constant temperature of 150 ^{O}C.

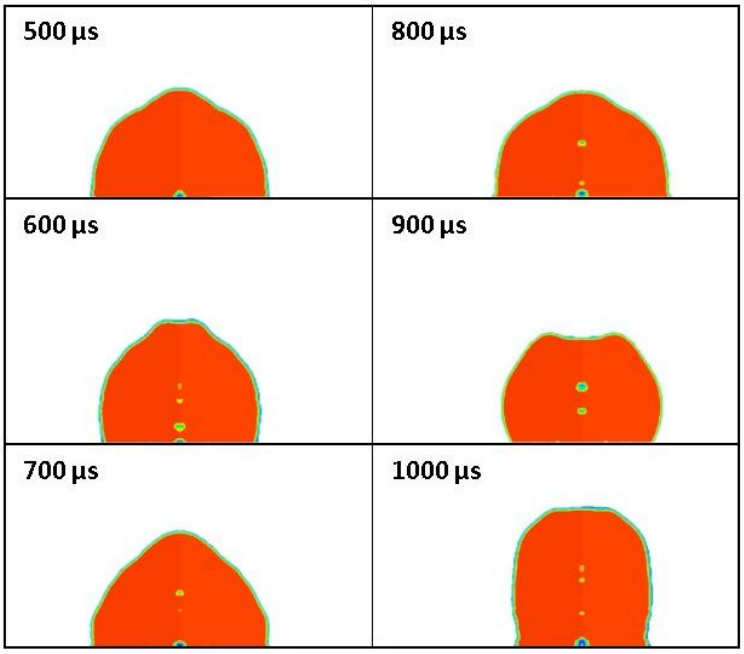

Figure 4.4: Droplet beginning to evaporate after impact.

4.2. Numerical Simulations

4.2.1. Isothermal Droplet Impingent on Stationary Boundary

The stationary boundary isothermal simulations were performed for four different droplet diameters impacting the surface at different velocities. These were to understand the effect of droplet size and velocity on droplet rebound. Simulations were performed for a water droplet in the presence of air impinging on a surface with a static contact angle of 110^{O}. The dynamic contact model was employed to apply the instantaneous contact angle at the wall boundary. The properties for air and

water were set for a temperature of 20^{O}C and the initial pressure for the numerical domain was set as atmospheric. The duration of simulations was limited to droplet's first oscillation after impact because after impact, droplet continuously loses its kinetic energy due to viscous forces and gradually settles down on the surface. Simulations for each droplet diameter started with a low velocity and increasing the velocity until rebound occurred. Table 4.2 provides the details of stationary boundary droplet impact simulations.

Table 4.2: Details of stationary boundary droplet impact simulations.

Simulation No	Droplet diameter (µm)	Droplet velocity (m/s)	Weber number
A1	30	6	14.82
A2	30	7	20.18
A3	30	7.5	23.16
A4	49	5	16.81
A5	49	6	24.21
A6	49	6.5	28.41
A7	75	3.5	12.61
A8	75	4.5	20.84
A9	100	3	12.35
A10	100	3.5	16.81

4.2.2. Isothermal Droplet Impingement on Moving Boundary

The simulations for isothermal droplet impingement on a moving boundary were performed to understand the effect of wall vibration on droplet rebound. Simulations were performed only for the 49 µm diameter droplet impacting the surface at the minimum impact velocity for rebound as identified from the stationary boundary simulations and also at 0.5 m/s less than the minimum impact velocity for rebound. Everything in the numerical model was same as the stationary boundary simulations except that the wall vibration model was switched on. Table 4.3 provides the details of the simulations ran for isothermal droplet impingement on moving boundaries.

Table 4.3: Details of Isothermal droplet impingement on moving boundary simulations.

Simulation No	Droplet diameter (μm)	Droplet Velocity (m/s)	Wall vibration amplitude (mm)	Wall vibration frequency (Hz)
B1	49	6.5	10	10
B2	49	6.5	10	100
B3	49	6.5	10	1000
B4	49	6.5	10	10
B5	49	6.5	10	100
B6	49	6.5	10	1000
B7	49	6	1	10
B8	49	6	1	100
B9	49	6	1	1000
B10	49	6	1	10
B11	49	6	1	100
B12	49	6	1	1000

4.2.3. Droplet Impingement and Onset of Evaporation on Stationary and Moving Boundaries

Fifteen simulations were performed for droplet impingement and evaporation on both stationary and moving boundaries. Only one droplet size, which had a diameter of 49 μm was used for all the simulations. The simulations were performed for a water droplet impinging on an Aluminium wall which has a static contact angle of 90^{O} [65]. Aluminium was chosen as the wall material as it is widely used as a cylinder-head material. Instead of air, steam was used as the primary phase, to avoid the contact angle problem posed by having three fluids coming into contact with the wall at the contact line. For all the simulations, the wall temperature was set at 150 ^{O}C, but the initial water droplet temperature was set as 100 ^{O}C, which is the saturation temperature to minimise the single-phase convection heat transfer. The initial pressure and temperature of the numerical domain was set as atmospheric pressure and 100 ^{O}C respectively. The vibration conditions for the different simulation cases were selected primarily based on engine vibration data. Applying more physics, for example dimensionless groups, will provide more insight into selecting the appropriate range of vibration conditions in order to sufficiently understand the problem. This, as a general case would allow the study to be presentable to a broader community. One way of determining the cases could be by using a dimensionless time scale i.e. a ratio of droplet relaxation time to the time it takes for the wall to go from trough to crest. Another way could be by using a dimensionless frequency scale i.e. a ratio of oscillation frequency of the wall to the oscillation frequency of the droplet. Table 4.4

gives the details of the simulations ran for droplet impingement with evaporation on stationary and moving boundaries. To calculate the dimensionless time and dimensionless frequency for each case, relaxation time and frequency of the droplet impinging on the stationary wall were used i.e. approximately 1000 μs and 17 KHz respectively. These vibrational cases could also be applicable for spray cooling of electronics onboard a vehicle, especially the higher amplitude, lower frequency cases owing to the road and suspension induced vibration.

Table 4.4: Simulations of droplet impingement with evaporation on stationary and moving boundaries.

Simulation No	Droplet Velocity (m/s)	Wall Vibration Amplitude (mm)	Wall Vibration Frequency (Hz)	Dimensionless time	Dimensionless frequency
C1	4	0	0	0	0
C2	1	0	0	0	0
D1	1	10	10	0.02	0.0058
D2	1	10	100	0.2	0.058
D3	1	10	1000	2	0.588
D4	1	1	10	0.02	0.0058
D5	1	1	100	0.2	0.058
D6	1	1	1000	2	0.588
D7	1	0.1	10	0.02	0.0058
D8	1	0.1	100	0.2	0.058
D9	1	0.1	1000	2	0.588
E1	1	0.5	60	0.12	0.035
E2	1	0.2	60	0.06	0.035
E3	1	0.08	200	0.4	0.117
E4	1	0.02	400	0.8	0.235

The case C is for the simulations ran for droplet impingement and evaporation on stationary boundary and the cases D and E are for moving boundary simulations with evaporative heat transfer switched on. Simulations for case D was performed for three different amplitudes at the same set of frequencies whereas the case E vibration amplitudes and frequencies were randomly chosen.

4.3. Results and Discussion

4.3.1. Isothermal Droplet Impingent on Stationary Boundary

The results for the isothermal droplet impingement on stationary boundaries simulations are presented here. Results show that, for droplet diameters of 30 µm, 49 µm, 75 µm and 100 µm, droplet rebound happened at droplet velocities of 7.5 m/s, 6.5 m/s, 4.5 m/s and 3.5 m/s respectively. The corresponding physical time at which droplets detach form the surface is 30 µs, 44 µs, 115 µs and 163 µs respectively. Figure 4.5 shows the droplet shape, a microsecond apart, leading to droplet detachment for the four different droplet diameters.

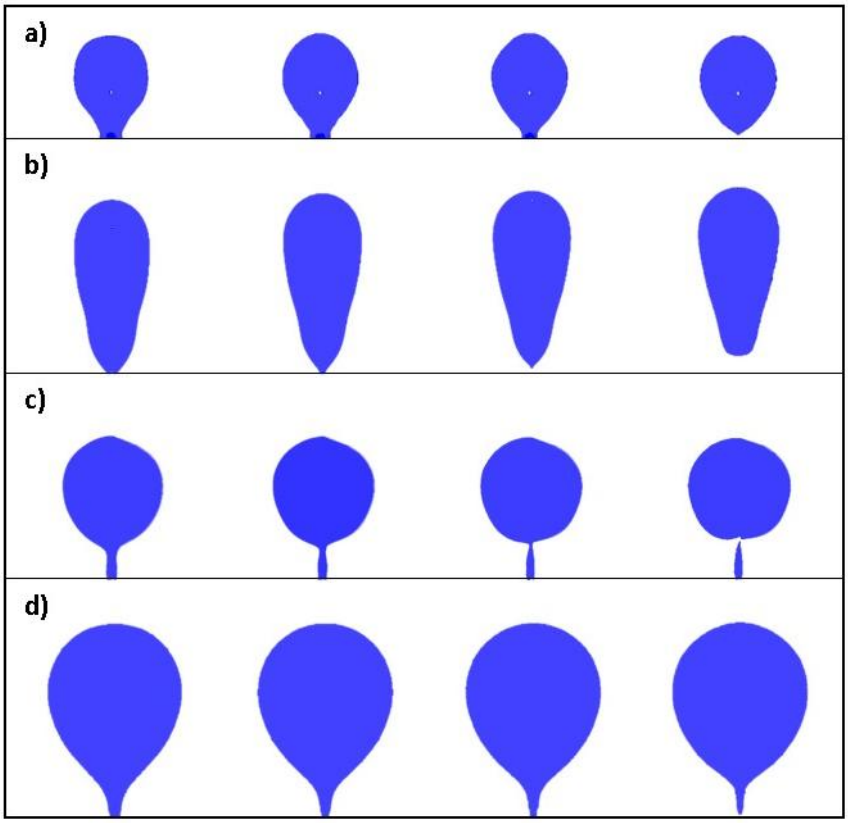

Figure 4.5: Droplet shape leading to and at detachment for droplet diameters: a.) 30 µm b.) 49 µm c.) 75 µm d.) 100 µm.

Figure 4.6 shows the droplet impact velocity for rebound plotted against droplet diameter along with a linear curve fit.

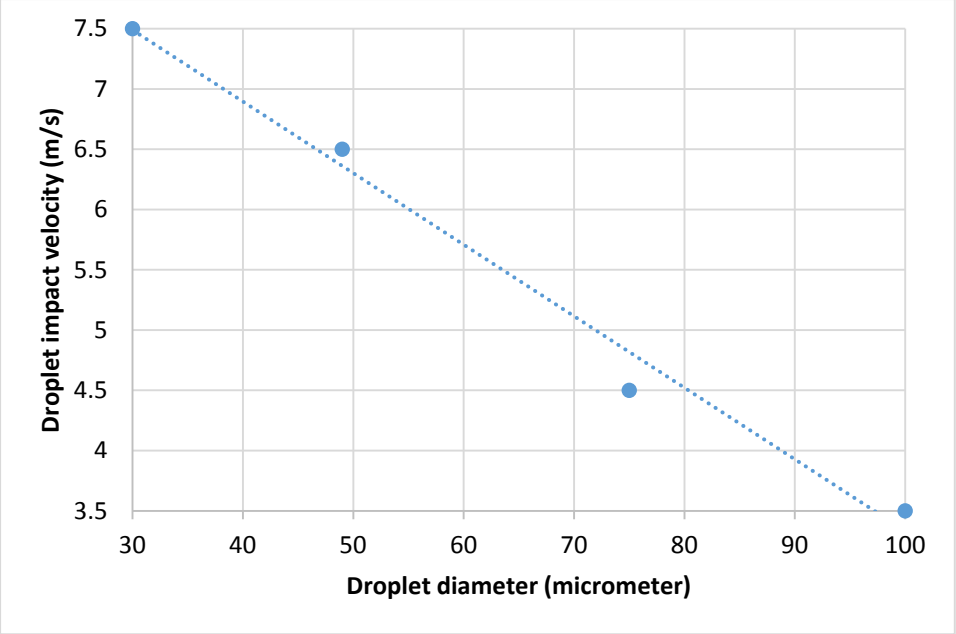

Figure 4.6: Droplet impact velocity for rebound plotted as a function of droplet diameter.

It can be seen from figure 4.6 that the doplet impact velocity for rebound decreases almost linearly with increasing droplet diameter. The linear curve fit shows that droplet impact velocity can be approximated for the doplet diameter using the following equation.

$$v_{re} = -0.059d_0 + 9.269 \tag{4.19}$$

where v_{re} is the droplet impact velocity for rebound and d_0 is the initial droplet diameter.

Another observation is that with increasing droplet diameter, the period for the oscialltion after impact or the time it takes for droplet detachment, increases. For the droplet diameters of 30 µm, 49 µm, 75 µm and 100 µm, droplet rebound occurred at 30 µs, 44 µs, 115 µs, and 163 µs respectively. Figure 4.7 shows droplet detachment time as a function of droplet diameter along with a linear curve fit.

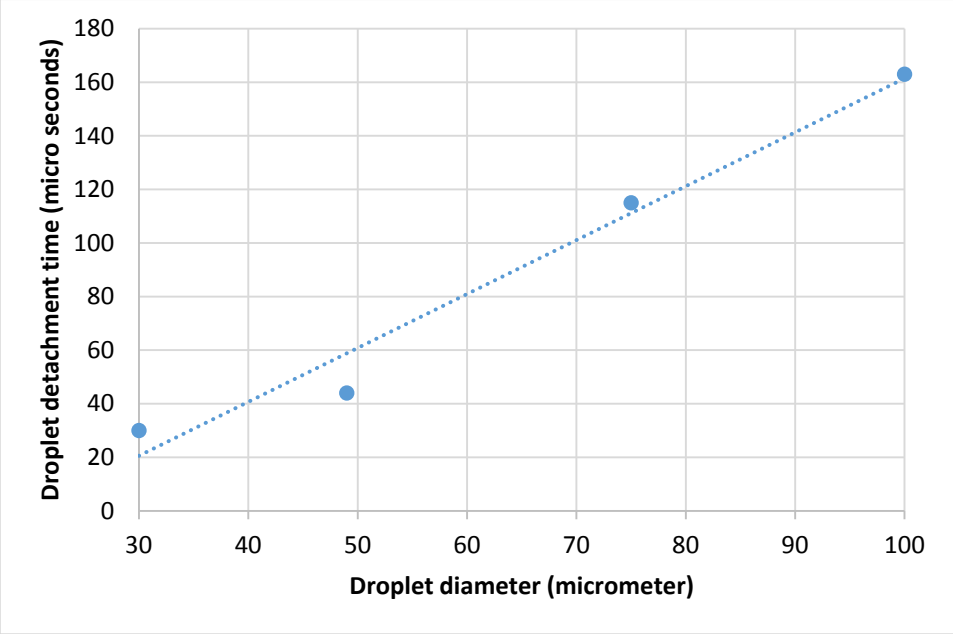

Figure 4.7: Time of droplet detachment plotted against droplet diameter.

The curve fit shows that the time for detachment increases almost linearly with increasing droplet diameter which can be calculated using the equation below.

$$t_{re} = 2.0125 d_0 - 39.795 \quad (4.20)$$

Where t_{re} is the time it takes for droplet to detach from the surface after impact.

4.3.2. Isothermal Droplet Impingement on Moving Boundary

From the identified minimum impact velocity for rebound for the 49 µm diameter droplet, the results for the simulations performed for moving boundaries, at the minimum impact velocity for rebound, and at 0.5 m/s less than the minimum impact velocity for rebound, are presented and discussed here. Table 4.5 provides the results for simulations B1 to B11.

Table 4.5: Results of the simulations for isothermal droplet impingement on a moving boundary.

Simulation No	Droplet Velocity (m/s)	Wall Vibration Amplitude (mm)	Wall Vibration Frequency (Hz)	Wall velocity at impact (m/s)	Rebound Occurred (Y/N)	Time at detachment (µs)
B1	6.5	10	10	0.628	Y	60
B2	6.5	10	100	6.28	Y	55

B3	6.5	10	1000	62.8	Y	57
B4	6.5	1	10	0.0628	N	N/A
B5	6.5	1	100	0.628	Y	60
B6	6.5	1	1000	6.28	Y	60
B7	6	10	10	0.628	Y	58
B8	6	10	100	6.28	Y	56
B9	6	10	1000	62.8	Y	42
B10	6	1	10	0.0628	Y	60
B11	6	1	100	0.628	N	N/A
B12	6	1	1000	6.28	N	N/A

The results show that the vibration of the wall has an effect on droplet rebound. For most of the frequencies and amplitudes, droplet rebounded for the impact velocity at and less than the minimum impact velocity for rebound except in three simulations, B4 (1 mm 10 Hz), B11 (1mm 100 Hz) and B12 (1 mm 1000 Hz), droplet rebound did not occur. Another observation is that the time for droplet detachment has increased, with majority of the droplet rebound occurring at times between 55 µs and 60 µs compared to the detachment time of 44 µs for the stationary wall case. The only exception being the simulation B9, in which the detachment time was 42 µs, which is less than the stationary case.

The droplet rebound at a velocity lower than the minimum impact velocity for rebound could be explained as the velocity of the wall moving upwards at the beginning of its sinusoidal path from its zeroth position produced a resultant velocity on impact higher than the minimum impact velocity for rebound. This is true for the cases B7 to B9 where the amplitude was 10 mm but for the amplitude of 1 mm this hypothesis does not apply. For the simulation B10, where the wall vibration amplitude and frequency were 1 mm and 10 Hz respectively, the resultant impact velocity was less than the minimum impact velocity for rebound, but still rebound occurred. Similarly, in simulation B4, droplet rebound did not occur for the wall vibration amplitude and frequency of 1 mm and 10 Hz respectively, even though the impact velocity was higher than the minimum impact velocity for rebound. It is unclear what mechanism is causing this phenomenon. It can also be noted that all the droplet rebounds did not occur at the amplitude of 1mm, which also could not be explained from the analysis.

4.3.3. Droplet Impingement and Onset of Evaporation on Stationary and Moving Boundaries

Results for the simulations performed for droplet impingement with onset of evaporation for both stationary and moving boundaries are presented and discussed here. All the simulations were only

performed for a droplet diameter of 49 µm. The wall had a constant temperature of 150 ^{O}C and the water droplet had an initial temperature of 100 ^{O}C. A pressure equal to atmospheric pressure was set as the initial pressure of the domain whereas the initial domain temperature was set at 100 ^{O}C. Figure 4.8 shows the surface averaged heat flux against time for the droplet impinging at a velocity of 4 m/s on a stationary boundary. A first order polynomial is applied to the data to see its trend over the duration of the simulation.

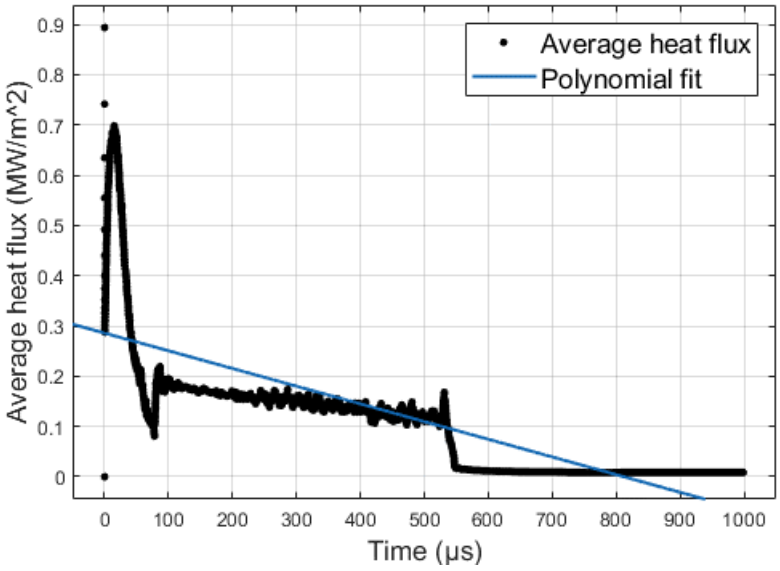

Figure 4.8: Plot of surface averaged heat flux for the droplet impinging at a velocity of 4 m/s on a stationary wall.

The droplet impingement produces the highest average heat flux on its initial spreading on the surface, the first spike in the plot. It can be seen, at the time of ~530 µs, the surface averaged heat flux suddenly drops to zero, which was caused by droplet rebound. Unlike the isothermal simulation used for the validation of the numerical model, the droplet has rebounded, even though the droplet velocity and diameter were the same. This is mainly due to the changes in dynamic viscosity and surface tension with respect to temperature. In order to avoid rebound, the droplet velocity was reduced to 1 m/s and set as the default droplet velocity for all the simulations mentioned thereafter. Figure 4.9 shows the plot for surface averaged heat flux against time for the droplet impinging at a velocity of 4 m/s on a stationary boundary. A first order polynomial is applied to the data to see its trend over the duration of the simulation.

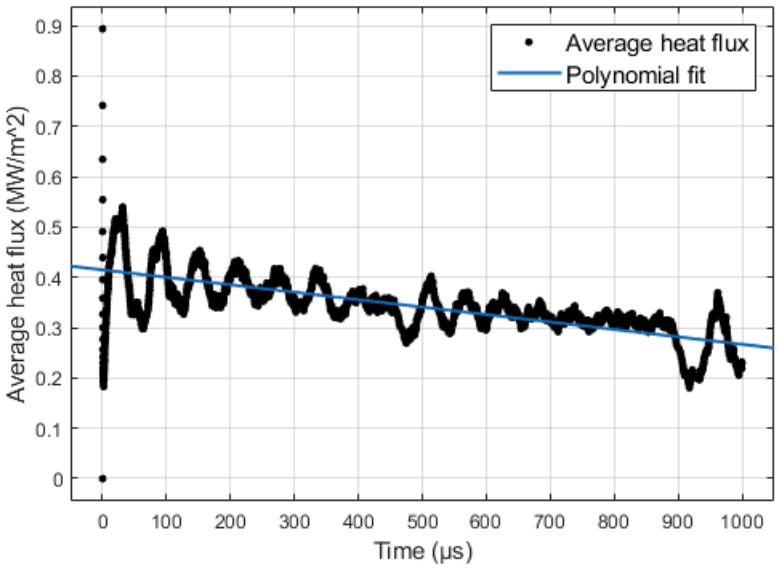

Figure 4.9: The surface averaged heat flux for the droplet impinging at a velocity of 1 m/s on a stationary wall.

Figure 4.9 shows that, similar to the heat flux plot for the droplet impinging at a velocity of 4 m/s, the average heat flux gradually decreases over the duration of the simulation owing to the losses in kinetic energy of the droplet due to viscous forces. There was a decrease in average heat flux by ~ 0.15 MW/m^2 over 1000 μs. It could be seen that there is a spike in amplitude at approximately 500 μs as well as at 1000 μs. The time averaged heat flux for the entire duration of the simulations was calculated to be 0.34 MW/m^2.

Figures 4.10 to 4.12 show the surface averaged heat flux as well as their first order polynomial fits for the simulations with surface vibration amplitudes of 0.1 mm, 1 mm and 10 mm at the frequencies of 10 Hz, 100 Hz, and 1000 Hz respectively for each amplitude. The average heat flux (Figure 4.10a) and its curve fits (Figure 4.10b) are shown in separate plots for easier comparison.

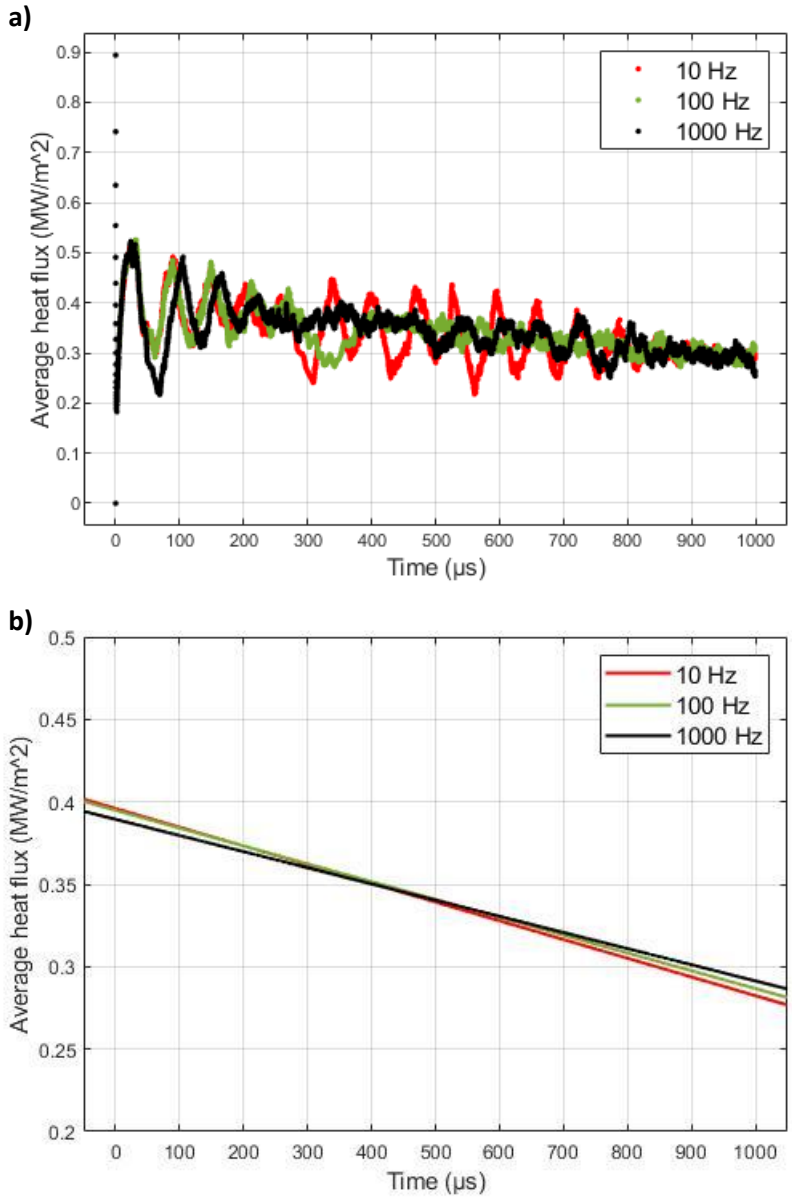

Figure 4.10: Surface averaged heat flux for the surface vibration amplitude of 0.1 mm at the frequencies of 10 Hz, 100 Hz and 1000 Hz. a) simulated values b) first order polynomial fit of the simulated values.

Figure 4.10 shows that the average heat flux follows the same trend for the three wall vibration frequencies. Frequency of 10 Hz produces the highest amplitudes of oscillations of average heat flux, which can be attributed to the oscillation of the droplet on the surface with higher amplitudes compared to that of other wall vibration frequencies. Increasing the wall vibration frequency reduces the amplitude of the average heat flux, as well the period of it. The time averaged heat flux calculated for the wall vibration frequencies of 10 Hz, 100 Hz and 1000 Hz, are 0.3383 MW/m^2, 0.3411 MW/m^2, and 0.3408 MW/m^2 respectively. The time averaged heat flux values indicate that the total heat flow has increased for the increase in wall vibration frequency from 10 Hz to 100 Hz

but the total heat flow was reduced with the increase in wall vibration frequency from 100 Hz to 1000 Hz.

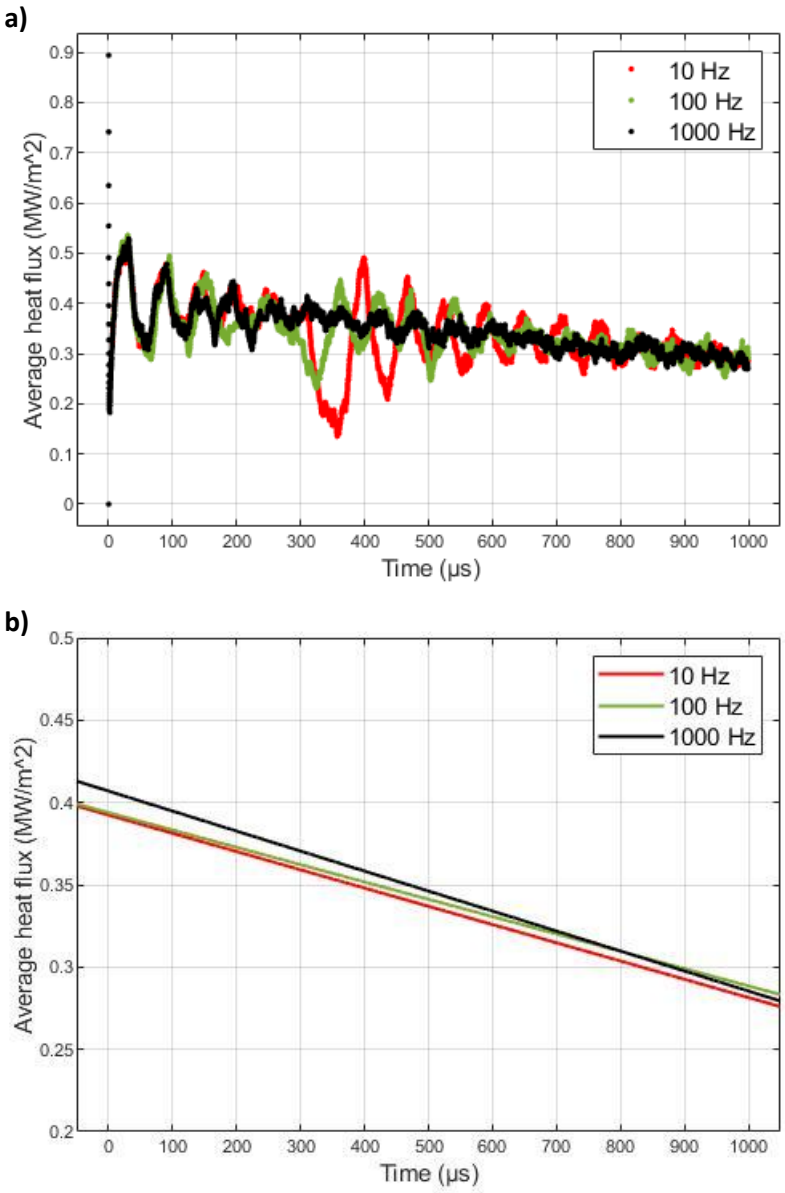

Figure 4.11: Surface averaged heat flux for the surface vibration amplitude of 1 mm at the frequencies of 10 Hz, 100 Hz and 1000 Hz. a) simulated values b) first order polynomial fit of the simulated values.

Similar to the average heat flux for the 0.1 mm amplitude simulations, the average heat flux plots for the 1 mm amplitude also follows a similar trend. The average heat flux has the highest amplitudes for the wall vibration frequency of 10 Hz. Again, increasing the wall vibration frequency reduces the amplitudes and periods of average heat flux. The time averaged heat flux calculated for the frequencies of 10 Hz, 100 Hz and 1000 Hz, are 0.3349 MW/m^2, 0.3399 MW/m^2, and 0.3453 MW/m^2

respectively. The time averaged heat flux values indicate an increase in total heat flow with increasing wall vibration frequencies for the same amplitude.

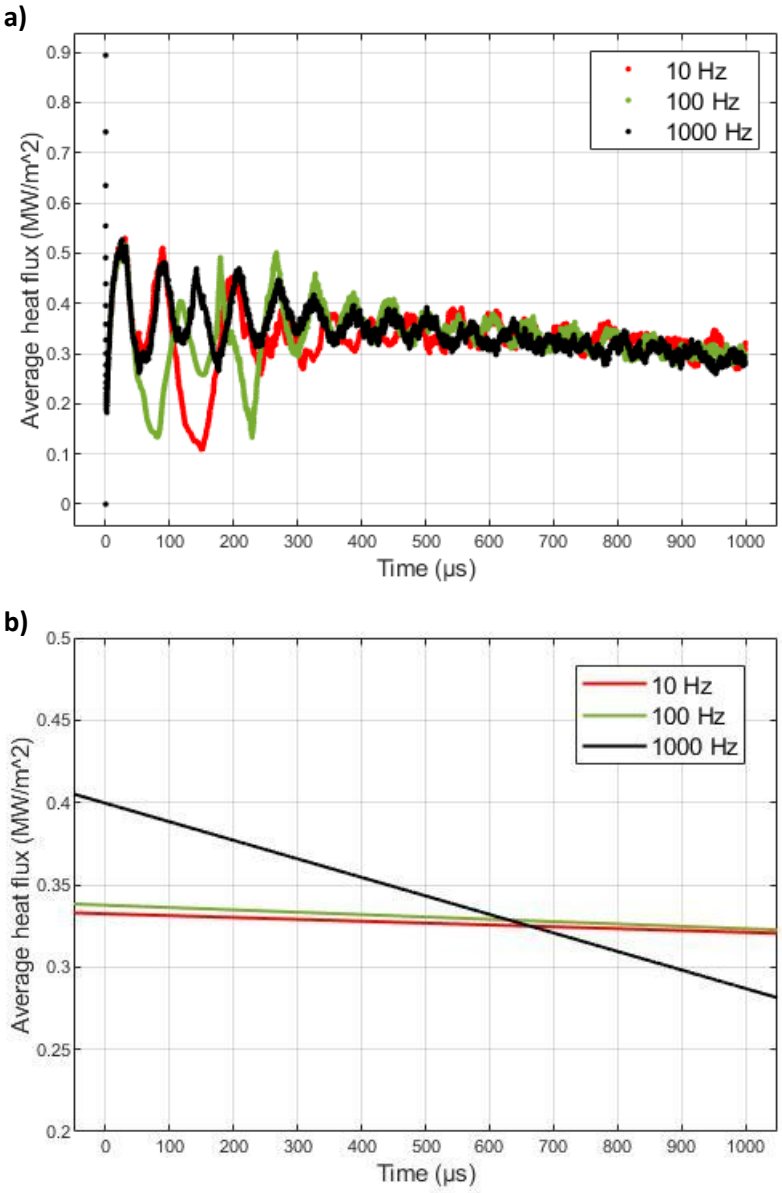

Figure 4.12: Surface averaged heat flux for the surface vibration amplitude of 10 mm at the frequencies of 10 Hz, 100 Hz and 1000 Hz. a) simulated values b) first order polynomial fit of the simulated values.

It can be seen form from figure 4.12 a, the increase in wall vibration amplitude to 10 mm have a significant effect on average heat flux for the frequencies of 10 Hz and 100Hz. The initial high amplitude oscillations of average heat flux, arising from the impact of droplet on the surface, are sustained for a longer time with the high wall vibration amplitude at the relatively low frequencies of 10 Hz and 100. Even though there is a small effect of this at the wall vibration frequency of 1000 Hz,

the oscillations settle down faster with reducing amplitudes of average heat flux. Figure 4.12 b) confirms this, as for the duration of ~600 µs, the average heat flux is higher than the other wall vibration frequencies. The time averaged heat flux values for the wall vibration amplitude of 10 mm for the frequencies of 10 Hz, 100 Hz and 1000 Hz are 0.3287 MW/m^2, 0.3309 MW/m^2, and 0.3415 MW/m^2 respectively.

In order to compare the effect of wall vibration on heat transfer, the time averaged heat flux for all the vibration cases are plotted against the stationary case. Figure 4.13 shows the time averaged heat flux values for the stationary case and the wall vibration cases.

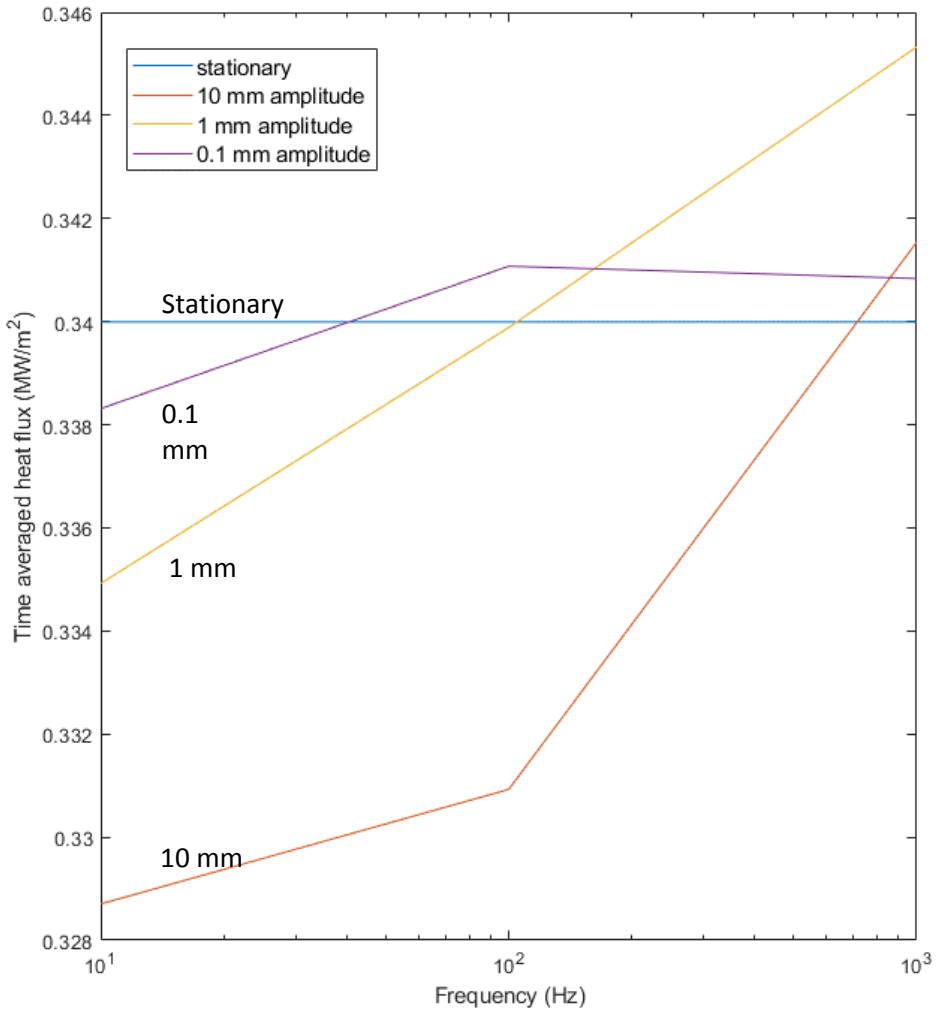

Figure 4.13: Time averaged heat flux for the vibration and stationary cases (D1 to D9, C2).

It can be seen from figure 4.13 that the stationary case has a higher time averaged heat flux compared to that of the 10 Hz frequency case for all amplitudes. This is believed to be due to the

low frequency wall vibration inducing lower frequency oscillations of the droplet with high amplitudes. This reduces the contact of the droplet with the surface, hence decreasing the heat flow. The increase in wall vibration frequency to 100 Hz has increased the time averaged heat flux to be above the stationary case for the wall vibration amplitudes of 0.1 mm and 1 mm but for the wall vibration amplitude of 10 mm the time averaged heat flux is still lower than the stationary case owing to the high amplitude oscillation of the droplet for longer periods. Further increase in the wall vibration frequency to 1000 Hz, for the wall vibration amplitudes of 1 mm and 10 mm, has increased the time averaged heat flux which are above the stationary case. But, for the case of 0.1 mm wall vibration amplitude, the time averaged heat flux almost stayed the same. It is also believed that the increase in heat transfer rate at high engine frequencies (i.e. at a dimensionless frequency of 0.588) is from the increased single-phase convection owing to the higher kinetic energy of the droplet. Table 4.6 provides the time averaged heat flux for each case as well as the percentage increase and decrease compared to the stationary case.

Table 4.6: Details of time averaged heat flux and its difference between the stationary case for simulations D1 to D9.

Simulation No	Wall vibration amplitude (mm)	Wall vibration frequency (Hz)	Time averaged heat flux (MW/m^2)	Difference in heat flux (%)
C2	0	0	0.34	0
D1	10	10	0.3287	-3.32 %
D2	10	100	0.3309	-2.67 %
D3	10	1000	0.3415	+0.44 %
D4	1	10	0.3349	-1.5 %
D5	1	100	0.3399	-0.029 %
D6	1	1000	0.3453	+1.56 %
D7	0.1	10	0.3383	-0.5 %
D8	0.1	100	0.3411	+0.32 %
D9	0.1	1000	0.3408	+0.23 %

From Table 4.6, the highest heat transfer rate increase of 1.56 % is achieved at the wall vibration amplitude and frequency of 1 mm and 1000 Hz respectively. The lowest heat transfer rate of 3.32 % less than the stationary case was found to be at the wall vibration amplitude and frequency of 10 mm and 10 Hz respectively.

Figure 4.14 shows the surface averaged heat flux and its curve fits for the random simulation cases E1 to E4. These simulations were ran for wall vibration amplitudes of 0.02 mm, 0.08 mm, 0.5 mm and 0.2 mm at the frequencies of 400 Hz, 200 Hz, 60 Hz and 60 Hz respectively.

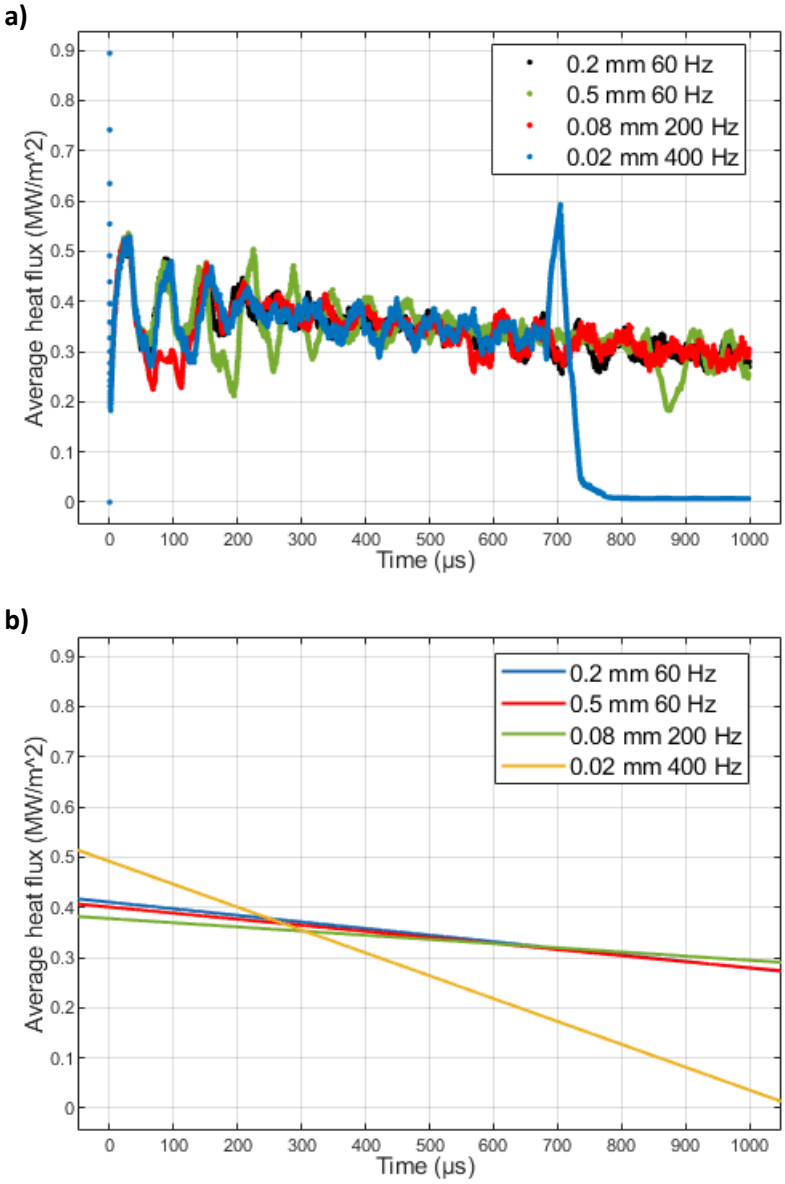

Figure 4.14: Surface averaged heat flux plots for the simulation cases E1 to E4.

The average heat flux plots and their curve fits show that the average heat flux for the four conditions are very close to each other. Like the previous set of simulations (D1 to D9), the highest wall vibration amplitude of 0.5 mm produced the highest heat flux amplitudes with large periods. For the case E4, where the wall vibration amplitude and frequency are 0.02 mm and 400 Hz respectively, droplet rebound occurred at approximately 700 µs. Hence, the heat transfer rate by the case E4 is not included in the discussion. To compare the total heat flow with the stationary case, the

time averaged heat fluxes were calculated. These values, along with its difference compared to the stationary case, are given in Table 4.7.

Table 4.7: Details of time averaged heat flux and its difference between the stationary case for simulations E1 to E4.

Simulation No	Wall vibration amplitude (mm)	Wall vibration frequency (Hz)	Time averaged heat flux (MW/m^2)	Difference in heat flux (%)
C2	0	0	0.34	0
E1	0.5	60	0.3401	+0.029 %
E2	0.2	60	0.3432	+0.94 %
E3	0.08	200	0.3380	-0.59 %
E4	0.02	400	0.2683	N/A (Droplet rebound occurred)

It can be seen that the differences in heat flux were very small and it raises the question whether those are from simulation errors. The impingement dynamics of the droplet were validated using experimental data but it was not possible to validate the heat transfer owing to the lack of experimental data for droplet impingement and onset of evaporation. A convergence study for heat flux using different mesh sizes should determine whether those are errors or an effect of vibration on heat transfer. But it was not possible to conduct the convergence study due to computing power limitations. With the existing element size, the vibrational simulations took approximately 4 days each to simulate a physical time of 1000 µs. For example, running the simulations with four different levels of mesh refinement by halving the element size in each refinement, the simulation running time is expected to be squared each time.

The highest heat transfer rate increase of 0.94 % compared to the stationary case was calculated to be at the wall vibration amplitude and frequency of 0.2 mm and 60 Hz respectively. There was hardly any increase in heat transfer for case E1, where the wall vibration amplitude and frequency were 0.5 mm and 60 Hz respectively. For the case E3, where the wall vibration amplitude is 0.08 mm and the frequency is 200 Hz, the heat transfer rate was 0.59 % less than the stationary case. This could be due to the wall vibration causing unusual droplet oscillations after impact, which can be seen from the average heat flux plot in figure 4.14 a).

4.4. Conclusion of Chapter 4

To conclude, simulations of droplet impingement dynamics were performed for the isothermal case to understand droplet rebound. Initially, the minimum impact velocity for droplet rebound was identified for four droplet diameters (30 µm, 49 µm, 75 µm and 100 µm). It was found that for increasing droplet diameter, the minimum impact velocity for rebound decreases almost linearly and a first-degree polynomial linear equation (equation (4.19)) was constructed. It was also found that the time for detachment after impact increases almost linearly with droplet diameter and this was correlated (equation (4.20)).

Isothermal droplet impingement for two wall vibration amplitudes (10 mm and 1 mm) at three different frequencies (10 Hz, 100 Hz and 1000 Hz) were simulated for the minimum impact velocity for rebound as well as 0.5 m/s less than that. Droplet rebound occurred for more than half of the cases with the impact velocity less than the minimum impact velocity for rebound. This was believed to be because of wall vibration produces a resultant velocity at impact higher than the minimum impact velocity for rebound. The only exception being the three cases with wall vibration amplitudes of 1 mm where droplet rebound did not happen when the resultant velocity was higher than the minimum impact velocity for rebound.

Finally, both stationary and vibrating boundary evaporative heat transfer simulations were performed for droplet impingement. For the moving boundary simulations, three different wall vibration amplitudes (0.1 mm, 1 mm and 10 mm) and three different wall vibration frequencies (10 Hz, 100 Hz and 1000 Hz) for each amplitude were used. Results showed that the highest wall vibration frequency of 1000 Hz enhanced heat transfer for all cases whereas the highest amplitude resulted in reduced heat transfer rate for 10 Hz and 100 Hz. The lowest frequency of 10 Hz reduced the heat transfer rate below the stationary condition for all the amplitudes. It is observed that increasing wall vibration frequency increases the frequency of the droplet oscillation on the surface by reducing the droplet oscillation amplitude faster. This facilitates more frequent contact of the droplet on the surface as well as increased kinetic energy of the droplet causing increased single-phase convection. High vibration amplitude tends to sustain the initial high amplitude droplet oscillation longer which reduces the contact of the droplet on the surface. These oscillations are also much slower compared to the cases with smaller wall vibration amplitudes. In chapter 6, the onset of evaporative heat transfer simulation results are compared with experimental data, using dimensionless numbers for analysis. The primary objective of the comparison is to check whether single droplet results could be used for predicting heat transfer for a spray. An attempt was made to create a correlation of spray evaporative heat transfer on moving boundaries.

Chapter 5. EXPERIMENTAL-RIG DESIGN, MANUFACTURE AND COMMISSIONING

To undertake stationary pool boiling experiments, stationary spray boiling experiments, and dynamic experiments on spray boiling for test pieces with a cylinder head geometry as well as a flat surface, test-rigs that meet the experiment requirements need to be designed, manufactured and commissioned for testing.

This chapter goes through the design, manufacture and commissioning of different experimental-rigs as part of the Evaporative Cooling Systems (ECS) project funded by the EPSRC (EP/M005755/1). The ECS project had three technical partners: Ford, Ricardo and Denso. The ECS project looked into the feasibility of cooling internal combustion engines using spray evaporative cooling. The majority of the work focused on spray evaporative heat transfer experiments on static and moving boundaries. The three different experimental rigs were: i) static pool boiling rig ii.) static spray boiling rig, and iii.) a dynamic spray rig with two test pieces: a) flat surface test piece, and b) a test piece representing the geometry of a cylinder head.

The static pool boiling rig and the static spray boiling rig were designed to undertake experiments to gain experience on taking heat transfer measurements for pool boiling and spray boiling heat transfer respectively. The dynamic spray rig with a flat surface test piece was designed to do experiments on spray boiling heat transfer for a moving boundary. The dynamic spray rig with a cylinder-head geometry test piece was designed to examine moving boundary evaporative cooling for geometries representing a quarter of an engine cylinder-head for one cylinder.

Since the project had nine members over its duration, every member contributed to some extend to the design of the rigs, selection of components required for the rigs and procurement of the parts. Each project member contributed in the design of the rigs which usually involved no more than hand sketches and possibly analytical calculations to support the design ideas. Most of the computer aided design, the production of manufacturing drawings, and the Finite Elements Analysis were completed by the author. Each section below describes the design, manufacture, and commissioning of the different test-rigs, focusing on the requirements of experiments.

5.1. Static Pool Boling Rig and Static Spray Boiling Rig

5.1.1. Design Overview

The static pool boiling rig, and the static spray boiling rig, share most of the test apparatus between each other. The test chamber is shared between both the rigs, the only difference being different

chamber top covers to fit different components. An overview of the design of both the rigs is given below, and the hardware shared between each rig is discussed in a separate section.

5.1.1.1. Static Pool Boiling Rig

The static pool boiling rig was designed to undertake experiments to benchmark pool and nucleate boiling characteristics for cast aluminium and iron surfaces. The design of the static pool boiling rig test apparatus is shown in figure 5.1

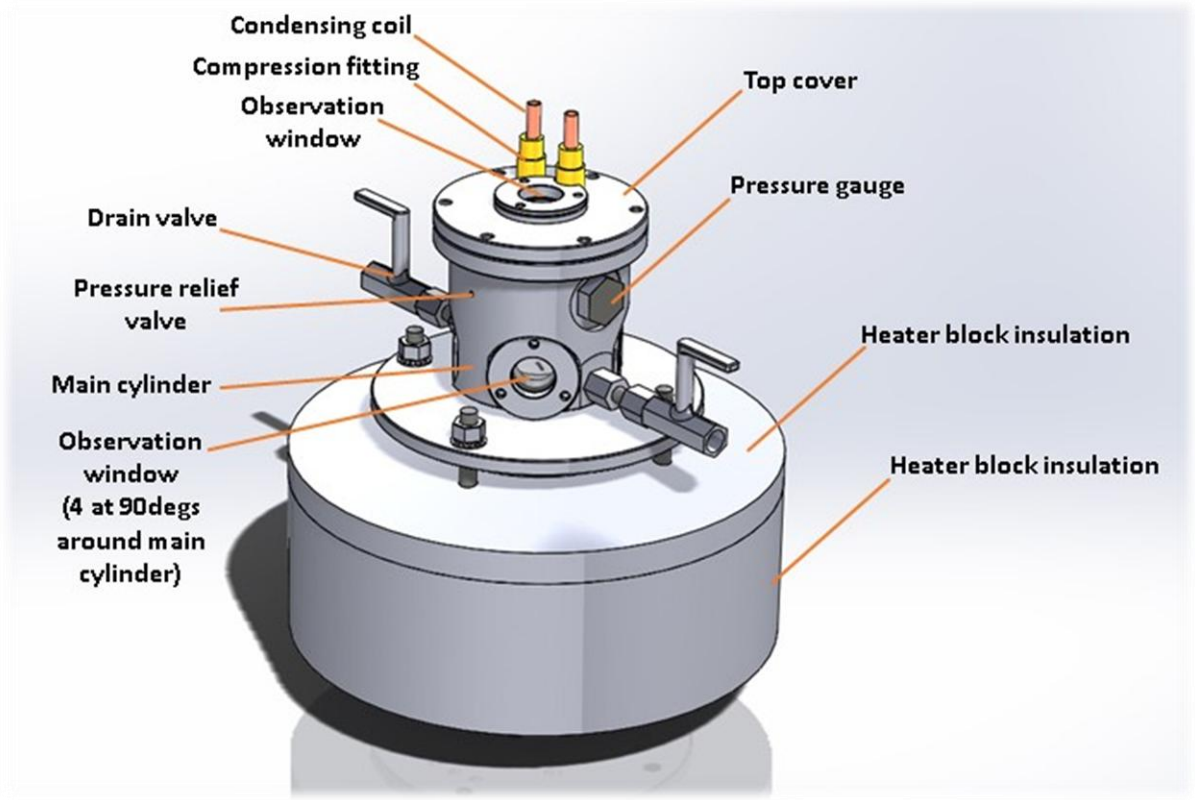

Figure 5.1: Static pool boiling rig test apparatus.

The main cylinder is where the boiling takes place and is where majority of the components are fitted to. A flat test piece is heated with a heater block (situated inside the insulation) using electric heaters. The test apparatus was fitted with a condensing coil on the top cover and the steam generated was condensed inside the main cylinder. The test apparatus was designed with a total of five observation windows, out of which four are around the main cylinder and one above, on the top cover. Two drains on either side of the test apparatus were used for draining the coolant when required. The condensing coil was connected with a water supply to provide sufficient cooling for condensing the steam.

5.1.1.2. Static Spray Boiling Rig

The static spray boiling rig was designed to undertake experiments to identify thermal capabilities of spray evaporative cooling for cast aluminium surfaces. The static spray boiling rig shared most of the test apparatus with the static pool boiling rig. The only difference being a different top cover to fit the nozzle as well as a vent. The design of the static spray boiling rig test apparatus with the main cylinder hidden, is shown in figure 5.2.

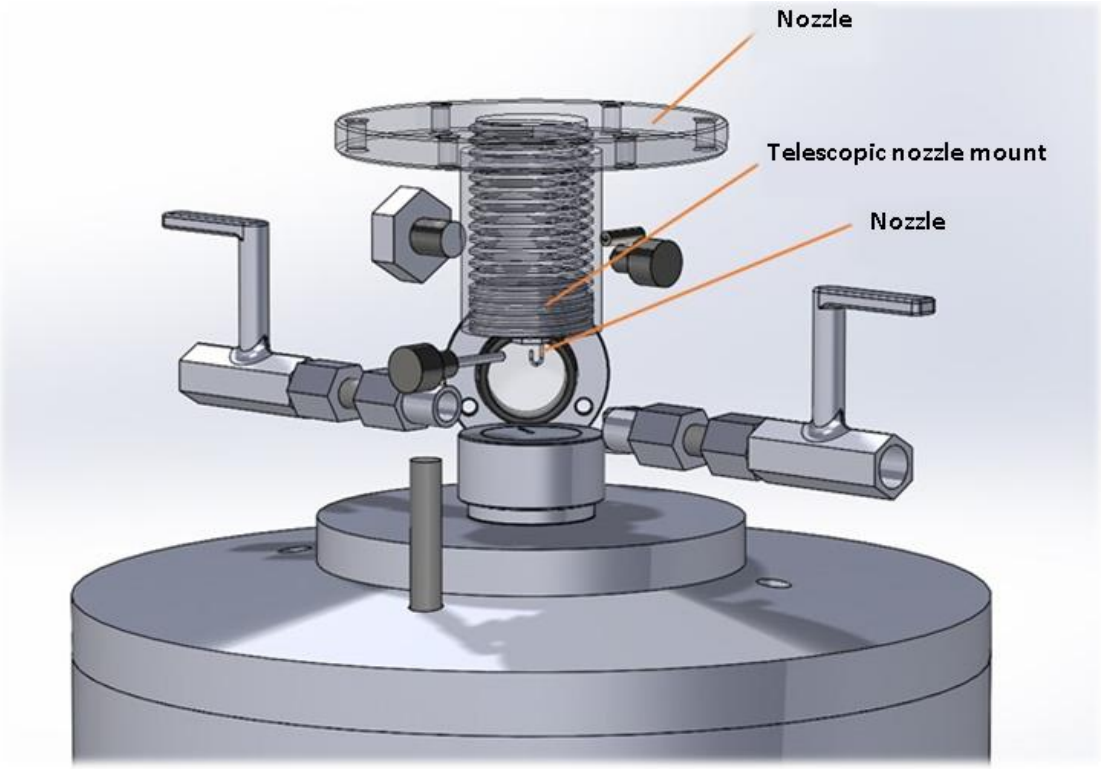

Figure 5.2: Static spray boiling rig test apparatus.

Inclusion of the nozzle mount and the steam vent required the top observation window to be removed owing to space constraints. The telescopic nozzle mount acts as a nozzle height adjuster (i.e from the cooling surface), so that the nozzle can be placed at a certain height where the spray only covers the test piece. The steam vent is connected to an outer condensing and pumping circuit which condenses the steam and the condensate is put back into the nozzle. The condensation and pumping circuit is discussed later in this chapter as it was shared between static and dynamic spray boiling test rigs. Unlike the static pool boiling test apparatus, the drains are used to remove any excess liquid built-up on the test-piece. Two different nozzles are chosen based on the flow rate as well as the mean droplet diameter requirements. The specifications of the spray nozzles are given in table 5.1.

Table 5.1: Spray nozzle specifications.

Nozzle model name	Type of nozzle	Specifications
Bete PJ 6	Full cone, fine fog	0.031 L/min at 5 bar to 0.114 L/min at 70 bar, orifice diameter 0.152 mm
Bete PJ 8	Full cone, fine fog	0.058 L/min at 5 bar to 0.217 L/min at 70 bar, orifice diameter 0.203 mm

5.1.1.3. Test Apparatus Design of the Static Pool Boiling Rig and the Static Spray Boiling Rig

The design of the test apparatus, which is shared between the static pool boiling rig and the static spray boiling rig is described here. Figure 5.3 shows the heater block and the test-piece assembly and the other internal components of the test apparatus.

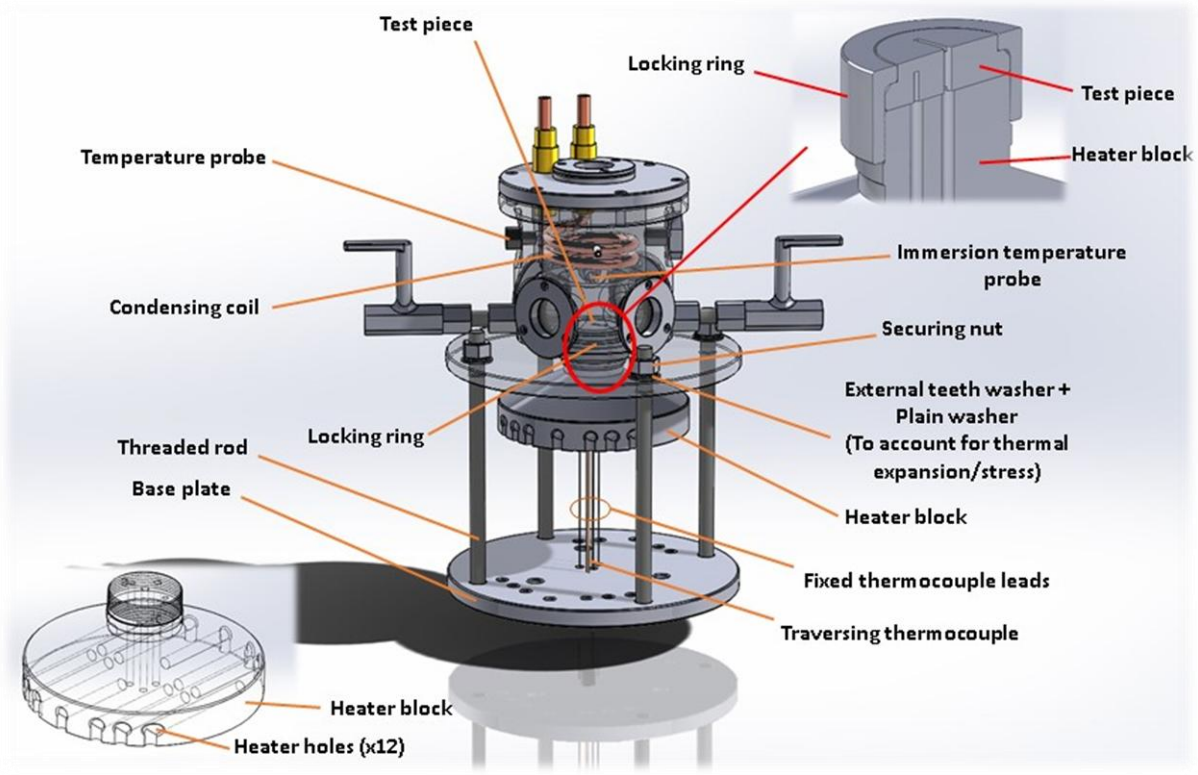

Figure 5.3: Test apparatus internal components, heater block, and test-piece assembly (Test apparatus shown is in the pool boiling rig configuration).

The heater block is to be made of copper and contains 12 electric cartridge heaters producing a maximum power output of 250W each. The test-piece was designed to be secured to the top of the heater block using a locking ring to enable easier replacement of the test-piece when required. The

test piece including the locking ring had a diameter of 47.6 mm. The main-cylinder, which carries the heater block, was fixed to the base plate using four threaded bolts. Different materials were used for test-piece design: for the pool boiling rig, Stainless steel and Aluminium were used whereas for the spray boiling rig, only Aluminium was used. Several thermocouples, fixed and traversing, were incorporated in to the test-piece design for accurate measurement of temperature at different locations. There were several temperature and pressure measurement instruments, and safety and control valves fitted to the test apparatus. The details of the instrumentation, and safety and control valves fitted to the test apparatus are given in the table below.

Table 5.2: Instrumentation, safety components, and control valves on the static pool and spray boiling test apparatus.

Component Name	Purpose
Surface thermocouple (x2)	To measure the temperature at the top and bottom surface of the test-piece
Embedded thermocouple (x2)	To measure the temperature inside the test-piece at different heights
Traversing thermocouple	To measure temperature at variable heights in the test-piece
Temperature probe (x2)	One to measure the ambient temperature inside the main cylinder for both pool and spray rig configurations. And the other to measure the bulk liquid temperature for pool boiling rig.
Pressure gauge with a temperature isolation coil	To measure the pressure inside the main cylinder
Pressure relief valve	To release the pressure inside the main-cylinder as a safety measure if there is pressure build-up.
Pressure reducing valve	To control the pressure inside the main cylinder

5.1.2. Detailed Design of the Major Components

The design of the test-apparatus was initiated by trying to achieve a heat flux of at least 1.2 MW/m^2 at the heating surface. Electric cartridge heaters inserted in a heater block were identified to be ideal for this, but it was difficult to achieve a heat flux of 1.2 MW/m^2 even with several kilowatts of heater

power. A heat amplification method using a conical heater design was examined as it drastically reduced the heater power requirement. One of the initial Finite Elements Analysis results on heat flux amplification is shown in figure 5.4.

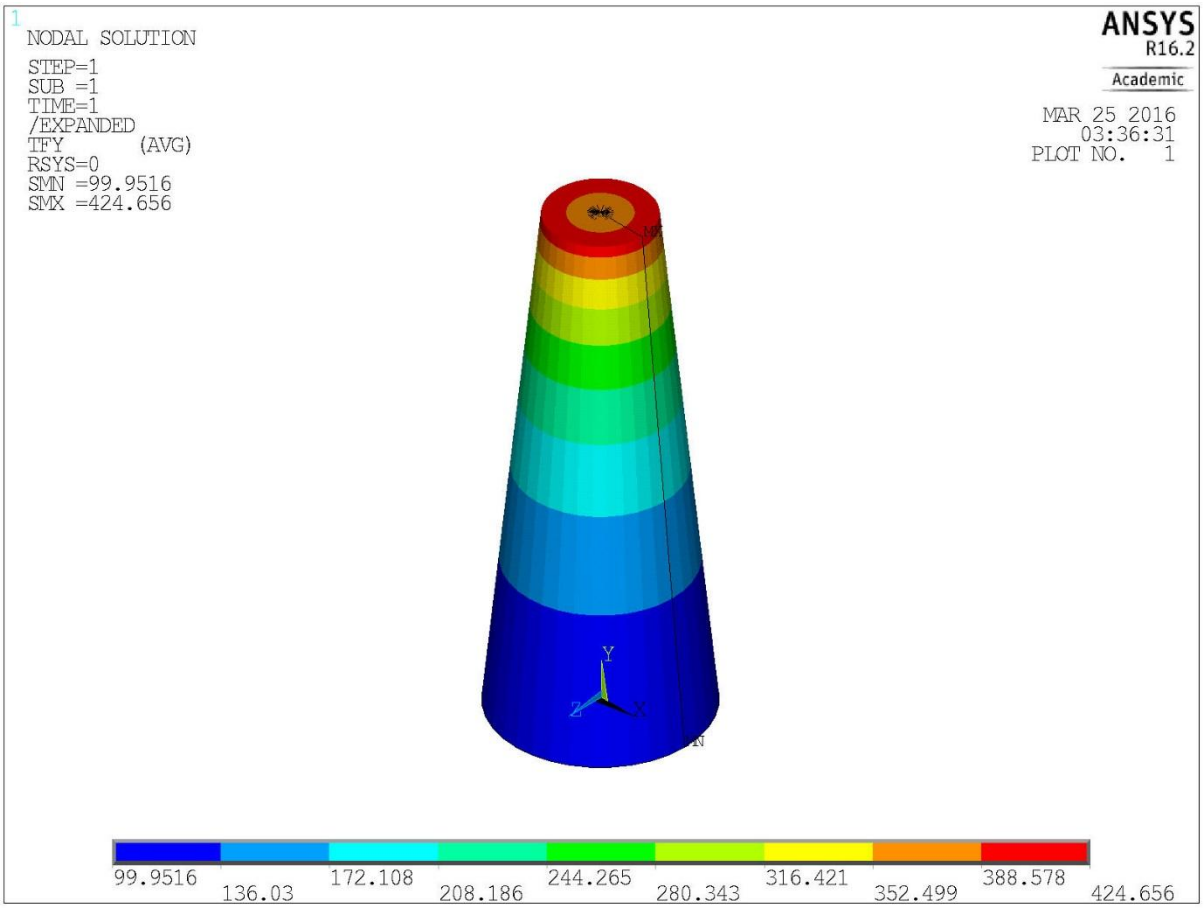

Figure 5.4: Heat flux distribution for a heat flux amplification cone with 100 W/m^2 heat flux input.

Steady state thermal FEA analysis was simulated using ANSYS Mechanical for a heat flux input of 100 W/m^2 at the bottom surface of the amplification cone. It can be seen from the figure that the heat flux increased by 4.25 times. The increase in heat flux is directly proportional to the reduction in surface area. Using this idea, a conical heater block with 12 cartridge electric heaters were used to achieve the required minimum heat flux of 1.2 MW/m^2. Each heater had a maximum power output of 250 W, providing a maximum total power output of 3000W. A steady state thermal FEA using Solidworks was performed to find the temperature and heat flux distribution of the heater block for the maximum power input of 3000 W. The evaporative heat transfer on the top of heater block was simulated by assigning it with a heat transfer coefficient of 10,000 W/m^{2}K and a coolant temperature of 120 ^{o}C. Figure 5.5 and 5.6 show the temperature distribution of the heater block and the heat flux at the top surface of the heater block respectively.

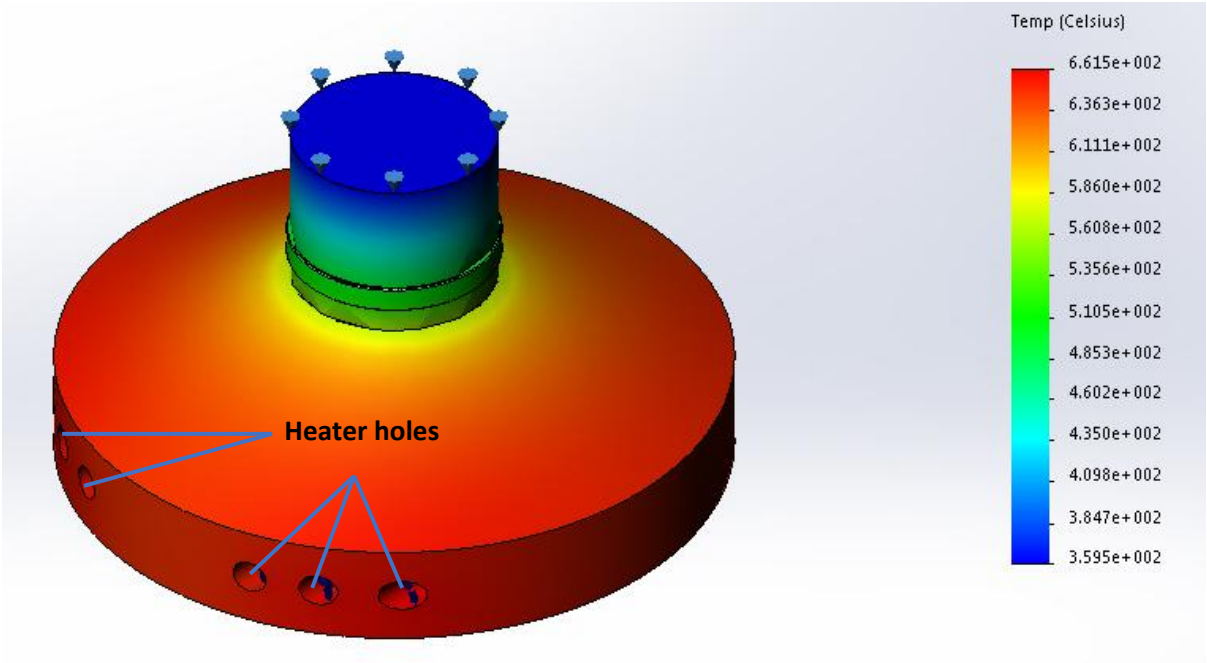

Figure 5.5: Temperature distribution of the heater block at a total heater power of 3000 W.

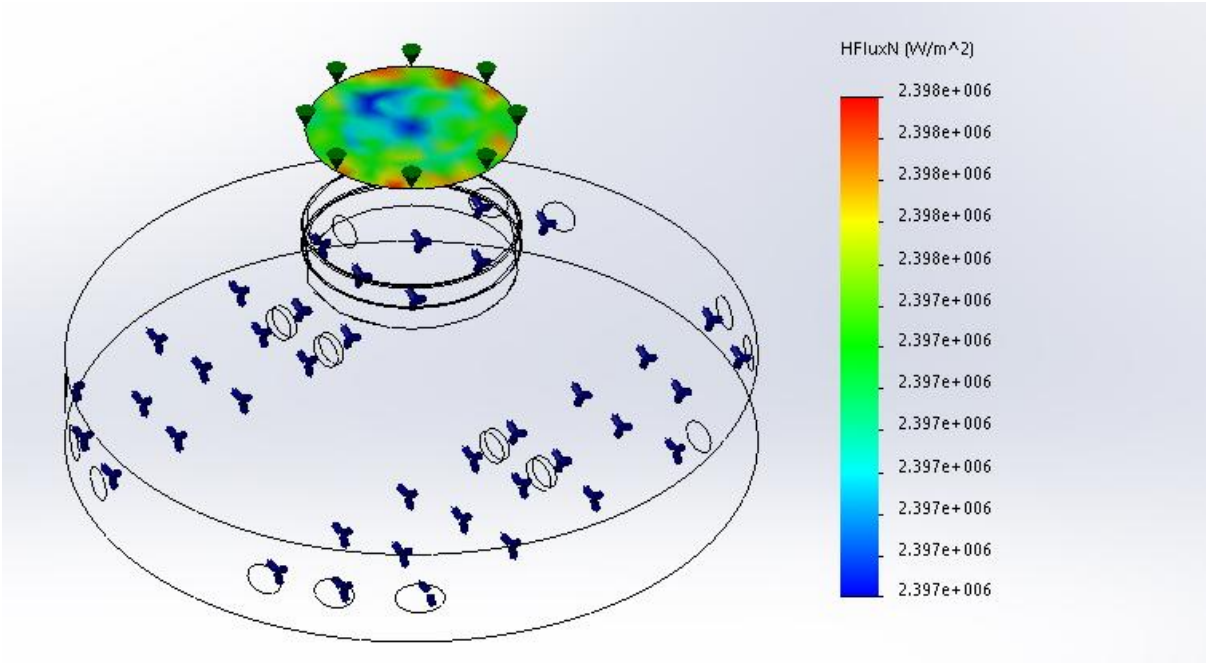

Figure 5.6: Heat flux at the top surface of the heater block at a total heater power of 3000 W.

The heat flux and temperature distribution plots for the test surface show a maximum heat flux and temperature of 2.4 MW/m^2 and 360 ^{O}C respectively. The maximum temperature of the heater block was calculated to be around 660 ^{O}C.

A transient Solidworks thermal FEA was also performed to find the time it takes to heat-up the heater block. The initial condition for temperature of the heater block was 90 ^{O}C. Initially, for 10

seconds, the heater block was being heated by the heaters with a total power of 375 W. At the time of 10 seconds, the heater power was increased to 3000 W. Figure 5.7 shows the FEA results for the heater block temperature at the electric heater surface, and at the test surface for a step change of total heater power from 375 W to 3000 W in which the heat transfer coefficient and ambient temperature were same as the previous steady state analysis.

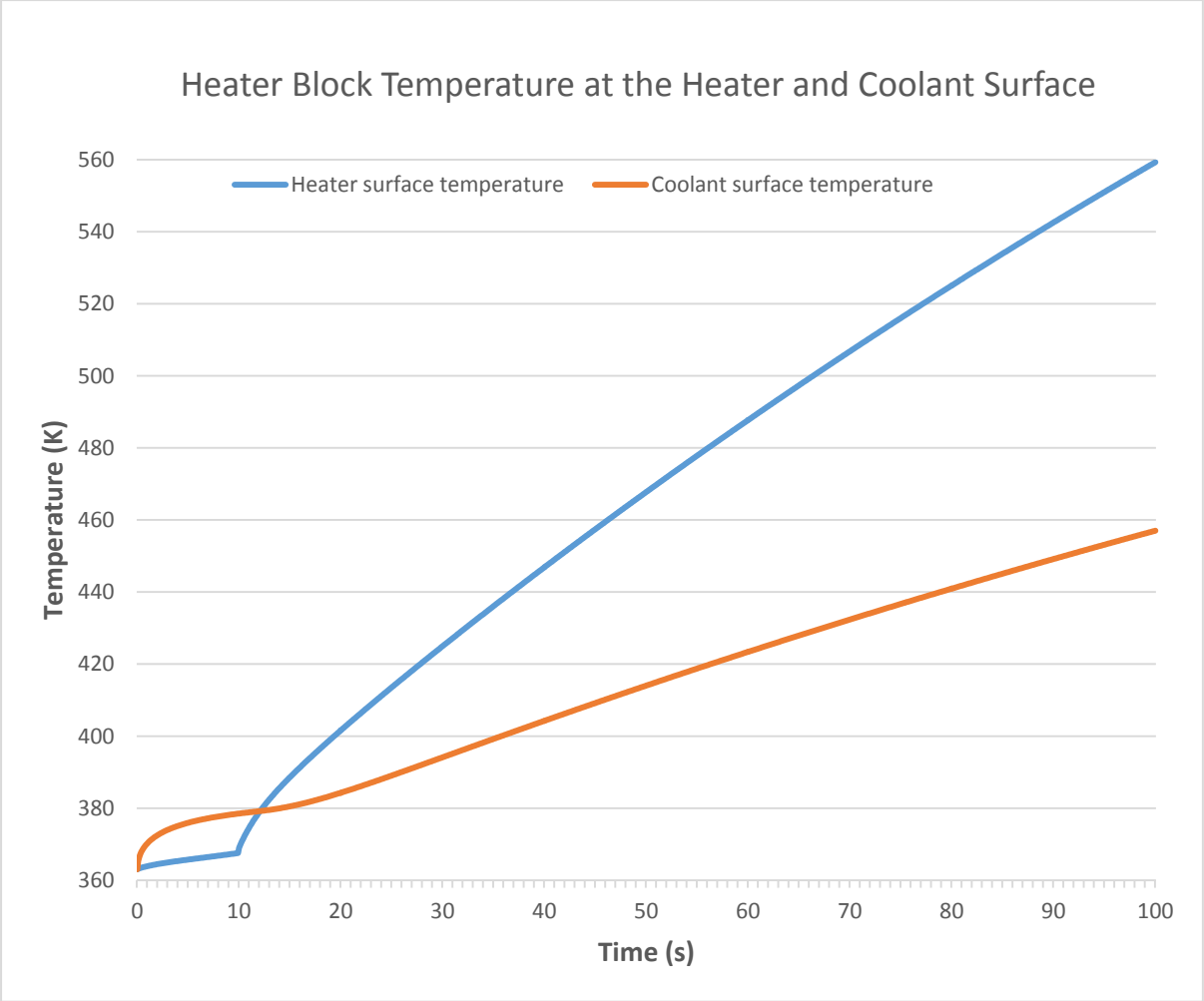

Figure 5.7: Transient maximum and minimum heater block temperature for a step change of heater power from 375 to 3000 W.

When the total heater power is at 375 W, the temperature of the block rises slowly and almost reaches a steady state at 10 s. At 10 s, when the total heater power was increased to 3000 W, the heater surface temperature and the coolant surface temperature started to increase at a rate of 2.34 K/s and 0.98 K/s respectively. The rate of increase of temperature at both the heater surface and the coolant surface stayed almost the same for the rest of the simulation (until 100 s). The results showed that within 30 s, the coolant surface temperature increased from the saturation temperature (100 ^{o}C) at atmospheric pressure to a temperature equal to the critical heat flux (~130 ^{o}C) excess temperature (Twall-Tsat). This showed that the heater block was capable of producing

enough heat to experiment most of the boiling curve in pool boiling and spray boiling within reasonable time scales.

Based on the above simulation results, the basic design of the heater block was finalised. In order to study heat transfer on different metal surfaces experimentally, an easily removable test-piece design was implemented. A thread was added on the outer surface of the top cylindrical section of the heater block. Test-pieces made of different materials could then be fitted on top of the heater block using a threaded metal cap (locking ring). Four fixed thermocouples and one traversing thermocouple are used to measure the temperature of the test piece at different heights. The temperature measurements at different heights can be used to calculate the heat flux. Out of the four fixed thermocouples, two were surface thermocouples. Figure 5.8a and 5.8b show the test piece and thermocouple arrangements.

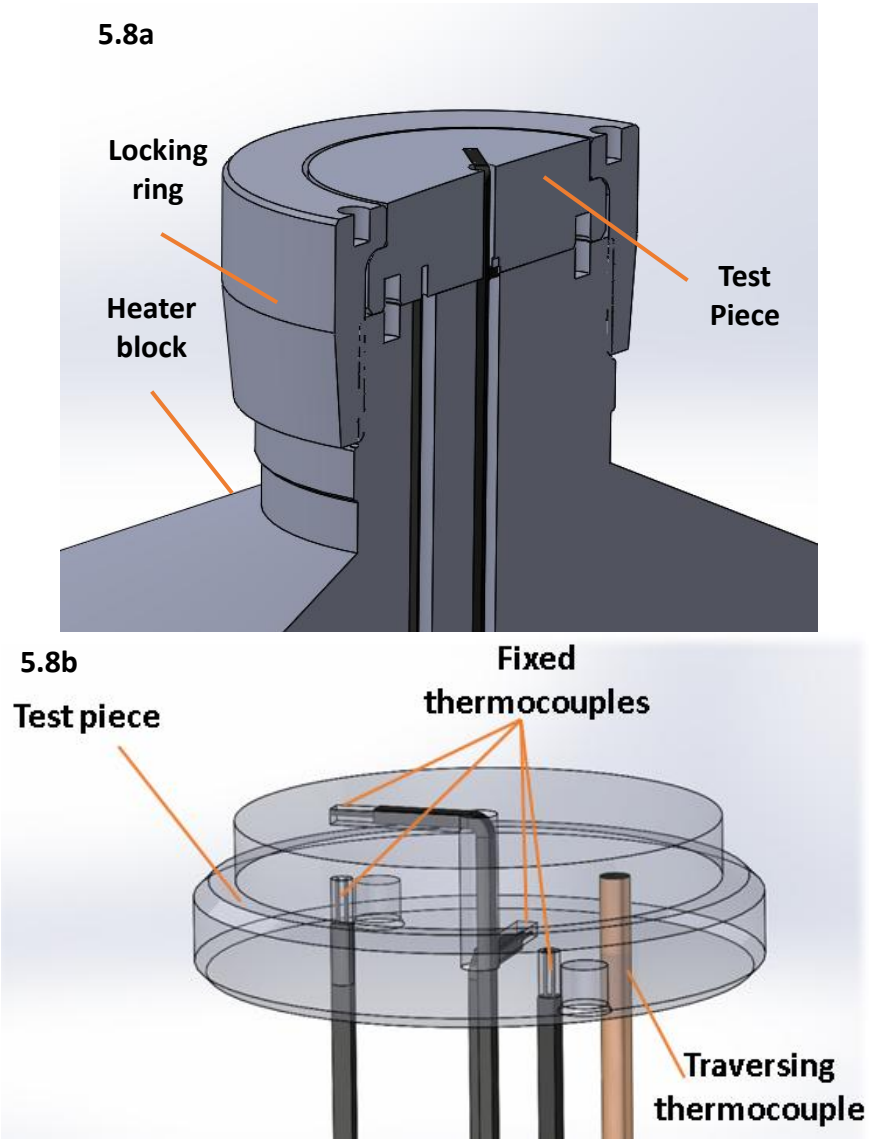

Figure 5.8: Test-piece and thermocouple arrangement.

The top cylindrical section of the heater block, and the test-piece, and locking ring assembly, sits inside the main cylinder. In the design, there had to be a gap left between the main cylinder and the locking ring/heater block to avoid heat loss from the heater block into the main cylinder. This required the gap to be sealed, but not permanently using any filling which would make it difficult to replace the test-pieces. Initially, metal C-section rings were considered owing to the high temperature at the location requiring sealing. Later, it was found that O-rings made of Viton can withstand temperatures up to 205 ^{o}C and these were chosen to be used. The outer cylindrical surface of the locking-ring was sealed against the test cylinder surfaces using O-rings as shown in figure 5.9.

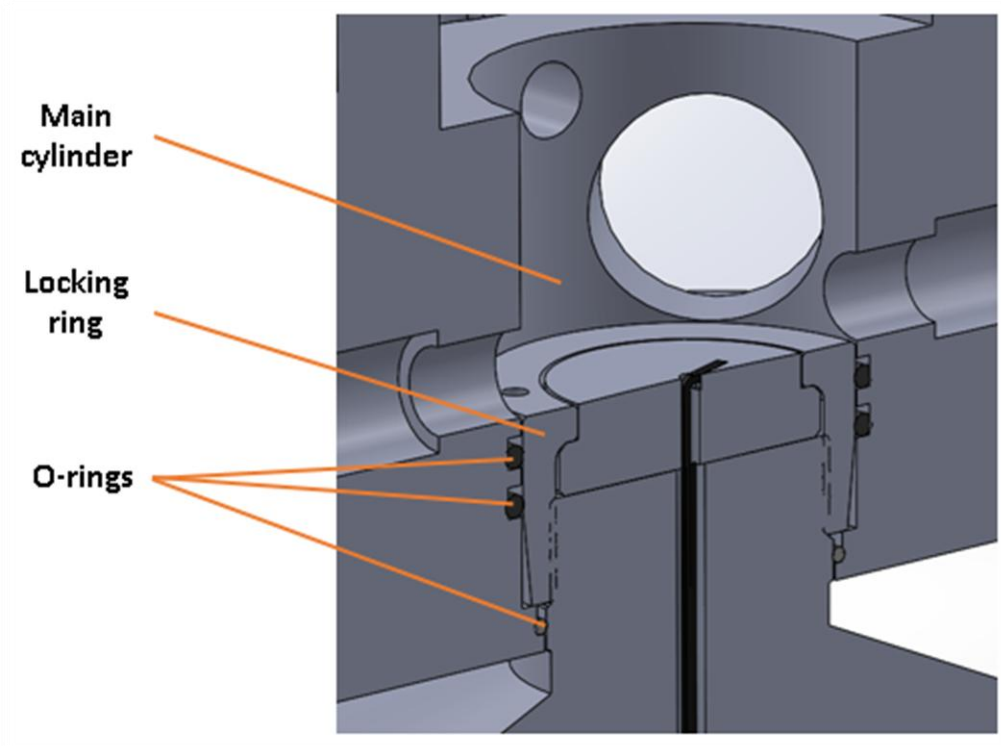

Figure 5.9: Heater block, locking ring, and main cylinder sealing arrangement.

Similarly, the top covers, and all the observation windows around the main cylinder and also on the top cover for the pool boiling configuration were all designed to be sealed by Viton O-rings as the temperature inside the chamber can go above 100 ^{o}C. A reciprocating O-ring seal design was used to seal the telescopic mount for the nozzle.

5.2. Dynamic Flat Surface Spray Boiling Test Piece

5.2.1. Design Overview

The dynamic spray evaporative boiling test piece was designed to undertake experiments on spray evaporative heat transfer on a moving boundary. A flat surface test piece was designed to meet the

objective of measuring one dimensional heat flow. A research fellow in the ECS project suggested having an external stationary enclosure to keep the weight of the moving components as low as possible. Figure 5.10 shows the design of the flat surface test-piece with the main cylinder (enclosure) and its cover transparent, revealing the internal components.

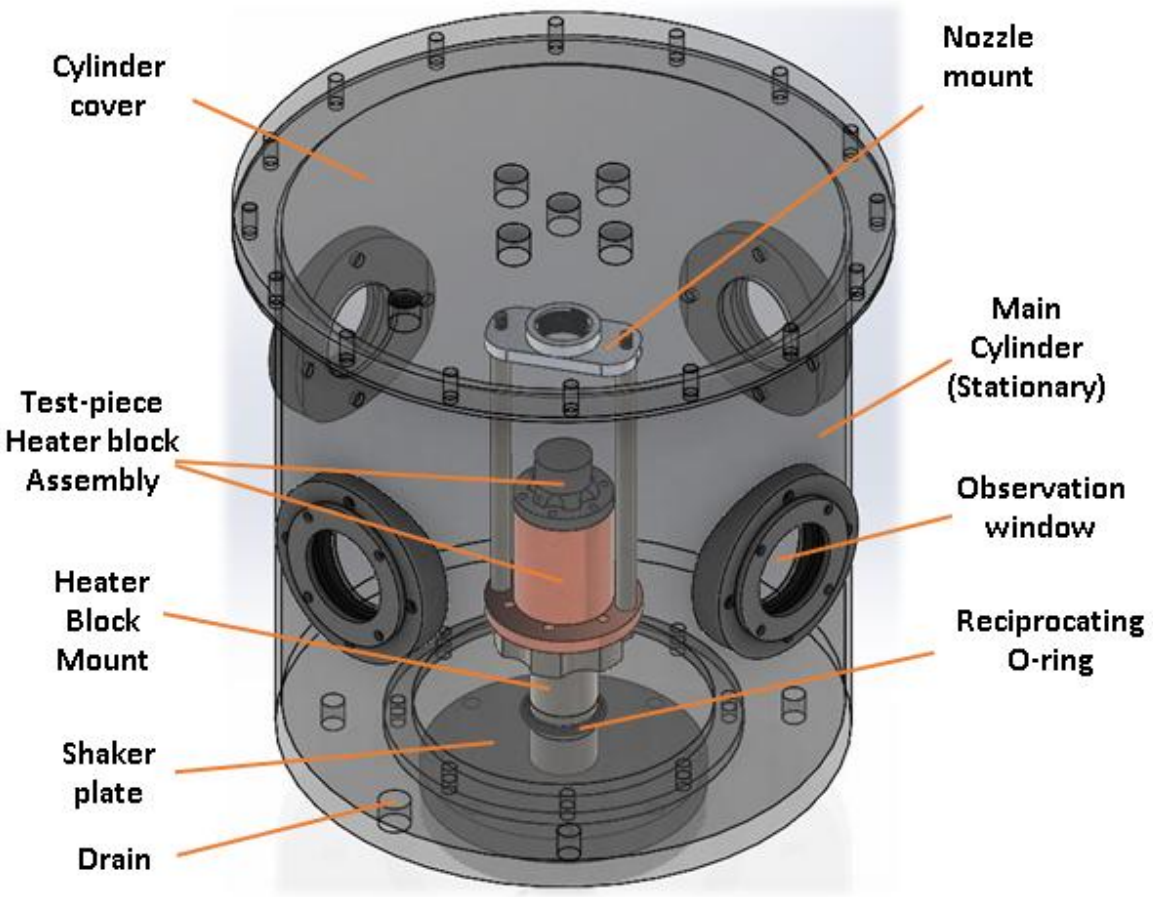

Figure 5.10: Dynamic flat surface spray boiling test piece with main cylinder and its cover transparent.

The test-piece, which is bolted on top of the heater block is connected to the shaker plate through a shaft. The shaft was sealed to the main cylinder using a reciprocating shaft O-ring. Three thermocouples were used to measure the temperature of the test piece at different heights, which were then used to calculate the heat flux. The shaker plate was bolted onto the shaker below which is not shown in the figure 5.10. A shaker capable of reaching a maximum amplitude of 12.47 mm with a frequency range between 5 to 6300 Hz was selected. The shaker specification is explained in more detail in the section 5.4.

To keep the design as light as possible, two threaded rods were used to fix the nozzle mount onto the heater block. The nozzle was fitted to the nozzle mount through a thread but it is not shown in the figure above. There were four observation windows around the main cylinder and these were sealed using O-rings. Two drains were used to remove any excess water getting collected at the bottom of the main cylinder. All the inlets and outlets, and measuring instruments, were designed to fit onto the cylinder cover for easier manufacturing. Figure 5.11 describes the fittings on the cylinder cover.

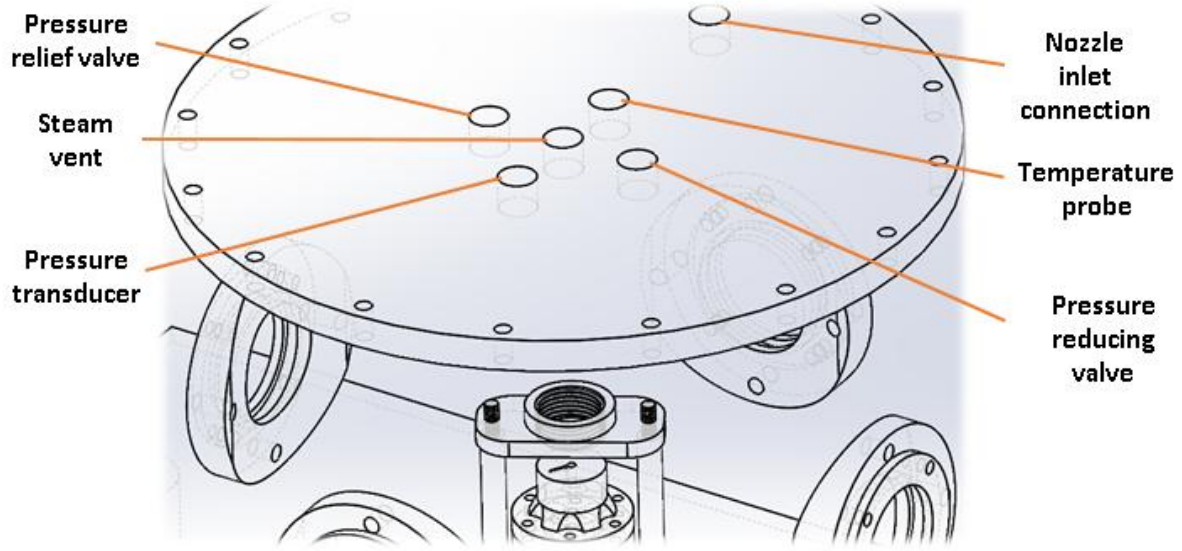

Figure 5.11: Cylinder cover fittings.

The thermocouple wires were also designed to be taken out through the cylinder cover which is not shown in figure 5.11. A flexible tube connects the nozzle with the inlet on the cylinder cover. The pressure relief valve was added to the design as a safety measure to release pressure in-case of pressure build-up in the cylinder beyond safe levels. There were several temperature and pressure measurement instruments, and safety and control valves fitted to the test piece. Instrumentation, and safety and control valves fitted to the test-rig are given in the table 5.3.

Table 5.3: Instrumentation, safety components, and control valves on the dynamic rig with flat test piece.

Component Name	Purpose
Embedded thermocouple (x4)	Three to measure the temperature of the test piece at different heights and one to measure the temperature of the heater block at the maximum temperature point.
Temperature probe	To measure the ambient temperature inside the main cylinder.
Pressure gauge with a temperature isolation coil	To measure the pressure inside the main cylinder.
Pressure relief valve	To release the pressure inside the main-cylinder as a safety measure if there is pressure build-up.
Pressure reducing valve	To regulate the pressure inside the main cylinder.

The specifications of the spray nozzle used in the dynamic flat surface spray boiling rig is given in table 5.4.

Table 5.4: Specifications of the nozzle used in the dynamic rig with flat test piece.

Nozzle model name	Type of nozzle	Specifications
Bete PJ 8	Full cone, fine fog	0.058 L/min at 5 bar to 0.217 L/min at 70 bar, orifice diameter 0.203 mm

5.2.2. Detailed Design of the Major Components

The design process started with designing the heater block. From previous experience of designing a heater block for the static pool boiling rig and the static spray boiling rig, it was decided to use the heat flux amplification method as before. Initially, the heater block and the test piece were designed to be a single part made out of copper, and it was called the heater block. Similar to the static pool boiling and the static spray boiling rig designs, the heater block had a cylindrical section where the heaters were located and a stepped cone was used for heat flux amplification. The flat test surface had a diameter of 20 mm and the main cylindrical section had a diameter of 35 mm. Instead of arranging the heaters horizontally, to save more weight from the heater block, the heaters were designed to be placed vertically inside the heater block. A total of six heaters with a power output of 250 W each were used. The following figures show the results for an FEA performed for a total heater power input of 650 W trying to achieve a target cooling heat flux of 2 MW/m^2.

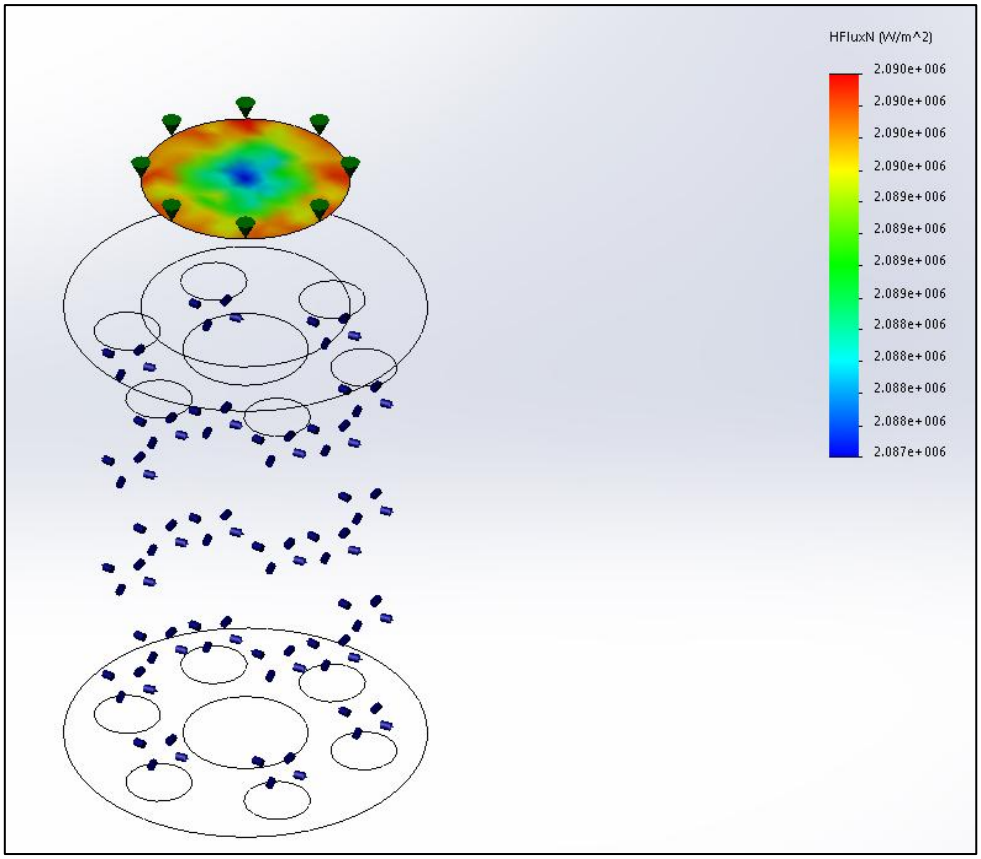

Figure 5.12: Cooling heat flux for a total heater power of 650 W.

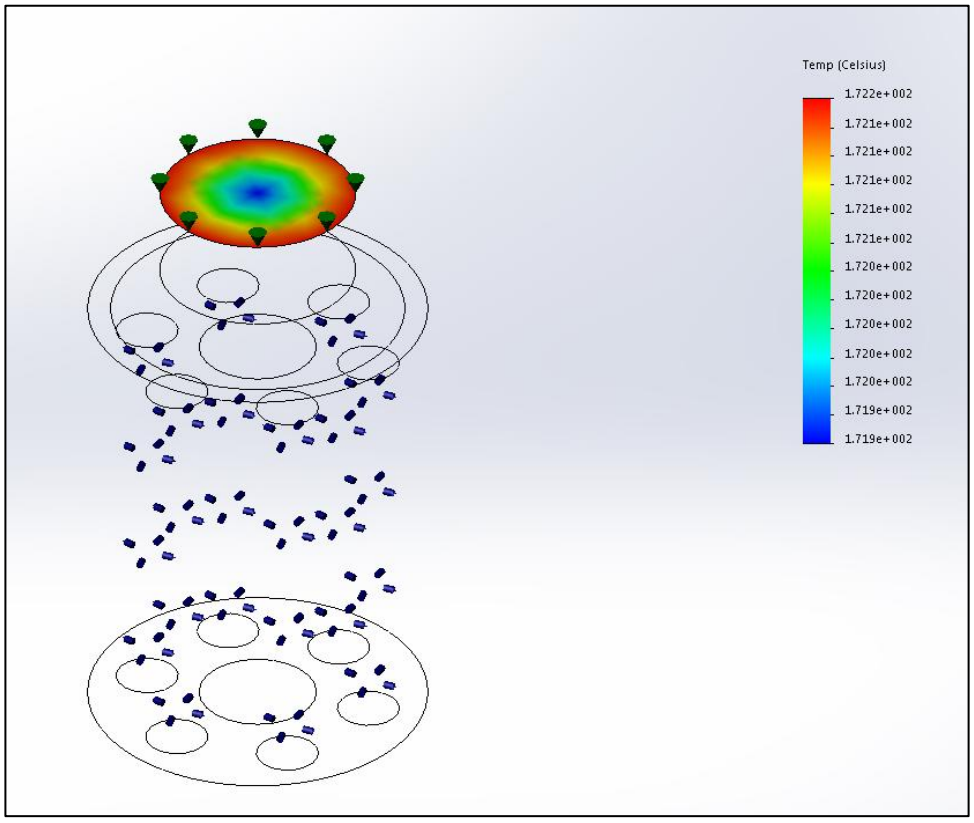

Figure 5.13: Coolant surface metal temperature for a total heater power of 650 W.

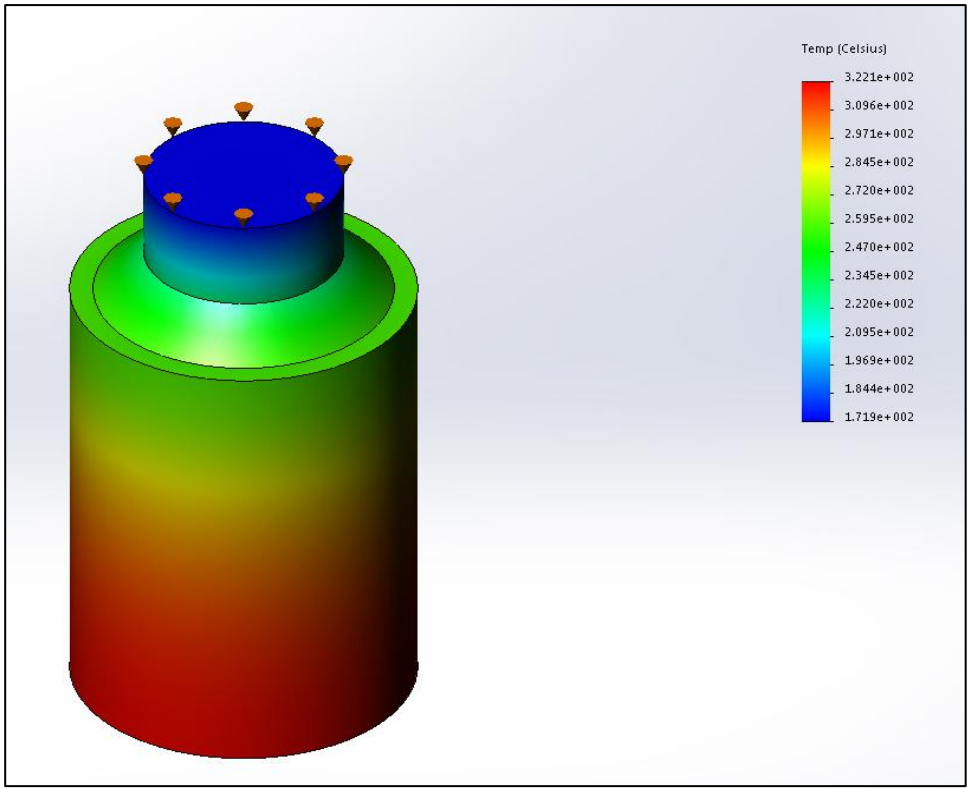

Figure 5.14: Heater block metal temperature for a total heater power of 650 W.

The results show that a cooling heat flux of 2 MW/m^2 could be achieved without reaching a very high metal temperature in the heater block, especially considering thermally loaded fatigue while being shaken. The coolant surface heat flux and metal temperature on the test surface plots show an even distribution, which was achieved using several iterations in the design. The maximum temperature in the heater block was calculated to be 320^{o}C. Initially, a heater block design with a fully conical top section was designed but it gave a very uneven heat flux and temperature distribution on the coolant surface. The second design was without a cone and the surface area reduction was achieved through a stepped top section for heat flux amplification. This gave a very even heat flux and temperature distribution but considering the stress concentrations on the edges, a step was added between the larger and smaller cylindrical section.

The heater block and the test surface section was later decided to be split into two as the test piece and the heater block. It was achieved so that different test pieces could be used in the future for different types of test surface geometries, surface finishes etc. At the bottom of the heater block, there was a flange to bolt the heater block to its mount. The heater block mount had a hollow shaft which was designed to take the heater wires out. This arrangement is shown in figure 5.15.

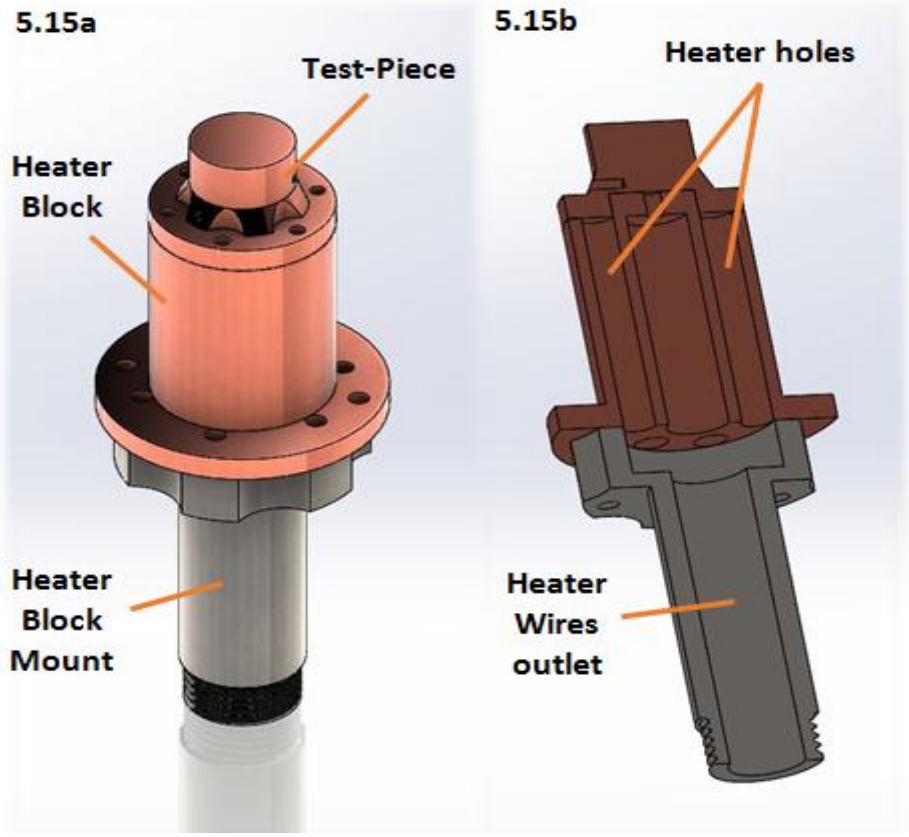

Figure 5.15: Heater block, test piece, and the heater block mount assembly.

The test piece was designed to have three embedded thermocouples at different heights. This design is shown in the following figure.

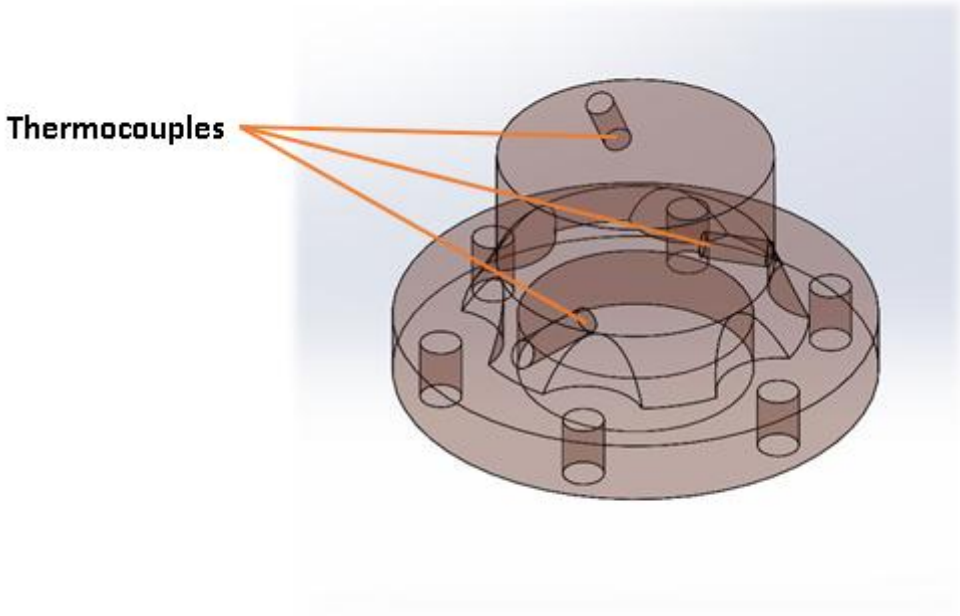

Figure 5.16: Thermocouple locations in the test piece.

Thermocouples were placed at 120^{o} angle each around the axis to avoid them being on one line vertically to minimise the disturbances to the vertical heat flow. All the thermocouples were at the same distance from the axis of the test piece to make sure that the measurements would be taken at the same locations radially.

5.3. Dynamic Cylinder-Head Geometry Test Piece

5.3.1. Design Overview

The dynamic cylinder-head geometry spray boiling test piece was designed to undertake experiments of spray boiling heat transfer on a test surface representing the geometry of a cylinder head. Only a quarter of the cylinder head geometry was modelled to be the test piece, mainly to reduce weight and increase the dynamic capability. The cylinder head of an engine producing 100 KW/L was used as a reference to design the test surface geometry. Initially, the whole cylinder head was modelled and 1/4th of one cylinder was cut and modified into a test piece. The test piece represents the area around the axis of the cylinder head for one cylinder and it had a diameter of 40 mm. Similar to the other test rigs, this test-rig also uses electric heaters located inside a copper heater block to heat the test piece. The heater block was made out of copper for maximum conduction whereas the test piece was designed to be in Aluminium to represent the modern engine cylinder head. A model of the dynamic cylinder-head geometry spray boiling rig is shown in figure 5.17.

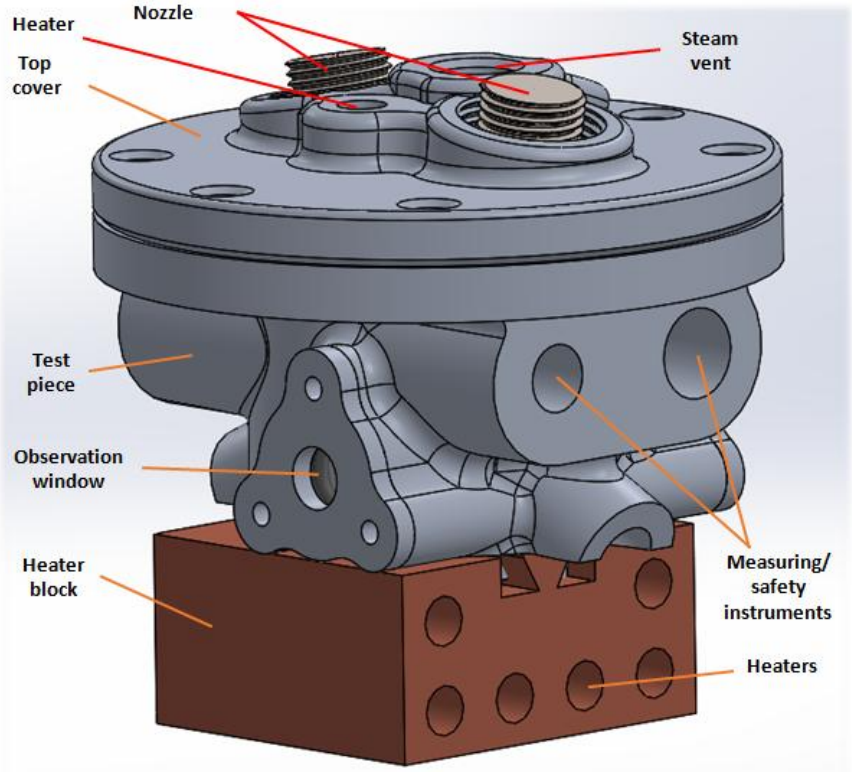

Figure 5.17: Design of the dynamic cylinder-head geometry spray boiling test piece.

Unlike the dynamic flat surface spray boiling test piece, this test piece has a moving enclosure (along with the test surface) carrying all the components. Two full cone spray nozzles were placed on the top cover at an angle pointing inwards into a test chamber, which was designed to cover most of the test surface area. The heater block was designed to be mounted below the test piece using a 'dove tail'. The test piece had two observation windows just large enough to check the conditions inside. The observation windows were too small to capture the inside of the chamber using any photography equipment. Like the previous test-rigs, these observation windows were also sealed using O-rings. There were two drains to remove any excess coolant in the chamber. The steam vent on the top cover connects to an outer condensation circuit, same as the dynamic flat surface spray boiling rig. All the measuring and safety instruments were also same as the dynamic flat surface spray boiling rig. Figure 5.18 shows the test piece and for convenience referred to as the 'quarter cylinder' test piece.

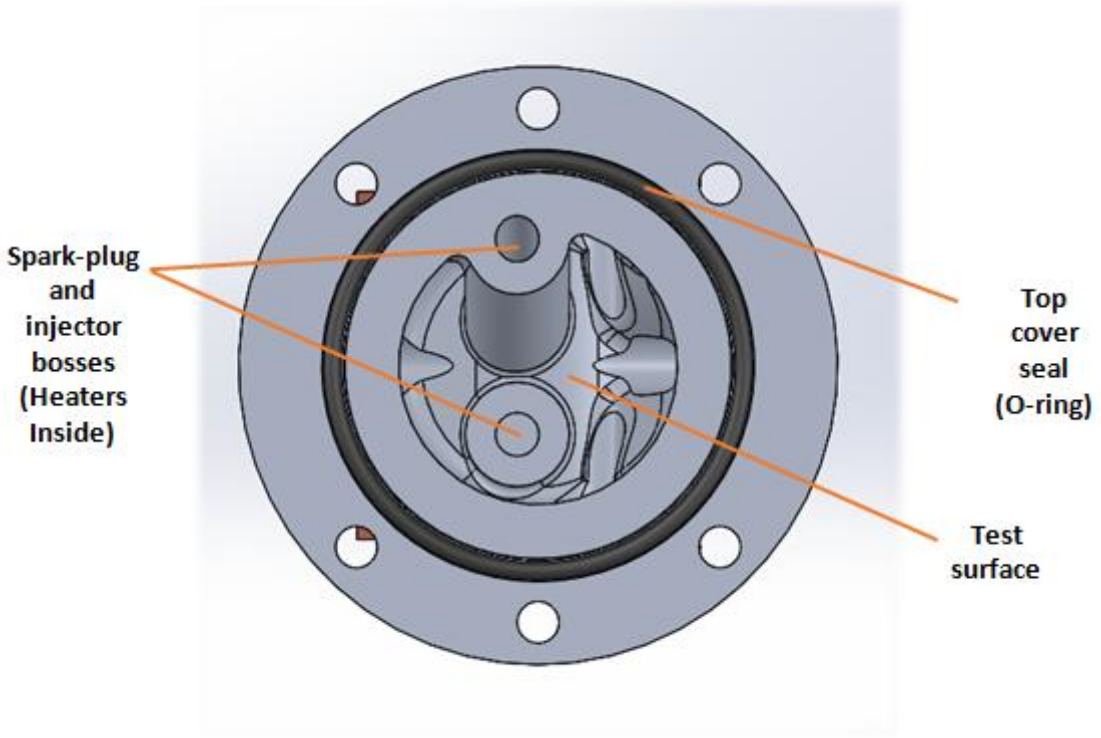

Figure 5.18: Quarter cylinder test piece.

Figure 5.18 shows the geometry of the coolant side of a cylinder head replicated as the test surface. The two bosses used to fit the spark plug and injector in an engine were designed to fit heaters in the test piece to provide sufficient heating to the critical areas of the test surface. An O-ring gland was designed to fit on a flange on top of the test piece for sealing the top cover.

There were several temperature and pressure measurement instruments plus safety and control valves fitted to the test piece. Instrumentation, and safety and control valves fitted to the test-rig are given in the table 5.5.

Table 5.5: Instrumentation, safety components, and control valves on the dynamic cylinder-head geometry spray boiling rig.

Component Name	Purpose
Embedded thermocouple (x1)	To measure the temperature at the maximum temperature area of the test piece.
Temperature probe	To measure the ambient temperature inside the main cylinder.
Pressure gauge with a temperature isolation coil	To measure the pressure inside the main cylinder.
Pressure relief valve	To release the pressure inside the main-cylinder as a safety measure if there is pressure build-up.
Pressure reducing valve	To regulate the pressure inside the main cylinder.

The same models of the nozzles used in the static spray boiling rig were also used in the dynamic cylinder-head geometry spray boiling rig.

5.3.2. Detailed Design of the Major Components

Even though several types of heating (including gas burning) was considered and analysed as a heat source to heat the test piece, a copper heater block design with four electric haters was eventually used. Gas burning was not used mainly because of difficulties in achieving the required heat flux without heating the test piece into very high temperatures. Initially, the design was to fit two heater blocks on either side of the heating plate of the test piece. A cross section of this arrangement is shown in figure 5.19.

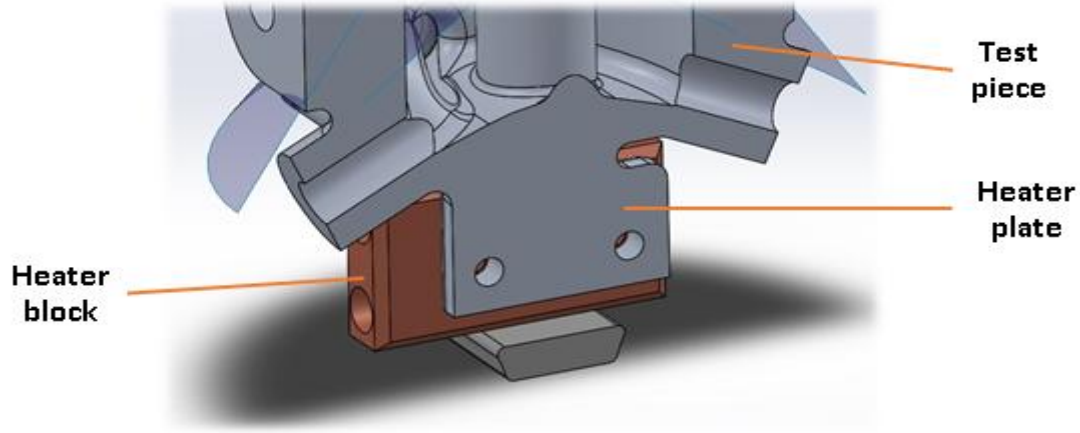

Figure 5.19: Cross sectional view of the heater plate and the heater block arrangement.

Each heater block had two electric cartridge heaters and each heater had a maximum power output of 170 W. An FEA was performed by one of the post-doctoral research fellows for the total maximum power output of 680 W from the four heaters. The heat flux and temperature plots from the analysis are given in figure 5.20 and 5.21.

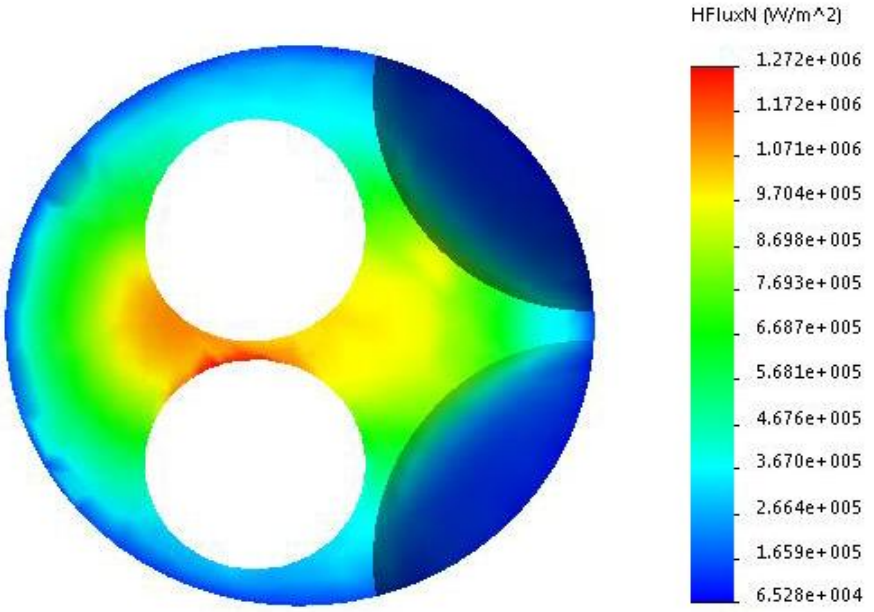

Figure 5.20: Heat flux distribution on the test surface.

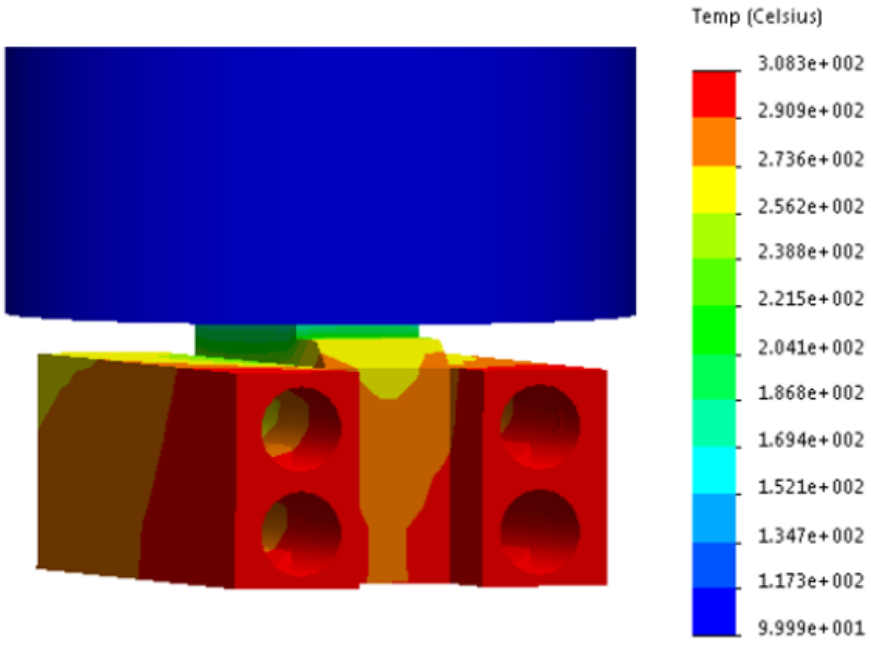

Figure 5.21: Temperature plot for the test piece and the heater block.

The results show that a heat flux of 1.27 MW/m^2 could be achieved at the critical areas of the test surface whilst only reaching a maximum temperature of 300 ^{o}C in the heater block. This design was modified into a single heater block owing to difficulties in assembly caused by differential thermal expansion. A dovetail design was used for easier assembly of the heater block onto the test piece. The design of the heater block used in the test rig is shown in figure 5.22.

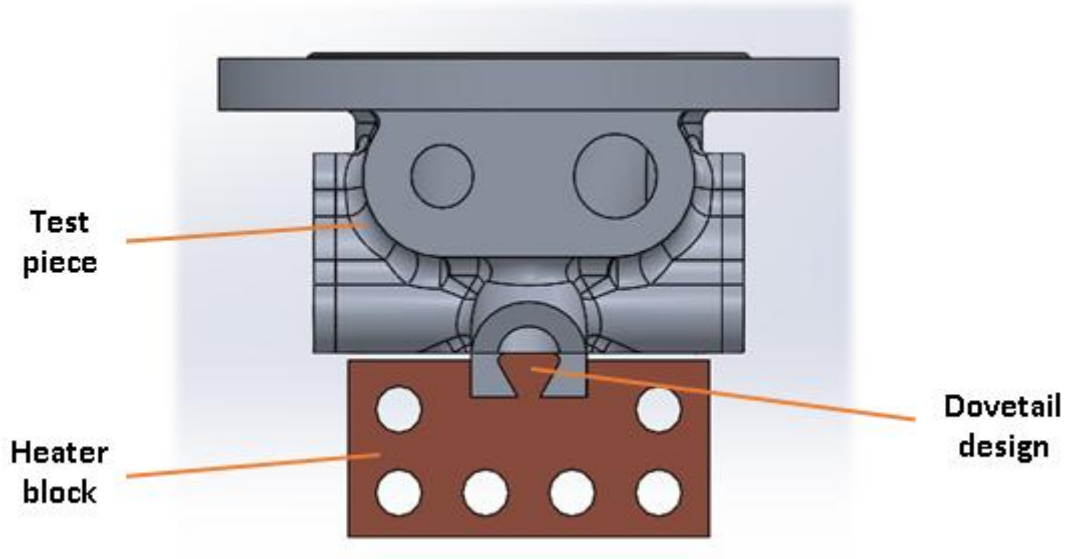

Figure 5.22: Heater block and test piece assembly showing the dovetail design.

The heater plate on the test piece was removed and a groove was cut into a dovetail shape to match the one on the heater block. Two retainers were used to secure the heater block on the test piece. The number of heaters were increased to six to increase the heat flux capabilities. And two heaters were also added into the sparkplug and injector bosses, making it a total of eight heaters. All the heaters had a maximum power output of 250 W each. A finite elements analysis was performed to identify the heat transfer as well as to find the stresses from the differential thermal expansion. The analysis was performed for a total heat power of 1000W whilst having a heat transfer coefficient of 40,000 W/m^{2}K with a coolant temperature of 120 ^{o}C on the test surface. A thermal contact resistance of 60 x 10^{-6} m^{2}K/W was applied between the mating surface of the heater block and the test piece. The results of the analysis are shown in the figures 5.23 – 5.25.

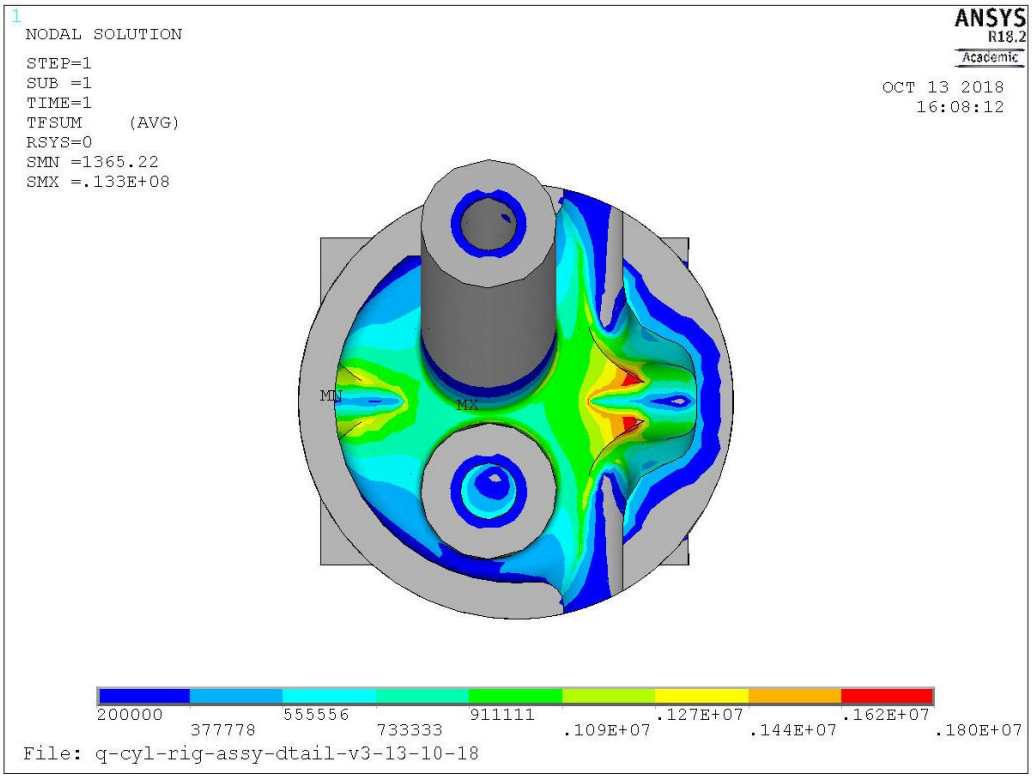

Figure 5.23: Heat flux distribution across the test surface.

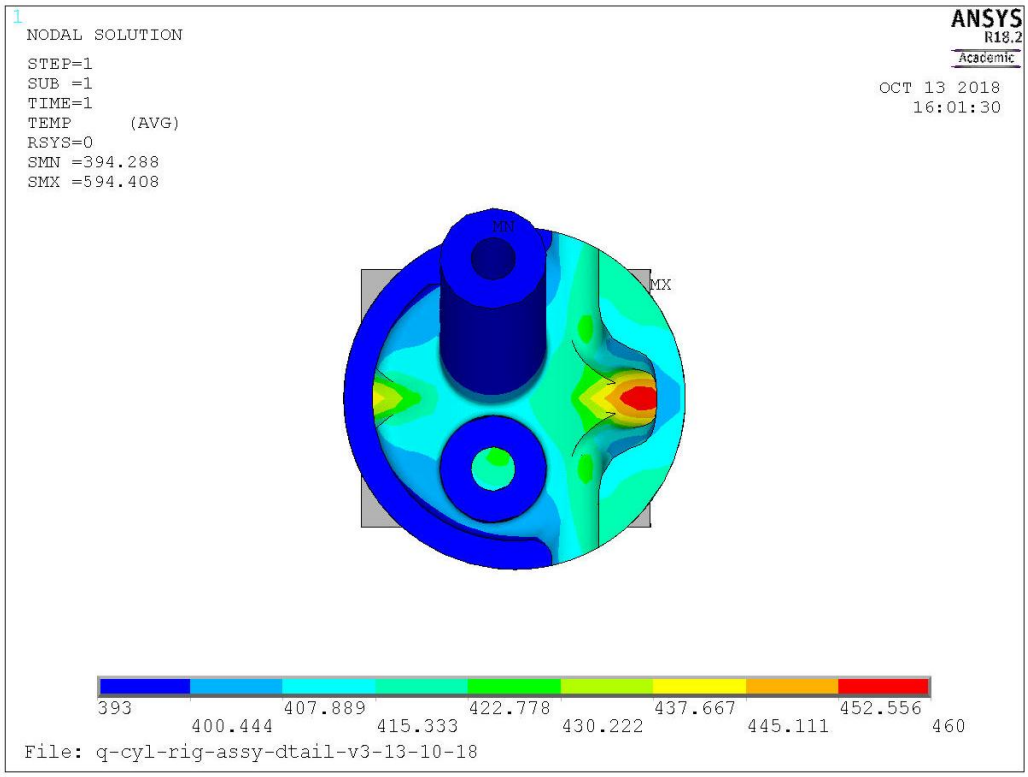

Figure 5.24 Temperature distribution across the test surface in K.

The heat flux plot shows a maximum heat flux of ~1.6 MW/m^2 on the outer regions of the test surface. In the centre region of the test surface, the heat flux was around 0.9 MW/m^2. These heat flux values were in the range required for experimenting most of the regimes in spray boiling. The temperature distribution plot shows that a minimum surface temperature of 150 ^{o}C could be achieved on the critical areas of the test surface. So, for a chamber pressure of 1 bar, an excess temperature of ~50 ^{o}C can be achieved, which is high enough to examine transition boiling regime experimentally.

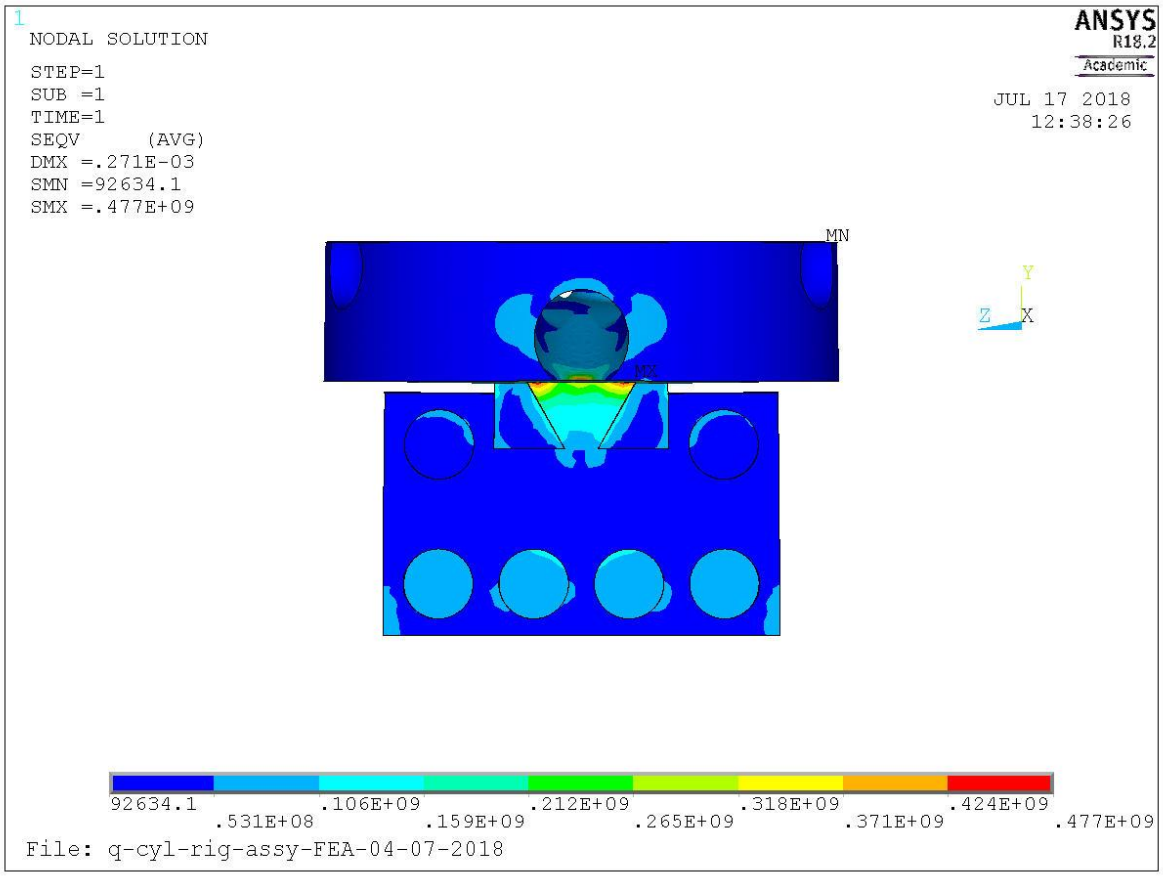

Figure 5.25: Von mises stress plot for the heater block and the test piece.

Differential thermal expansion caused very high stresses in the dovetail section of the copper heater block. High stresses could lead to failure of the structure especially when it is shaken at high frequencies and amplitudes. In order to avoid the possibility of stresses caused by differential thermal expansion, a cold clearance of 0.05 mm was created between the dovetail of the heater block and the groove of the test piece. This resulted in reducing the stresses to almost none as the dovetail and the groove just comes in to contact to each other when the heater block is heated up to the operating temperature.

5.4. Shaker, Condensation and Pumping Circuit, and Data Acquisition System

5.4.1. Shaker

A shaker from Bruel and Kjaer was chosen for inducing vibrating motion in the test piece. The shaker had a maximum trough to crest displacement of 25.4 mm with a vibrating frequency range of 5-6300 HZ. The range of amplitudes and frequencies were wide enough to cover the engine vibration amplitudes and frequencies of interest for the experiments. Specifications of the shaker is given in the Table 5.6.

Table 5.6: Bruel and Kjaer shaker specifications.

Shaker Model	V550
Armature diameter	110 mm
Maximum force - sine peak	667 N
Maximum acceleration – sine peak	675 m/s^2
Maximum velocity – sine peak	1.06 m/s
Shaker mass	97.5kg

5.4.2. The condensation and pumping circuit

The condensation and pumping circuit was designed to condense the steam generated from the test piece and to put the condensate back into the inlet through a pump. One of the requirements was to remove the steam generated whilst maintaining the pressure required inside the test chamber. The other important design objective was to provide the inlet with coolant at the required pressure and temperature. Figure 5.26 shows the condensation and pumping circuit diagram.

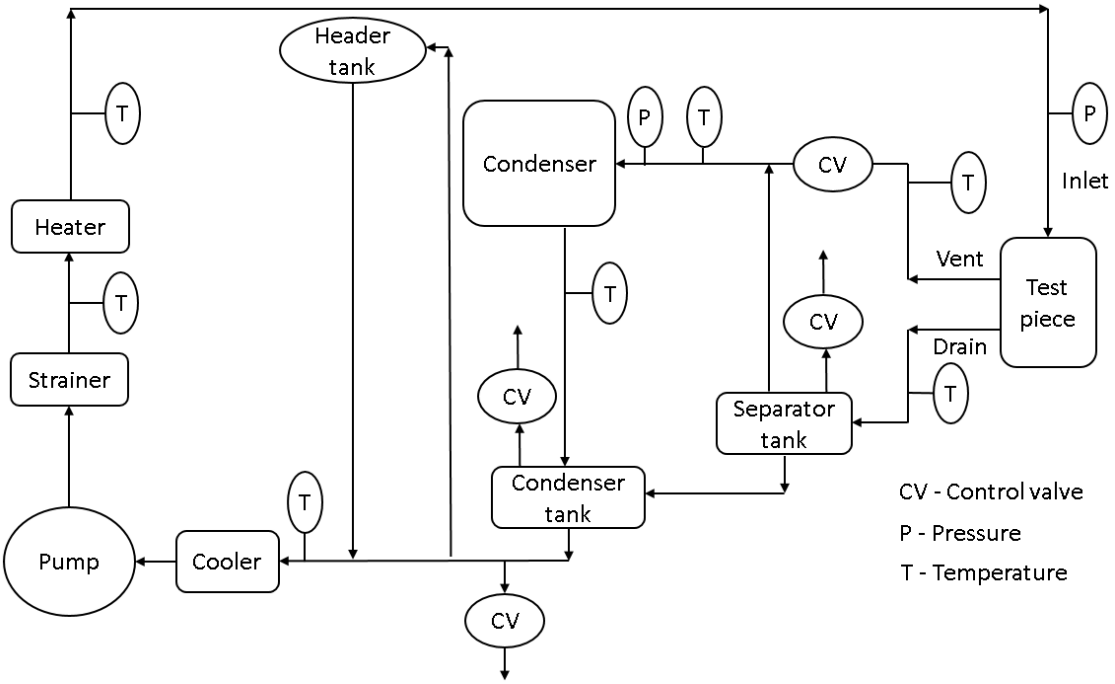

Figure 5.26: Condensation and pumping circuit diagram.

The steam generated from the test piece was taken out through the vent and passed to the condenser. A control valve was used to control the flow of steam going into the condenser. The temperature, before and after the control valve, was measured using temperature probes. A pressure gauge was used to monitor the pressure of the steam flowing into the condenser. On another channel, the drain from the test piece was collected by a separator tank, which separates steam and water. The separated steam was then sent to the condenser whereas the water was sent to the condenser tank in which the water gets mixed with the condensate from the condenser. A temperature probe was used to monitor the temperature of the condensate from the condenser. Control valves were fitted on top of the separator tank as well as the condenser tank to release pressure from these tanks if necessary. A control valve located at the lowest position of the circuit was used to fully drain the liquid from the circuit when required. In order to release any air trapped in the circuit, a header tank was used. To keep the temperature of the coolant entering the pump within the operating limits of the pump, a cooler was added to the circuit. The temperature of the coolant entering the cooler was monitored by a temperature probe. A strainer was used to filter out any large particles going into the inlet. A band heater was fitted in the circuit to heat the coolant to the required temperature before it goes into the inlet. Temperature probes were employed to measure the temperature before and after the heater. Finally, a pressure transducer measures the nozzle inlet pressure and the readings were used to control the pump speed to achieve the required inlet pressure.

5.4.3. Data Acquisition System

Data acquisition hardware from the National Instruments was selected to capture the data generated by the test-rigs. It was selected based on the temperature and pressure measurement requirements as well as the control requirements. The temperature and pressure measurement requirements was to acquire all the data produced by the thermocouples and the pressure transducers. The control requirements was to control the pump as well as the heaters if necessary.

The hardware selected was the National Instruments CompactRIO Controller which had eight slots for different modules. Only five modules were used: a.) Analogue input module b.) Analogue output module c.) Digital input/output module d.) Two temperature input modules. To save all the readings from the data acquisition hardware, NI LabView programs were created. The sampling for all the experiments was set at 1 Hz. The specifications of the CompactRIO Controller as well as the modules are given in table 5.7.

Table 5.7: Data acquisition system specifications.

Component Name	Specification
CompactRIO Controller, cRIO-9035	1.33 GHz dual core CPU, 1GB DRAM, 4 GB storage, and Kintex-7 70T FPGA 8-slot controller
Analogue input module, NI-9205	32-Channel, ±200 mV to ±10 V module
Analogue output module, NI-9264	16-Channel, ±10 V module
Digital input/output module, NI-9472	8-Channel, 6 V to 30 V module
Temperature input module, NI-9212 (x2)	8-Channel, ±78 mV module

5.5. Manufacture and Commissioning of the Test Rigs

5.5.1. Condensation and Pumping Circuit

Most of the items for the condensation and pumping circuit were bought in and assembled. The majority of the work was on plumbing. The pipes for plumbing were cut into the right shapes and sizes to fit the components in the circuit. Two pipe sizes were used: for gas channels, a pipe size of 3/8 inch was used whereas for the liquid channels a pipe size of 1/4 inch was used. The design of the plumbing, fitting arrangements and electrical arrangements, were completed by one of the research fellows and technicians from the University of Sussex workshop. Several items had to be manufactured at the university workshop to assist in fitting.

5.5.2. Static Pool Boiling Rig and Static Spray Boiling Test Rig

Most of the components were manufactured at the University of Sussex workshop. Tubing for the condensing coil along with the coil drawing was sent to a specialist company to bend it to the required shape. The rigs were assembled and commissioned by one of the research fellows and a technician from the university workshop. For both the static pool boiling rig and the static spray boiling rig, the main cylinder was pressure tested and also the heater block/test piece assembly was heated up to the operating temperature in each configuration before the test rigs were commissioned. Figures 5.27 and 5.28 show the commissioned static pool boiling rig and the static spray boiling rig.

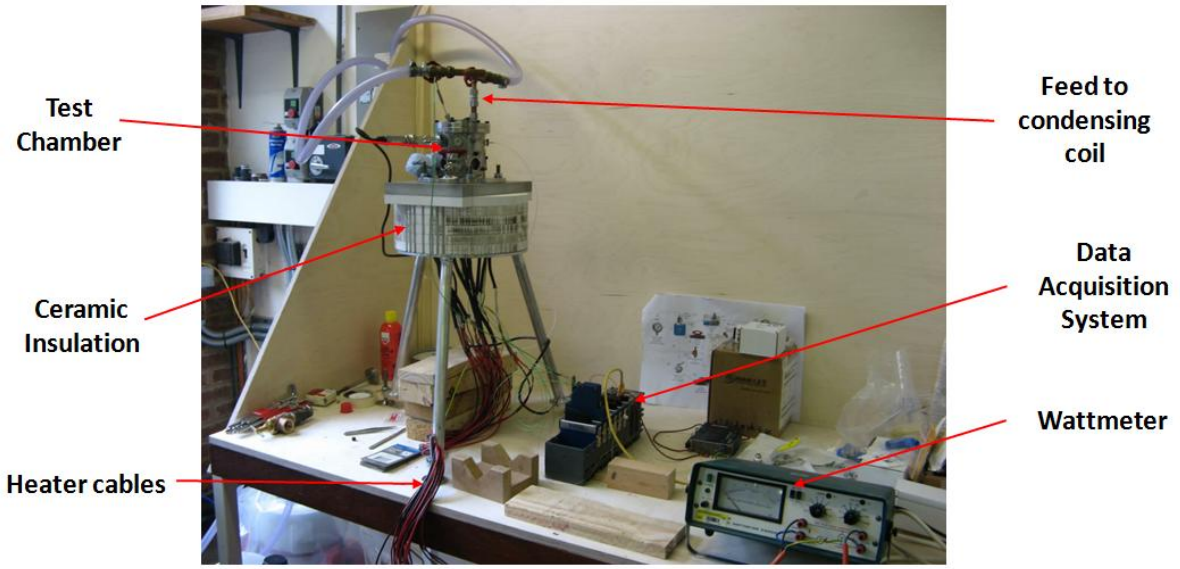

Figure 5.27: Static pool boiling rig.

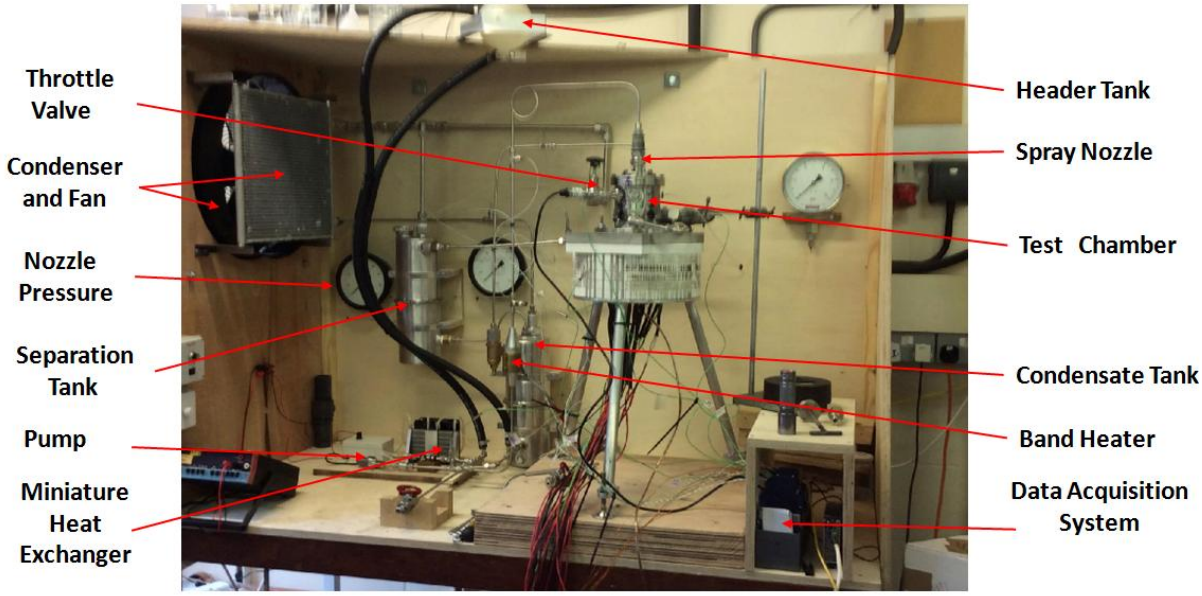

Figure 5.28: Static spray boiling rig with the condensation and pumping circuit.

5.5.3. Dynamic Flat Surface Test Piece

Majority of the components for the dynamic flat surface test piece was also manufactured at the University of Sussex workshop. The rigs were assembled and commissioned by the author, a research fellow, and another student working in the ECS project. The chamber was tested for leaks under both stationary and vibrating conditions. The test piece was heated up to the operating temperatures before the rig was commissioned. Figure 5.29 shows the commissioned dynamic test rig with the flat surface test piece.

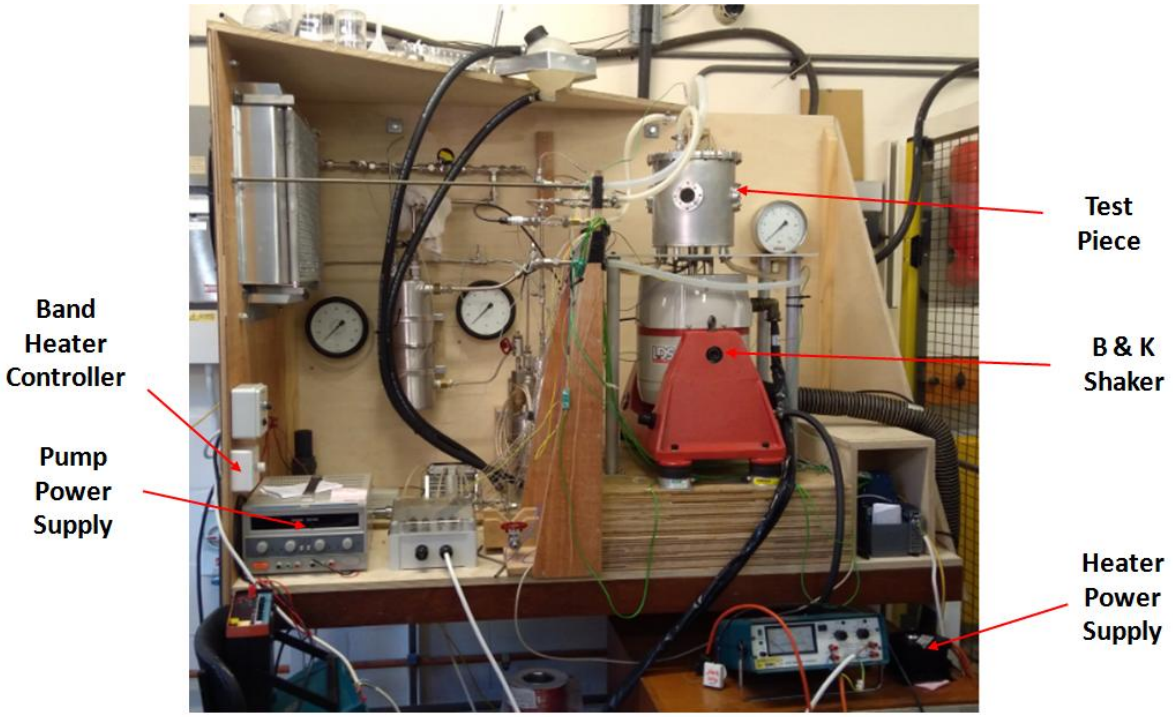

Figure 5.29: Dynamic rig with flat surface test piece.

5.5.4. Dynamic Cylinder-Head Geometry Test Piece

The cylinder-head geometry test piece was manufactured by casting at Ford, and the university workshop machined it to make provisions for fitting components. The rigs were assembled and commissioned by one of the research fellows and the technicians from the university workshop. The test piece was pressure tested and also heated up to the operating temperatures to check for any issues before it was commissioned. Figures 5.30 and 5.31 show the commissioned dynamic cylinder-head geometry test piece and the test piece/shaker assembly connected to the condensation and plumping circuit respectively.

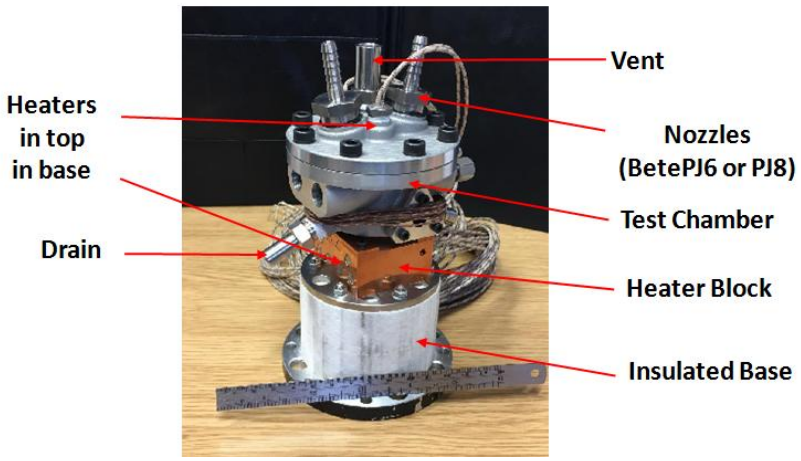

Figure: 5.30: Dynamic cylinder-head geometry test piece.

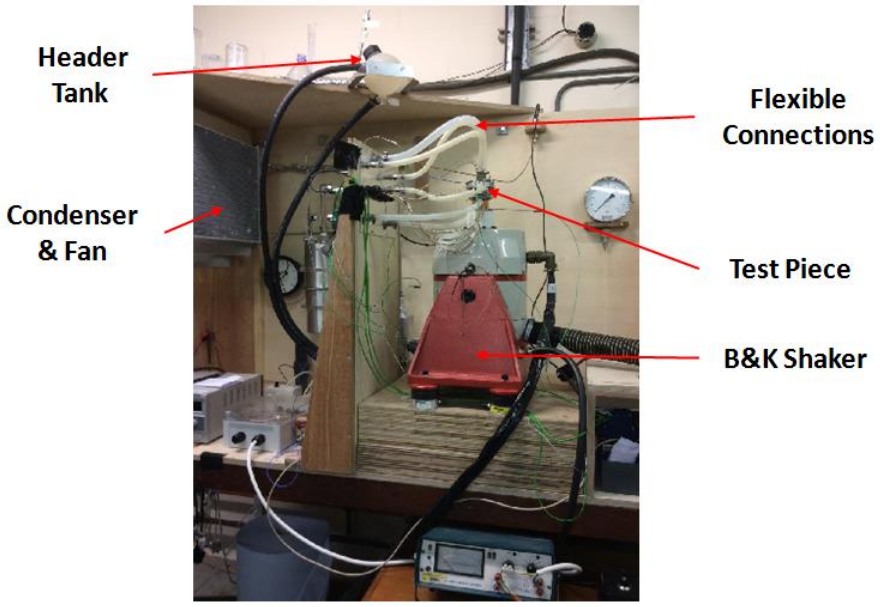

Figure 5.31: Dynamic test rig with the cylinder head geometry test piece.

5.6. Conclusion of chapter 5

Design of the static pool boiling rig, the static spray boiling rig, and the dynamic rig with the flat test piece and the cylinder-head geometry test piece were discussed. A more detailed description of the major components such as the test pieces and heater blocks along with the Finite Elements Analysis were provided. These designs met the objectives for testing static pool boiling and spray boiling heat transfer as well as the dynamic capability to test spray boiling heat transfer on moving boundaries for a flat test piece and a test piece representing the geometry of the engine cylinder-head. The next chapter provides the details of the experiments undertaken using these test rigs. A discussion of the results and the theories/correlations developed are also given in the chapter 6.

Chapter 6. TEST RIG EXPERIMENTAL RESULTS

This chapter presents the results from experiments conducted on the three different test-rigs. The first two being the static pool boiling rig and the static spray boiling rig, and the third one being the dynamic spray rig with two different test pieces. Both the static test rigs had flat test surfaces. The dynamic rig had one test piece with a flat surface and another one with geometries representing an engine cylinder-head coolant side.

The experiments from the static pool boiling rig, the static spray boiling rig, and the dynamic spray rig with engine cylinder-head geometry test piece were undertaken for the Evaporative Cooling Systems project and only selected results are presented here (but no analysis have been conducted). Only the dynamic spray rig experimental results with the flat surface test piece have been analysed.

The static pool boiling rig and the static spray boiling experiments were undertaken to meet the objective of gaining experience in taking measurements of pool and spray boiling heat transfer under stationary conditions, before moving on to dynamic tests. The dynamic rig experiments with the flat surface test piece was conducted to measure spray boiling heat transfer on moving boundaries using thermocouples at different heights in the test piece for calculating the heat flow. The cylinder-head geometry test piece could only collect one temperature measurement, just below the test surface, to identify how the metal temperature varies at different vibration amplitudes and frequencies. The metal temperature readings show whether the surface is sufficiently cooled and high increases in readings with respect to vibration show that heat transfer deteriorates.

6.1. Static Pool Boiling Experiments

The static pool boiling experiments were conducted to gain experience in taking temperature measurements for pool boiling heat transfer. Figure 6.1 shows the calculated heat flux as a function of excess temperature ($T_{wall} - T_{sat}$) for an experiment undertaken to collect temperature data for pool boiling with saturated liquid at a chamber pressure of 1 bar.

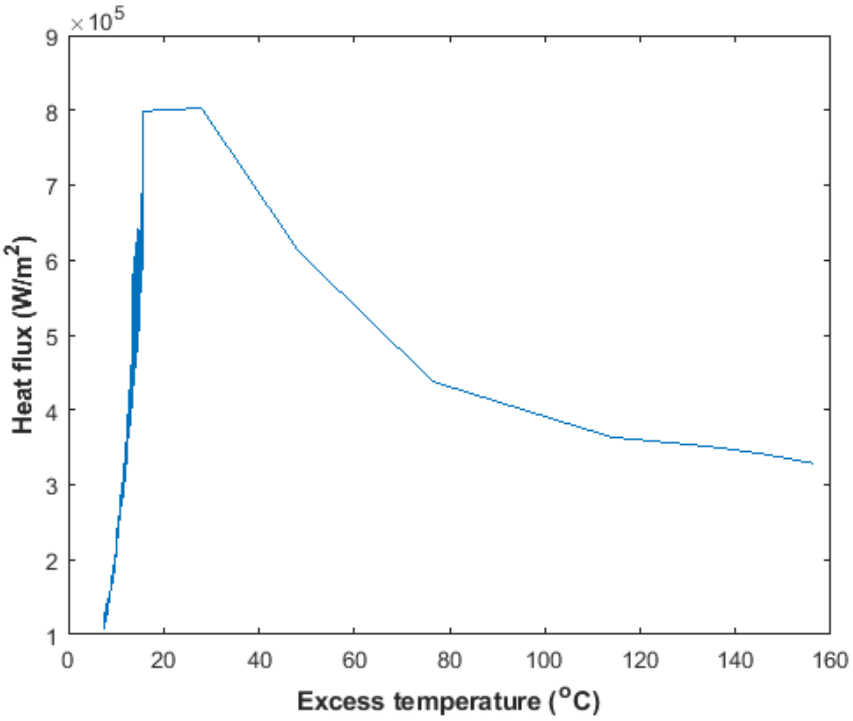

Figure 6.1: Pool boiling heat flux plotted as a function of excess temperature for coolant at saturation for a pressure of 1 bar.

Figure 6.1 shows a pool boiling curve which progresses through the incipient boiling regime, the nucleate boiling regime, and to some point into the transition boiling regime. The heat flux increases with excess temperature until it reaches a value of 0.8 MW/m^2 at an excess temperature of ~20 ^{o}C. This point marks the critical heat flux as the heat flux starts to decrease after this point with increasing excess temperature. The decreasing heat flux after an excess temperature of 20 ^{o}C shows that the boiling has now entered the transition boiling regime. The heat flux continues to decrease to ~0.3 MW/m^2 where the experiment was stopped when the excess temperature reached 160 ^{o}C. This experiment shows the rigs capability to conduct pool boiling experiments until at least critical heat flux.

6.2. Static Spray Boiling Experiments

The static spray boiling experiments were undertaken to gain experience in taking temperature measurements for spray boiling heat transfer. Figure 6.2 shows the calculated heat flux as a function of excess temperature for an experiment undertaken to collect temperature data at high heat flux values for a spray with a mass flow rate of 0.6 g/s. The coolant had a sub cooling of ~25 ^{o}C while the chamber pressure was 1 bar.

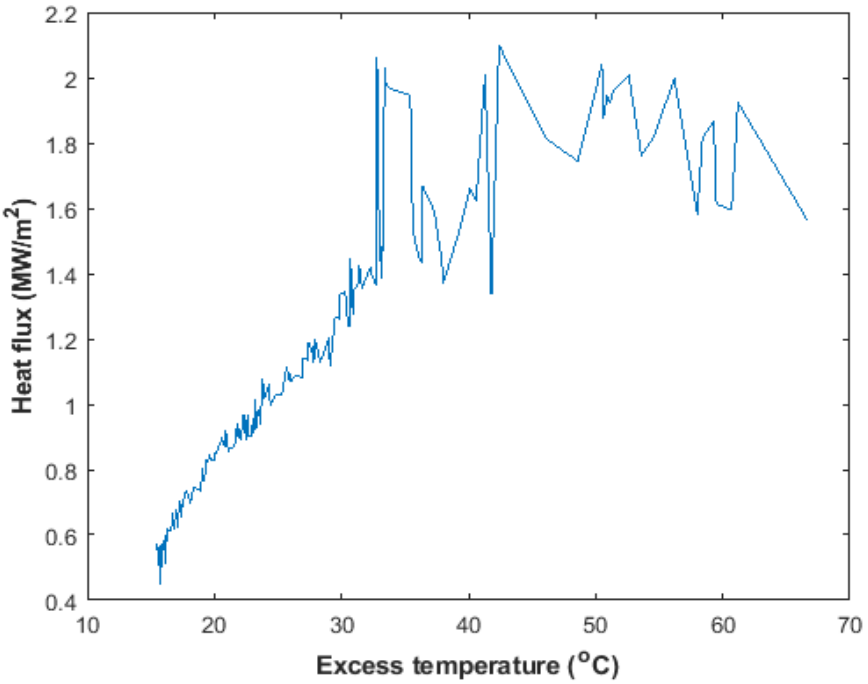

Figure 6.2: Spray boiling heat flux plotted as a function of excess temperature for a nozzle flow rate of 0.6 g/s.

Figure 6.2 shows that a maximum heat flux of just above 2 MW/m^2 could be achieved before it starts to deteriorate with further increase in excess temperature. This indicates that the critical heat flux has been reached before heat flux had started to deteriorate. The results from this experiment shows the test-rig's capability to run experiments for boiling at high temperatures, which is useful for collecting temperature measurements for critical heat flux.

6.3. Dynamic Spray Boiling Experiments

6.3.1. Flat Surface Test Piece Experiments

Flat surface test piece experiments were designed and conducted by the author to collect data for spray evaporative heat transfer for water as coolant on a flat vibrating surface. Using a flat test surface restricts the heat transfer to mostly one dimensional, which allowed the comparison of spray evaporative heat transfer between different vibration amplitudes and frequencies. To meet the main objective of finding the effect of boundary motion on spray evaporative heat transfer, the objective of performing the dynamic flat surface test piece experiments was to collect temperature measurements from different vertical locations of the test piece for different vibration cases for calculating the critical heat flux.

Flat surface test piece experiments were performed for spray impingement from a nozzle located above the test piece, perpendicular to the test surface. The nozzle was fixed to the test piece

assembly, which moved with the test piece when vibration was induced. Figure 6.3 shows the test piece and nozzle arrangement, as well as the direction of the motion of the assembly.

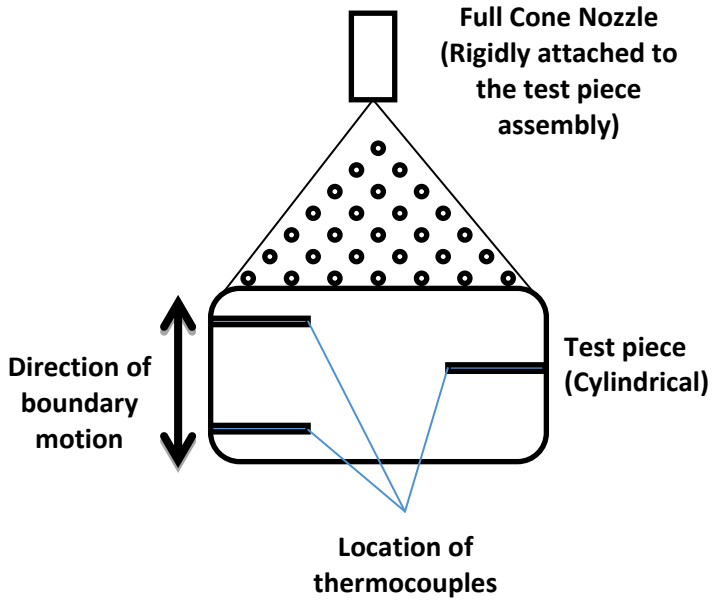

Figure 6.3: Schematic of the test piece and nozzle arrangement.

As shown schematically in figure 6.3, the full cone nozzle was positioned at a distance from the test surface, that is to achieve a 20 mm diameter path where the spray just covers the test surface. The nozzle used was a Bete PJ8 fine misting nozzle which produced a homogeneous fog with majority of droplets less than 50 microns in diameter [56]. A vertical sinusoidal motion was induced onto the test piece assembly by the shaker at the desired amplitude and frequency when required. The thermocouples were 5.5 mm apart vertically, the top one was 1 mm below the test surface. All the thermocouples were positioned 120^{o} around the axis of the cylindrical test piece, which were radially located at the centre between the axis and the outer surface of the test piece. This was to make sure that measurements were taken at similar heat flow paths as well as to minimise obstruction to vertical heat flow compared to the case where the thermocouples were situated on the same line vertically. The temperature measurements from thermocouples from top to bottom are referred to here as T1, T2 and T3 respectively.

6.3.1.1. Experimental Procedure

To collect temperature measurements for calculating the critical heat flux for a spray impinging on the test surface, the test piece had to be heated step-by-step above the saturation temperature until T1, T2 and T3 had the highest difference between them. Then the temperature gap between them started to decrease gradually whilst T1 was still increasing. The highest difference between T1, T2, and T3, and its reduction afterwards indicated that critical heat flux was achieved, and the boiling

was in the transition boiling regime [54]. The procedure of conducting experiments to collect the required temperature measurements are as follows:

All the controls on the test rig were manual. Therefore, achieving the required system temperatures, pressures and flow rates were crucial in the accuracy of the measurements. Before performing the experiments, it had to be ensured that the conditions inside the test chamber were the same for all the experiments to avoid them influencing the results. Initial test runs showed that the pressure and temperature inside the chamber tended to vary over the duration of the tests and were critical for the accuracy of results. It was intended to perform all the experiments at a chamber pressure equal to the atmospheric pressure and it was achieved by keeping the control valve on the condenser tank open to atmosphere. The temperature inside the chamber increased over the duration of the tests and reached a steady state once it was equal to the saturation temperature. To avoid the variation of chamber temperature during an experiment, the chamber was initially heated to saturation temperature by generating steam from water sprayed on sufficiently heated test piece for a certain amount of time.

If an experiment had to be performed at a certain coolant temperature, the coolant temperature had to reach a steady-state before performing the experiment. Similarly, the pump pressure had to reach a steady state for the time being if the experiment had to be performed at a particular flow rate which is determined by the pressure difference across the nozzle. Over the duration of tests, pump pressure varied very slowly over time due to the change in temperature of the coolant entering the pump. The temperature of the coolant entering the pump reached steady-state after few hours of testing. The thermal inertia of the condensation and pumping circuit was very high compared to the coolant flow rates involved, which resulted in very long times required for coolant temperature entering the pump to reach a complete steady state. Trial runs showed that it takes about half an hour to run an experiment to collect enough temperature measurements to calculate the critical heat flux. It was not therefore practical to reach the complete steady state of the pump inlet temperature for the first several experiments of an experimental session and the pump pressure had to be monitored and controlled over the duration of an experiment.

For an experiment with boundary motion, the test piece assembly was initially shaken at the desired vibration amplitude and frequency. Their values were monitored to check whether there were any variations. If the vibration amplitudes and frequencies were stable, the experiment could start.

At the beginning of the experiments, after achieving all the steady state system parameters, (such as the chamber pressure and temperature, the coolant temperature, and the pump pressure) the test piece heater power was set to a constant at a level required for the test surface temperature to

reach a steady state near to 120^{o}C. Only after this point, was data collected, and the heater power increased step by step until the boiling reached the transition boiling regime. After critical heat flux was achieved, the heater power was turned down to the initial steady state condition at the beginning of the data collection. Data was collected until the surface temperature had returned to the steady state temperature at the beginning of the data collection.

6.3.1.2. Details of Experiments

It was intended to run experiments for a maximum and minimum vibration amplitudes of 10 mm and 0.1 mm respectively for a minimum and maximum frequencies of 10 Hz and 1000 Hz respectively. The maximum stable vibration amplitude that was achievable for the minimum frequency of 10 Hz was 7 mm owing to the force limit by the shaker. The maximum stable vibration frequency measurable was around 400 Hz for an amplitude of 0.02 mm. Higher frequencies were not limited by the shaker but rather by the fact that accelerometer was unable to detect frequencies higher than 450 Hz even though it was specified to be capable of measuring up to 10 KHz. It is unclear what the cause for this was. It is possible that, as the accelerometer was glued to the test piece assembly, the connection was not stiff enough. Table 6.1 provides the range of possible combinations of vibration frequencies and amplitudes using the shaker and test piece arrangement for a frequency range of 10 Hz to 400 Hz. The cells shaded green were the combination of vibration amplitudes and frequencies selected for the experiments. The unshaded cells are the possible combination of vibration amplitudes and frequencies, which were not used for the experiments. The combination of vibration amplitudes and frequencies in the cells shaded red were not possible owing to the force limit by the shaker.

Table 6.1: Test matrix.

Frequency (Hz)	Amplitude (mm)	Amplitude (mm)	Amplitude (mm)	Amplitude (mm)	Amplitude (mm)	Amplitude (mm)	Amplitude (mm)
10	0.02	0.08	0.1	0.2	0.5	1	7
60	0.02	0.08	0.1	0.2	0.5	1	7
100	0.02	0.08	0.1	0.2	0.5	1	7
200	0.02	0.08	0.1	0.2	0.5	1	7
400	0.02	0.08	0.1	0.2	0.5	1	7

Two sets of experiments were undertaken for the selected combination of amplitudes and frequencies. Each set of experiments were for different sub-cooling levels of 5^{o}C and 15^{o} for the same coolant flow rate. Instead of repeating the same set of experiments to check repeatability, the

two different sub cooling levels were used to check if the trends in heat transfer were similar for the same set of amplitudes and frequencies. All the experiments were performed for a pressure difference (ΔP) of 4 bar across the nozzle. The 4 bar ΔP produced a flow rate of 51.8 cc/min. The ΔP had a tolerance of ± 0.1 bar which resulted in a flow rate tolerance of 0.00082 cc/min. The coolant temperature had a tolerance of ± 1.5 ^{o}C. The nozzle had a specified full cone angle of 90^{o} at a ΔP of 4.0 bar, but it did have small fluctuations, which could stem from slightly fluctuating pump pressure. The nozzle height was increased by several millimetres to make sure the spray always covered the test surface. When all the spray were impinging on the test surface, it had a volumetric flux of 0.00275 $m^3/s/m^2$. The droplet velocity could not be accurately calculated owing to the special design of the nozzle. The nozzle had a hook like structure at the outlet where the liquid first impinges vertically upwards on a surface then falls back forming a full cone fog spray. Figure 6.4 shows a photograph of the nozzle.

Figure 6.4: Bete PJ series full cone fog nozzle [56]**.**

The droplet velocity was approximated to be 28.8 m/s using the inviscid equation $\sqrt{2\Delta P/\rho}$ [26] for calculating the velocity at the orifice exit (assuming the droplets rebounding downwards as a full cone fog had the same velocity). It is possible that the real velocity of the droplet could be different from calculated value.

In order to establish the effect of moving boundary on spray evaporative heat transfer, experiments were first performed for stationary boundary for the two different sub cooling levels, as the base cases. The required heater power for the initial test surface temperature to be near to 120 ^{o}C was identified to be 300 W for the stationary cases. It was used as the initial heater power for all the experiments. All the data was collected at a sample rate of 1 Hz for all the experiments. The details of two sets of experiments performed for different amplitudes and frequencies are given in table 6.2.

The experiments F7 and G7 were supposed to be conducted at a frequency of 60 Hz but the amplitude was unstable and the frequency had to be reduced to 53.7 Hz for the vibration to be stable. The unstable vibration was due to the shaker reaching its force limit.

Table 6.2: Details of dynamic flat surface test piece spray boiling experiments.

Experiment No.	Spray volumetric flux ($m^3/s/m^2$)	Coolant temperature (^oC)	Vibration amplitude (mm)	Vibration frequency (Hz)
F1 G1	0.00275	95 85	Stationary	Stationary
F2 G2	0.00275	95 85	0.02	400
F3 G3	0.00275	95 85	0.08	200
F4 G4	0.00275	95 85	0.1	100
F5 G5	0.00275	95 85	0.2	60
F6 G6	0.00275	95 85	0.5	60
F7 G7	0.00275	95 85	1	53.7
F8 G8	0.00275	95 85	0.1	10
F9 G9	0.00275	95 85	1	10
F10 G10	0.00275	95 85	7	10

6.3.1.3. Results and Discussion

First, the test piece temperatures and heat flux were plotted for the stationary test piece experiments for the two sub cooling levels. To calculate the heat flux, the one-dimensional conduction equation was used. The one-dimensional conduction is

$$q = -K\frac{dT}{dx} \tag{6.1}$$

where K is the thermal conductivity, dT is the temperature difference, and dx is the distance between two points for which the temperature difference is calculated. A material thermal

conductivity of 385 W/mK was used for the calculations. The instantaneous heat flux was calculated using the temperature difference between the measured T1 and T2. For the experiments F1 and G1, plot of measured temperatures T1, T2, and T3 and the calculated heat flux are given in figure 6.5 and 6.6 respectively.

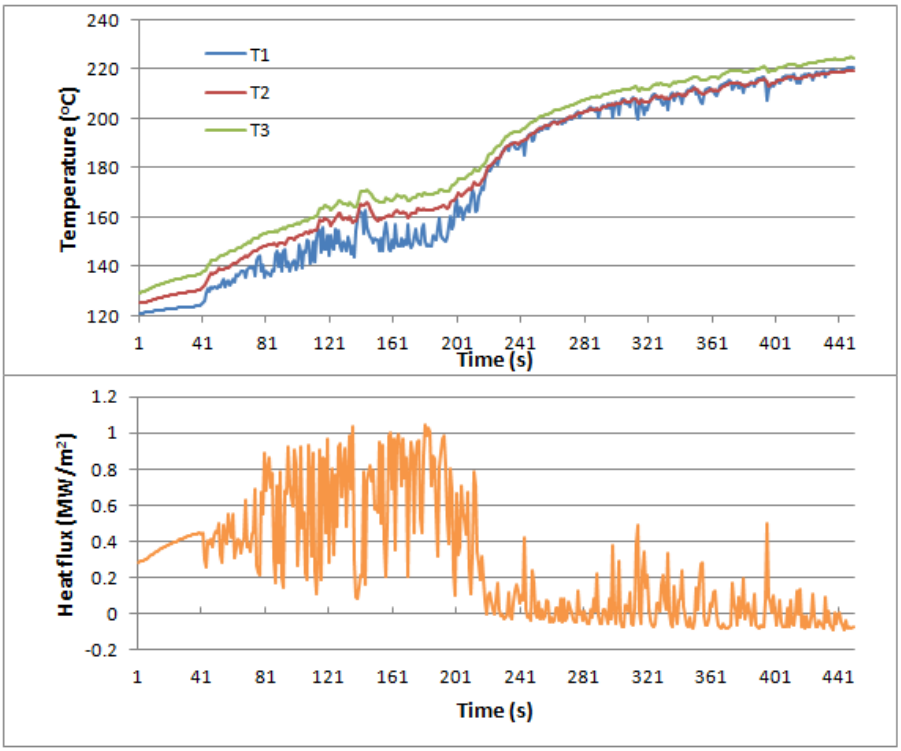

Figure 6.5: Measured test piece temperatures (top) and the heat flux calculated for the stationary test piece experiment at 5 °C sub-cooling (bottom)

The temperature in figure 6.5 shows that the surface temperature (T1) was initially steadily increasing and then started to fluctuate after its value went above ~130 °C. This suggests that the boiling process was initially in the nucleate boiling regime with isolated bubble generation until it reached the excess temperature of ~30 °C [54]. Further increase in the surface temperature resulted in fluctuating temperatures which could be the result of the more violent slug flow in the nucleate boiling regime. Because the sub cooling was only 5 °C, another reason could be all the water that was being sprayed evaporated quickly creating intermittent vapour blanketing of very short periods owing to the not-so-high excess temperature. At a surface temperature of ~150 °C, the difference between the temperatures were at the maximum and then the gap suddenly started to diminish. This indicates that the critical heat flux was achieved and the boiling was moving onto transition boiling regime. At the excess temperature of 180 °C, T1 and T2 had converged to each other which showed that the Leidenfrost temperature had been reached and the boiling was entering the film boiling region [54].

Figure 6.6 shows that the heat flux starts to fluctuate with the surface temperature as it was directly calculated from the difference in temperature at two points a certain distance apart. But, in reality the thermal diffusivity of the material would smooth out the fluctuations. Similarly, when boiling is in the film boiling regime, the calculated heat flux had negative values which in reality is not possible as the test surface is at a much higher temperature than the coolant. This showed that calculating the heat flux using the instantaneous temperature results in very large errors under transient conditions and the solution of one-dimensional transient conduction was required to analyse the data.

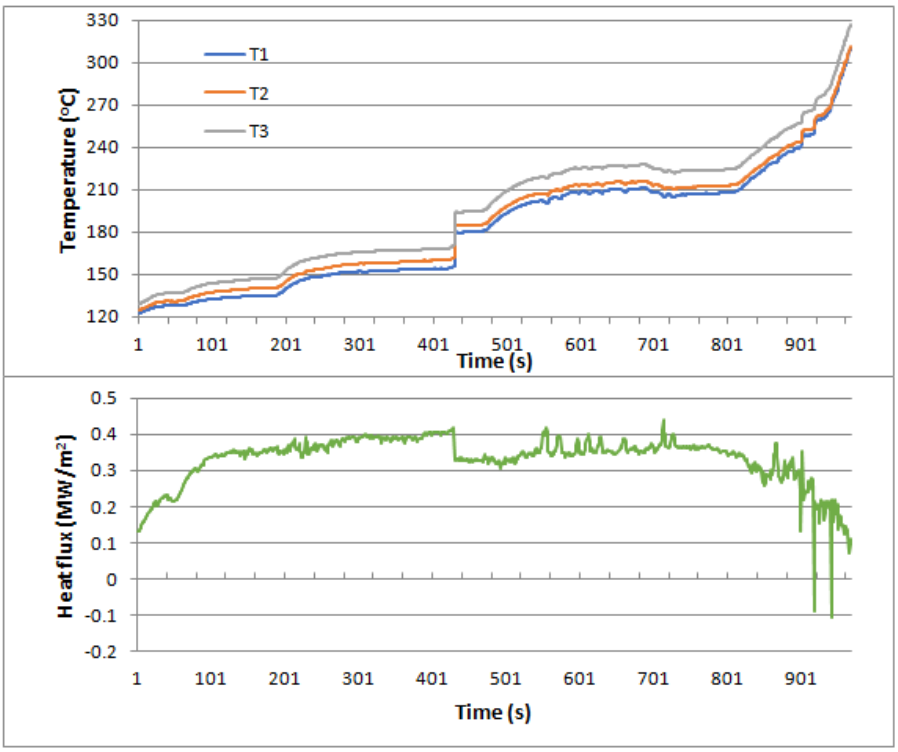

Figure 6.6: Measured test piece temperatures (top) and the heat flux calculated from it for the experiment at 15 °C sub-cooling (bottom).

It can be seen from both the temperature and heat flux plots on the figure 6.6, at a time near to 430 s, there is a step on the temperature measurements as well as the calculated heat flux. Some temperature measurements had to be removed from the 15 °C sub cooling data because temperatures were decreasing even though the heater power was increasing. What was causing this is unknown. After some time, the temperature came back to the point where it started to reduce. The temperatures from this point is then joined to where it was stopped. That's why there is a step in temperatures and heat flux in figure 6.6 at a time of 401 s. The temperature measurements from the stationary test piece experiment with 15 °C sub cooling, was smoother compared to the

experiment with 5 ^{o}C sub cooling. It could be due to the greater time it takes to add sensible heat to the liquid to raise its temperature to the boiling point. The only unstable boiling was seen after the critical heat flux had been reached and the boiling was in the transition boiling regime. This was evident from the heat flux reaching the highest point and then a sudden decrease with increasing surface temperature. This was also confirmed by the sudden increase in the test piece temperatures and, by T1 and T2 converging to each other. Again, towards the end of the heat flux plot, it could be seen that the heat flux going negative few times. Therefore, a solution to the transient one-dimensional conduction equation was required to analyse the data.

A Matlab code (written by one of the research fellows involved on the EPSRC funded project) utilising a numerical solution to the one-dimensional transient heat conduction equation was used to analyse the transient temperature measurement data generated by the experiments. The numerical method is the same as the one in Chapter 3 which was used for calculating the transient heat conduction through the cylinder head wall except that the boundary conditions here are the measured temperatures instead of the heat transfer coefficients and the fluid temperatures. The numerical method is however reviewed here, with some information specific to the data analysis problem.

The numerical solution uses the finite difference method to approximate the temperature at different points across the thickness of a material by using discrete time steps. For this, the thickness of the material had to be spatially discretised into nodes. The approximation to the Fourier's one-dimensional transient conduction equation was then used to calculate the temperature at each node for each time step. The Fourier's one dimensional transient conduction equation is given as [66].

$$\frac{\partial^2 T}{\partial x^2} = \frac{1}{\alpha}\frac{\partial T}{\partial t} \tag{6.2}$$

where T is the temperature, x is the position, $\alpha = {}^{K}/_{\rho C_p}$ is the thermal diffusivity, and t is the time. The values of ρ and C_p were 8900 kg/m^3 and 395 J/kg K respectively. Spatial derivative on the LHS, and the temporal derivative on the RHS, could be approximated in equation (6.2) to obtain the following form:

$$\frac{T_{(i+1)}^{(n)} - 2T_{(i)}^{(n)} + T_{(i-1)}^{(n)}}{\delta x^2} = \frac{T_{(i)}^{(n+1)} - T_{(i)}^{(n)}}{\alpha \delta T} \tag{6.3}$$

in which the subscript '*I*' stands for the current grid point and '*i-1*' and '*i+1*' are the grid points before and after the grid point *i* respectively. The superscript '*n*' stands for the current time step, and '*n+1*' stands for the following time step. Rearranging equation (6.3) gives the solution for calculating temperature at the interior grid points.

$$T_{(i)}^{(n+1)} = \delta Fo.T_{(i+1)}^{(n)} + (1 - 2\delta Fo)T_{(i)}^{(n)} + \delta Fo.T_{(i-1)}^{(n)} \quad (6.4)$$

where $\delta Fo = {}^{\alpha\delta t}/_{\delta x^2}$ is the Fourier number in which δt is the time step size, and δx is the distance between the grid points. In order to achieve accurate results, two stability criteria need to be met, which are

$$\delta Fo(1 + \delta Bi) < 0.5 \quad (6.5)$$

and

$$\delta t < \frac{0.5\ \delta x^2}{\alpha\left(1 + {}^{\delta xh}/_{k}\right)} \quad (6.6)$$

where $\delta Bi = {}^{\delta xh}/_{k}$ is the Biot number. Based on the stability criteria, the distance between the first and third thermocouple was split into 22 nodes which gave a δx of ~5.24 x 10^{-4} m and the δt was set as 0.0004 s. As the time-step was much smaller than the sampling rate, the boundary temperatures, T1 and T3, had to be interpolated between the measured temperatures. Piecewise polynomials were used to interpolate the measured temperatures.

To calculate the heat flux at an instance, the surface temperature gradient $\nabla T = {}^{\partial T}/_{\partial x}$ was calculated using a second-order backward difference scheme in the following form.

$$\frac{\partial T}{\partial x} \approx \frac{3T_i - 4T_{i-1} + T_{i-2}}{2\ \delta x} \quad (6.7)$$

Using the numerical solution method described, the heat flux, q, along with the excess temperature, ΔTex, were first plotted for the experiment F1 where the test surface was stationary and the coolant was at a sub cooling temperature of 5 ^{o}C. A sampling rate at which the data is sampled could be specified in the Matlab code and it was set at one per measured temperature points. The heat flux and the excess temperature were plotted in order to identify the critical heat flux. The heat flux,

and the excess temperature, plotted for a sampling rate of one per measured temperature points for the experiment F1, are shown in figure 6.7.

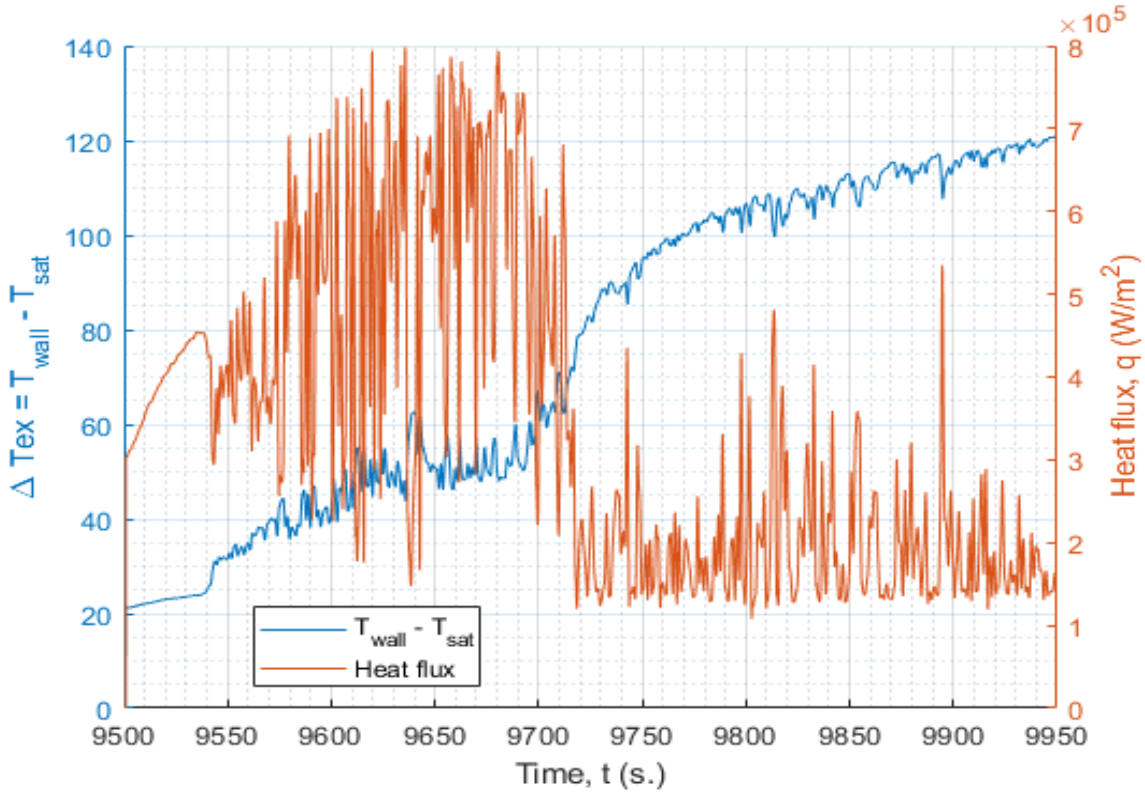

Figure 6.7: Heat flux and excess temperature plot with respect to time for the experiment F1 with a sampling rate of one per measured temperature points.

From the heat flux shown in figure 6.7, it can be seen that the critical heat flux occurred at some point between the experiment time of 9620 s and 9680 s, as the fluctuating heat flux during that period had the highest values before gradually reducing with respect to increasing excess temperature. But it is unclear where exactly the critical heat flux occurs. Another heat flux and excess temperature plot was generated for a sampling rate of one per five measured temperature points. The reduced sampling rate reduced the frequency of fluctuating heat flux with respect to time as the heat flux was plotted using the interpolated temperatures between the points at which the measured temperature was sampled. Figure 6.8 shows the plot of heat flux for the experiment F1 with a sample rate of one per five measured temperature points.

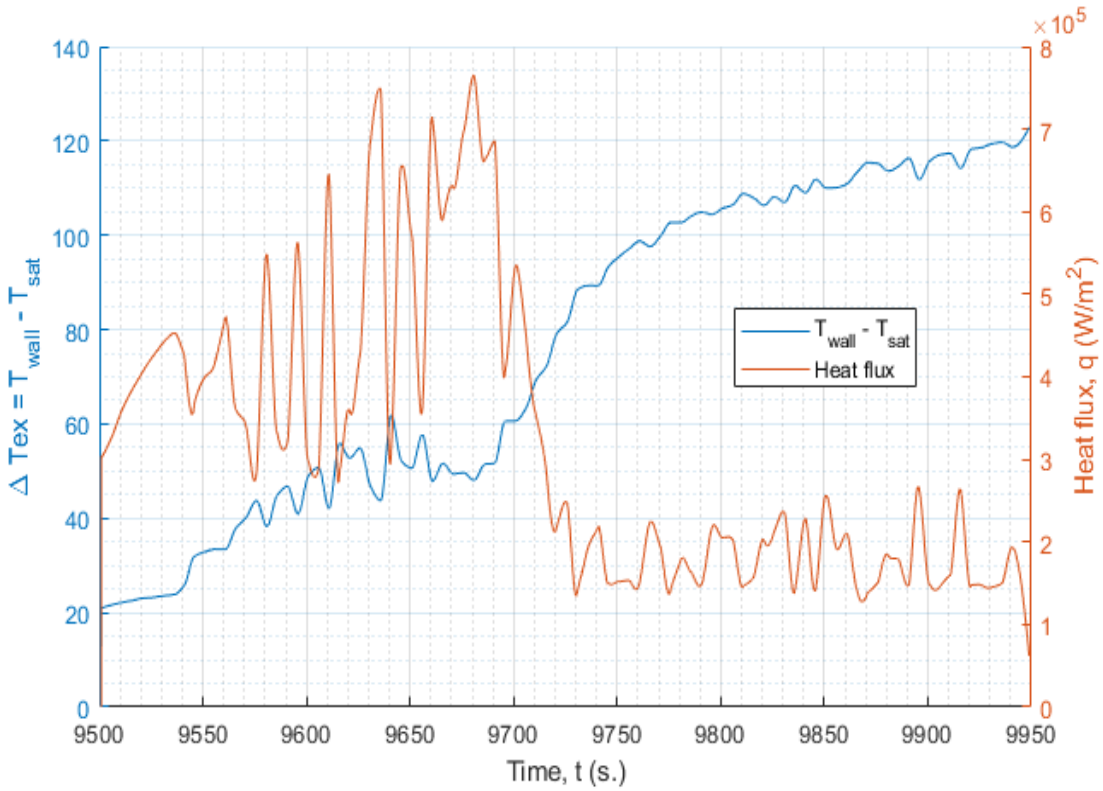

Figure 6.8: Heat flux and excess temperature plot with respect to time for the experiment F1 with a sampling rate of one per five measured temperature points.

From the heat flux shown in figure 6.8, the critical heat flux could be more easily identified as the heat flux gradually increased to a maximum and then suddenly starting to decrease with increasing excess temperature. The critical heat flux was identified as the maximum heat flux value before the heat flux started to decrease with increasing excess temperature. To support this finding, the temperature plot for all the test piece temperature measurements at a sampling rate of one per measured temperature points for the experiment F1 are given in figure 6.9.

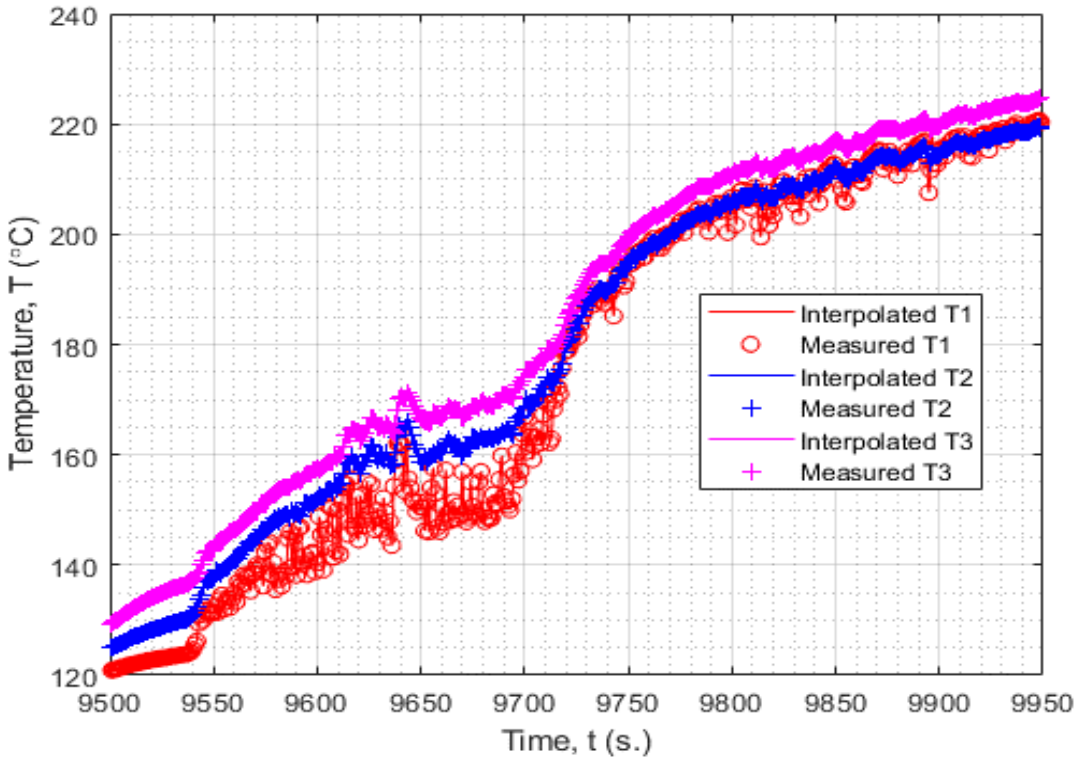

Figure 6.9: Plot of the test piece temperature measurements for the experiment F1 with a sampling rate of one per measured temperature points.

It could be seen from the figure 6.9 that between experiment times of 9660 s and 9690 s, the difference between T1, T2, and T3 was at the highest value before the difference between T1, T2, and T3 started to quickly reduce with rapid increase in temperatures. Again, this was indicating that the critical heat flux was achieved and the boiling moved onto the transition boiling regime.

Similarly, the critical heat flux for the experiment G1 (stationary test surface with coolant sub cooling of 15 ^{o}C) was identified by showing the heat flux and the excess temperature at a sampling rate of one per five measured temperature points. Plot of the heat flux and the excess temperature with respect to time for a sampling rate of one per five measured temperature points is shown in figure 6.10.

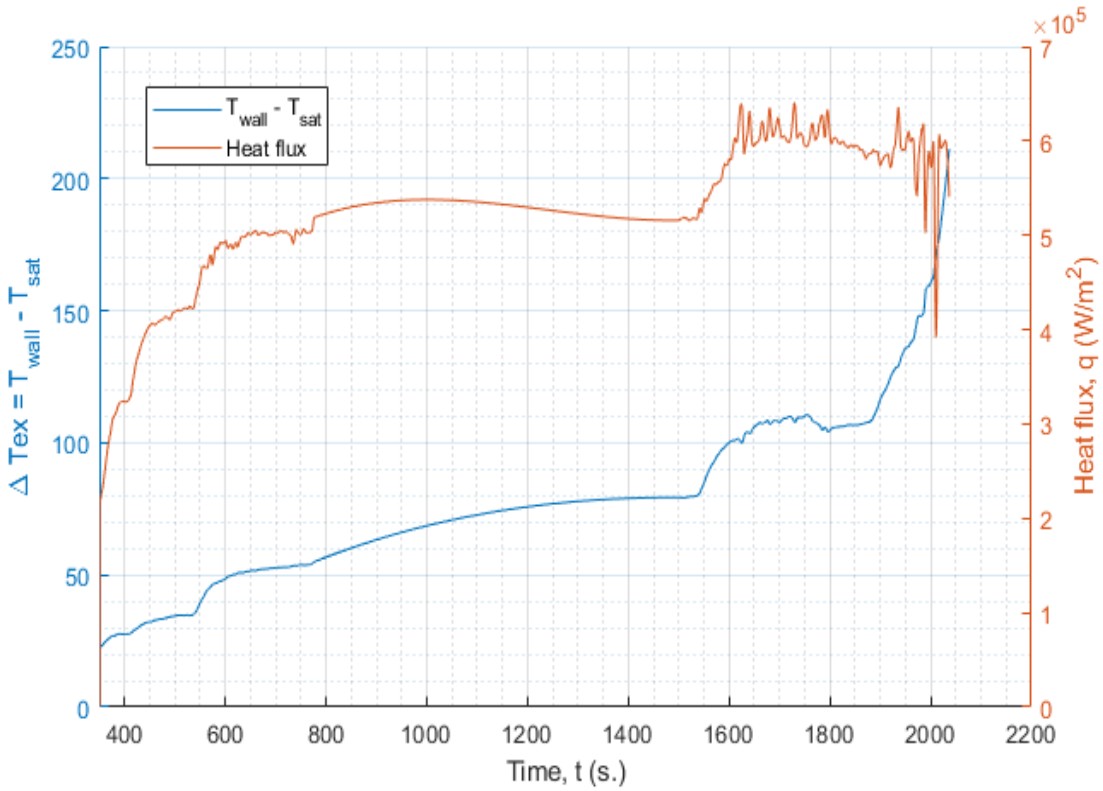

Figure 6.10: Heat flux and excess temperature plot with respect to time for the experiment G1 with a sampling rate of one per five measured temperature points.

During the experiment G1, between the experiment time of 800 s and 1500 s, the test piece temperatures were unstable, which were largely decreasing and increasing over time, instead of the expected increase over time with increasing heater power. The cause for this could not be identified as all the other parameters were at the expected levels. The temperature measurement data between 80 s and 1500 s were removed and interpolated using the numerical scheme. The heat flux in figure 6.10 shows that the highest heat flux values were between the experiment time of 1600 s and 1800 s. Even though the excess temperature reduced after 1750 s and then started to increase again near to 1900 s, the heat flux started to fluctuate when the excess temperature was higher than the excess temperature at the stage where the highest heat flux values occurred. After approximately 1900 s, the excess temperature started to rapidly increase with decreasing heat flux, which indicated that the boiling was entering the transition boiling regime. Again, a plot of the test piece temperature measurements at a sampling rate of one per measured temperature point is used to confirm the findings. The plot of the test piece temperature measurements at a sampling rate of one per measured temperature points for the experiment G1 is shown in figure 6.11.

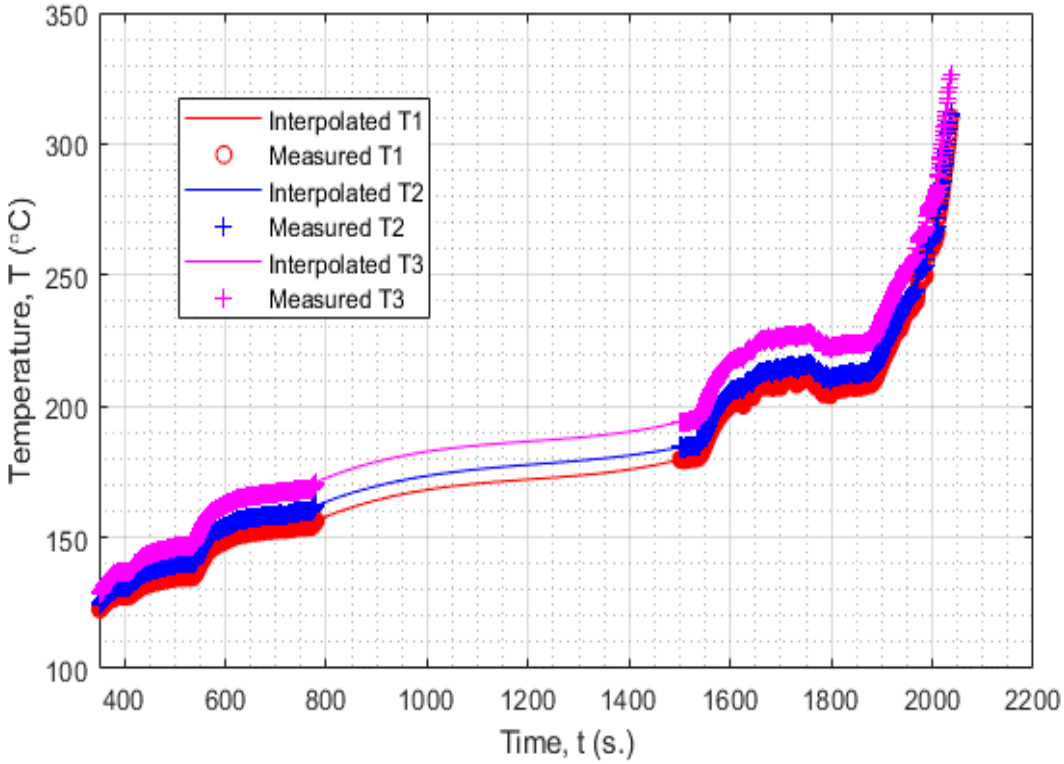

Figure 6.11: Test piece temperature measurements for the experiment G1 with a sampling rate of one per measured temperature points.

The critical heat flux along with the excess temperature at which it occurred were identified for all the experiments using the same method employed to calculate the critical heat flux for stationary experiments. The only exception was that, for the experiments with a test piece vibration amplitude of 7 mm, a distinct region of high heat flux, followed by decreasing heat flux values could not be identified. Heat flux and excess temperature plots for both the experiments, experiments F10 and G10, are given in figures 6.12 and 6.13 respectively and these were plotted for a sampling rate of one per five measured temperature points.

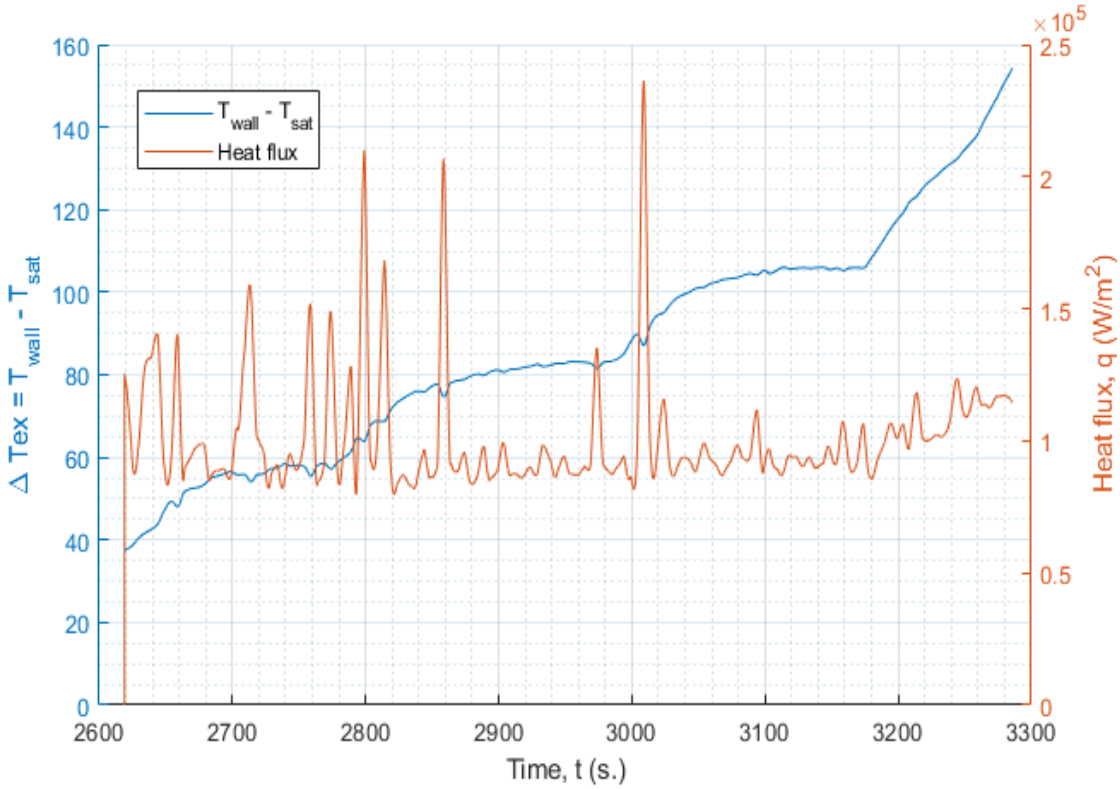

Figure 6.12: Heat flux and excess temperature for the experiment with test surface vibration amplitude of 7 mm at a coolant sub-cooling of 5 °C for a sampling rate of one per five measured temperature points.

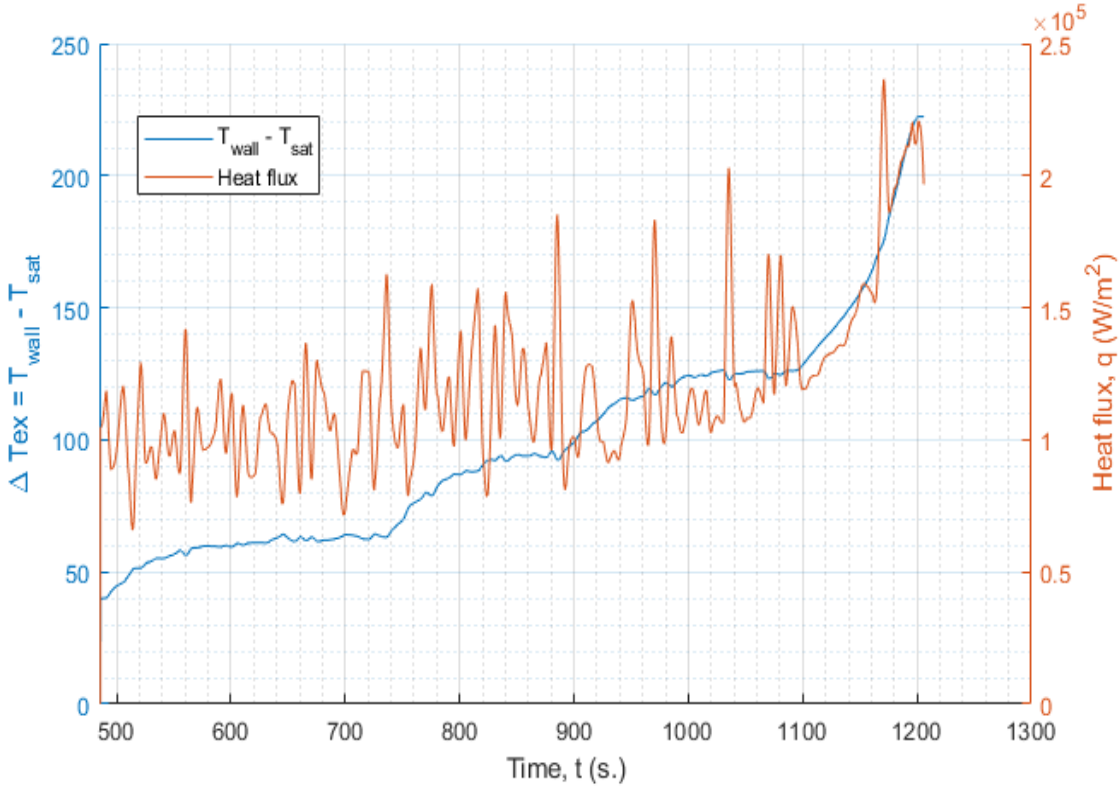

Figure 6.13: Heat flux and excess temperature plot for the experiment with test surface vibration amplitude of 7mm at a coolant sub-cooling of 15 °C for a sampling rate of one per five measured temperature points.

As can be seen from the heat flux shown in figure 6.12 and figure 6.13, a distinct region of transition between nucleate boiling and transition boiling was not found. Also, the heat fluxes were constantly fluctuating until a certain excess temperature had been reached, where the amplitudes of the fluctuations had reduced and the heat fluxes had started to increase with increasing excess temperature. To examine the transient nature of these fluctuations, the heat fluxes and excess temperatures are shown in figure 6.14 and 6.15 for experiments F10 and G10, plotted at a sampling rate of one per measured temperature points.

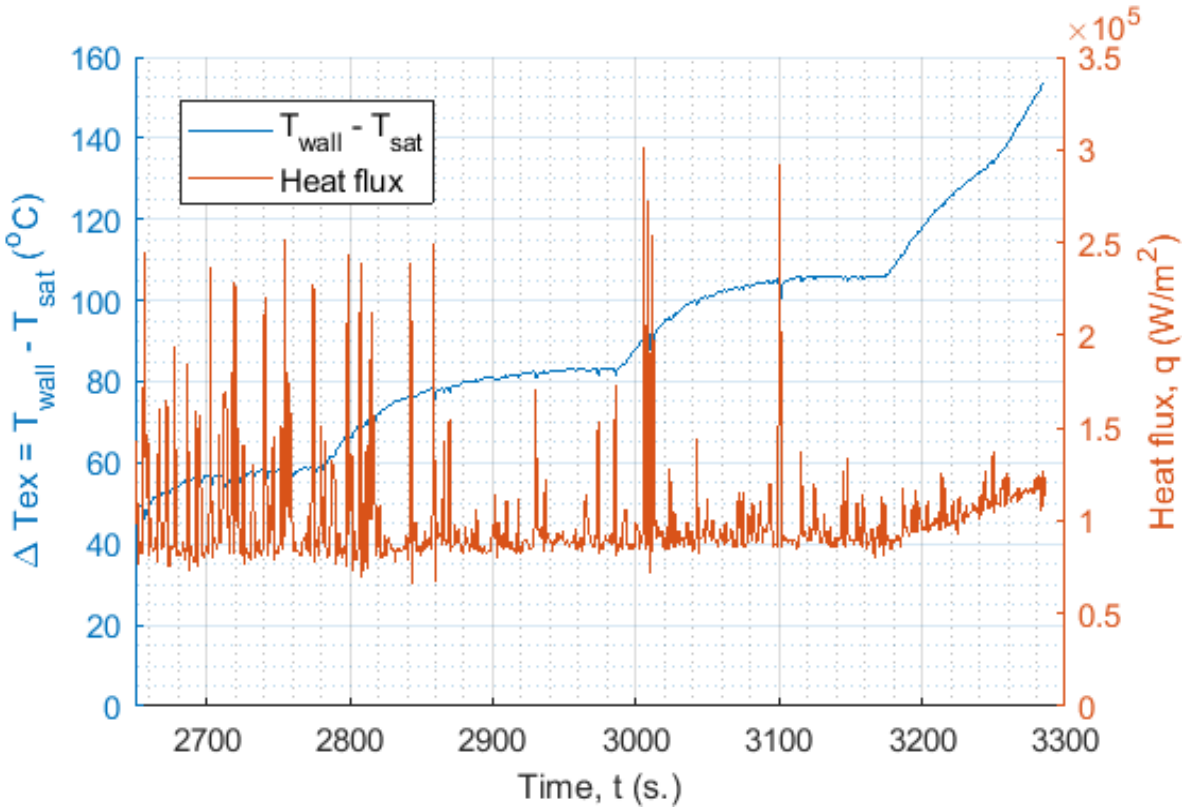

Figure 6.14: Heat flux and excess temperature for the experiment with test surface vibration amplitude of 7 mm at a coolant sub cooling of 5 ^{o}C for a sampling rate of one per measured temperature points.

The heat flux and excess temperature shown in figure 6.14 indicate the more transient nature of heat transfer owing to the increased data sampling rate. Even though it is difficult to identify the boiling regimes, it can be seen that the initial fluctuations in heat flux reached peak values, which are sustained for a small duration between 3000 s and 3020 s before gradually reducing to much smaller values. Except the spike at 3100 s, the heat flux values stay low until the excess temperature started to increase rapidly after approximately 3180 s, where the heat flux starts to increase slightly with respect to the excess temperature. It can be therefore said that the critical heat flux is achieved before 3020 s, i.e. before the boiling seemingly enters the transition boiling regime. The highest peak value between 3000 s and 3020 s was identified as the critical heat flux.

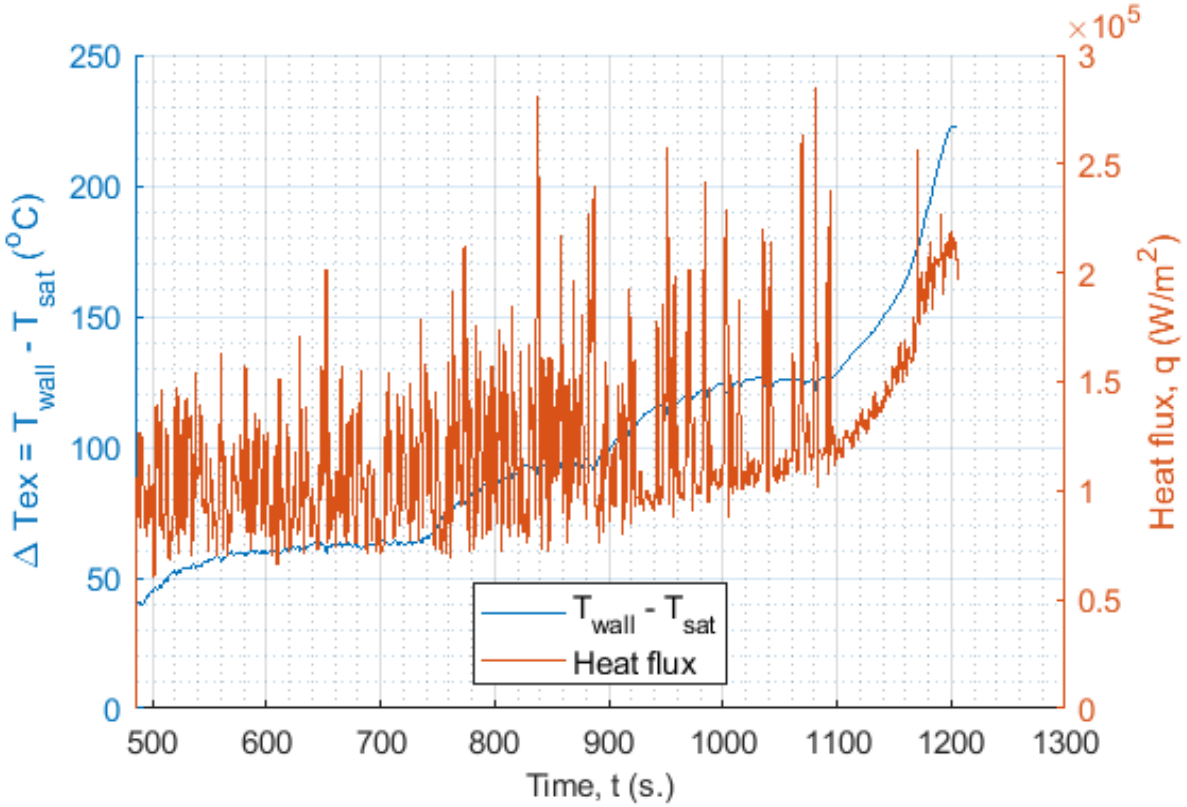

Figure 6.15: Heat flux and excess temperature for the experiment with test surface vibration amplitude of 7 mm at a coolant sub cooling of 15 ^{o}C for a sampling rate of one per measured temperature points.

In a similar way to figure 6.14, the heat flux and excess temperature are shown in figure 6.15. The fluctuating heat flux values increases with increasing excess temperature and reaches a peak value before the heat flux has suddenly dropped, at around 1100 s. The maximum heat flux value occurring just before the average heat flux values had reduced, was identified as the critical heat flux.

It was observed during these experiments where the vibration amplitude was 7 mm, the coolant was ejected from the test surface owing to the high amplitude. This could have made it difficult for the spray to continuously form a layer of liquid over the test surface. Therefore, the fluctuating heat transfer until the excess temperatures was very high. The smoothened heat transfer when the excess temperature was very high was probably due to film boiling. This occurred in both experiments when the excess temperature was above ~105 ^{o}C for 5 ^{o}C sub cooling, and ~125 ^{o}C for 15 ^{o}C sub cooling. All the identified critical heat fluxes and the associated excess temperatures for experiments F1 to F10, and G1 to G10, are given in table 6.3. The heat flux and excess temperatures plots for all the cases are given in Appendix B, and the measured temperatures for all the cases are given in Appendix C.

Table 6.3: Critical heat flux and excess temperature for experiments F1 to F10, and G1 to G10.

Experiment No.	Coolant temp (^oC)	Vibration amplitude (mm)	Vibration frequency (Hz)	CHF (MW/m^2)	Tex (^oC) (Tex=Twall-Tsat)	CHF variation from stationary (%)
F1	95	Stationary	Stationary	0.765	48	0
G1	85			0.641	108	0
F2	95	0.02	400	0.713	156	-6.85
G2	85			0.761	104	+18.75
F3	95	0.08	200	0.714	56.5	-6.72
G3	85			0.709	145	+10.65
F4	95	0.1	100	0.614	114	-19.72
G4	85			0.692	119	+8.05
F5	95	0.2	60	0.770	73	+0.64
G5	85			0.704	105	+9.87
F6	95	0.5	60	0.702	51	-8.26
G6	85			0.618	155	-3.46
F7	95	1	53.7	0.520	77.5	-32.03
G7	85			0.494	62	-22.82
F8	95	0.1	10	0.684	111	-10.59
G8	85			0.708	123.5	+10.55
F9	95	1	10	0.702	164	-8.26
G9	85			0.695	178	+8.41
F10	95	7	10	0.302	86	-60.58
G10	85			0.285	122	-55.52

6.3.1.3.1. Estimation of error from spatial discretisation in the calculation of critical heat flux.

In order to estimate the error due to spatial discretisation in the calculation of critical heat flux, different grids with higher and smaller number of grid points (than the one used for all the critical heat flux calculations i.e. with 22 grid points) were used for a convergence study. The critical heat flux calculated using each grid were checked for convergence. Data from experiment F1 were used

for the study. Table 6.4 provides the details of the grids and the critical heat flux calculated using each grid in which grid number 3 was the one used for all the critical heat flux calculations.

Table 6.4: Critical heat flux calculated using different grids.

Grid No:	Number of nodes	δx (m)	Maximum δt to meet stability criteria(s) (Equation (6.6))	Applied δt (s)	Critical heat flux calculated (MW/M^2)
1	3	0.005500	0.111355	0.05	0.76472
2	5	0.002750	0.030471	0.01	0.76500
3	22	0.000524	0.001197	0.0004	0.76504
4	50	0.000224	0.000223	0.0001	0.76504
5	75	0.000149	0.000097	0.00005	0.76504
6	100	0.000111	0.000054	0.00002	0.76504

Note: The stability criteria suggests that the δt should be less than the value calculated using equation (6.6). Hence a smaller δt is applied for each grid.

It can be seen from the results in table 6.4 that the calculated critical heat flux have already converged from grid number 3 and only the grid number 1 and 2, which had much lesser number of grid points, produced a slightly different critical heat flux. It shows that the calculated critical heat fluxes are independent of errors from the spatial discretisation.

6.3.1.3.2. Uncertainty analysis.

Table 6.5 provides the uncertainties in the measured variables and these uncertainties are then used to calculate the combined uncertainty in calculated values. The uncertainties in the measurements were taken from the manufacturers' catalogs.

Table 6.5: Uncertainties in measured variables.

Instrument	Uncertainty	Units
Thermocouples	±0.4%	℃
Pressure transducers	±0.25%	bar
Diameter	±0.01	mm
Length	±0.01	mm
Accelerometer amplitude	±10%	mm
Accelerometer frequency	±5%	Hz

An uncertainty analysis was conducted to identify the errors in calculated volumetric flux as well the critical heat flux from the experimental results. The method described by Moffat (1988) [67] was used to calculate the uncertainties. It uses a root-sum-square method to combine all the errors in a calculated value from different variables with measurement uncertainty associated with it. The equation to calculate the combined uncertainty is given as:

$$\delta R = \left[\sum_{i=1}^{n}\left(\frac{\partial R}{\partial X_i}\delta X_i\right)^2\right]^{\frac{1}{2}} \tag{6.8}$$

where δR is the combined uncertainty, R is the calculation of the result, X_i is the measured variable, and δX_i is the uncertainty of the measured variable. The uncertainties of calculated volumetric flux and critical heat flux are ±2.82% and ±7.38% respectively. For the calculation of uncertainty in critical heat flux, the maximum critical heat flux calculated among all the experiments was used i.e. 0.765 MW/m^2 from experiment F1. The uncertainty calculations are given Appendix A.

6.3.1.3.3. Effect of sub-cooling and vibration frequency and amplitude on critical heat flux.

Looking at the variation in critical heat flux values for different vibration amplitudes and frequencies, it turns out that the critical heat flux reduces with surface vibration for most of the cases with coolant sub-cooling of 5 ^{o}C, whereas for the coolant sub-cooling of 15 ^{o}C, the critical heat flux increases significantly. The higher degree of sub-cooling needs more sensible heat to enable the coolant to reach saturation temperature, because droplet impingent is a highly dynamic process which initially takes heat away through single phase convection. The coolant with a lower degree of sub-cooling quickly reaches the boiling point, which results in faster evaporation. Surface motion has most certainly enhanced single-phase convection in experiments with a higher degree of sub-cooling. In the case of lower degree of sub-cooling, the sensible heat could not be utilised much by the moving surface as the heat transfer was mostly through evaporation. Therefore, there is hardly any improvement in heat transfer with surface vibration was seen for the sub-cooling of 5 ^{o}C.

To further examine the effect of surface motion on spray evaporative heat transfer, the critical heat fluxes and the associated excess temperatures were plotted against vibration amplitudes and frequencies for all the experiments. Figures 6.16 and 6.17 show the critical heat flux and excess temperature with respect to vibration amplitudes and frequencies for the experiments with the two different degrees of sub-cooling.

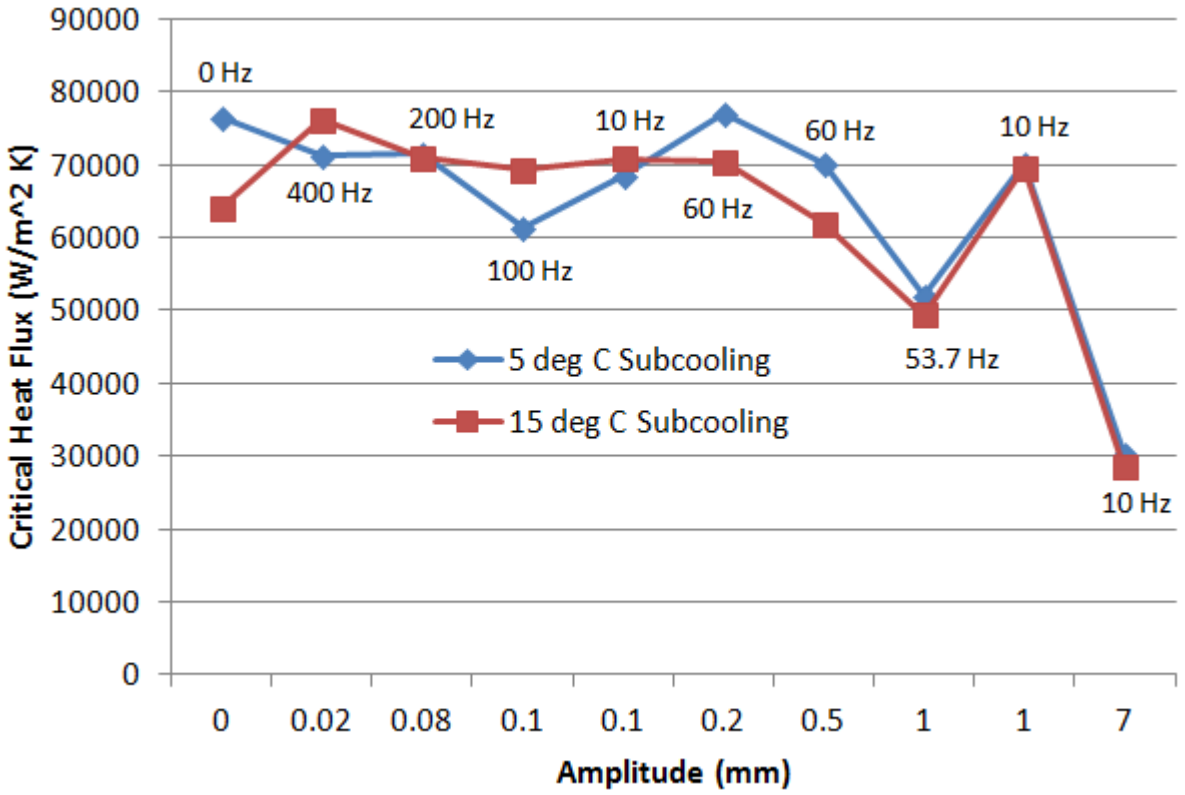

Figure 6.16: Critical heat flux as a function of vibration amplitude and frequencies for two levels of sub cooling.

Figure 6.16 shows that the critical heat flux calculated for the two different degrees of sub-cooling followed similar trends with respect to the combination of vibration amplitude and frequency. In the case of 5 ^{o}C sub-cooling, the critical heat flux was more prone to vibration amplitude rather than frequency whereas in the case of 15 ^{o}C sub-cooling, the vibration frequency had a higher effect on the critical heat flux compared to the stationary cases. For the 15 ^{o}C sub-cooling of the coolant, the heat transfer was enhanced by 18.75% at a vibration frequency of 400 Hz, but for 5 ^{o}C sub-cooling, high frequencies did not bring any increase in heat transfer. The heat transfer deteriorated for both the sub-cooling cases at two amplitudes, 7 mm and 1 mm respectively. For the 1 mm amplitude, the deterioration was at the frequency of 53.7 Hz and did not occur at the frequency of 10Hz. This could be due to the much lower test surface acceleration at 10Hz. The highest deterioration in heat flux occurred at an amplitude of 7 mm, where both the sub-cooling cases had similar critical heat flux. The critical heat flux deteriorated by ~60% and ~55% for the sub-cooling degrees of 5 ^{o}C and 15 ^{o}C respectively. As observed during the experiment at a test surface vibration of 7 mm and 10 Hz, the deterioration in critical heat flux at high amplitudes could be associated with difficulty in forming a liquid layer over the test surface by the spray owing to the test surface throwing liquid around. Similarly, a similar phenomenon could occur at the amplitude and frequency of 1 mm and 53.7 Hz respectively.

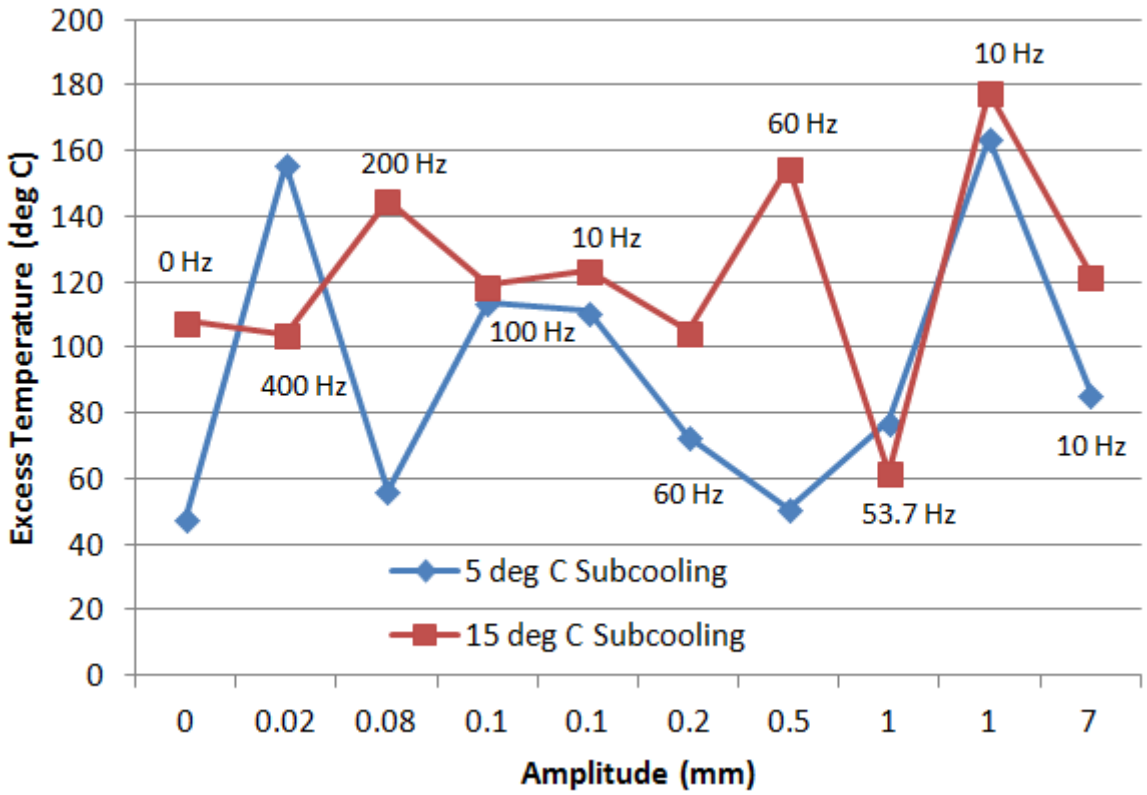

Figure 6.17: Excess temperature as a function of vibration amplitude and frequency for two different levels of sub-cooling.

As expected in general, the excess temperatures at which the critical heat fluxes were occurring, were much higher for the case with higher degree of sub cooling. For both the degrees of sub-cooling, no particular trend was visible with respect to both the vibration amplitudes and frequencies.

6.3.2. Comparison of Results with Single Droplet Impingent Simulation Results

The single droplet numerical simulation results and the experimental results were compared in an attempt to meet the one of the main objectives, namely to establish whether there is any correlation between single droplet evaporation and spray evaporation on moving boundaries, and to check whether the droplet simulation results could be used to predict the evaporative heat transfer for a full spray. Until only the onset of evaporation was simulated for droplet impingement, only the average heat flux could be calculated and these were compared with the critical heat flux from the spray evaporation experiments. As there is a big difference between the magnitudes of heat fluxes, only the qualitative trends can be compared for different vibration amplitudes and frequencies for both the simulations and experiments. For example, the case where the vibration amplitude was 7 mm in the experiment, was compared with a 10 mm amplitude case in the simulation for the same frequency. The amplitude was limited to 7 mm for a frequency of 10 Hz owing to the force limit by the shaker.

Table 6.6: Time averaged heat flux from the numerical simulations.

Simulation No	Wall vibration amplitude (mm)	Wall vibration frequency (Hz)	Time averaged heat flux (MW/m^2)	Difference in heat flux (%)
C2	0	0	0.34	0
E3	0.08	200	0.3380	-0.59 %
D8	0.1	100	0.3411	+0.32 %
E2	0.2	60	0.3432	+0.94 %
E1	0.5	60	0.3401	+0.029 %
D7	0.1	10	0.3383	-0.5 %
D4	1	10	0.3349	-1.5 %
D1	10	10	0.3287	-3.32 %

Figures 6.18 shows the droplet numerical simulation heat fluxes as a function of the vibration frequencies and amplitudes. Figure 6.19 shows the experimental critical heat fluxes as a function of the vibration frequencies and amplitudes.

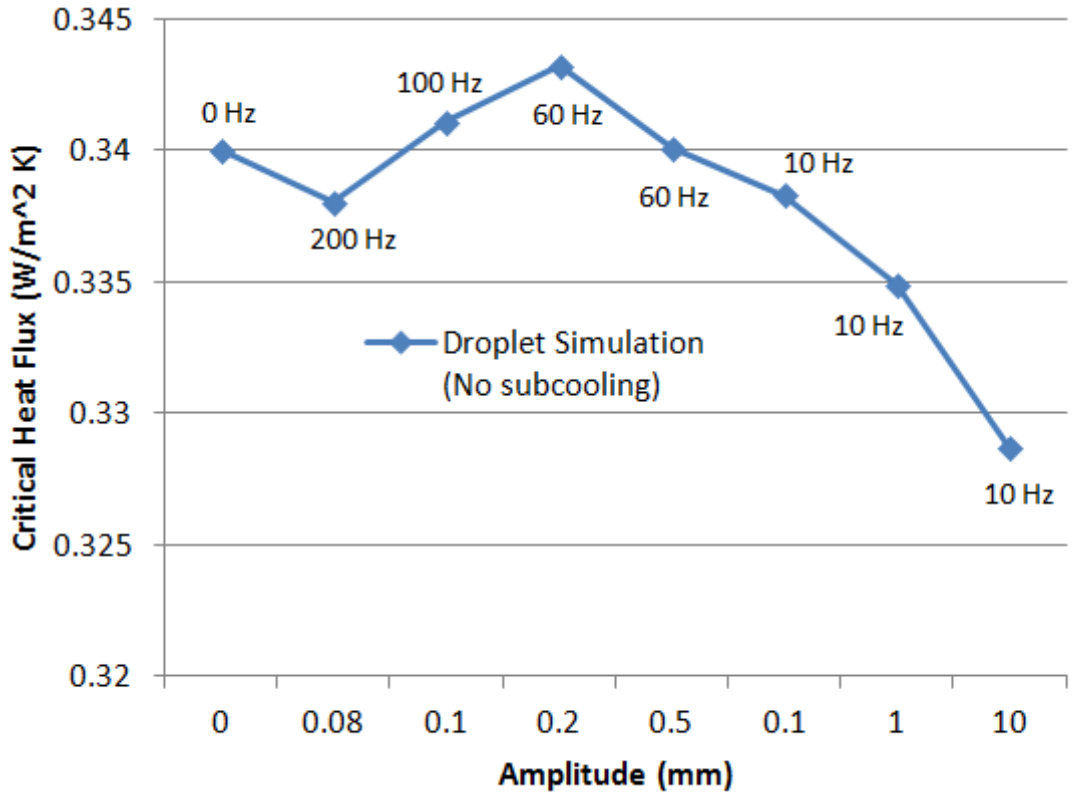

Figure 6.18: Time averaged heat flux from the numerical simulations plotted against vibration amplitudes and frequencies.

Comparing figure 6.18 with figure 6.19, the heat flux from the simulations are seen to be only half of the critical heat flux from the experiments. The heat flux in the simulations only varies by a maximum of 3.3% whereas in the experiments, it was 60.6%. For both experiments and simulations, the heat flux deteriorates at high amplitudes. At high frequencies, a higher heat flux was observed for both the simulations and experiments. It seems that the simulation and experimental heat flux results were following a similar trend with respect to vibration frequency and amplitude, but the large difference between the experimental and simulation results (with respect to changes in vibration amplitude and frequency) shows that the simulation results (with the onset of evaporation) could not be used to correlate spray evaporative heat transfer. If simulations were possible and performed for full evaporation of droplets, much higher heat fluxes would have been obtained.

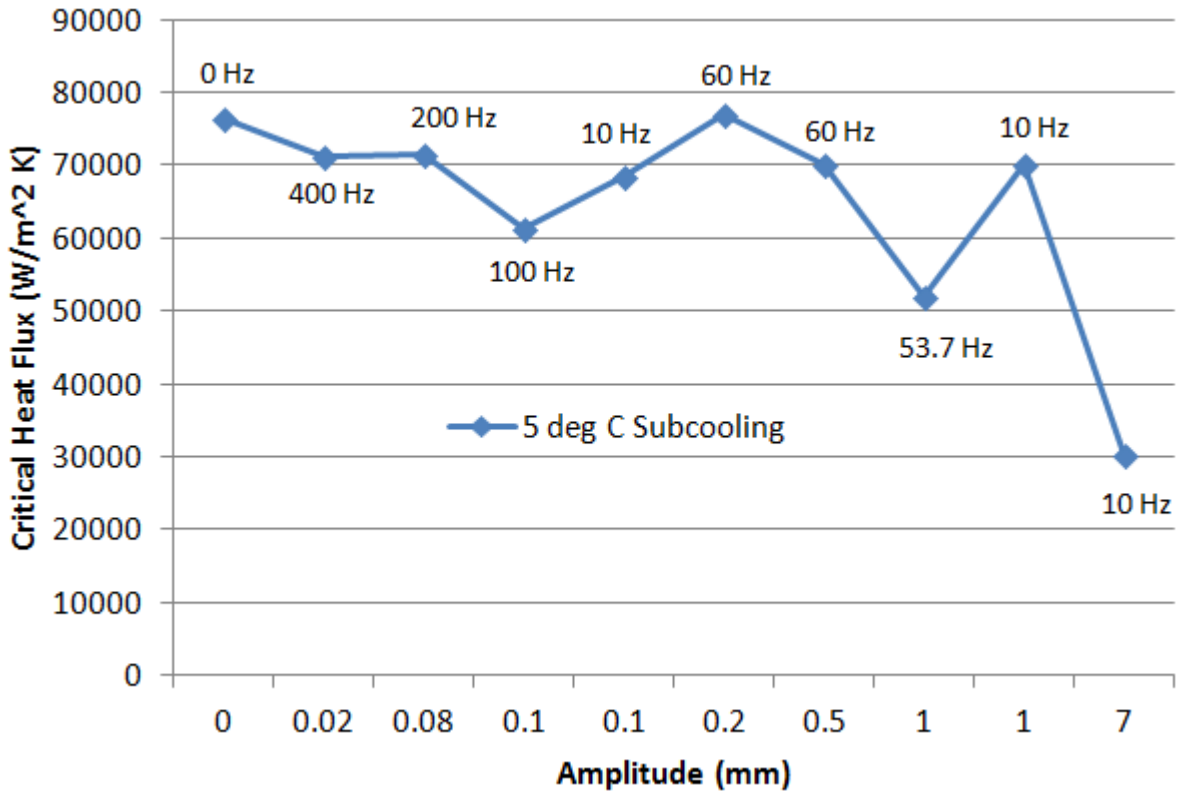

Figure 6.19: Time averaged heat flux from the experiments for 5 ^{o}C sub-cooling plotted against vibration amplitudes and frequencies.

6.3.3. Quarter Cylinder Geometry Test Piece Experiments

Dynamic test rig with cylinder head geometry test piece experiments were undertaken to find the effect of vibration on overall spray evaporative cooling. Only one temperature measurement was taken, 1 mm below the test surface, and the heat transfer was two dimensional, which restricted

direct heat flow calculations. A temperature ratio was used to plot the measurements taken, to identify the effect of vibration. The temperature ratio is given as:

$$\theta = \frac{T_t - T_{ref}}{T_{t=0} - T_{ref}} \tag{6.9}$$

where T_t is the temperature measured with respect to time, T_{ref} is the reference temperature, and $T_{t=0}$ is the initial temperature. The temperature ratio for a stationary case, and vibration conditions of 0.08 mm - 200 Hz, and 0.02 mm - 400 Hz respectively, is shown with respect to time in figure 6.20. These tests used two PJ 6 nozzles that provided a total coolant mass flow rate of 0.9 g/s. The coolant temperature was 85 ^{o}C. Experiments were performed by first heating up the test piece until the test surface has a steady state temperature of about 125 ^{o}C and then let it cool down with spray evaporation whilst the test piece is being shaken at the desired amplitude and frequency. The reference temperature used for calculating the temperature ratio was 110 ^{o}C.

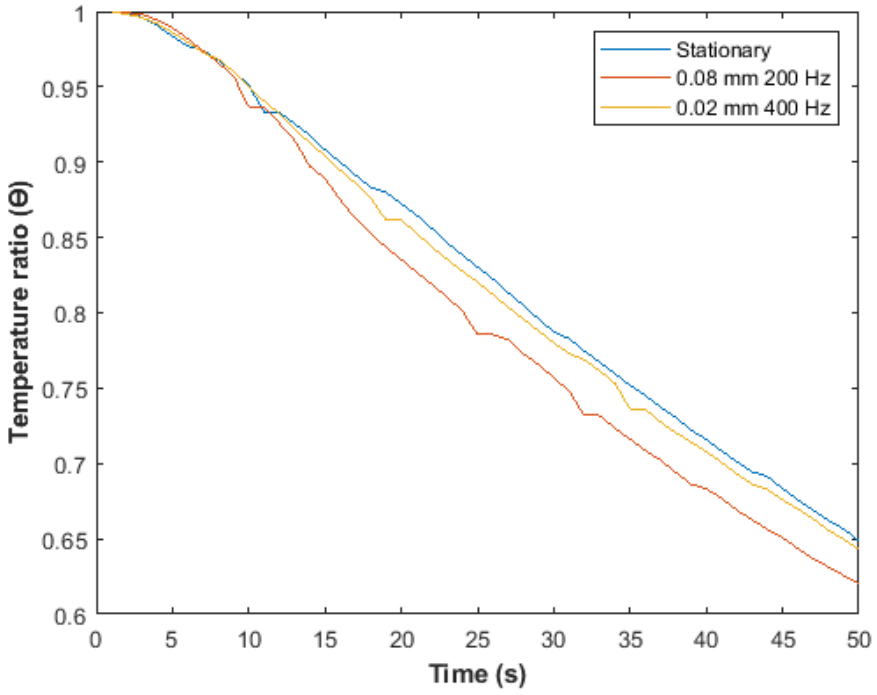

Figure 6.20: Temperature ratios with respect to time for stationary and vibration cases.

From figure 6.20, it can be seen that both the vibration conditions resulted in faster cooling, which indicates higher heat transfer than the stationary case. The case where the vibration amplitude and frequency were 0.02 mm and 400 Hz respectively, has the highest cooling rate, which indicates the highest heat transfer rate among the three cases compared.

6.4. Dimensionless Number Analysis and Correlation of Critical Heat Flux for Spray Evaporation on Moving Boundaries

The calculated critical heat fluxes from the flat test piece dynamic rig were analysed using the dimensionless number, vibration Reynolds number [68]. The vibrational Reynolds number is a measure for turbulence induced by the surface vibration. Vibrational Reynolds number uses the same dimensional groups as the Reynolds number used for calculating turbulence in fluid flow over a surface. Both Reynolds number and vibrational Reynolds number use the ratio of inertial forces to viscous forces to determine turbulence in fluid movement. Whilst the Reynolds number is used for flow induced turbulence, the vibrational Reynolds number attempts to calculate the turbulence caused by vertical oscillating movement of the surface. As it is a ratio of inertial forces to the viscous forces, the vibrational Reynolds number is also expected to indicate transition from laminar motion to turbulent motion of the fluid. The vibrational Reynolds number is given in equation (6.10).

$$Re_v = \frac{\alpha f D}{v} \tag{6.10}$$

where α is the vibration amplitude, f is the vibration frequency, D is the surface diameter and v is the kinematic viscosity of the coolant.

The Strouhal number was also initially considered for the analysis, but was not used as it did not take viscosity changes of the coolant with respect to temperature into consideration. The critical heat flux plotted against the vibrational Reynolds number is given in figure 6.21.

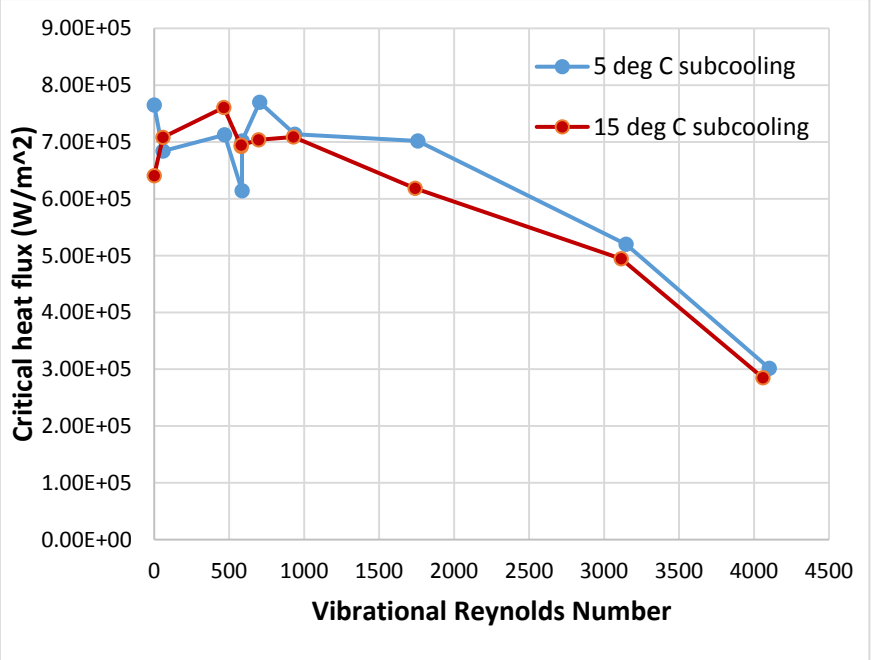

Figure 6.21: Critical heat flux plotted against the vibrational Reynolds number for the two different degrees of sub-cooling.

Figure 6.21 shows that, for both the cases, heat transfer deteriorated with increase in vibrational Reynolds numbers above 1000. At vibrational Reynolds numbers below 1000, the critical heat flux fluctuates around the critical heat flux at vibrational Reynolds number equal to 1000. For the set of vibration amplitudes and frequencies used in the experiments, the vibrational Reynolds number of 1000 can be seen as the transition point before heat transfer started to deteriorate. The deterioration of heat transfer above vibrational Reynolds number of 1000 can be attributed to liquid film movement on the heater surface becoming turbulent. Turbulent liquid film promotes single-phase forced convection owing to its higher kinetic energy, but it suppresses boiling which has a much higher rate of heat transfer. Turbulence increases with increasing vibrational Reynolds number above 1000, and the single-phase forced convection becomes more and more prominent, hence the deterioration of heat transfer above vibrational Reynolds number of 1000.

The critical heat flux for the stationary experimental cases for both the degrees of sub cooling were calculated using the critical heat flux correlation by Mudawar and Estes [26].

$$\frac{q_{max}}{\rho_g h_{fg} Q^{"}} = 2.3\left(\frac{\rho_l}{\rho_g}\right)^{0.3}\left(\frac{\rho_l Q^{"2} d_{32}}{\sigma}\right)^{-0.35} \times \left(1 + 0.0019\frac{\rho_l C_{Pl}\Delta T_{sub}}{\rho_g h_{fg}}\right) \qquad (2.18)$$

where q_{max} is the critical heat flux, ρ is the liquid density, $Q^{"}$ is the volumetric flux, d_{32} is the Sauter mean diameter, σ is the surface tension, C_P is the specific heat capacity of the liquid, ΔT_{sub} is the degree of sub cooling, and h_{fg} is the latent heat of vaporisation. The subscripts l and g stand for liquid and gas respectively. The calculated critical values of 12.03 MW/m^2 and 12.85 MW/m^2 were ~15.7 and ~20 times higher than what was measured. This could be due to the Mudawar and Estes correlation is fit using the data measured at a degree of sub-cooling of 76.5 to 77.5 ^{o}C and at much higher droplet sizes, in which the minimum diameter was 0.405 mm. The degree of sub cooling was much smaller at 5 and 15 ^{o}C as well as ten times smaller droplets.

Equation (2.14) was first adjusted to fit the measured stationary surface critical heat fluxes. This was achieved by modifying the power for the term involving the Suater mean diameter to -0.105 and dividing the last term by the square of degree of the sub-cooling. The modified equation is in the following form:

$$\frac{q_{max}}{\rho_g h_{fg} Q^{"}} = 2.3\left(\frac{\rho_l}{\rho_g}\right)^{0.3}\left(\frac{\rho_l Q^{"2} d_{32}}{\sigma}\right)^{-0.105} \times \left(1 + 0.0019\frac{\rho_l C_{Pl}}{\rho_g h_{fg}\Delta T_{sub}}\right) \qquad (6.11)$$

The relationship between the critical heat fluxes with respect to the vibrational Reynolds number was found and then added to the correlation. The final form of the modified correlation to calculate spray critical heat flux with moving boundaries for the range of vibrational Reynolds from 0 to 4000 is given in equation (6.6):

$$\frac{q_{max}}{\rho_g h_{fg} Q^{"}} = 2.3\left(\frac{\rho_l}{\rho_g}\right)^{0.3}\left(\frac{\rho_l Q^{"2} d_{32}}{\sigma}\right)^{-0.105} \times \left(1 + 0.0019\frac{\rho_l C_{Pl}}{\rho_g h_{fg}\Delta T_{sub}}\right) \times \left[\left(-4 \times 10^{-8} \times {Re_v}^2\right) + \left(7 \times 10^{-6} \times Re_v\right) + 0.95 + \frac{\Delta T_{sub}}{100}\right] \qquad (6.12)$$

The correlation has a mean and a maximum error of -4.7 % and -24.7 % respectively. The critical heat flux calculated using the correlation, plotted against the measured values from the experiments, is given in figure 6.22.

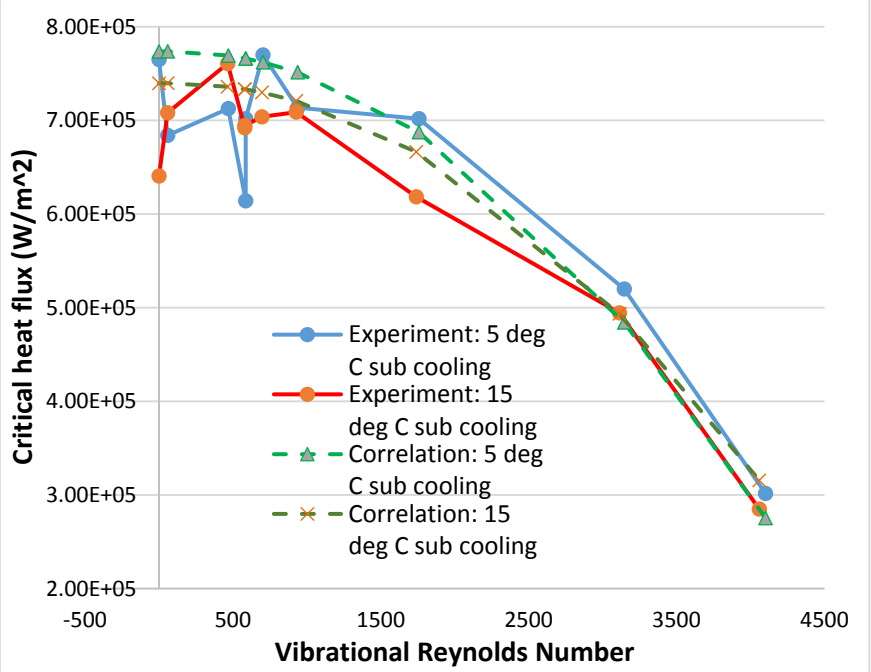

Figure 6.22: Measured and calculated values of critical heat flux.

6.5. Conclusion of Chapter 6

Selected results from the static pool boiling rig, the static spray boiling and the dynamic rig with cylinder head cylinder head geometry test piece has been presented. These results have not however been analysed as it was not used for the research conducted. The primary objective of the static pool boiling rig and the static spray boiling rig was to gain experience on taking temperature measurements during boiling heat transfer. The objective of the dynamic rig with the cylinder-head geometry test piece was to find out whether sufficient spray evaporative cooling can be achieved on more realistic surfaces under vibration.

The dynamic test rig with a flat surface test piece was used for spray boiling experiments under vibration amplitudes and frequencies ranging from 0.02 mm to 7 mm, and 400 Hz to 10 Hz respectively. Two sets of experiments were conducted for sub-cooling levels of 5 ^{o}C and 15^{o}C. First, the experiments were conducted for the stationary case for the two sub-cooling levels. A method for identifying the critical heat flux from the heat flux plots generated using a finite difference method and solving transient conduction equation was discussed. Critical heat fluxes for all the experiments were identified, along with the excess temperature at which the critical heat flux was achieved.

A comparison between the critical heat flux values at two sub-cooling levels for the stationary cases showed that the 5 ^{o}C sub-cooling had achieved higher heat flux than the degree of sub-cooling of 15 ^{o}C. The effect of vibration amplitude and frequency was then analysed between the set of experiments undertaken for the two sub-cooling levels. Results showed that, for high frequencies,

the heat transfer was enhanced for the sub-cooling of 15 ^{o}C, but in the case of 5 ^{o}C sub-cooling, the critical heat flux was similar to that of the stationary case. For both the sub-cooling levels, high amplitudes, above 0.5 mm, deteriorated heat transfer with increasing amplitudes. The highest heat flux deterioration was found to be occurring at the maximum vibration amplitude of 7 mm at a frequency of 10 Hz. The reductions in heat transfer from the stationary cases were ~ 60.5 % and ~ 55.5 % for the sub-cooling degrees of 5 ^{o}C and 15 ^{o}C respectively.

A qualitative comparison between the average heat flux values from the droplet simulations and the critical heat fluxes from the experiments was conducted. The analysis was to look into the trends in heat transfer with respect to the vibration amplitudes and frequencies. It was found that the average heat flux values from the droplet simulations were only half that of the critical heat fluxes calculated from the experiments. The heat flux values from the simulations were high at high frequencies, like in the experiments. Similarly, at high amplitudes, heat flux values had reduced. In the case of simulations, the maximum heat flux change was ~-3.3%, but for the experiments, it was -60.5%. This made it not possible to make any correlations between droplet evaporation and a full spray evaporation.

A dimensionless number analysis with respect to vibration was performed with the critical heat flux values from the experiments. The Vibrational Reynolds Number (Re_v) was used for the analysis. From the analysis, it was found that at an Re_v above 1000, the heat flux starts to reduce. With increasing Re_v above 1000, the critical heat flux values reduces. A correlation, including the additional term of vibration Reynolds number, was constructed by modifying the Mudawar and Estes correlation for critical heat flux. This correlation predicts the spray evaporative critical heat flux with good accuracy with respect to boundary motion.

Chapter 7. CONCLUSIONS AND FURTHER WORK

7.1. Conclusions

A literature review was first undertaken to identify published work on internal combustion engine evaporative cooling systems, and heat transfer associated with different forms of boiling processes. The effect of heater surface vibration in boiling heat transfer was then reviewed. Various dynamic contact angle models required for the numerical simulations were explained. Different numerical methods available for the simulation of droplet impingement dynamics and evaporation were also examined, combined with a review of previous work on numerical simulation of droplet impingement and evaporation. The five research objectives (of this thesis) were then constructed. Correlations models for calculating pool boiling, flow boiling and spray boiling were fully examined and have been discussed separately. For the benefit of the reader these five objectives are restated as follows.

- To create a one-dimensional control model representing an engine cylinder head wall, based on a validated static spray evaporative correlation model, and to check whether spray evaporative cooling can be controlled on engines running with transient loads.
- To perform numerical simulations of droplet impingement dynamics and evaporation using appropriate models to examine the effect of moving boundaries on droplet evaporative heat transfer and to establish whether there is any correlation between single-droplet evaporative cooling and spray evaporative cooling.
- To design an experimental test-rig to examine spray boiling with moving boundaries for a flat heating surface.
- To perform spray boiling experiments on a vibrating flat surface with vibration amplitudes and frequencies in the range of 0.1 mm to 10 mm, and 1000 Hz to 10 Hz, respectively, (corresponding to typical engine-in-vehicle conditions) to identify only the effect of vibration with all other parameters that affect spray boiling heat transfer kept constant (such as flow rate, velocity, droplet size etc.).
- To examine the possibility of creating a dynamic correlation to predict spray evaporative heat transfer on moving boundaries.

To meet the first objective of creating a transient one-dimensional control model for a spray evaporatively cooled engine cylinder head wall to check whether sufficient control could be achieved, a control model was created in Simulink using a finite difference method for the solution of one-dimensional transient heat conduction equation. The simulations were for a 7 mm thick wall

representing an engine cylinder-head wall. On the gas-side of the cylinder head wall, a transient heat transfer coefficient and gas temperature for a cycle with respect to crank angle, generated by an AVL boost simulation for an engine producing 100 KW/L, was used to set the boundary conditions. Initially, a simulation was performed using a pool boiling heat flux curve as the boundary condition on the coolant side to check the effect of fluctuating metal temperature caused by the combustion gas on the coolant side. There was hardly any fluctuation of temperature on the coolant-side due to the thermal diffusivity of the metal, which indicated that the per cycle fluctuating metal temperature on the gas side per cycle will not have any effect on the heat transfer at the coolant-side. For a step-by-step change of engine load from full-load to half-load at which the maximum heat flux is 1.6 MW/m^2, a simulation was performed using the heat flux calculated by nucleate boiling correlation by Hsieh et al [69] as the boundary condition for the coolant-side. A proportional and integral controller, with gain scheduling from the engine load, was employed to control the nozzle flow rate. The results showed that good control could be achieved with a response time of less than one second.

For the objective of simulating droplet impingement and evaporative heat transfer on moving boundaries (to find out the effect of moving boundaries on evaporative heat transfer), several sets of simulations were performed using the Volume of Fluid method via ANSYS. Simulations were performed for both isothermal and thermal cases with and without wall vibration.

For the non-moving boundary isothermal case, the minimum impact velocity for rebound was calculated for droplet diameters of 30 µm, 49 µm, 75 µm, and 100 µm. The minimum impact velocity for rebound decreased almost linearly with increasing droplet diameter. Based on this, a droplet rebound equation was derived for the minimum impact velocity for rebound for a given droplet diameter. An expression for the time taken for detachment was also derived.

Isothermal droplet impingement simulations for wall vibration amplitudes of 10 mm and 1 mm at frequencies of 10 Hz, 100 Hz and 1000 Hz were performed. For most of the cases, droplet rebound occurred with the impact velocity less than the minimum impact velocity for rebound. The wall vibration, producing a resultant velocity at droplet impact, i.e. higher than the minimum impact velocity for rebound, was believed to be cause of this. At wall vibration amplitudes of 1 mm, droplet rebound did not occur when the resultant velocity was higher than the minimum impact velocity for rebound.

Stationary and moving boundary evaporative heat transfer simulations were performed for droplet impingement at 1m/s for a droplet diameter of 49 micrometer. Three different wall vibration amplitudes (0.1 mm, 1 mm and 10 mm) and three different wall vibration frequencies (10 Hz, 100 Hz

and 1000 Hz) were used. The extremely long running time of simulations, restricted simulations to only the onset of evaporation. Results showed that the highest wall vibration frequency enhanced heat transfer whereas the highest wall vibration amplitude reduced heat transfer. The lowest frequency of 10 Hz deteriorated the heat transfer rate at all amplitudes. High wall vibration frequency produces high frequency droplet oscillations after impact on the surface and reduces the droplet oscillation amplitude faster. Frequent contact of the droplet on the surface, as well as increased kinetic energy of the droplet, provided better heat transfer at high wall vibration frequency. High vibration amplitude sustains the high amplitude droplet oscillations (from impact) longer with slower oscillations and this reduces surface contact.

The design of a dynamic test rig with a flat test piece has been discussed. This was to meet the objective of designing a test rig which could measure spray evaporative heat transfer on moving boundaries. A detailed description of the major components was provided along with the results of Finite Elements Analysis performed for heat transfer and thermal expansion problems. This was to check whether the design was capable of performing experiments at the desired conditions. The chosen instrumentation of the test piece, as well as the data acquisition system to collect data, were discussed. Manufacturing of the parts and commissioning of the rig has also been discussed, along with the design, manufacture and commissioning of test rigs for the Evaporative Cooling Systems project have also been covered. These three rigs were to test static pool boiling, static spray boiling, and dynamic testing of a test piece, for example representing cylinder-head geometry under spray cooling, or a flat test piece. The static pool boiling and the static spray boiling test rigs were designed to conduct experiments to gain experience on temperature measurements for boiling heat transfer. The dynamic rig with cylinder-head geometry test piece was designed to check whether spray cooling could be achieved under dynamic conditions for realistic geometries.

As part of the Evaporative cooling systems project, to meet the objective of gaining experience on taking temperature measurements during pool boiling and spray boiling, the static pool boiling, and the static spray boiling experiments were conducted. A plot for the heat flux during one of the static pool boiling, and the static spray boiling experiment were presented. Dynamic rig experiments for the cylinder-head geometry test piece, as part of the Evaporative Cooling Systems project, were conducted to meet the objective to check the effect of vibration on evaporative cooling on realistic geometries. A plot for the temperature ratio for different vibration conditions was presented.

Dynamic flat test piece experiments were conducted for vibration amplitudes and frequencies of 0.02 mm to 7 mm, and 400 Hz to 10 Hz respectively. Experiments were conducted to meet the objective of understanding the effect of vibration on spray evaporative heat transfer. Two sub-

cooling levels were used, and the results showed that, for the stationary case, the sub-cooling of 5 ^{o}C had higher critical heat flux than the sub-cooling degree of 15 ^{o}C. For the vibration cases, high frequencies resulted in the enhancement of critical heat flux for the sub-cooling of 15 ^{o}C. High vibration amplitudes resulted in deterioration of critical heat flux, and the maximum reduction in critical heat flux was calculated to be ~60.5 % and ~55.5 %, at an amplitude of 7 mm, for the sub-cooling levels of 5 ^{o}C and 15 ^{o}C respectively.

Heat flux values from the droplet simulations were qualitatively compared to the experimental critical heat flux values. This was to check whether there is any correlation between the simulated droplet data and the experimental spray data. It was found that, the heat flux values for the simulations were half those of the experiments, and also the difference between the changes in heat transfer with respect to vibration was very different. However, there were some similarities between the simulation results and the experimental results. Heat flux was high at high frequencies for both the cases and heat flux deteriorated to its minimum at the highest amplitude for both the cases. The maximum difference between the heat fluxes with respect to vibration was -3.3 % and 60.5 %, for the droplet simulations and the spray experiments respectively. This big difference indicates that the droplet results cannot be correlated with the experimental spray results.

To further understand the effect of vibration on spray evaporation, a dimensionless number analysis was conducted using the vibrational Reynolds Number. It was found that at low vibrational Reynolds Numbers (below 1000), vibration hardly had any effect on spray evaporative heat transfer. The vibrational Reynolds Number of 1000 can be seen as a transition point, as after that point, the critical heat flux started to continuously decrease with increase in vibrational Reynolds number. A correlation, including an additional term of vibration Reynolds number, was created by modifying the Mudawar and Estes [1] correlation for critical heat flux. This correlation is useful for calculating the spray evaporative critical heat flux with respect to boundary motion.

7.2. Further Work

Using the correlation created for the calculation of critical heat flux for moving boundaries, the spray cooling control model could be updated with surface vibration. Simulations could be conducted for various combinations of engine vibration amplitudes and frequencies to check whether sufficient control could be achieved. This should however be undertaken using high performance computing facilities.

The possibility of extending the numerical simulations until full droplet evaporation instead of just onset of evaporation should be examined. This will provide more accurate information on heat transfer during droplet evaporation and the results could be compared with experimental results to

check whether droplet simulation results could be used to correlate spray evaporative heat transfer on moving boundaries.

An uncertainty analysis could be conducted to identify any errors involved in the experimental measurements as well as the values calculated from the measured temperatures, pressures, and flow rates.

Using the existing dynamic flat test-piece, more experiments, at more vibration amplitudes and frequencies, various flow rates, different chamber pressures, and different degrees of sub-cooling could be conducted. This data would then be useful to create a better correlation that takes into consideration, all these aspects. Finally, a control model simulation could be again updated with the new dynamic correlation and simulations could be performed for different pressures, flow rates, temperatures and wall vibration amplitudes and frequencies.

Chapter 8. REFERENCES

[1] K. A. Estes and I. Mudawar, “Correlation of sauter mean diameter and critical heat flux for spray cooling of small surfaces,” *International Journal of Heat and Mass Transfer*, vol. 38, no. 16, pp. 2985–2996, Nov. 1995, doi: 10.1016/0017-9310(95)00046-C.

[2] N. a. F. Campbell, D. G. Tilley, S. A. MacGregor, and L. Wong, “Incorporating Nucleate Boiling in a Precision Cooling Strategy for Combustion Engines,” SAE Technical Paper, Warrendale, PA, SAE Technical Paper 971791, May 1997.

[3] S. Jafari *et al.*, “A review of evaporative cooling system concepts for engine thermal management in motor vehicles,” *Proceedings of the Institution of Mechanical Engineers, Part D: Journal of Automobile Engineering*, vol. 231, no. 8, pp. 1126–1143, Jul. 2017, doi: 10.1177/0954407016674606.

[4] M. R. Pais, L. C. Chow, and E. T. Mahefkey, “Surface Roughness and Its Effects on the Heat Transfer Mechanism in Spray Cooling,” *Journal of Heat Transfer*, vol. 114, no. 1, p. 211, 1992, doi: 10.1115/1.2911248.

[5] M. D. Leshner, “Evaporative engine cooling for fuel economy-1983,” SAE Technical Paper, 1983.

[6] H. C. Harrison, “Evaporative Cooling,” SAE Technical Paper, Warrendale, PA, SAE Technical Paper 260015, Jan. 1926.

[7] T. Kubozuka, N. Ogawa, Y. Hirano, and Y. Hayashi, “The Development of Engine Evaporative Cooling System,” SAE Technical Paper, Warrendale, PA, SAE Technical Paper 870033, Feb. 1987.

[8] S. C. Lee, J. Y. Kim, B. H. Han, T. M. Choi, and S. H. Bae, “Development of an evaporative cooling system for small four-stroke engines,” *KSME Journal*, vol. 4, no. 2, pp. 150–155, 1990.

[9] M. Pretscher and N. S. Ap, “Nucleate boiling engine cooling system-vehicle study,” SAE Technical Paper, 1993.

[10] J. T. Jose, J. F. Dunne, J.-P. Pirault, and C. A. Long, “Spray Evaporative Cooling System Design for Automotive Internal Combustion Engines,” 2018, p. V002T07A008, doi: 10.1115/ICEF2018-9659.

[11] N.-S. Ap and M. Tarquis, “Innovative Engine Cooling Systems Comparison,” SAE Technical Paper, 2005.

[12] C. Long, *Essential heat transfer*. Harlow: Longman, 1999.

[13] M.-G. Kang, “Effect of surface roughness on pool boiling heat transfer,” *International Journal of Heat and Mass Transfer*, vol. 43, no. 22, pp. 4073–4085, Nov. 2000, doi: 10.1016/S0017-9310(00)00043-0.

[14] S. M. Ghiaasiaan, *Two-Phase Flow, Boiling and Condensation: In Conventional and Miniature Systems*. Cambridge: Cambridge University Press, 2007.

[15] S. H. Yang, W.-P. Baek, and S. H. Chang, “Pool-boiling critical heat flux of water on small plates: Effects of surface orientation and size,” *International Communications in Heat and Mass Transfer*, vol. 24, no. 8, pp. 1093–1102, Dec. 1997, doi: 10.1016/S0735-1933(97)00103-6.

[16] K. N. Rainey and S. M. You, “Effects of heater size and orientation on pool boiling heat transfer from microporous coated surfaces,” *International Journal of Heat and Mass Transfer*, vol. 44, no. 14, pp. 2589–2599, 2001.

[17] L. C. Chen Tingkuan, “STUDY OF FLOW BOILING HEAT TRANSFER IN A TUBE WITH AXIAL MICROGROOVES,” *Experimental Heat Transfer*, vol. 14, no. 1, pp. 59–73, Jan. 2001, doi: 10.1080/089161501461648.

[18] M. Piasecka, “The use of enhanced surface in flow boiling heat transfer in a rectangular minichannel,” *Experimental Heat Transfer*, vol. 27, no. 3, pp. 231–255, May 2014, doi: 10.1080/08916152.2013.782374.

[19] W.-L. Cheng, W.-W. Zhang, H. Chen, and L. Hu, “Spray cooling and flash evaporation cooling: The current development and application,” *Renewable and Sustainable Energy Reviews*, vol. 55, pp. 614–628, Mar. 2016, doi: 10.1016/j.rser.2015.11.014.
[20] B. M. Pikkula, J. H. Torres, J. W. Tunnell, and B. Anvari, “Cryogen spray cooling: Effects of droplet size and spray density on heat removal,” *Lasers in Surgery and Medicine*, vol. 28, no. 2, pp. 103–112, 2001, doi: 10.1002/lsm.1024.
[21] G. Aguilar, W. Verkruysse, B. Majaron, L. O. Svaasand, E. J. Lavernia, and J. S. Nelson, “Measurement of heat flux and heat transfer coefficient during continuous cryogen spray cooling for laser dermatologic surgery,” *IEEE Journal of Selected Topics in Quantum Electronics*, vol. 7, no. 6, pp. 1013–1021, Nov. 2001, doi: 10.1109/2944.983307.
[22] B. M. Pikkula, J. W. Tunnell, D. W. Chang, and B. Anvari, “Effects of Droplet Velocity, Diameter, and Film Height on Heat Removal During Cryogen Spray Cooling,” *Annals of Biomedical Engineering*, vol. 32, no. 8, pp. 1133–1142, Aug. 2004, doi: 10.1114/B:ABME.0000036649.80421.60.
[23] W. Jia, G. Aguilar, G. X. Wang, and J. S. Nelson, “Heat-transfer dynamics during cryogen spray cooling of substrate at different initial temperatures,” *Physics in Medicine and Biology*, vol. 49, no. 23, pp. 5295–5308, Dec. 2004.
[24] B. Chen, J. Tian, R. Wang, and Z. Zhou, “Theoretical study of cryogen spray cooling with R134a, R404A and R1234yf: Comparison and clinical potential application,” *Applied Thermal Engineering*, vol. 148, pp. 1058–1067, Feb. 2019, doi: 10.1016/j.applthermaleng.2018.11.117.
[25] G. S. H. Lock, *Latent Heat Transfer: An Introduction to Fundamentals*. Oxford Engineering Science Series 43, 1996.
[26] K. A. Estes and I. Mudawar, “Correlation of sauter mean diameter and critical heat flux for spray cooling of small surfaces,” *International Journal of Heat and Mass Transfer*, vol. 38, no. 16, pp. 2985–2996, Nov. 1995, doi: 10.1016/0017-9310(95)00046-C.
[27] I. Mudawar and W. S. Valentine, “Determination of the local quench curve for spray-cooled metallic surfaces,” *Journal of heat treating*, vol. 7, no. 2, pp. 107–121, 1989.
[28] J. R. Rybicki and I. Mudawar, “Single-phase and two-phase cooling characteristics of upward-facing and downward-facing sprays,” *International Journal of Heat and Mass Transfer*, vol. 49, no. 1–2, pp. 5–16, Jan. 2006, doi: 10.1016/j.ijheatmasstransfer.2005.07.040.
[29] E. A. Silk, J. Kim, and K. Kiger, “Spray cooling of enhanced surfaces: Impact of structured surface geometry and spray axis inclination,” *International Journal of Heat and Mass Transfer*, vol. 49, no. 25–26, pp. 4910–4920, Dec. 2006, doi: 10.1016/j.ijheatmasstransfer.2006.05.031.
[30] C.-C. Hsieh and S.-C. Yao, “Evaporative heat transfer characteristics of a water spray on micro-structured silicon surfaces,” *International Journal of Heat and Mass Transfer*, vol. 49, no. 5–6, pp. 962–974, Mar. 2006, doi: 10.1016/j.ijheatmasstransfer.2005.09.013.
[31] D. H. Kim, Y. H. Lee, and S. H. Chang, “Effect of mechanical vibration on critical heat flux in vertical annulus,” in *Proc. KNS Spring Meeting*, 2002.
[32] C. Sodtke and P. Stephan, “Spray cooling on micro structured surfaces,” *International Journal of Heat and Mass Transfer*, vol. 50, no. 19–20, pp. 4089–4097, Sep. 2007, doi: 10.1016/j.ijheatmasstransfer.2006.12.037.
[33] A. Sathyabhama and S. P. Prashanth, “Enhancement of Boiling Heat Transfer Using Surface Vibration,” *Heat Transfer-Asian Research*, p. n/a-n/a, Sep. 2015, doi: 10.1002/htj.21197.
[34] H. Atashi, A. Alaei, M. H. Kafshgari, R. Aeinehvand, and S. K. Rahimi, “New Pool Boiling Heat Transfer in the Presence of Low-Frequency Vibrations Into a Vertical Cylindrical Heat Source,” *Experimental Heat Transfer*, vol. 27, no. 5, pp. 428–437, Oct. 2014, doi: 10.1080/08916152.2013.797940.
[35] Z. Wang, Y. Xing, X. Liu, L. Zhao, and Y. Ji, “Computer modeling of droplets impact on heat transfer during spray cooling under vibration environment,” *Applied Thermal Engineering*, vol. 107, pp. 453–462, Aug. 2016, doi: 10.1016/j.applthermaleng.2016.06.176.

[36] “Young’s Equation - an overview | ScienceDirect Topics.” [Online]. Available: https://www.sciencedirect.com/topics/engineering/youngs-equation. [Accessed: 29-Sep-2019].
[37] š. Šikalo, H.-D. Wilhelm, I. V. Roisman, S. Jakirlić, and C. Tropea, “Dynamic contact angle of spreading droplets: Experiments and simulations,” *Physics of Fluids*, vol. 17, no. 6, p. 062103, Jun. 2005, doi: 10.1063/1.1928828.
[38] I. V. Roisman, L. Opfer, C. Tropea, M. Raessi, J. Mostaghimi, and S. Chandra, “Drop impact onto a dry surface: Role of the dynamic contact angle,” *Colloids and Surfaces A: Physicochemical and Engineering Aspects*, vol. 322, no. 1–3, pp. 183–191, Jun. 2008, doi: 10.1016/j.colsurfa.2008.03.005.
[39] J. Hu, X. Xiong, H. Xiao, and K. Wan, “Effects of Contact Angle on the Dynamics of Water Droplet Impingement,” p. 6, 2015.
[40] R. G. Cox, “The dynamics of the spreading of liquids on a solid surface. Part 1. Viscous flow,” *Journal of Fluid Mechanics*, vol. 168, no. 1, p. 169, Jul. 1986, doi: 10.1017/S0022112086000332.
[41] T. D. Blake and C. J. De, “The influence of solid-liquid interactions on dynamic wetting,” *Adv Colloid Interface Sci*, vol. 96, no. 1–3, pp. 21–36, Feb. 2002.
[42] R. A. Hayes and J. Ralston, “The molecular-kinetic theory of wetting,” *Langmuir*, vol. 10, no. 1, pp. 340–342, Jan. 1994, doi: 10.1021/la00013a051.
[43] J. Chen, Z. Zhang, R. Xu, X. Ouyang, and P. Jiang, “Numerical Investigation of the Flow Dynamics and Evaporative Cooling of Water Droplets Impinging onto Heated Surfaces: An Effective Approach To Identify Spray Cooling Mechanisms,” *Langmuir*, vol. 32, no. 36, pp. 9135–9155, Sep. 2016, doi: 10.1021/acs.langmuir.6b02205.
[44] H. Dong, W. W. Carr, and J. F. Morris, “Visualization of drop-on-demand inkjet: Drop formation and deposition,” *Review of Scientific Instruments*, vol. 77, no. 8, p. 085101, Aug. 2006, doi: 10.1063/1.2234853.
[45] A. M. Briones, J. S. Ervin, S. A. Putnam, L. W. Byrd, and L. Gschwender, “Micrometer-Sized Water Droplet Impingement Dynamics and Evaporation on a Flat Dry Surface,” *Langmuir*, vol. 26, no. 16, pp. 13272–13286, Aug. 2010, doi: 10.1021/la101557p.
[46] W. M. Rohsenow, “A method of correlating heat transfer data for surface boiling of liquids,” Cambridge, Mass.: MIT Division of Industrial Cooporation,[1951], 1951.
[47] J. H. Lienhard, V. K. Dhir, Lewis Research Center., and University of Kentucky., *Extended hydrodynamic theory of the peak and minimum pool boiling heat fluxes*. Washington, D.C. : Springfield, Va.: National Aeronautics and Space Administration ; For sale by the National Technical Information Service], 1973.
[48] J. C. Chen, “Correlation for boiling heat transfer to saturated fluids in convective flow,” *Industrial & engineering chemistry process design and development*, vol. 5, no. 3, pp. 322–329, 1966.
[49] I. C. Finlay, R. J. Boyle, J. P. Pirault, and T. Biddulph, “Nucleate and film boiling of engine coolants flowing in a uniformly heated duct of small cross section,” SAE Technical Paper, 1987.
[50] N. Karwa, S. R. Kale, and P. M. V. Subbarao, “Experimental study of non-boiling heat transfer from a horizontal surface by water sprays,” *Experimental Thermal and Fluid Science*, vol. 32, no. 2, pp. 571–579, Nov. 2007, doi: 10.1016/j.expthermflusci.2007.06.007.
[51] W.-L. Cheng, F.-Y. Han, Q.-N. Liu, and H.-L. Fan, “Spray characteristics and spray cooling heat transfer in the non-boiling regime,” *Energy*, vol. 36, no. 5, pp. 3399–3405, May 2011, doi: 10.1016/j.energy.2011.03.039.
[52] S.-S. Hsieh, T.-C. Fan, and H.-H. Tsai, “Spray cooling characteristics of water and R-134a. Part I: nucleate boiling,” *International Journal of Heat and Mass Transfer*, vol. 47, no. 26, pp. 5703–5712, Dec. 2004, doi: 10.1016/j.ijheatmasstransfer.2004.07.022.
[53] G. Liang and I. Mudawar, “Review of spray cooling – Part 1: Single-phase and nucleate boiling regimes, and critical heat flux,” *International Journal of Heat and Mass Transfer*, vol. 115, pp. 1174–1205, Dec. 2017, doi: 10.1016/j.ijheatmasstransfer.2017.06.029.

[54] C. Long, *Essential Heat Transfer*. Harlow: Longman, 1999.
[55] J. T. Jose, J. F. Dunne, J.-P. Pirault, and C. A. Long, “Spray Evaporative Cooling System Design for Automotive Internal Combustion Engines,” in *Volume 2: Emissions Control Systems; Instrumentation, Controls, and Hybrids; Numerical Simulation; Engine Design and Mechanical Development*, San Diego, California, USA, 2018, p. V002T07A008, doi: 10.1115/ICEF2018-9659.
[56] “Fine Fog Nozzles | PJ Series Impingement Nozzles.” [Online]. Available: https://www.bete.com/products/pj. [Accessed: 29-Aug-2019].
[57] Š. Šikalo, H.-D. Wilhelm, I. V. Roisman, S. Jakirlić, and C. Tropea, “Dynamic contact angle of spreading droplets: Experiments and simulations,” *Physics of Fluids*, vol. 17, no. 6, p. 062103, Jun. 2005, doi: 10.1063/1.1928828.
[58] I. Malgarinos, N. Nikolopoulos, M. Marengo, C. Antonini, and M. Gavaises, “VOF simulations of the contact angle dynamics during the drop spreading: Standard models and a new wetting force model,” *Advances in Colloid and Interface Science*, vol. 212, pp. 1–20, Oct. 2014, doi: 10.1016/j.cis.2014.07.004.
[59] W. H. Lee, *Computational Methods for Two-Phase Flow and Particle Transport: (With CD-ROM)*. WORLD SCIENTIFIC, 2013.
[60] “ANSYS Fluent Theory Guide: 18.3 Volume of Fluid (VOF) Model Theory.” ANSYS, Inc.
[61] J. U. Brackbill, D. B. Kothe, and C. Zemach, “A continuum method for modeling surface tension,” *Journal of Computational Physics*, vol. 100, no. 2, pp. 335–354, Jun. 1992, doi: 10.1016/0021-9991(92)90240-Y.
[62] “ANSYS Fluent User’s Guide: 26 Modelling Multiphase Flows.” ANSYS, Inc.
[63] “ANSYS Fluent Theory Guide: 28 Solver Theory.” ANSYS, Inc.
[64] “ANSYS Fluent Customisation Manual: Part I: Creating and Using User Define Functions.” ANSYS, Inc.
[65] J. D. Bernardin, I. Mudawar, C. B. Walsh, and E. I. Franses, “Contact angle temperature dependence for water droplets on practical aluminum surfaces,” *International Journal of Heat and Mass Transfer*, vol. 40, no. 5, pp. 1017–1033, Mar. 1997, doi: 10.1016/0017-9310(96)00184-6.
[66] C. Long, “Chapter 3:Conduction - Numerical methods and application,” in *Essential Heat Transfer*, Harlow: Longman, 1999.
[67] R. J. Moffat, “Describing the uncertainties in experimental results,” *Experimental Thermal and Fluid Science*, vol. 1, no. 1, pp. 3–17, Jan. 1988, doi: 10.1016/0894-1777(88)90043-X.
[68] A. Sathyabhama and S. P. Prashanth, “Enhancement of Boiling Heat Transfer Using Surface Vibration,” *Heat Transfer-Asian Research*, p. n/a-n/a, Sep. 2015, doi: 10.1002/htj.21197.
[69] S.-S. Hsieh, T.-C. Fan, and H.-H. Tsai, “Spray cooling characteristics of water and R-134a. Part I: nucleate boiling,” *International Journal of Heat and Mass Transfer*, vol. 47, no. 26, pp. 5703–5712, Dec. 2004, doi: 10.1016/j.ijheatmasstransfer.2004.07.022.

Appendix A: Calculation of Uncertainties

Uncertainty in Volumetric Flux Calculation

$$\delta R = \left[\sum_{i=1}^{n}\left(\frac{\partial R}{\partial X_i}\delta X_i\right)^2\right]^{\frac{1}{2}}$$

$$Volumetric\ flux = \frac{\dot{V}/60000}{\pi\frac{d^2}{4}} = \frac{k\sqrt{\Delta P}/60000}{\pi\frac{d^2}{4}}$$

$k = 0.0259$ (from nozzle manufacturer)

$$\Delta P = P_2 - P_1$$

$$\delta R_{\Delta P} = [(\delta P_2)^2 + (\delta P_1)^2]^{1/2} = [(5 \times 0.0025)^2 + (1 \times 0.0025)^2]^{1/2}$$
$$= 0.01275$$

$$\delta R_{VF:0.00275} = \left[\left(\frac{\partial}{\partial \delta R_{\Delta P}}\frac{0.0259\sqrt{\delta R_{\Delta P}}/60000}{\pi\frac{d^2}{4}}\delta R_{\Delta P}\right)^2 + \left(\frac{\partial}{\partial d}\frac{0.0259\sqrt{\Delta P}/60000}{\pi\frac{d^2}{4}}\delta d\right)^2\right]^{1/2}$$

$$= \left[\left(\frac{0.0259/60000}{2\sqrt{\delta R_{\Delta P}} \times \pi\frac{d^2}{4}}\delta R_{\Delta P}\right)^2 + \left(\frac{-2 \times 0.0259\sqrt{\Delta P}/60000}{\pi\frac{d^3}{4}}\delta d\right)^2\right]^{1/2}$$

$$= \left[\left(\frac{\frac{0.0259}{60000}}{2\sqrt{0.01275} \times \pi\frac{0.02^2}{4}} \times 0.01275\right)^2 + \left(\frac{-2 \times \frac{0.0259\sqrt{4}}{60000}}{\pi\frac{0.02^3}{4}}0.00001\right)^2\right]^{1/2}$$
$$= [(6.0179 \times 10^{-9}) + (7.551 \times 10^{-12})]^{1/2} = 7.762 \times 10^{-5}$$

$$\%\delta R_{VF:0.00275} = \frac{7.762 \times 10^{-5}}{0.00275} \times 100 = 2.82\%$$

Uncertainty in Heat Flux Calculation

$$\delta R = \left[\sum_{i=1}^{n}\left(\frac{\partial R}{\partial X_i}\delta X_i\right)^2\right]^{\frac{1}{2}}$$

$$q = k\frac{dT}{dx}$$

$$K = 385\ W/mK$$

$$dx = 0.0055\ \text{m}$$

$$\delta dx = 0.00001\ \text{m}$$

$dT = 10.928$ °C (calculated from the maximum heat flux of 0.765 MW/m^2 in the experiments)

$$\delta T = 0.004 \times T$$

$$\delta T_1 = 0.004 \times 148 = 0.592$$

$$\delta T_2 = 0.004 \times 137.072 = 0.548$$

$$\delta dT = [0.592^2 + 0.548^2]^{1/2} = 0.8067$$

$$\delta R_q = \left[\left(\frac{\partial}{\partial \delta dT}\frac{k\delta dT}{dx}\delta dT\right)^2 + \left(\frac{\partial}{\partial dx}\frac{kdT}{dx}\delta dx\right)^2\right]^{1/2}$$

$$\delta R_q = \left[\left(\frac{k}{dx}\delta dT\right)^2 + \left(\frac{-kdT}{dx^2}\delta dx\right)^2\right]^{1/2}$$

$$\delta R_{q:765000\ W/m^2} = \left[\left(\frac{385}{0.0055}\times 0.8067\right)^2 + \left(\frac{-385\times 10.928}{0.0055^2}0.00001\right)^2\right]^{1/2}$$

$$= [(3188747961) + (1934425.79)]^{1/2} = 56486.125$$

$$\%\delta R_{q:765000\ W/m^2} = \frac{56486.125}{765000}\times 100 = 7.38\ \%$$

Appendix B: Excess Temperature and Heat Flux Plots of Dynamic Flat Surface Test Piece Experiments

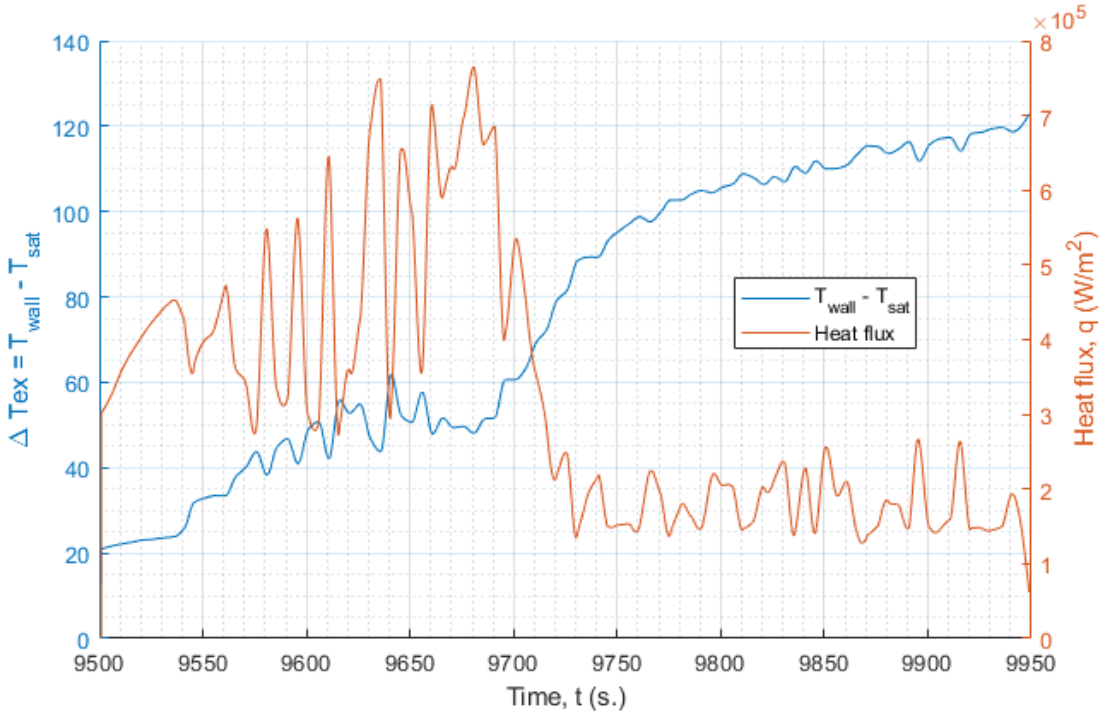

Figure B1: Heat flux and excess temperature for the stationary case with 5 °C sub-cooling.

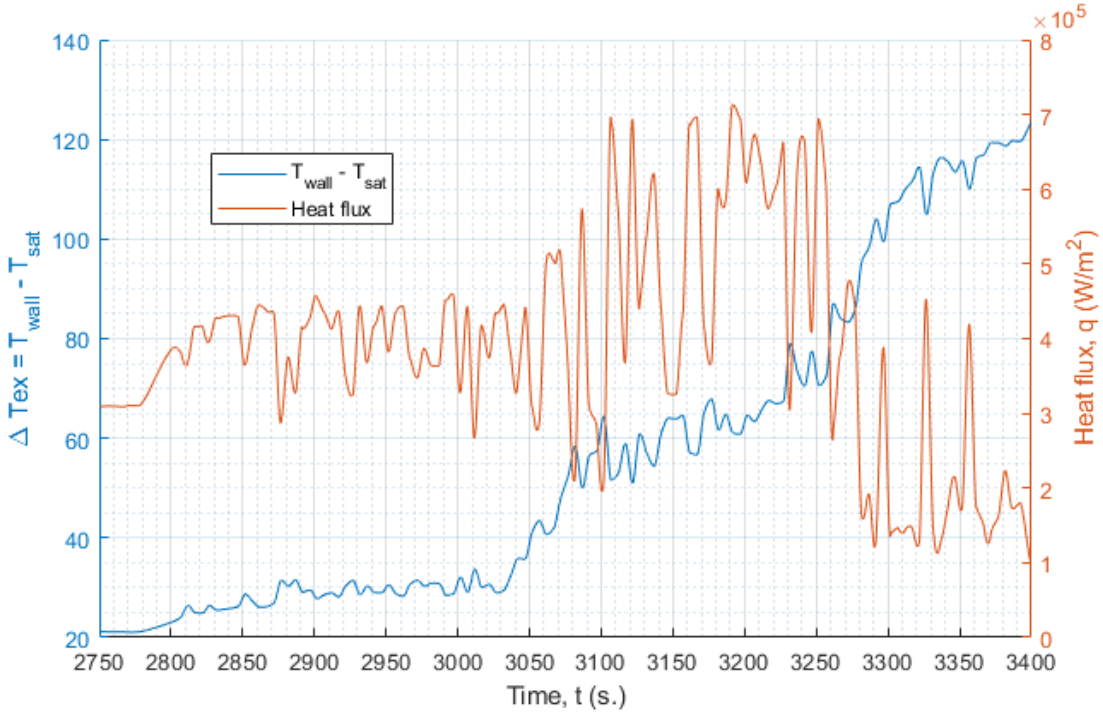

Figure B2: Heat flux and excess temperature for the 0.08 mm – 200 Hz vibration case with 5 °C sub-cooling.

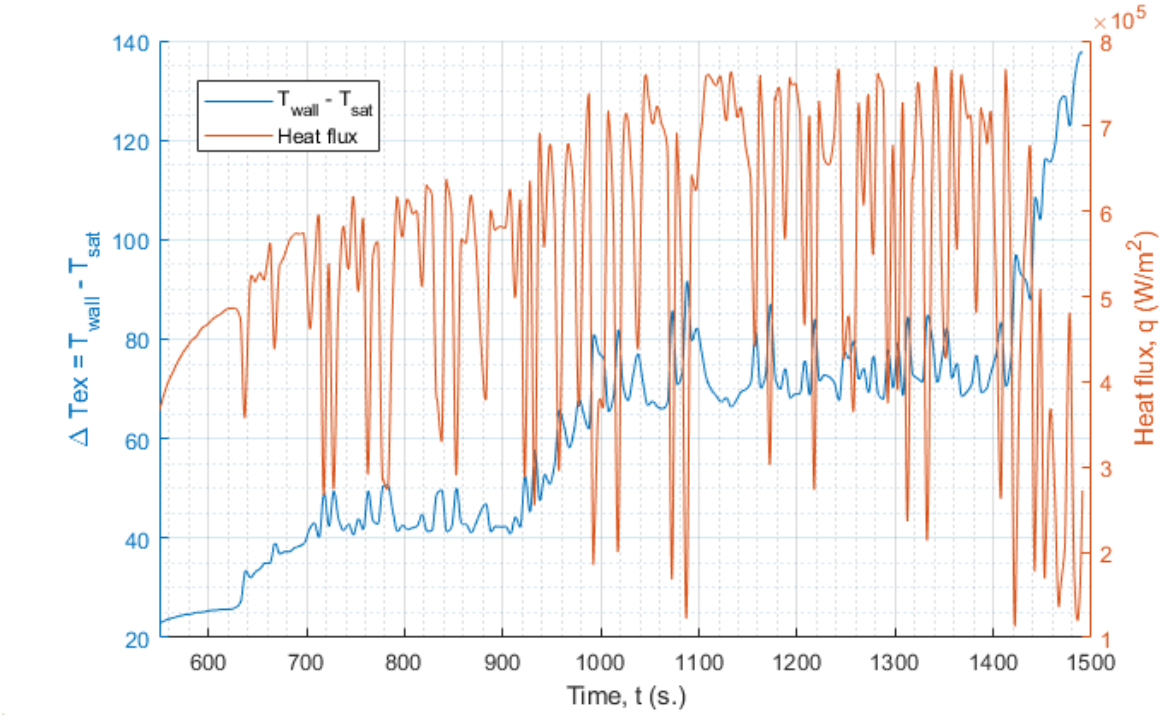

Figure B3: Heat flux and excess temperature for the 0.2 mm - 60 Hz vibration case with 5 °C sub-cooling.

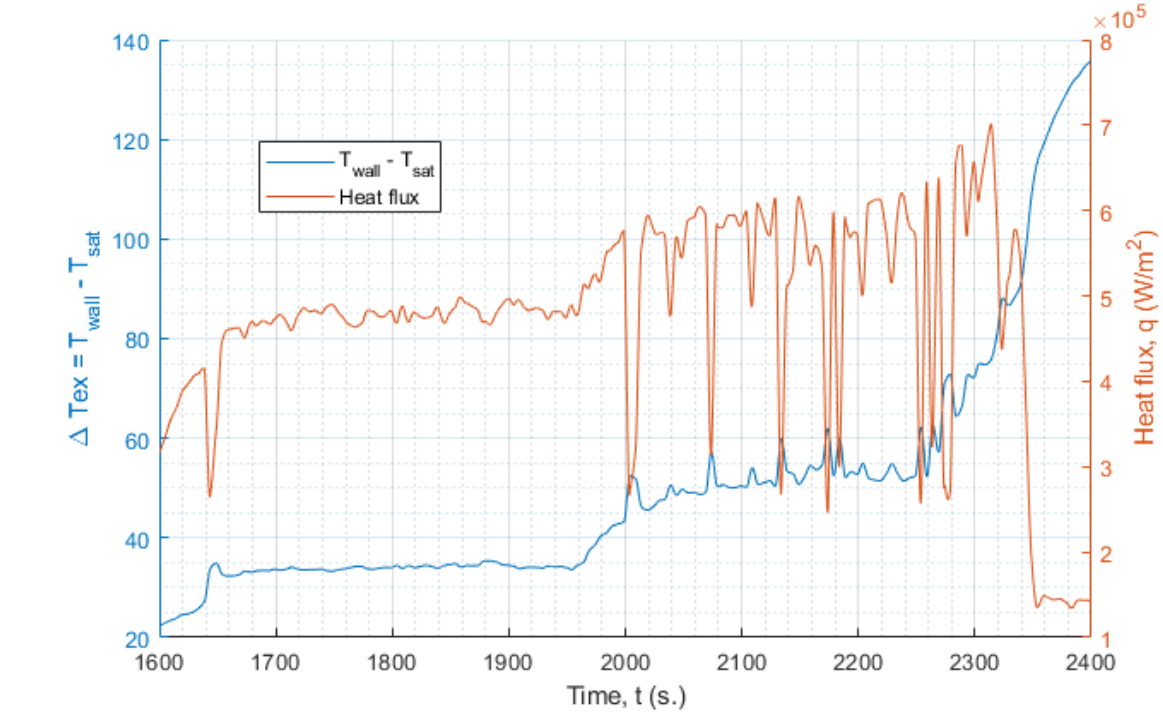

Figure B4: Heat flux and excess temperature for the 0.5 mm - 60 Hz vibration case with 5 °C sub-cooling.

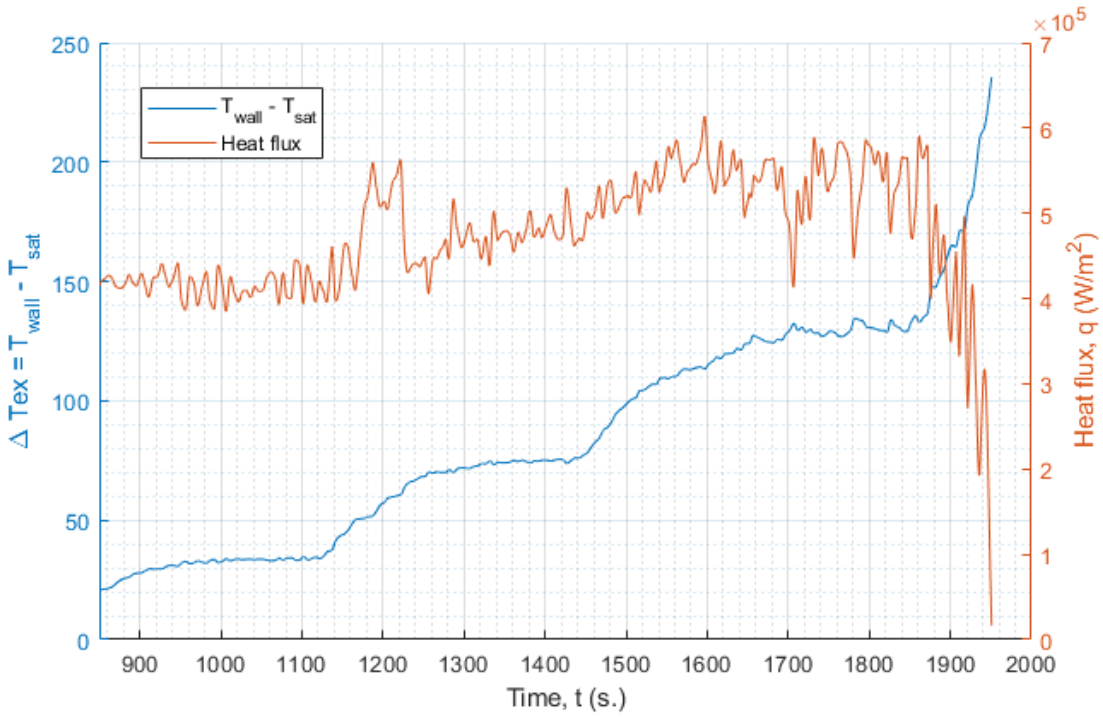

Figure B5: Heat flux and excess temperature for the 0.1 mm - 100 Hz vibration case with 5 ^{o}C sub-cooling.

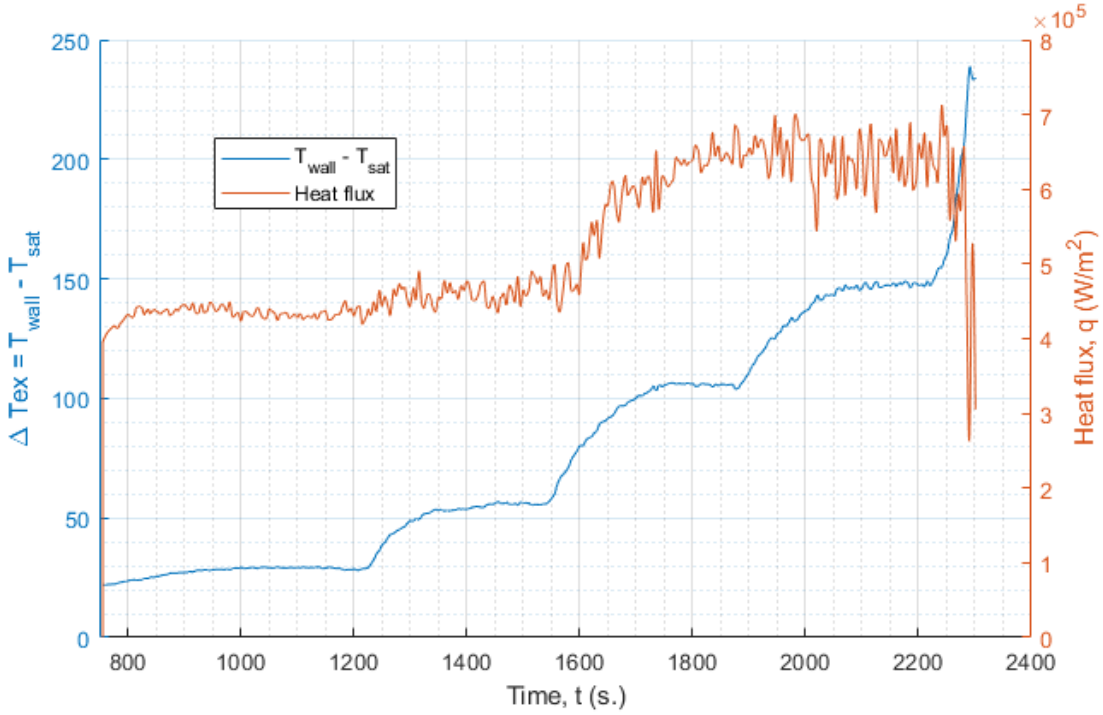

Figure B6: Heat flux and excess temperature for the 0.02 mm - 400 Hz vibration case with 5 ^{o}C sub-cooling.

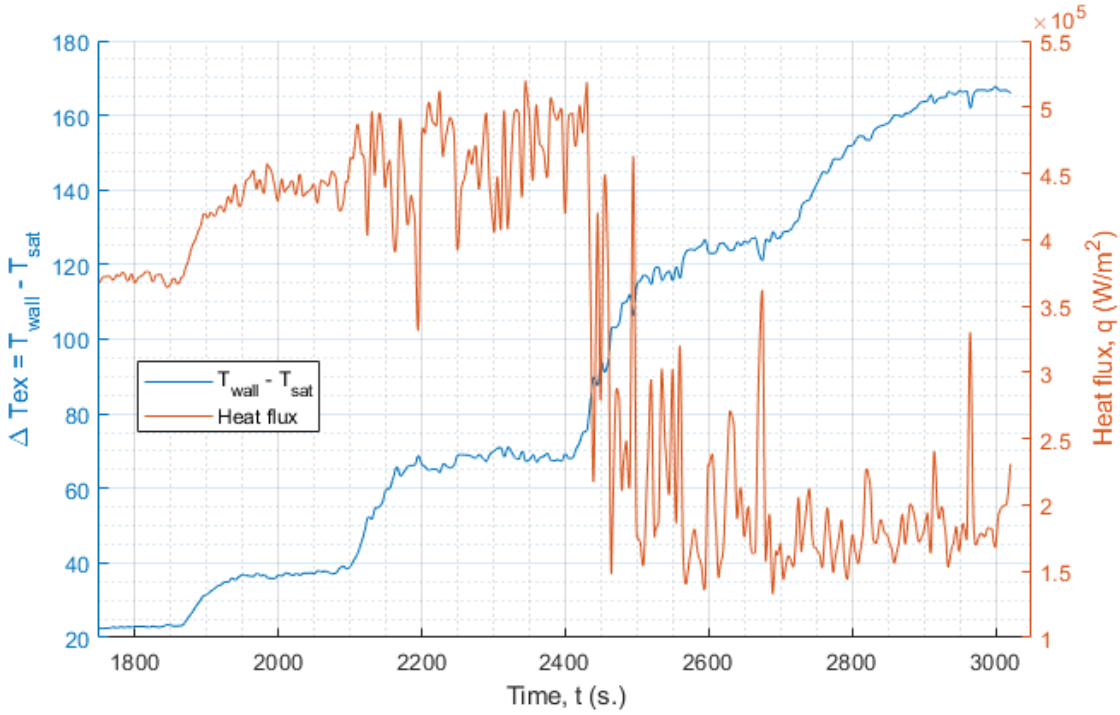

Figure B7: Heat flux and excess temperature for the 1 mm – 53.7 Hz vibration case with 5 ^{o}C sub-cooling.

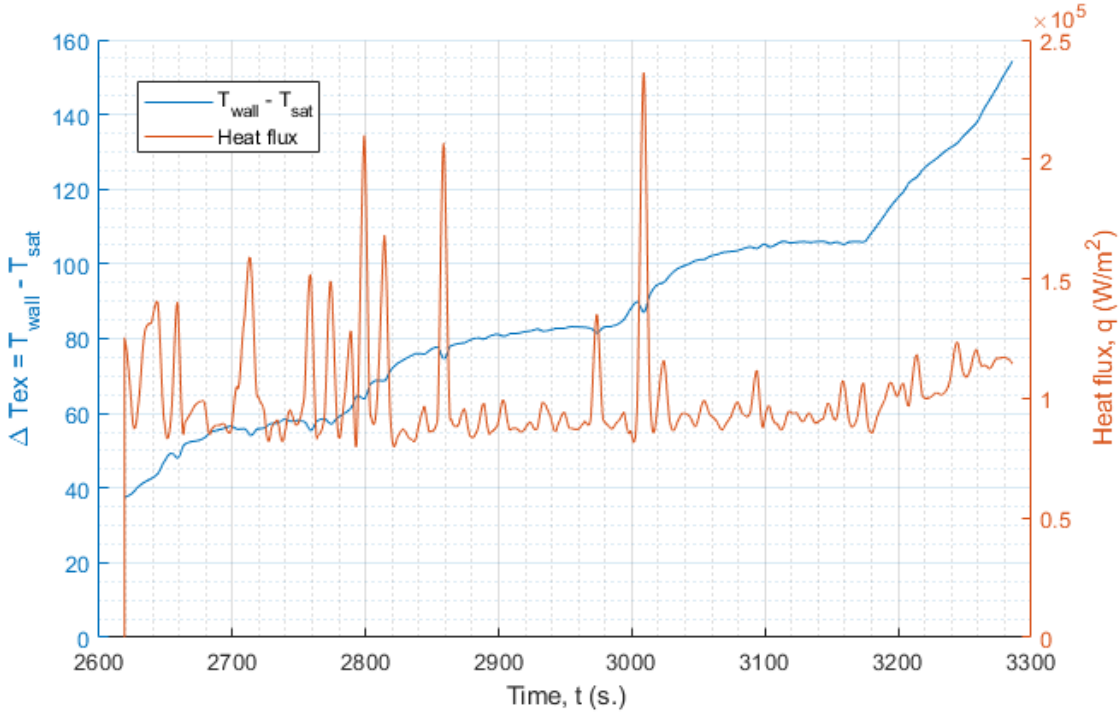

Figure B8: Heat flux and excess temperature for the 7 mm – 10 Hz vibration case with 5 ^{o}C sub-cooling.

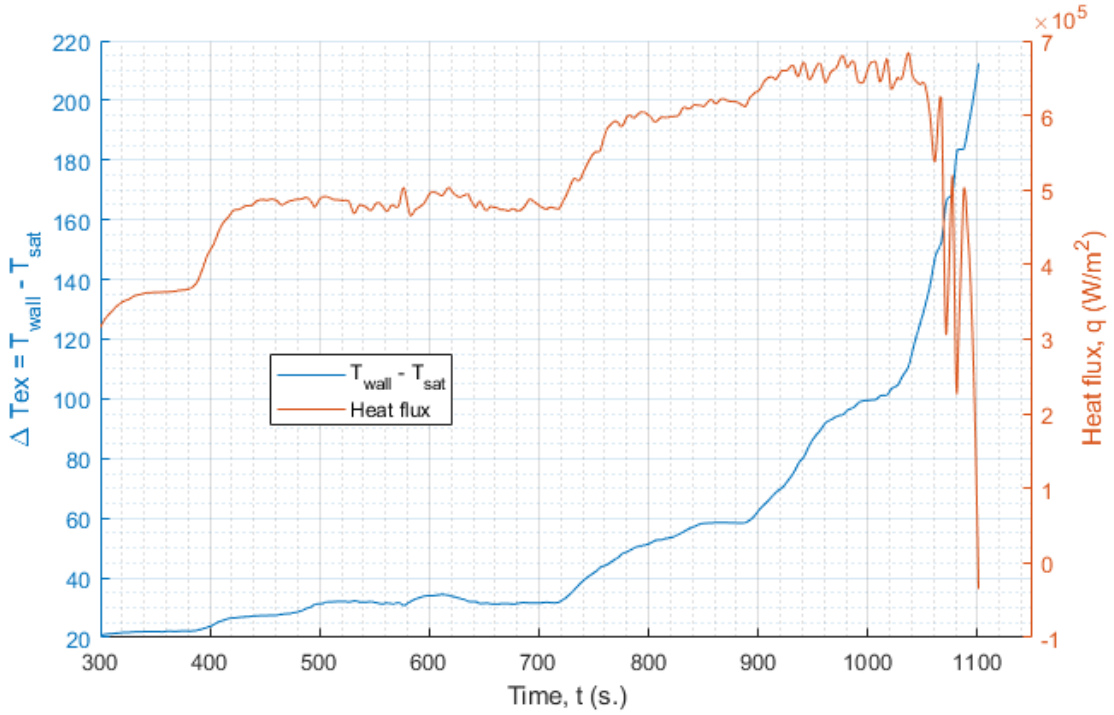

Figure B9: Heat flux and excess temperature for the 0.1 mm – 10 Hz vibration case with 5 °C sub-cooling.

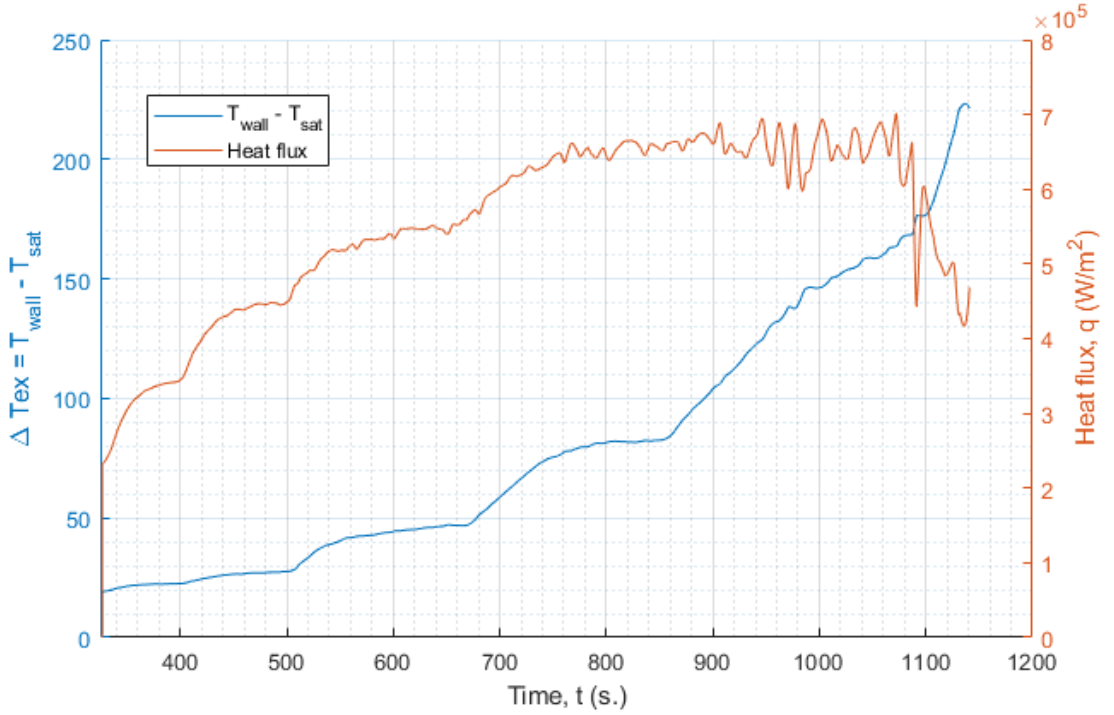

Figure B10: Heat flux and excess temperature for the 1 mm – 10 Hz vibration case with 5 °C sub-cooling.

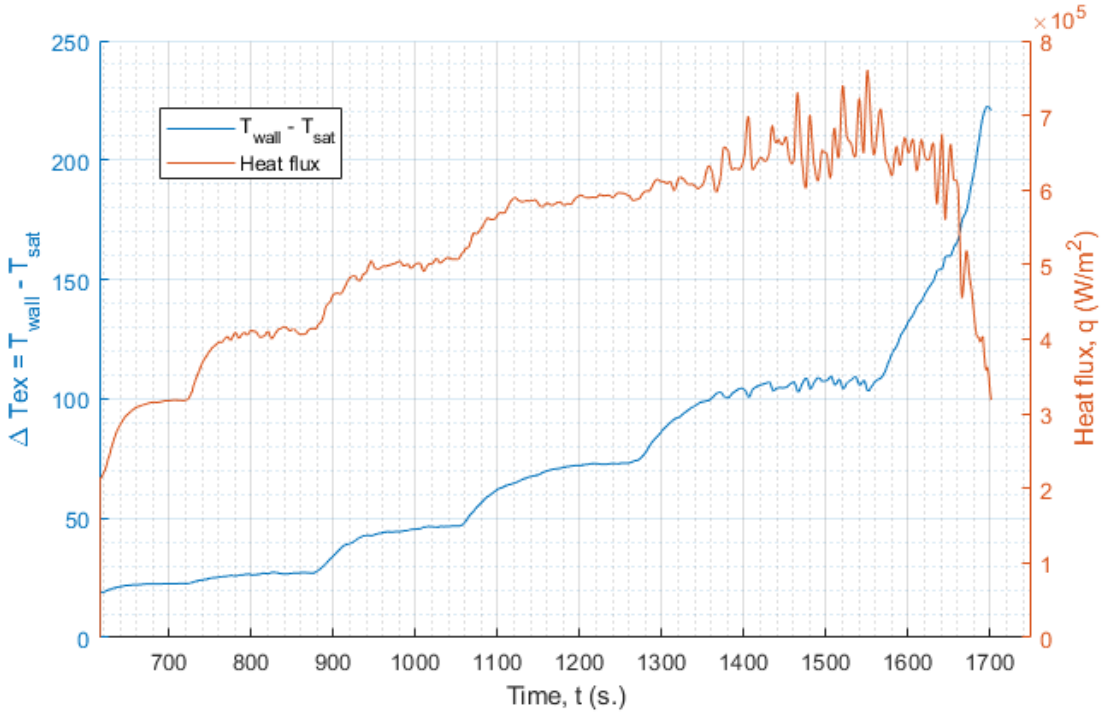

Figure B11: Heat flux and excess temperature for the 0.02 mm – 400 Hz vibration case with 15 °C sub-cooling.

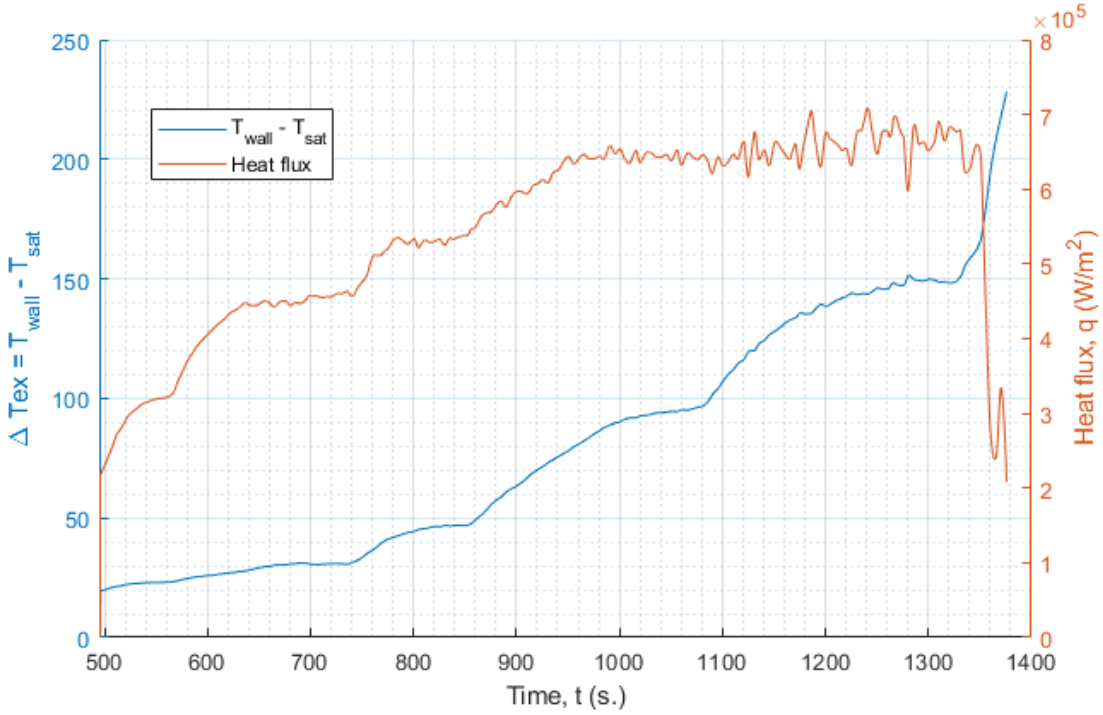

Figure B12: Heat flux and excess temperature for the 0.08 mm – 200 Hz vibration case with 15 °C sub-cooling.

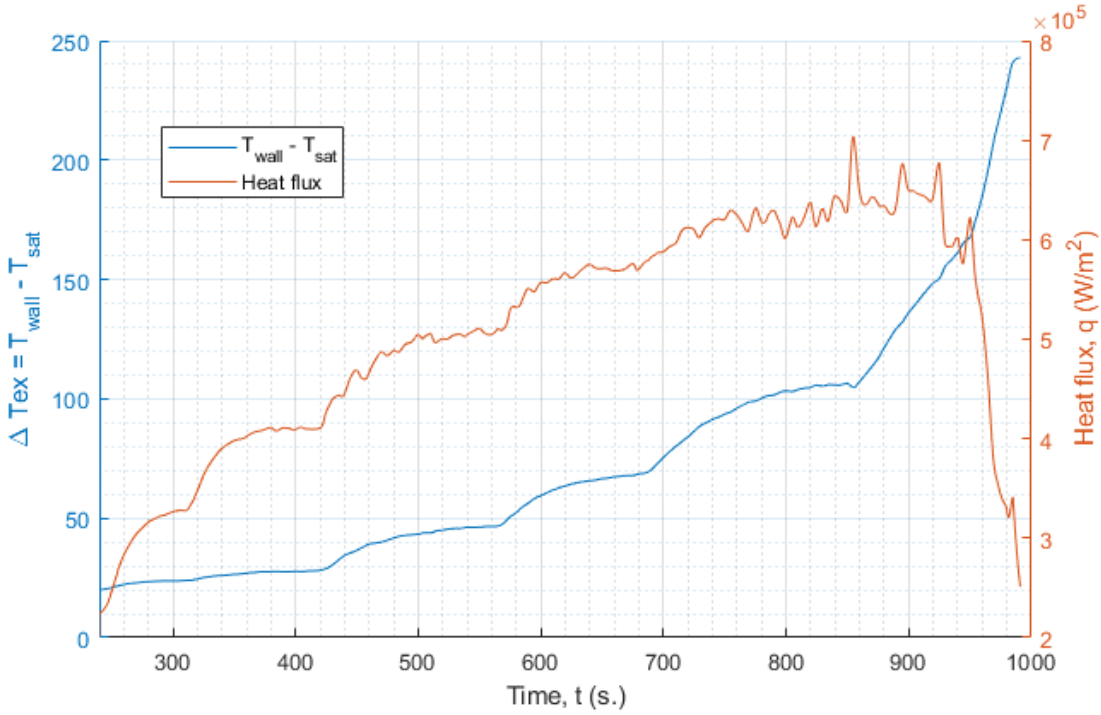

Figure B13: Heat flux and excess temperature for the 0.2 mm – 60 Hz vibration case with 15 ^{o}C sub-cooling.

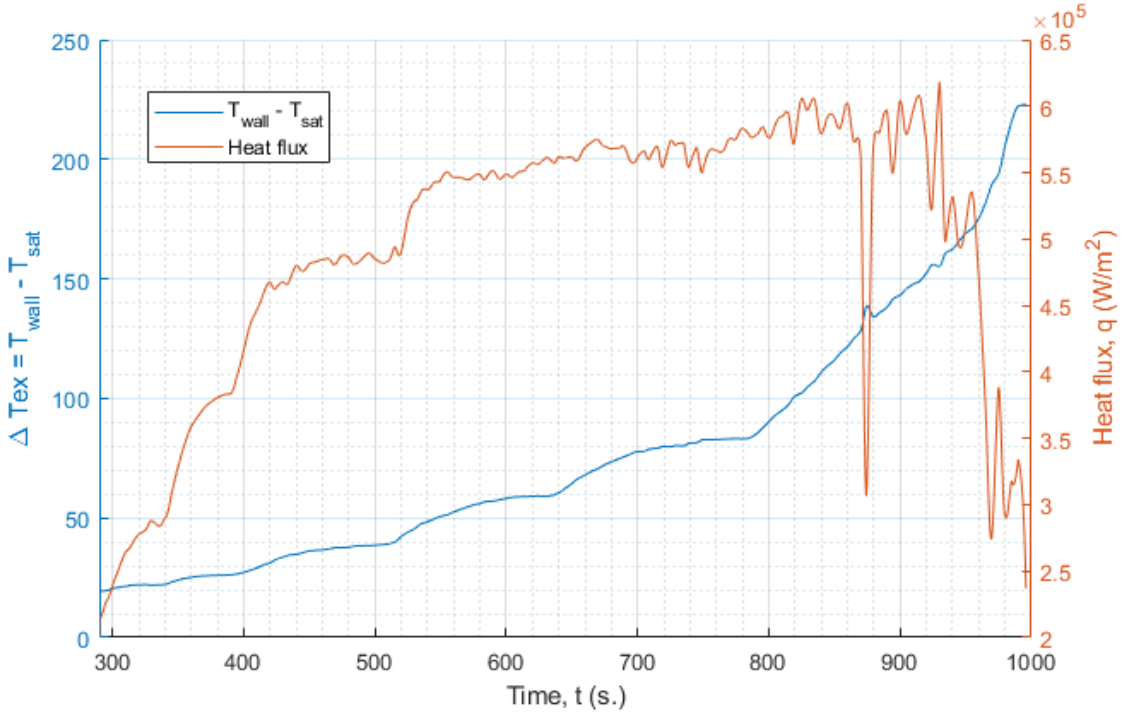

Figure B14: Heat flux and excess temperature for the 0.5 mm – 60 Hz vibration case with 15 ^{o}C sub-cooling.

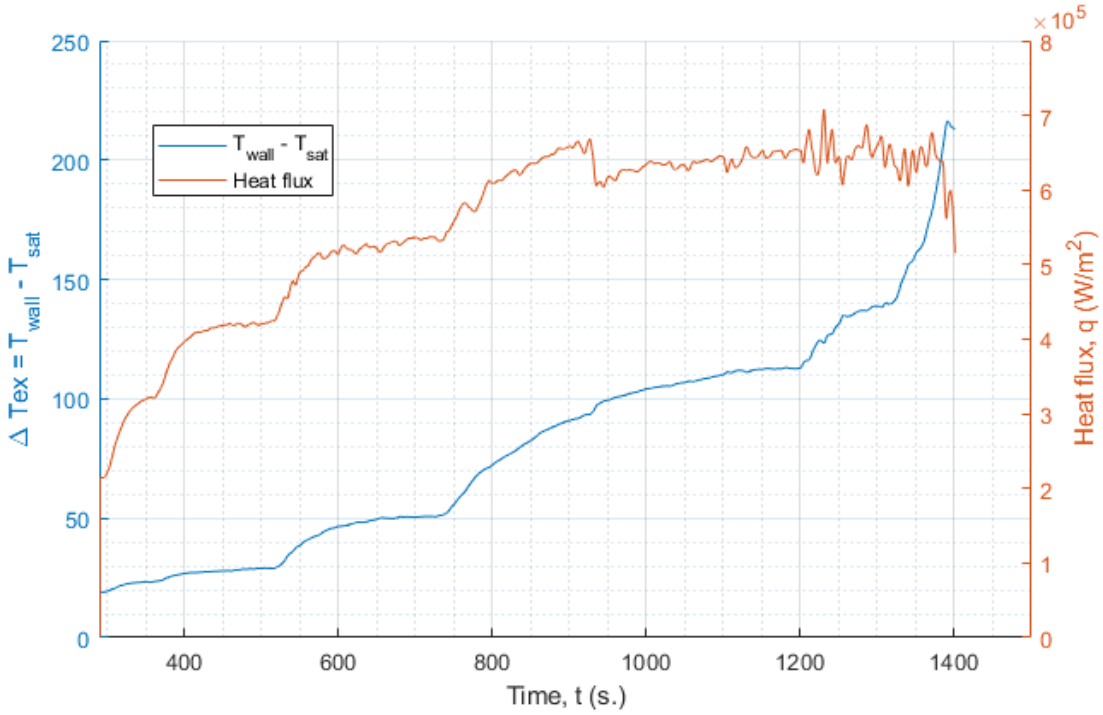

Figure B15: Heat flux and excess temperature for the 0.1 mm – 10 Hz vibration case with 15 °C sub-cooling.

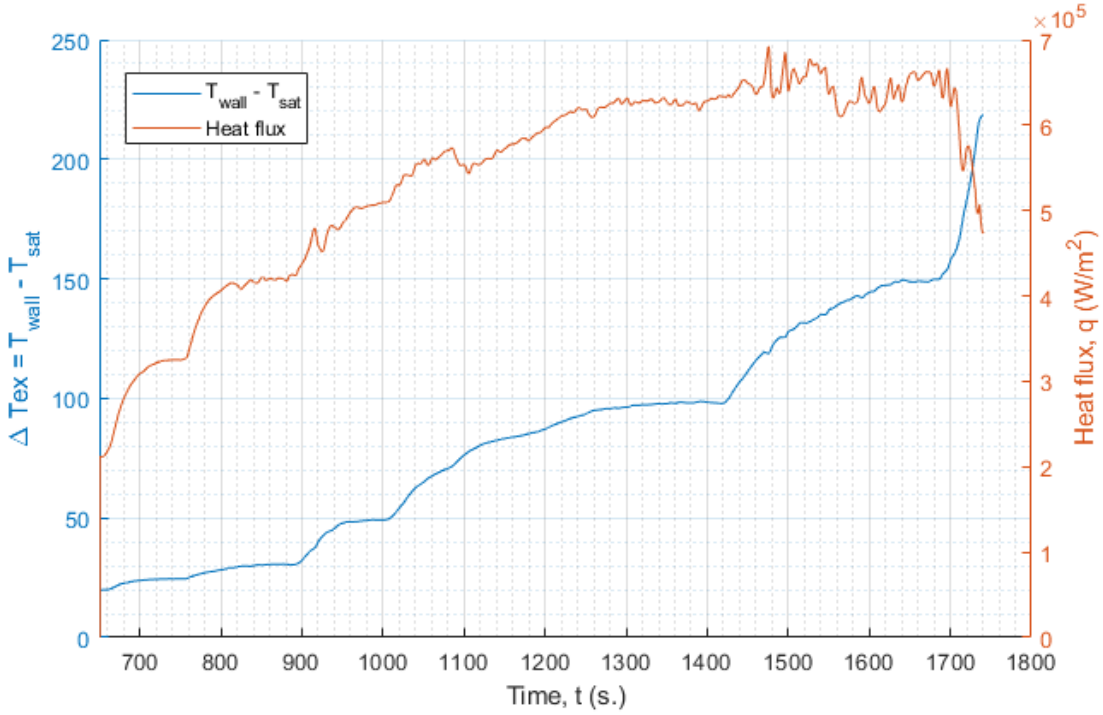

Figure B16: Heat flux and excess temperature for the 0.1 mm – 100 Hz vibration case with 15 °C sub-cooling.

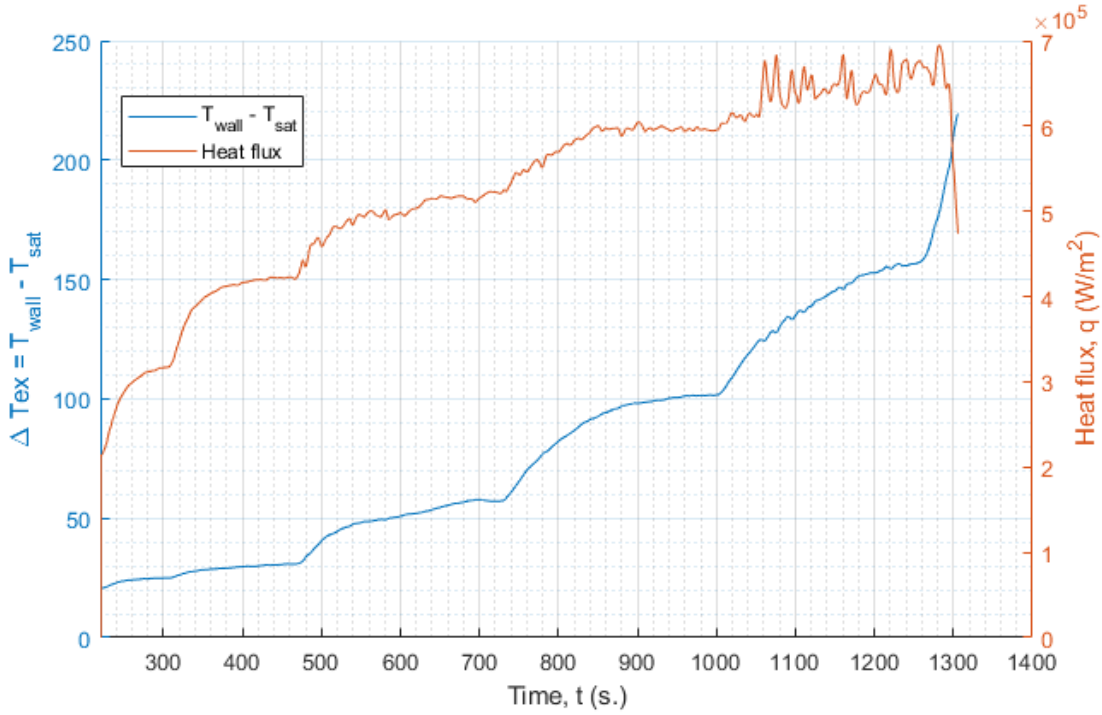

Figure B17: Heat flux and excess temperature for the 1 mm – 10 Hz vibration case with 15 ^{o}C sub-cooling.

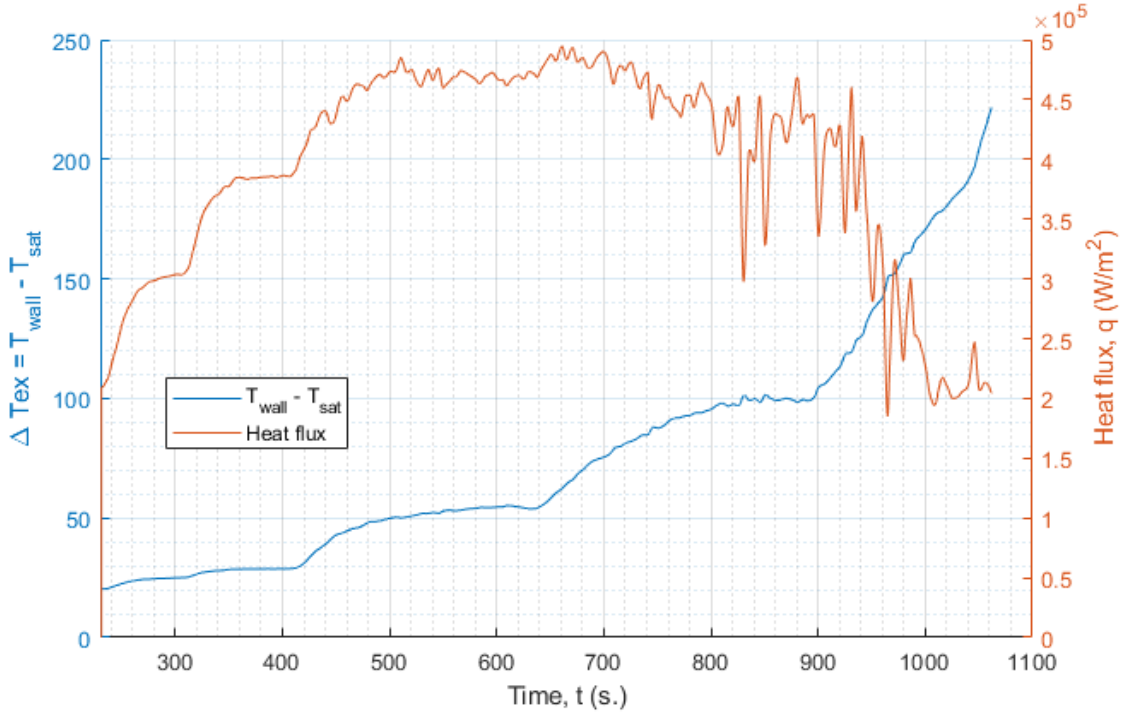

Figure B18: Heat flux and excess temperature for the 1 mm – 53.7 Hz vibration case with 15 ^{o}C sub-cooling.

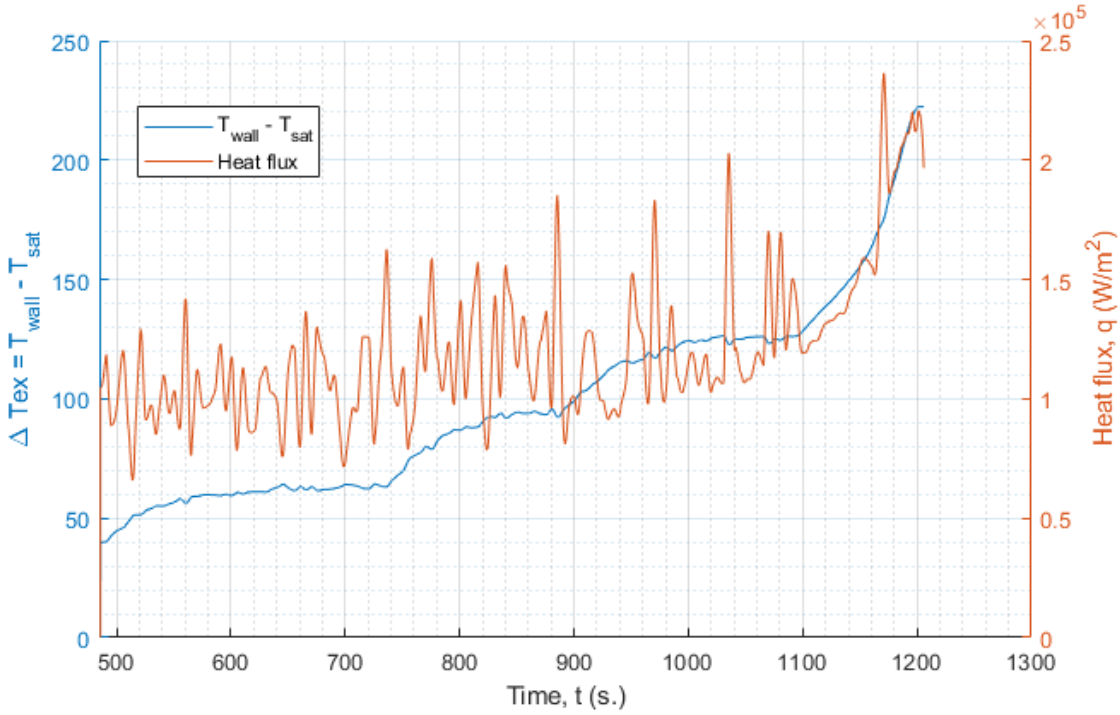

Figure B19: Heat flux and excess temperature for the 7 mm – 10 Hz vibration case with 15 ^{o}C sub-cooling.

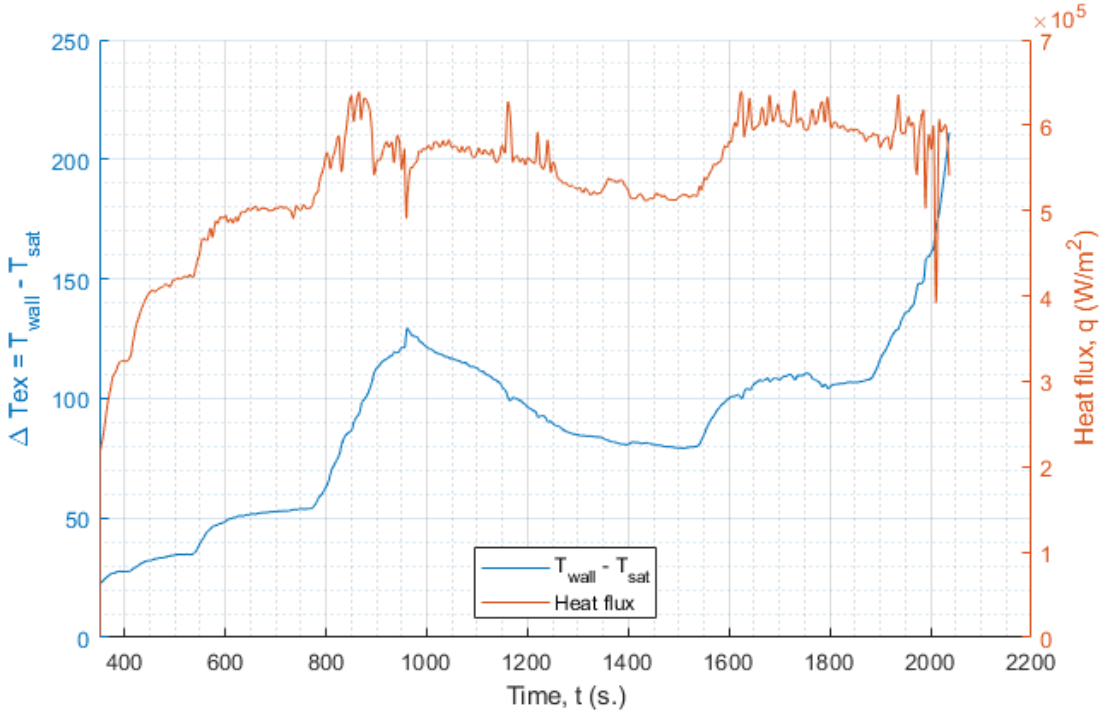

Figure B20: Heat flux and excess temperature for the stationary case with 15 ^{o}C sub-cooling.

Appendix C: Measured Test Piece Temperatures from the Dynamic Flat Surface Test Piece Experiments

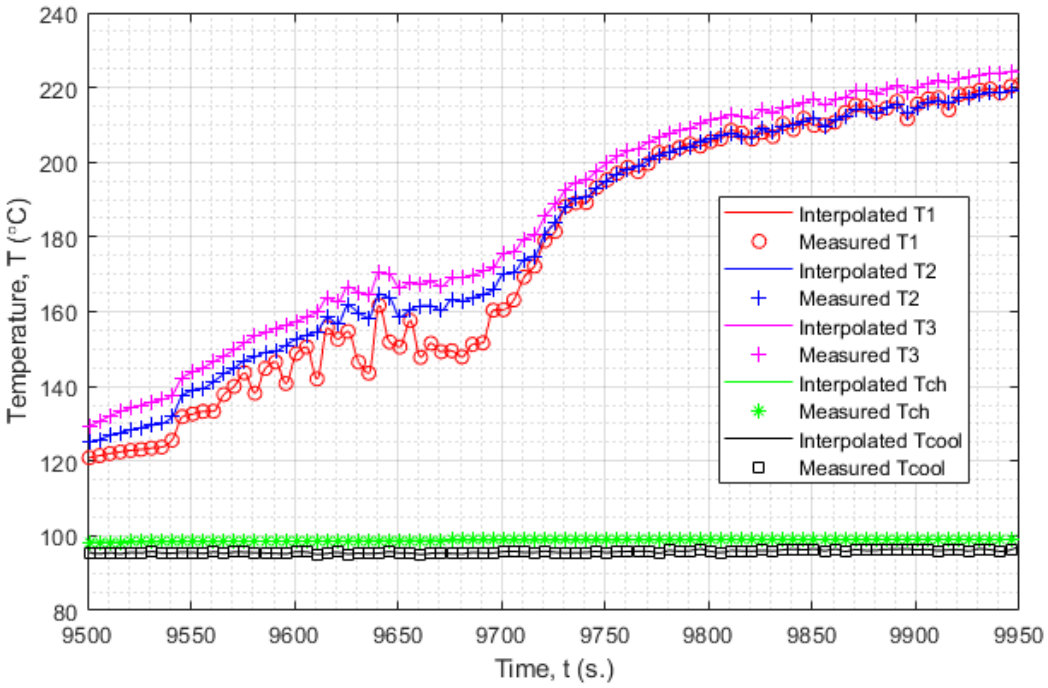

Figure C1: Measured test piece temperatures for the stationary case with 5 °C sub-cooling.

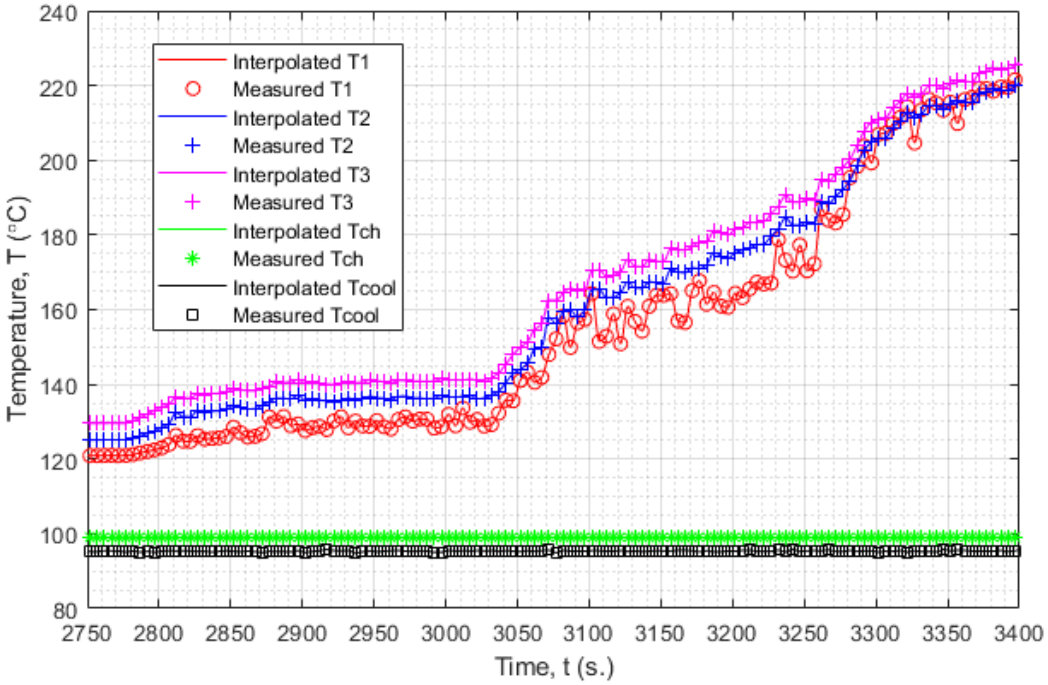

Figure C2: Measured test piece temperatures for the 0.08 mm - 200 Hz vibration case with 5 °C sub-cooling.

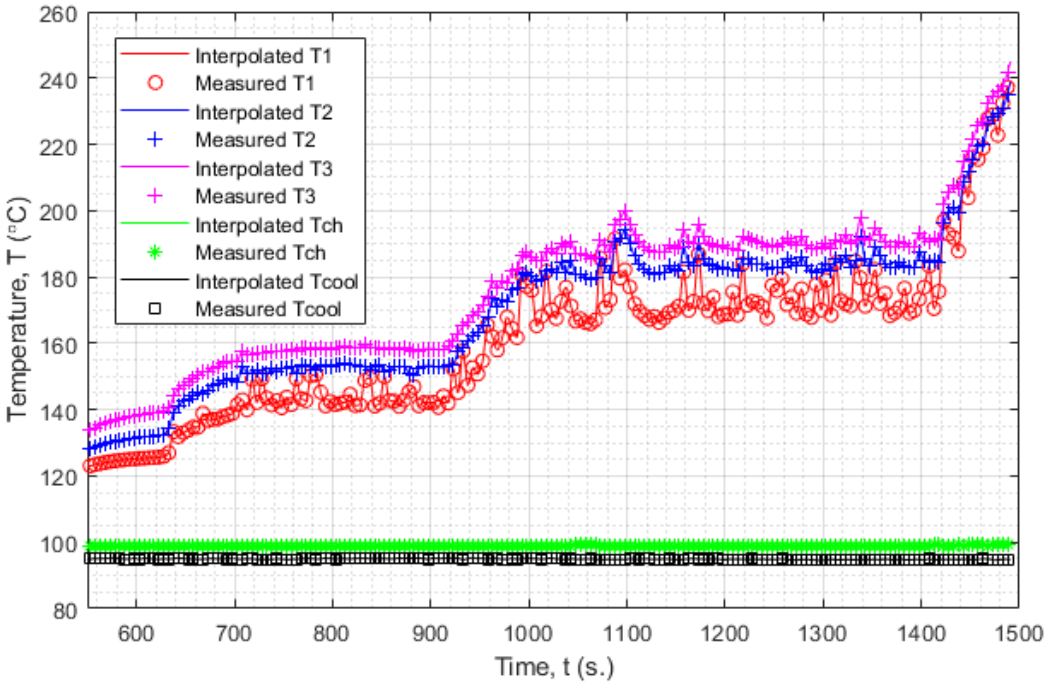

Figure C3: Measured test piece temperatures for the 0.2 mm - 60 Hz vibration case with 5 °C sub-cooling.

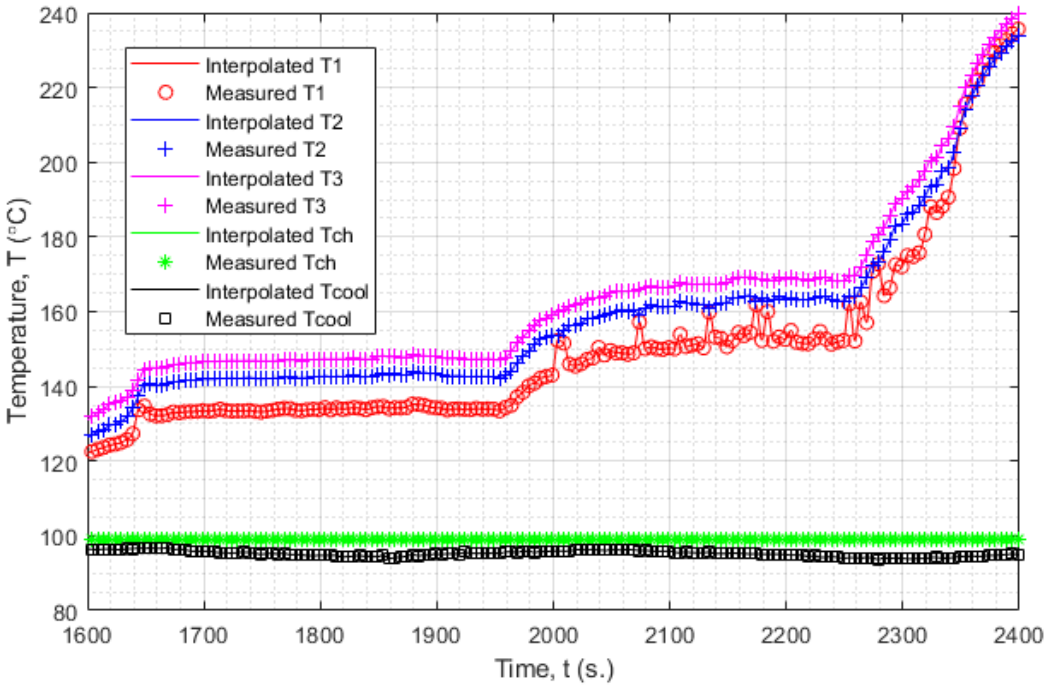

Figure C4: Measured test piece temperatures for the 0.5 mm - 60 Hz vibration case with 5 °C sub-cooling.

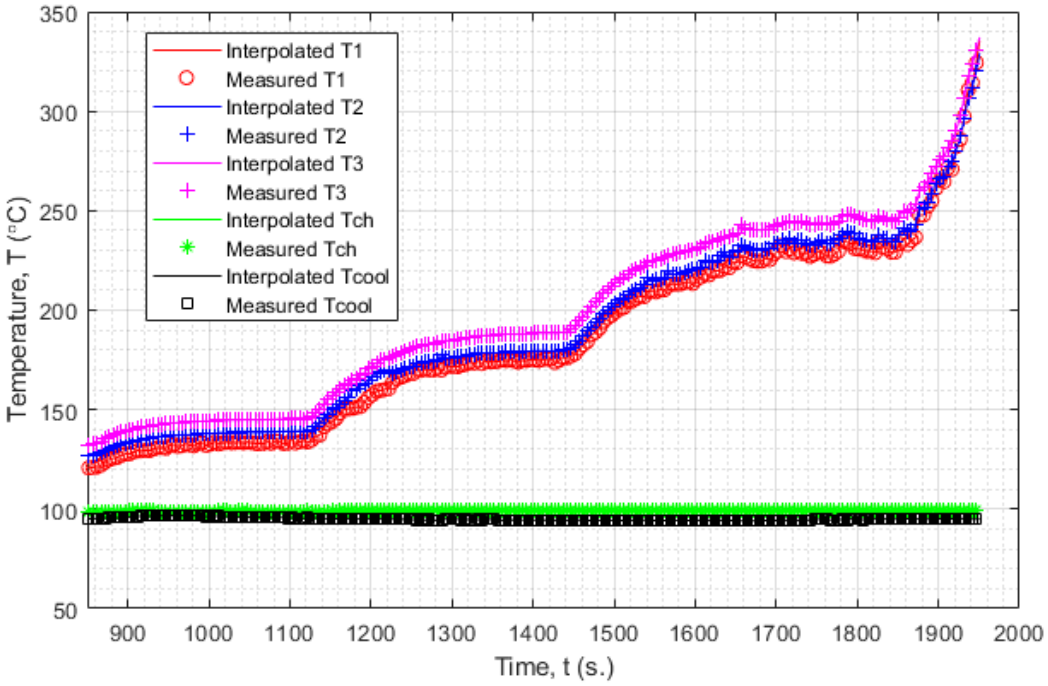

Figure C5: Measured test piece temperatures for the 0.1 mm - 100 Hz vibration case with 5 °C sub-cooling.

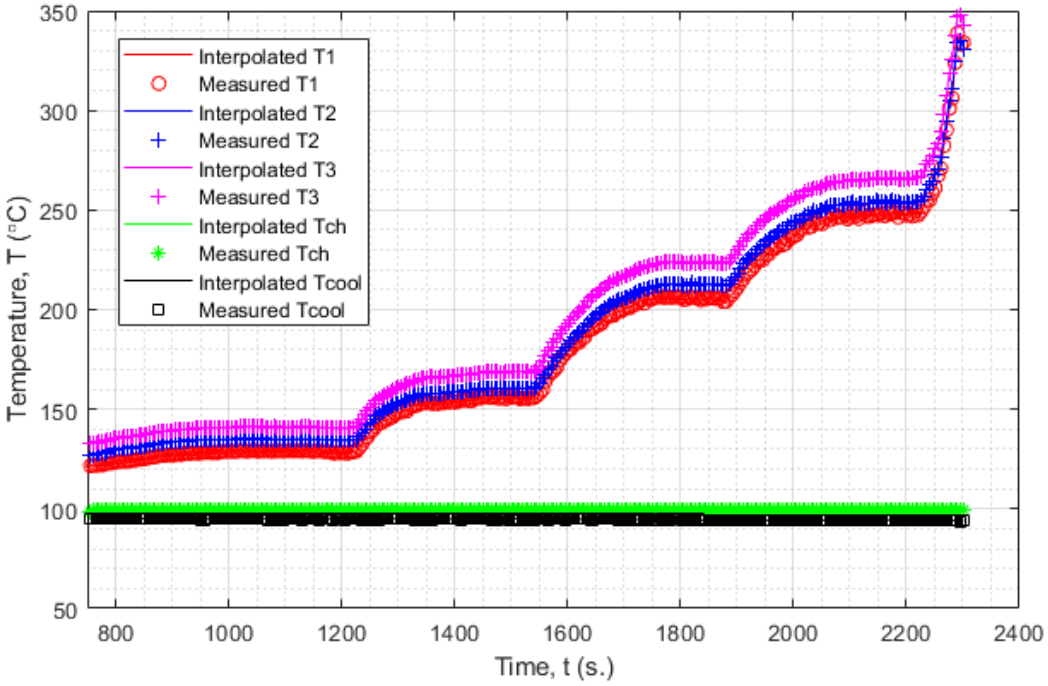

Figure C6: Measured test piece temperatures for the 0.02 mm - 400 Hz vibration case with 5 °C sub-cooling.

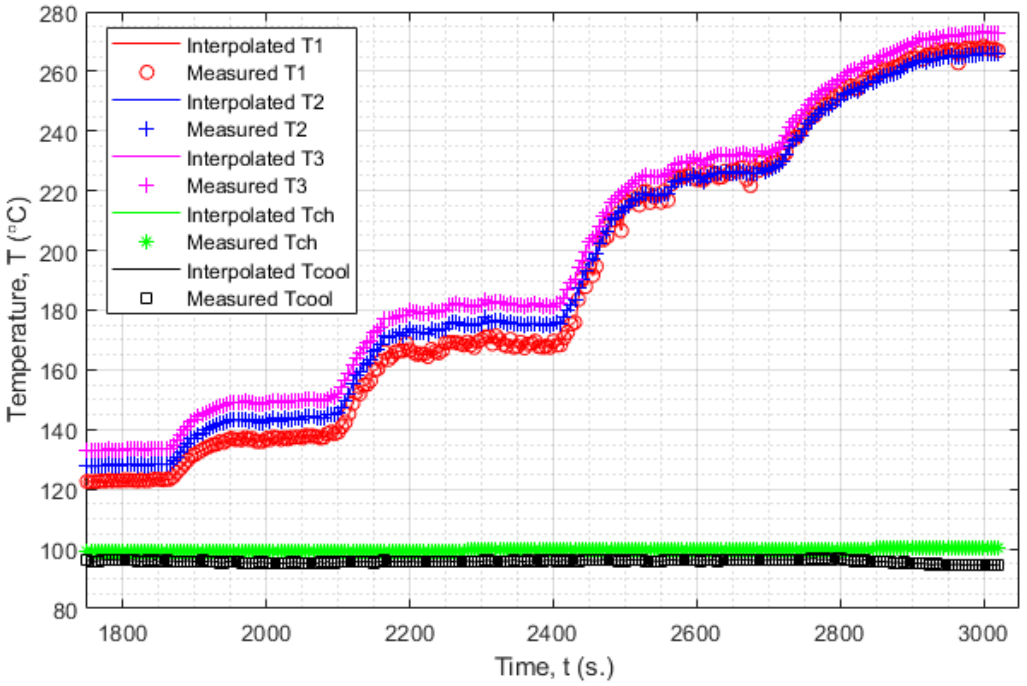

Figure C7: Measured test piece temperatures for the 1 mm – 53.7 Hz vibration case with 5 °C sub-cooling.

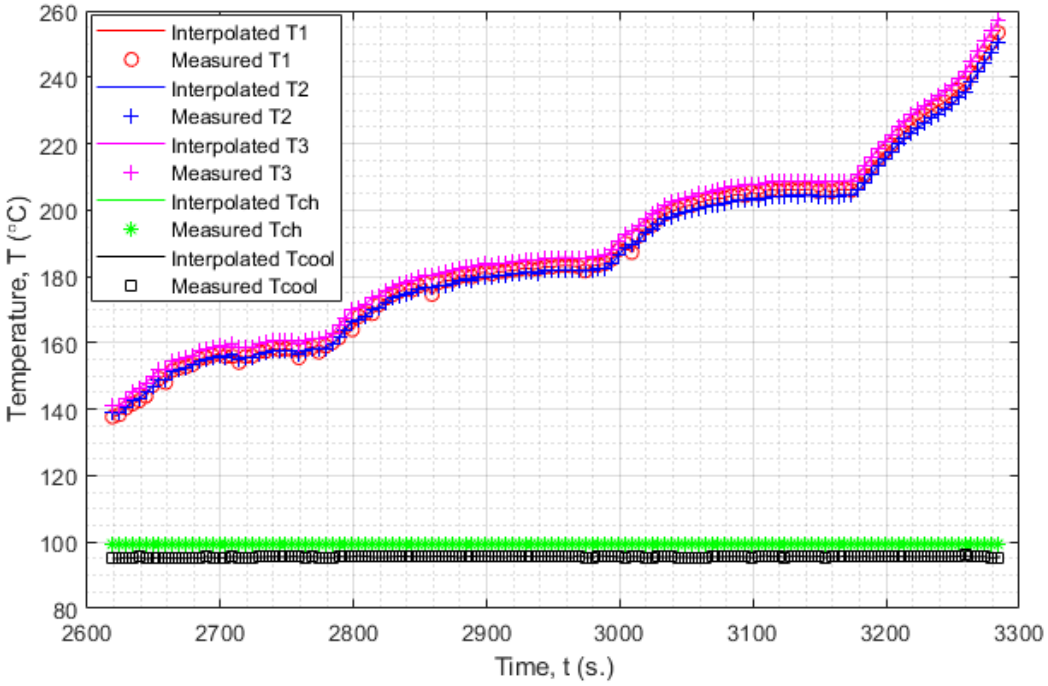

Figure C8: Measured test piece temperatures for the 7 mm – 10 Hz vibration case with 5 °C sub-cooling.

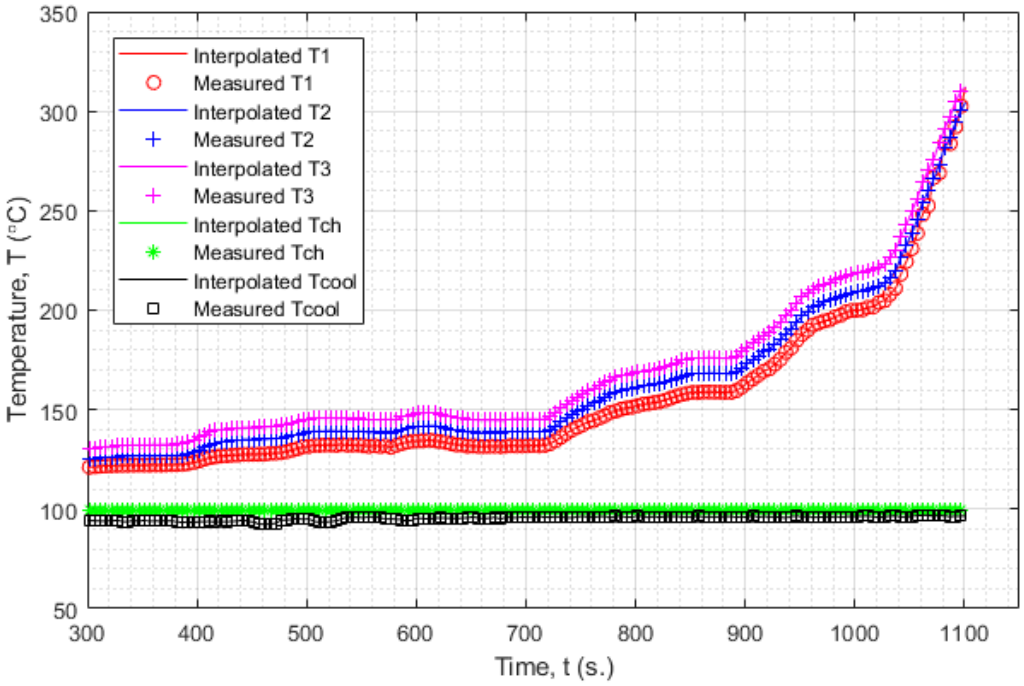

Figure C9: Measured test piece temperatures for the 0.1 mm – 10 Hz vibration case with 5 ^{o}C sub-cooling.

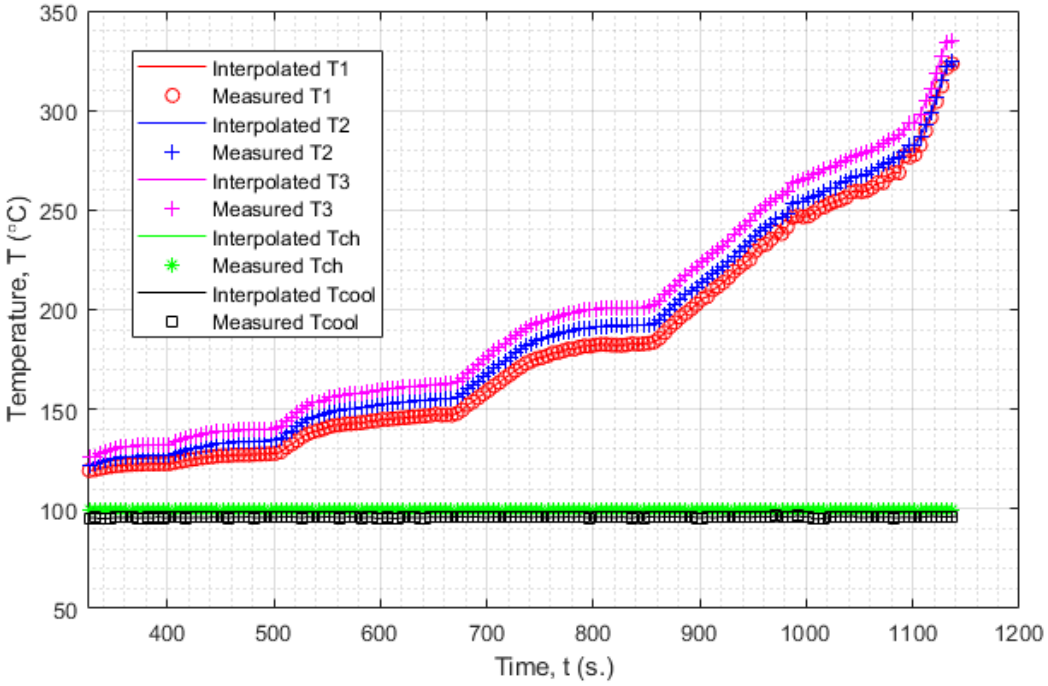

Figure C10: Measured test piece temperatures for the 1 mm – 10 Hz vibration case with 5 ^{o}C sub-cooling.

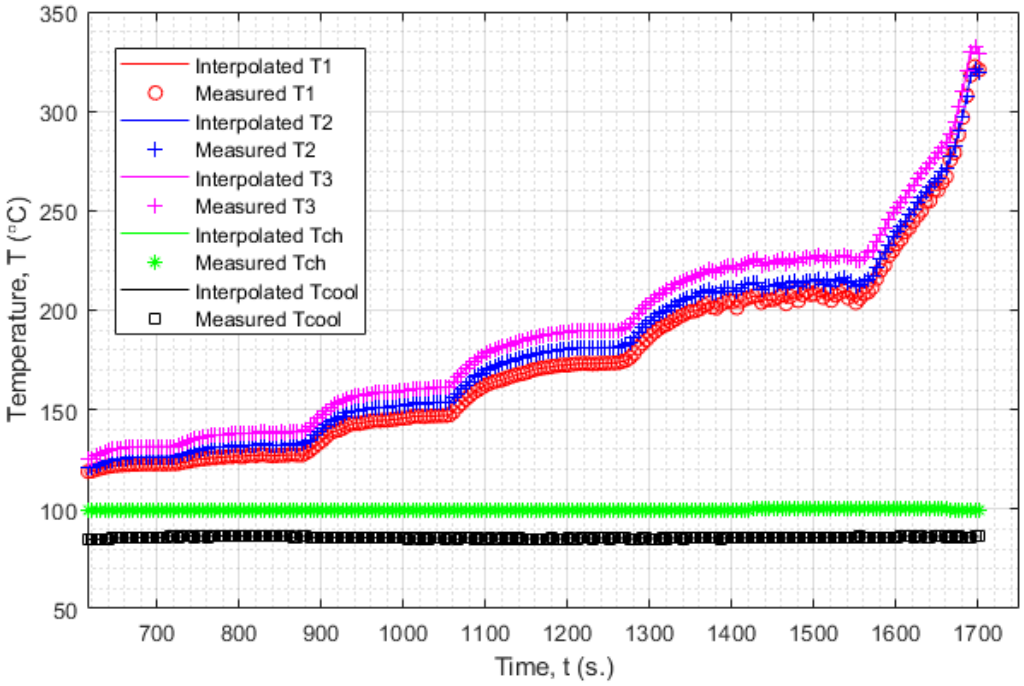

Figure C11: Measured test piece temperatures for the 0.02 mm – 400 Hz vibration case with 15 °C sub-cooling.

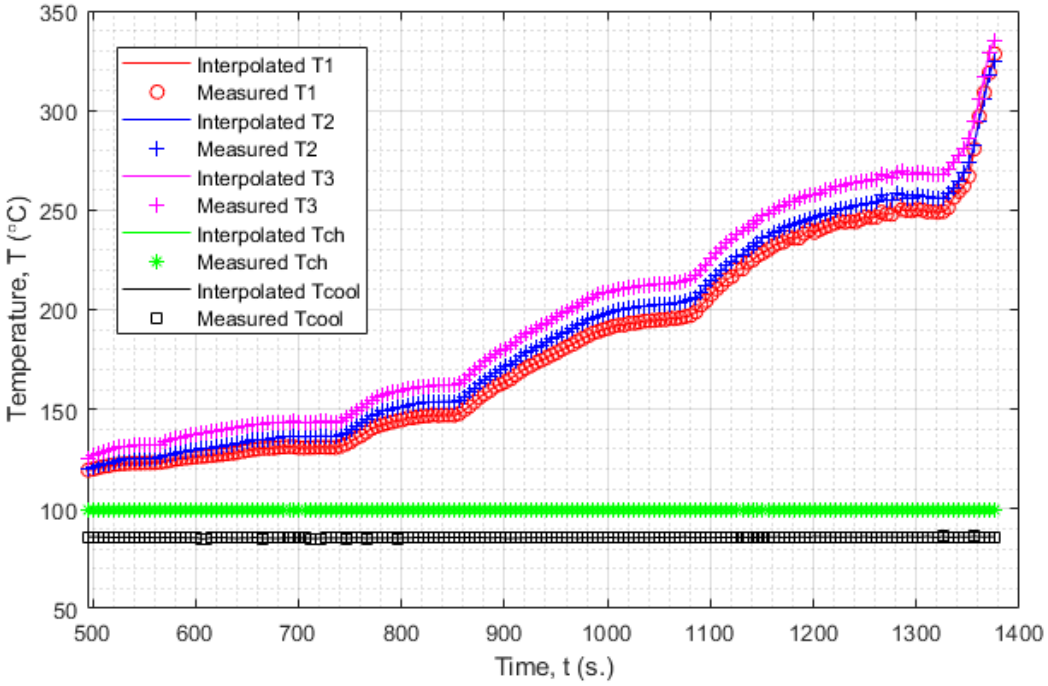

Figure C12: Measured test piece temperatures for the 0.08 mm – 200 Hz vibration case with 15 °C sub-cooling.

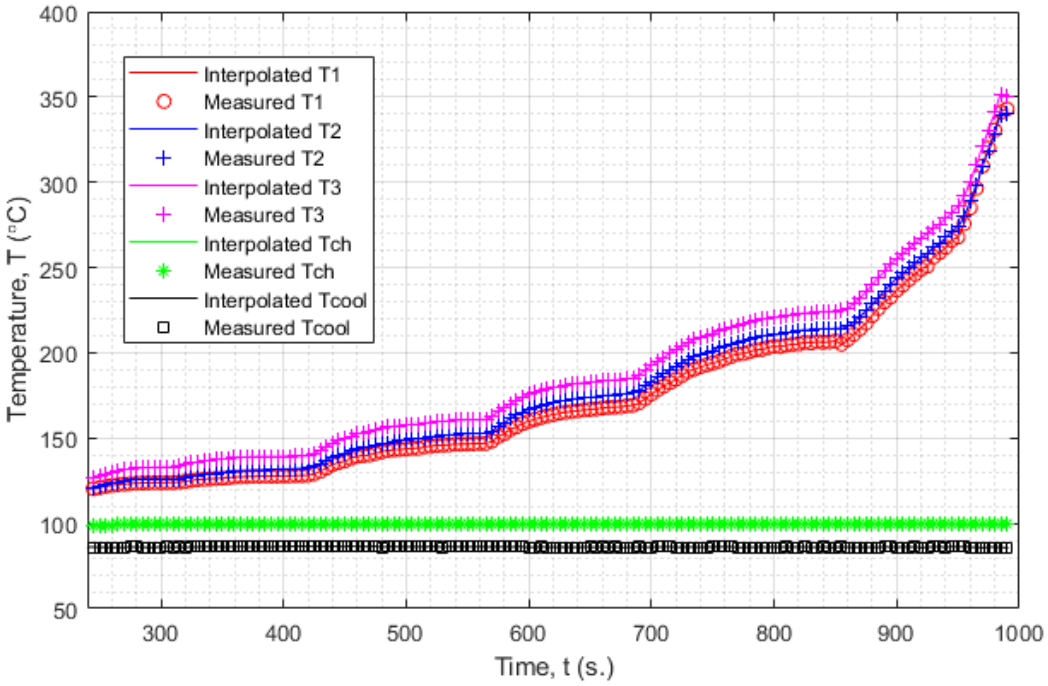

Figure C13: Measured test piece temperatures for the 0.2 mm – 60 Hz vibration case with 15 ^{o}C sub-cooling.

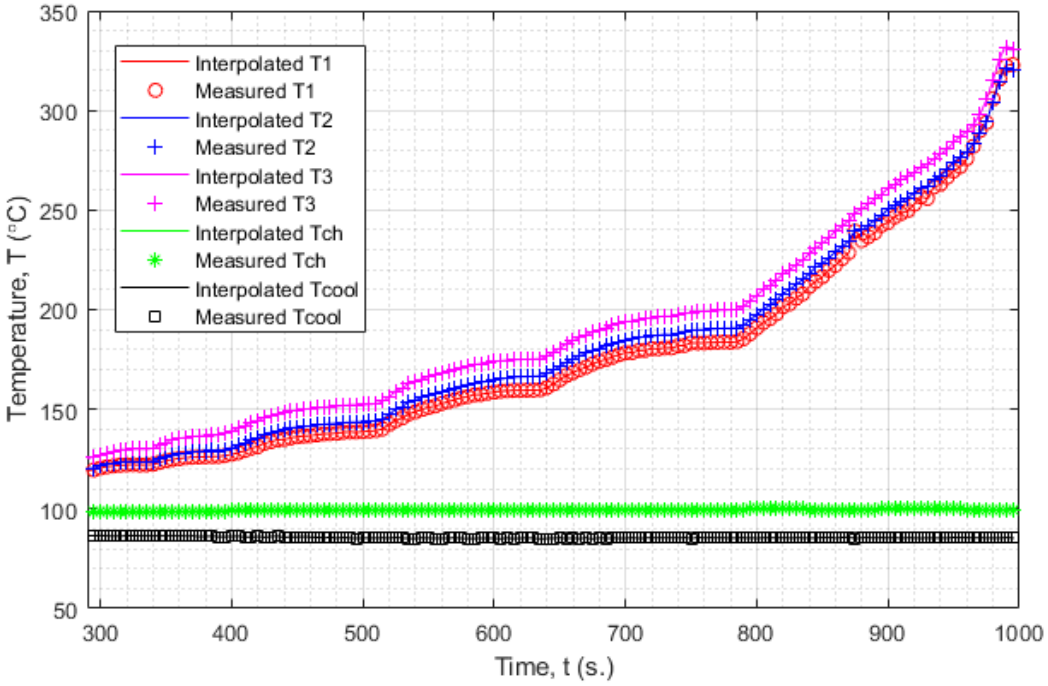

Figure C14: Measured test piece temperatures for the 0.5 mm – 60 Hz vibration case with 15 ^{o}C sub-cooling.

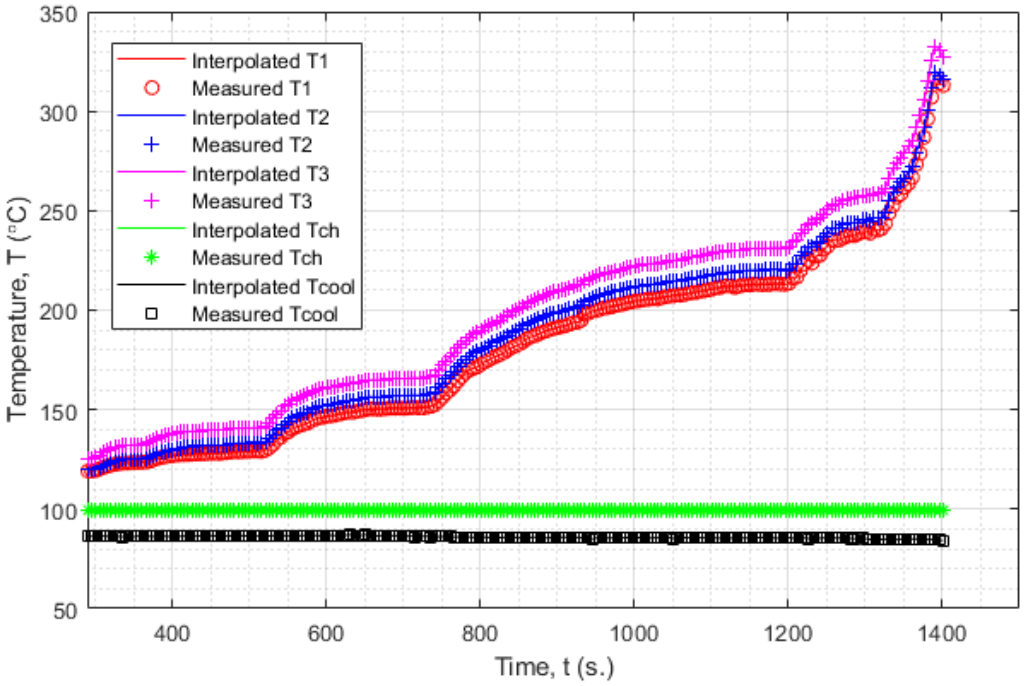

Figure C15: Measured test piece temperatures for the 0.1 mm – 10 Hz vibration case with 15 °C sub-cooling.

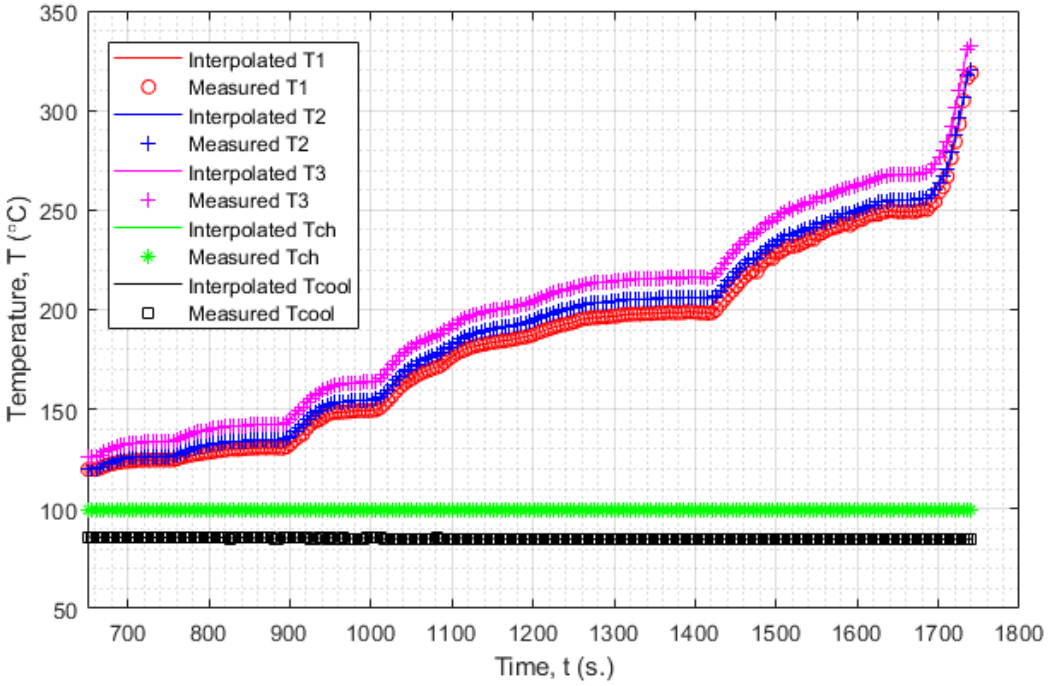

Figure C16: Measured test piece temperatures for the 0.1 mm – 100 Hz vibration case with 15 °C sub-cooling.

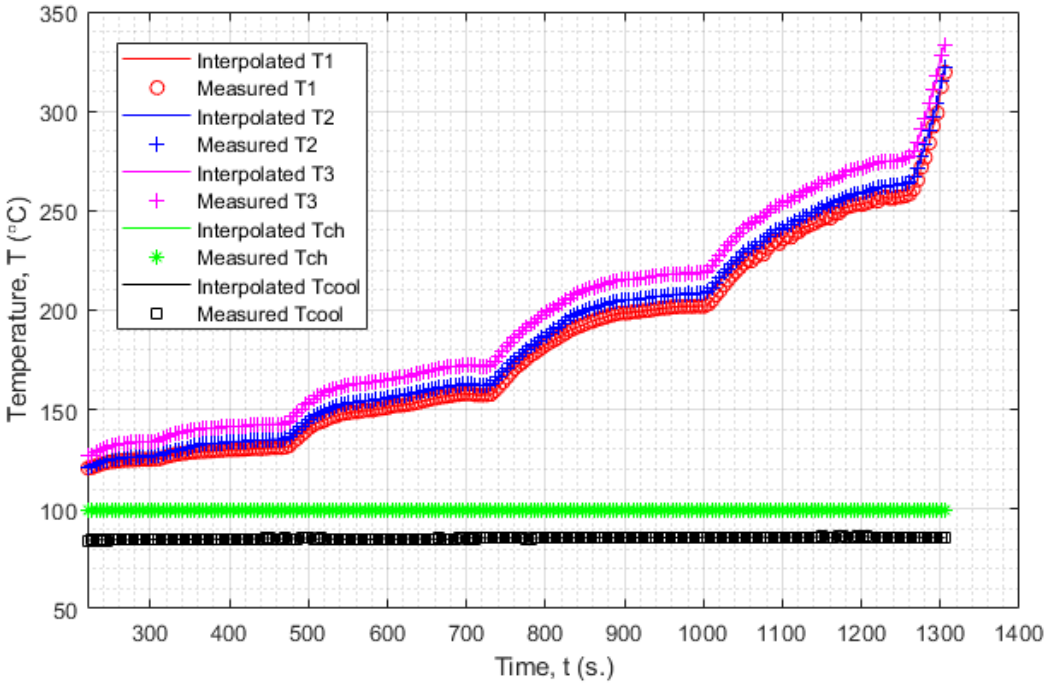

Figure C17: Measured test piece temperatures for the 1 mm – 10 Hz vibration case with 15 °C sub-cooling.

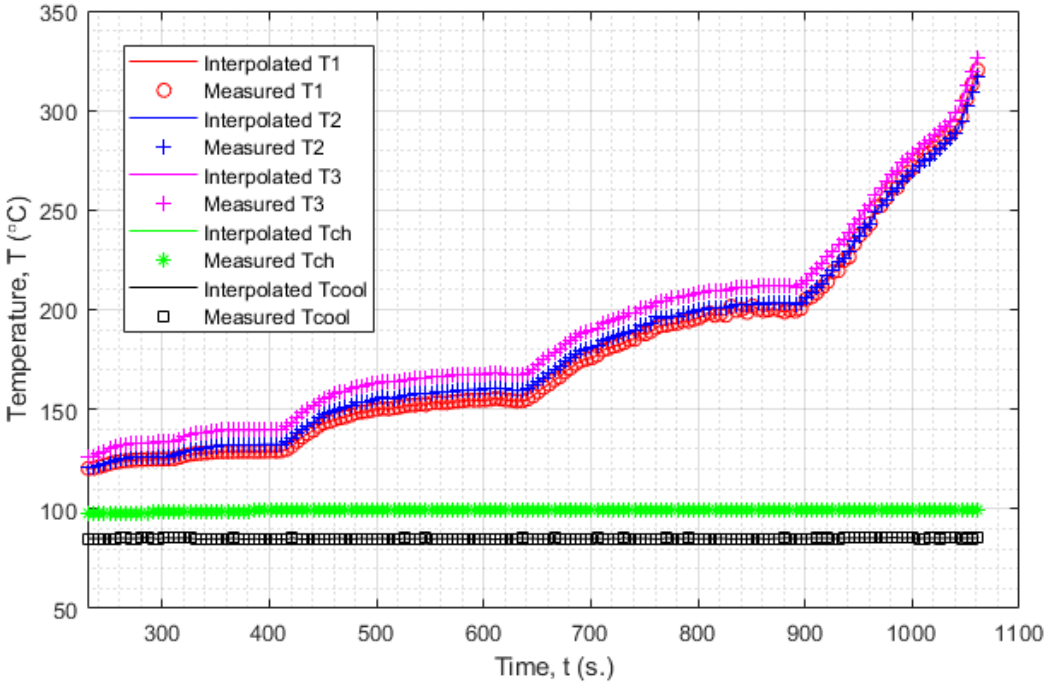

Figure C18: Measured test piece temperatures for the 1 mm – 53.7 Hz vibration case with 15 °C sub-cooling.

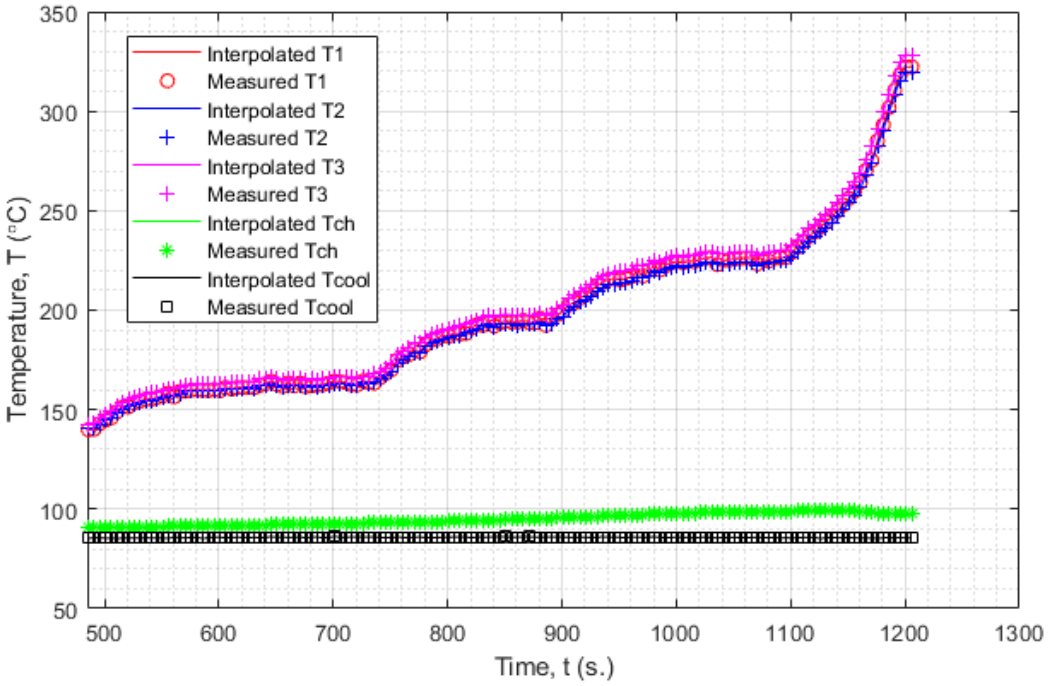

Figure C19: Measured test piece temperatures for the 7 mm – 10 Hz vibration case with 15 °C sub-cooling.

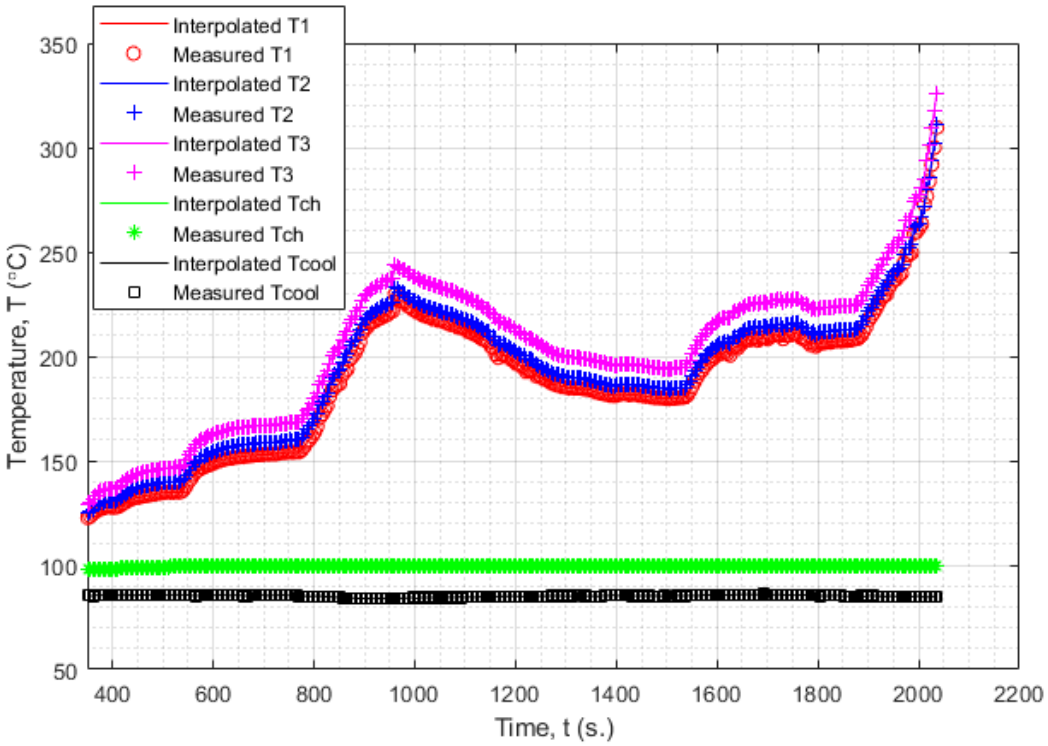

Figure C20: Measured test piece temperatures for the stationary case with 15 °C sub-cooling.

List of Author's Publications

1.) Jose, Jisjoe, Julian Dunne, Jean-Pierre Pirault, and Christopher Long. 2018. “Spray Evaporative Cooling System Design for Automotive Internal Combustion Engines.” In , V002T07A008. https://doi.org/10.1115/ICEF2018-9659.

2.) Langari, M., Zhiyin Yang, J.F. Dunne, S. Jafari, J.-P Pirault, C. Long, and J. Jose. 2018a. “Conjugate Heat Transfer Predictions for Subcooled Boiling Flow in a Horizontal Channel Using a Volume-of-Fluid Framework.” *Journal of Heat Transfer* 140 (July). https://doi.org/10.1115/1.4040358.

3.) Jafari, Soheil, Julian Dunne, Mostafa Langari, Zhiyin Yang, Jean-Pierre Pirault, Chris Long, and Jisjoe Jose. 2018. “CONTROL OF SPRAY EVAPORATIVE COOLING IN AUTOMOTIVE IC ENGINES.” *Journal of Thermal Science and Engineering Applications* 10 (March). https://doi.org/10.1115/1.4039701.

4.) Langari, M, Zhiyin Yang, JF Dunne, S Jafari, J-P Pirault, CA Long, and JT Jose. 2018b. “Multiphase Computational Fluid Dynamics–Conjugate Heat Transfer for Spray Cooling in the Non-Boiling Regime.” *The Journal of Computational Multiphase Flows* 10 (March): 1757482X1774692. https://doi.org/10.1177/1757482X17746921.

5.) Langari, M., J. Dunne, S. Jafari, J-P Pirault, Zhiyin Yang, C. Long, and J. Jose. 2017. “A Benchmark Analysis of Subcooled Heat Transfer in a Novel Half-Unit-Cylinder-Head for Verifying in-Vehicle Engine Evaporative Cooling under Dynamic Conditions.” In .

6.) Jafari, Soheil, Julian Dunne, Mostafa Langari, Zhiyin Yang, J.-P Pirault, Chris Long, and Jisjoe Jose. 2016. “A Review of Evaporative Cooling System Concepts for Engine Thermal Management in Motor Vehicles.” *Proceedings of the Institution of Mechanical Engineers, Part D: Journal of Automobile Engineering* 231 (November). https://doi.org/10.1177/0954407016674606.